Hojjat Gholizadeh

The Influence of Alloying and Temperature on the Stacking-fault Energy of Iron-based Alloys

Dissertation

written at the Montanuniversität Leoben,
Chair of Atomistic Modelling and Design of Materials

under supervision of
Univ. Prof. Dr. Dr. h.c. Claudia Draxl

Leoben, May 2013

Affidavit

I declare in lieu of oath, that I wrote this thesis and performed the associated research myself, using only literature cited in this volume.

May, 2013 Hojjat Gholizadeh

Abstract

The mechanical properties of steels are influenced by their plastic deformations. In austenitic steels, plastic deformations may occur through different mechanisms including dislocation gliding, twinning (twinning-induced plasticity, TWIP), and phase transformation (transformation-induced plasticity, TRIP). The stacking-fault energy (SFE) governs the activation of these mechanisms; therefore it is a crucial parameter for understanding the plastic deformations. The aim of this thesis is to calculate the SFE in austenitic steels.

In order to investigate the influence of interstitial carbon on the SFE in austenitic carbon steels, we calculate the γ-curve which contains the SFE. Explicit faults are simulated in pure iron, $Fe_{24}C$, and Fe_3C, corresponding to 0, 0.89, and 6.67 wt.% of carbon, respectively. Our first-principles calculations are performed using the all-electron full-potential linearized augmented planewave (FP-LAPW) method implemented in the WIEN2k code. Our results demonstrate a strong dependence of the behavior of the γ-curve on (i) the carbon content, and also on (ii) the position of the interstitial carbon with respect to the fault plane. In agreement with the earlier experimental and theoretical works, we find that the SFE increases with carbon content. Moreover, our results show that the increase rate is not constant, but it is smaller at high concentrations. Finally, we expand the γ-curve to evaluate the entire γ-surface.

In order to investigate the temperature dependence of the SFE in stainless steels, we calculate it for the random alloy $Fe_{0.716}Cr_{0.200}Ni_{0.084}$ over the temperature range of 298–1273 K (25–1000 °C). The SFE is calculated using the axial next-nearest-neighbor Ising (ANNNI) model. The random alloy and the paramagnetic state are taken into account, respectively, using the coherent-potential approximation (CPA) and the disordered local moments (DLM) approach, as implemented in the exact muffin-tin orbitals (EMTO) code. The lattice parameter at different temperatures is provided using the thermal lattice expansion data measured by X-ray diffraction (XRD). The temperature dependence of the local magnetic moments is evaluated by accounting for the fluctuations in the size of magnetic moments. The influence of different approximations and contributions, *i.e.*, the electronic entropy, the thermal expansion, the frozen-core approximation, and the exchange–correlation functional, are intensively investigated. Our results demonstrate that the SFE increases with temperature due to an increase in the lattice volume and in the local magnetic moments. We find that the temperature dependence of the SFE is mainly influenced by the lattice expansion. The thermal excitations of magnetic moments exhibit a rather small influence on the temperature dependence of the SFE. We also find that the choice of the exchange–correlation functional significantly influences the SFE. Good agreement with experimental data can be achieved using the generalized-gradient approximation (GGA).

Zusammenfassung

Plastische Verformungen bestimmen die mechanischen Eigenschaften von Stählen. In austenitischen Stählen können plastische Verformungen durch verschiedene Mechanismen erfolgen, wie etwa durch Versetzungsgleiten, Zwillingsbildung (twinning induced plasticity, TWIP), und Phasenumwandlung (transformation induced plasticity, TRIP). Die Stapelfehlerenergie (SFE) hat Einfluss auf die Aktivierung dieser Mechanismen; deshalb ist sie ein Schlüsselparameter für das Verständnis plastischer Verformungen. Das Ziel dieser Arbeit ist die Berechnung der SFE in austenitischen Stählen.

Um den Einfluss von interstitiellem Kohlenstoff auf die SFE in austenitischen kohlenstoffhaltigen Stählen zu untersuchen, berechnen wir die γ-Kurve, aus der wir die Stapelfehlerenergie ableiten. Explizite Stapelfehler werden in reinem Eisen, $Fe_{24}C$ und Fe_3C berechnet, was Konzentrationen von 0, 0.89 und 6.67 Gew.% Kohlenstoff entspricht. Unsere Ab-initio-Rechnungen werden mit der sogenannten Full-Potential All-Electron Linearized Augmented Plane-Wave (FP-LAPW) Methode durchgeführt, wie sie im Wien2k-Code implementiert ist. Unsere Ergebnisse zeigen ein starke Abhängigkeit des Verhaltens der γ-Kurve (i) vom Kohlenstoffgehalt und auch (ii) von der Lage des interstitiellen Kohlenstoffs in Bezug auf die Stapelfehlerebene. In Übereinstimmung mit früheren experimentellen und theoretischen Arbeiten finden wir, dass die SFE mit dem Kohlenstoffgehalt ansteigt. Darüber hinaus zeigen unsere Resultate, dass der Anstieg nicht konstant erfolgt, sondern bei hohen Konzentrationen niedriger ist. Schließlich erweitern wir die γ-Kurve, um die gesamte γ-Oberfläche auszuwerten.

Um die Temperaturabhängigkeit der SFE in Edelstählen zu untersuchen, berechnen wir den Mischkristall $Fe_{0.716}Cr_{0.200}Ni_{0.084}$ im Temperaturbereich von 293–1273 K (25–1000 °C). Die SFE wird unter Verwendung des *Axial Next-Nearest Neighbor Ising* (ANNNI) Modells berechnet. Die zufällige Verteilung der Elemente auf dem Gitter und der paramagnetische Zustand werden dabei durch Verwendung der *Coherent Potential Approximation* (CPA) bzw. der *Disordered Local Moments* (DLM) Näherung berücksichtigt, wie sie im Exact Muffin-Tin Orbitals (EMTO) Code implementiert sind. Die Gitterkonstanten bei verschiedenen Temperaturen werden dabei von Temperaturausdehnungsdaten aus Röntgenbeugungsmessungen gewonnen. Die Temperaturabhängigkeit der lokalen magnetischen Momente wird unter Berücksichtigung von Schwankungen in der Größe des magnetischen Moments ausgewertet. Der Einfluss verschiedener Näherungen und Beiträge, das heißt der elektronischen Entropie, der Wärmeausdehnung, der sogenannten Frozen-Core-Näherung und des Austausch-Korrelations-Funktionales, werden eingehend untersucht. Unsere Ergebnisse zeigen, dass die SFE deshalb mit der Temperatur ansteigt, weil das Gittervolumen und die lokalen magnetischen Momente größer werden. Wir finden, dass die Temperaturabhängigkeit der SFE hauptsächlich auf die Gitterausdehnung zurückgeht. Die thermische Anregung der magnetischen Momente zeigt einen eher kleinen Einfluss auf die Temperaturabhängigkeit der SFE. Wir finden auch, dass die Wahl des Austausch-Korrelations-Potentials die SFE signifikant beeinflusst. Gute Übereinstimmung mit experimentellen Daten erhält man durch Verwendung der *Generalized Gradient Approximation* (GGA).

Contents

1

Introduction

Iron is widely and abundantly available over the Earth's surface. However, for a long period, iron-nickel meteoroids were the only available resource of iron for mankind [1], as in the terrestrial resources the element is found only in combination with other elements, mainly in the form of oxides mixed with earthy materials [2]. As soon as human learned how to process iron from its ore, the new material was spread everywhere and greatly influenced tool-making technologies. About the importance of iron and its influence on the mankind life style, it is just enough to mention that the third period of human prehistory is called *Iron Age*, following the *Stone Age* and the *Bronze Age* as the first and the second periods [3]. Although iron has always been used since the beginning of the Iron Age (1200 BC in the Middle East and southeastern Europe [3]), its usage increased drastically during the last two centuries, when significant advances in material science and metallurgical technologies introduced many iron-based alloys, *i.e*, *steels*, with great properties. The availability of these materials, together with considerable demands as a consequence of rapid development, has made steels by far the most used metal at the moment.

Properties of iron and steels have been subject of many studies in different fields of science during the past decades [4]. Particularly, plastic deformations of steels are interesting as they influence the mechanical properties of the material which, in turn, are of great importance in both production and operation processes. It has been shown that the mechanism of plastic deformation in high-manganese steels with face-centered cubic (fcc) lattice is related to the value of the *stacking-fault energy* (SFE) [5–7]. The SFE is the energy change upon a fault in the stacking of the close-packed atomic layers of the bulk structure (see Chap. 2). In the fcc structure, the γ-curve and the γ-surface present the energy changes as two crystal halves glide with respect to each other along the close-packed layers (see Chap. 2). The γ-curve and the γ-surface include the SFE, and also much more information about the behavior of the material under shear stress.

There has been many works around the measurement of the SFE or its estimation using semi-empirical methods [8–32]. However, the experimental results are questionable because of the broad range of reported values, and also because of significant uncertainties arising from the microstructure of samples (see Sec. 2.5). Therefore, a theoretical

approach which is not suffering from the mentioned complications is highly desirable for the determination of the SFE. Moreover, to the best of our knowledge, there is currently no experimental approach which is capable of measuring the γ-surface. Thus, the only possible way to provide more information about it is to calculate it.

When studying the structure of materials on the atomic scale, *density-functional theory* (DFT) [33–36] is the most successful and most widely used first-principles approach in computational materials science. Thanks to the significant advances in computational power in the past two decades, nowadays DFT can be applied in order to provide a detailed understanding of material properties. Also, in the case of SFE calculations in steels, DFT results have already been proven to be in good agreement with available experimental data [37, 38].

A few *ab-initio* studies on the evaluation of the SFE and the γ-surface in steels with *interstitial* alloying elements have already been published. For instance, Kibey *et al.* [39] have published the γ-surface calculated in Fe–N alloys, and Abbasi *et al.* [40] have evaluated the SFE for Fe–C alloys. However, to the best of our knowledge, the γ-curve and the γ-surface have never been calculated for Fe–C alloy. In this work, we calculate both quantities for pristine iron, Fe_3C, and $Fe_{24}C$, and the γ-surface for $Fe_{24}C$ (see Chap. 5) [41]. For these calculations, we use the LAPW+LO and the APW+lo basis sets in the supercell approach (see Sec. 4.6) implemented in the WIEN2k code [42]. This code allows us to account for local lattice displacements introduced by atomic forces around the interstitial carbons.

The *ab-initio* evaluation of the SFE has also been the subject of few works on steels with *substitutional* alloying elements. For instance, Vitos *et al.* [37] have calculated the influence of temperature and the chemical composition on the SFE of Fe–Cr–Ni alloys, and Reyes-Huamantinco *et al.* [38] have studied the temperature dependence of the SFE in Fe–Mn alloys. However, the field is still open for further investigations, as the temperature dependence of the SFE is influenced by many parameters. In this study, we calculate the temperature dependence of the SFE in an Fe–Cr–Ni stainless steel, with a especial focus on the influence of different approximations and simplifications on the final results. Particularly, we take into account the thermal lattice expansion of the alloy, a parameter which, to the best of our knowledge, has not been accounted for in Fe–Cr–Ni alloys before. In these calculations, we use the coherent-potential approximation (CPA) [43–45] and the disordered local moment (DLM) approach [46] implemented in the exact muffin-tin orbitals (EMTO) code [47]. This code provides a relevant tool for simulating the random alloy in the paramagnetic state.

This work is organized as follows. Chap. 2, *Stacking-fault Energy*, starts with a general introduction to the close-packing of atomic spheres. As two highly symmetric examples of close-packed structures, we discuss the arrangements of atoms in the face-centered cubic (fcc) and the hexagonal close-packed (hcp) structures. Focusing on the fcc lattice, we introduce the most common stacking faults in this structure. Particularly, the geometry of the intrinsic stacking fault and the related displacements are discussed in detail. In the next step, the energy associated to the stacking fault, *i.e.*, the stacking-fault energy (SFE) and its great influence on the partials dissociation are described

briefly. Finally, the motivations for this study are presented in the last section of the chapter.

Chap. 3, *Metallurgical Background*, covers some general knowledge in the metallurgy of alloys which are subject of this study. We start with the properties of pristine iron, as it is the main component of the alloys we study here. As one of the simplest iron-based alloys, we present the carbon steels with the interstitial carbon as the only alloying element. The discussion covers the introduction of the most important phases in carbon steel, as well as the possible interstitial sites in the considered phase. The third topic in this chapter is about ternary Fe–Cr–Ni stainless steels, their most important phases, and the transformations between these phases.

In Chap. 4, *Theoretical Background*, we give a short summary of the required theoretical background, including density functional theory (DFT), Kohn–Sham equations, and their implementations in two codes, *i.e.*, WIEN2k and EMTO. The WIEN2k code utilizes the linearized augmented plane wave basis set with local orbitals, abbreviated as LAPW+LO. On the other hand, the EMTO code, which is based on the Green's function formalism, utilizes the coherent potential approximation (CPA) and the disordered local moments (DLM) approach in order to simulate random alloys in the paramagnetic state. These approaches are briefly discussed in this chapter.

In Chap. 5, *The Fe–C System*, we present the SFE and the γ-curve calculated for pristine iron, $Fe_{24}C$, and Fe_3C in the fcc phase. Moreover, the γ-surface is evaluated for $Fe_{24}C$. As carbon occupies interstitial sites, significant local lattice deformations are introduced around it, resulting in a global increase in the lattice volume. This effect is taken into account by calculating the equilibrium volume for every composition, and also by relaxing atomic forces in the bulk unit cell. We use the WIEN2k code for our calculations, as the code allows for the relaxation of atomic forces. In order to calculate the entire γ-curve, two crystal halves are glided with respect to each other, and the atomic positions around the displacement are relaxed normal to the slide plane. Carbon can be located in different sites with respect to the fault plane, resulting in significantly different influence on the γ-curve and on the SFE. We consider all possible positions for carbon, and average over them. Finally, using a Fourier expansion which obeys the symmetry properties of the $\{111\}$ plane of the fcc structure, the entire γ-surface is calculated for $Fe_{24}C$.

In Chap. 6, *The Fe–Cr–Ni System*, we present the temperature dependence of the SFE calculated for a random alloy $Fe_{0.716}Cr_{0.200}Ni_{0.084}$ in the range of 298–1273 K (25–1000 °C). The alloy is found in the paramagnetic state in the entire range. Unlike the Fe–C system for which the SFE is calculated explicitly, we use the axial next-nearest-neighbor Ising (ANNNI) model [48, 49], where the SFE is approximated by an expansion whose terms are the Helmholtz free energies of the bulk phases fcc, hcp, double-hcp (dhcp), *etc.* The random alloy and the paramagnetic state are simulated using the EMTO code. Simulating the alloy at finite temperature requires relevant knowledge about the temperature dependence of the lattice spacing and of the local magnetic moments. The former is provided using the thermal lattice expansion data measured by X-ray diffraction (XRD), while the latter is evaluated by accounting for

the fluctuations in the size of magnetic moments. The electronic and the magnetic entropies are calculated for evaluating the free energies of the three above-mentioned phases. Using these free energies, the SFE is calculated as a function of temperature. In order to investigate the influence of different approximations and approaches, *i.e.*, the electronic entropy, the thermal expansion, the frozen-core approximation, and the exchange-correlation functional, we have performed many test calculations and analyzed their results.

There are also two appendices in the thesis. In App. 6.5, *Conclusion*, we present a two-dimensional Fourier expansion which follows the symmetry properties of the {111} plane of fcc structure. This expansion is useful when a two-variable function $f(x, y)$, *e.g.*, the γ-surface, is fitted to a set of data points in the form of (x_i, y_i, f_i). In order to derive this expansion, we apply all symmetry properties of the {111} plane to the general form of the Fourier expansion in two dimensions.

App. A, *Experimental Data*, presents a summary of available experimental data which may be useful when investigating the Fe–Cr–Ni system. These data have been collected from more than 20 references [8–32].

2

Stacking-fault Energy

The aim of this chapter is to define the required terms and to introduce the topic of this work, as well as its importance. We start by describing the geometry of close-packed lattices and then introduce some possible faults and defects related to it. A connection between these faults and the plasticity of materials is shown, which indicates the importance of the topic.

2.1 Close-packed Stacking

In geometry, *close-packing* of spheres of equal size is a dense arrangement of congruent spheres in an infinite and regular lattice. The term close-packing is used in crystallography by considering atoms as hard spherical balls with identical radii. A close-packed atomic layer, *i.e.*, the densest arrangement of atoms in two dimensions, is formed when atoms are packed in a hexagonal lattice (see Fig. 2.1(a)). A three-dimensional close-packed structure is then constructed by stacking such layers on top of one another, so that their atoms occupy one of the sites A, B, or C, whose projections onto a plane normal to the stacking direction are demonstrated in Fig. 2.1(a). Obviously, atomic sites which lie within the same close-packed layer have the same label, and, as a result of translational symmetry of the close-packed layers, feel the same environment. In short, this means that they are equal. Note that such a condition is not necessarily established for sites which are lying within different layers, since, depending on the stacking order, they may feel different environments. However, we will notice two structures where all atomic positions, disregarding their layers and labels, are exactly equal.

The close-packing criterion requires that no two layers of the same label, such as AA, are stacked in juxtaposition to one another [50]. This restriction locates the atomic spheres on the vertices of regular tetrahedra, whose sides equal the interatomic distance a (see Fig. 2.1(b)). The distance between two consecutive atomic layers, the interlayer spacing, equals the height of the tetrahedron which is $d = a\sqrt{2/3}$. Since every tetrahedron contains only 1/3 of an atom, the lattice volume per atom equals $V_{\text{p.atom}} = 3V_{\text{tetrahedron}} = a^3\sqrt{2}/4$. The packing fraction, *i.e.*, the fraction of space occupied by atomic spheres, is calculated by dividing the actual volume of a sphere of

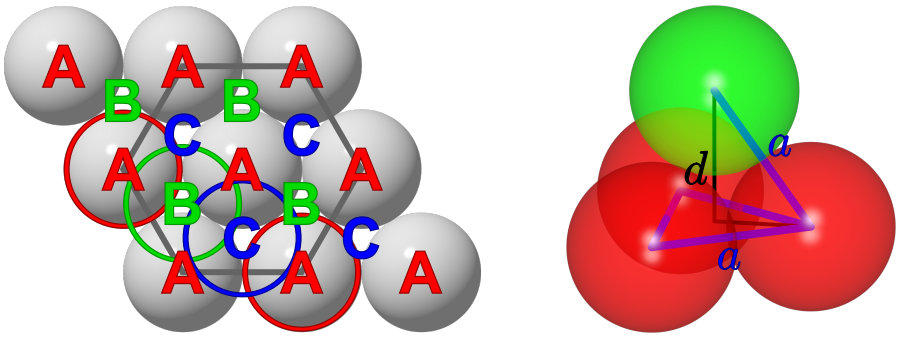

(a) (b)

Figure 2.1: (a) Top view of a close-packed layer with the hexagonal cell and different stacking cites highlighted. Considering the given layer as A, atoms in the second layer would occupy either B or C positions. (b) Geometry of the stacking positions in a close-packed structure presented as a regular tetrahedron of side length a.

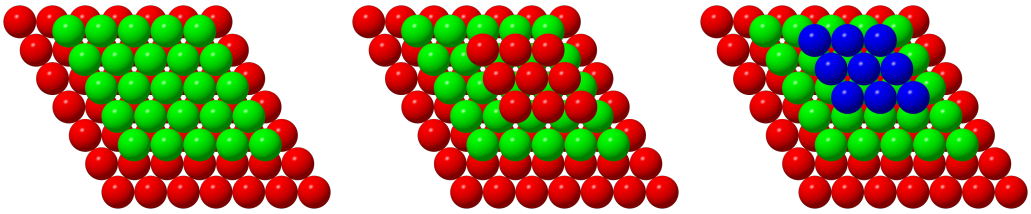

(a) (b) (c)

Figure 2.2: (a) Top view of a two-layer close-packed structure, where the first and the second layers occupy A and B positions, respectively; (b) Given two-layer stacking as AB, the third layer can occupy the same stacking positions as the first layer, leading to an hcp structure with $ABABAB$ sequence. (c) Here, the third layer occupies C positions. If the fourth layer occupies the same stacking positions as the first layer, the result is an fcc structure with $\cdots ABCABC\cdots$ sequence.

diameter a, *i.e.*, $V_0 = \frac{4\pi}{3}(a/2)^3$, by the lattice volume per atom $V_{\text{p.atom}}$. It is quite straightforward to show that any stacking sequence where consecutive layers are of different labels forms a close-packed structure with packing fraction of $\pi/\sqrt{18} \approx 0.74048$, which is the maximum for a lattice of equal atoms [51].

Until now, we have discussed only the general properties of a close-packed structure of atoms. However, in order to have a crystal with translational symmetry in three dimensions, the stacking of the close-packed layers must follow a certain order. Given a layer A, a hexagonal close-packed (hcp) structure is generated by stacking the atomic layers as $\cdots ABABAB\cdots$ (or equally $\cdots ACACAC\cdots$), where every second layer has the same label (see Figs. 2.2(a) and 2.2(b)). In such a structure, all atomic positions are surrounded by the same environment; hence they are equal. The periodicity of this structure along the stacking direction equals two atomic layers. The primitive cell is

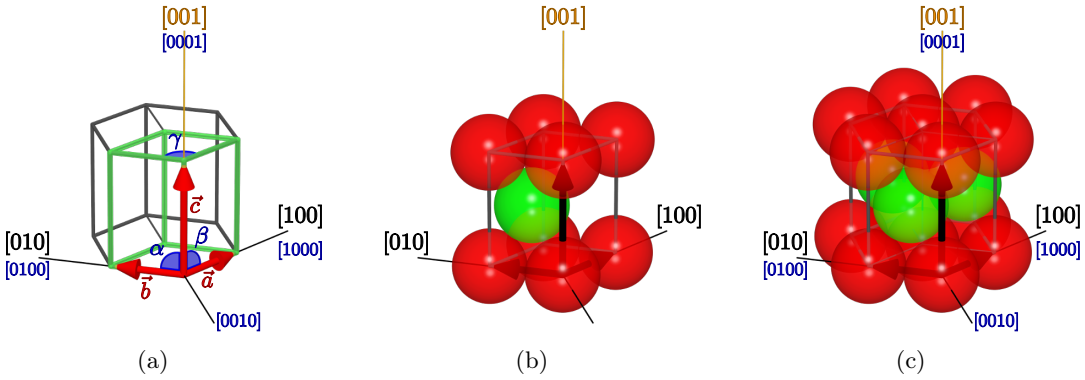

Figure 2.3: (a) Comparison of the conventional hexagonal cell (gray cage) and the primitive cell (highlighted by green color) of the hcp structure. In order to make permutation symmetries apparent, the Miller indices for this lattice are usually presented in the $[hkil]$ scheme, where $i = -(h + k)$ (blue color). (b) Atomic positions in the primitive cell colored regarding to their stacking positions. (c) Atomic positions in the conventional cell.

found as a rhombus-based prism of base sides a and height c, where $c = 2d = a\sqrt{8/3}$, $\alpha = \beta = 90°$, and $\gamma = 120°$ (see Fig. 2.3). With volume of $a^3/\sqrt{2}$, the cell contains two atoms. The conventional unit cell, however, is a hexagonal-based prism which is simply three times as big as the primitive cell. According to the primitive lattice vectors, the close-packed layers lie within the $\{001\}$ planes (or $\{0001\}$, using the four-index scheme). In this lattice, both primitive and conventional cells have the same set of lattice vectors, where the stacking direction is indicated by [001] ([0001]).

The face-centered cubic (fcc) structure is determined by the stacking sequence $\cdots ABCABC \cdots$, which may be equally represented by $\cdots ACBACB \cdots$, where every third layer has the same label (see Fig. 2.2(c)). Although the periodicity of this structure along the stacking direction equals three atomic layers, by choosing a tilted axis for the third lattice vector, $\mathbf{c}$, it is possible to find a primitive cell so that its height is equal to only one atomic layer (see Figs. 2.4(a) and 2.4(b)). This unit cell is a rhombohedron of side length a, angles $\alpha = \beta = \gamma = 60°$, and volume $a^3/\sqrt{8}$ which contains only one atom. The symmetry of the structure allows us to build the same unit cell using a different set of lattice vectors, where all three lattice vectors are equal along the stacking direction (see Figs. 2.4(c)). The conventional unit cell is a cube of side length $a_c = a\sqrt{2}$, where a is the side length of the primitive cell and equals the interatomic distance (see Figs. 2.4(d), 2.4(e), and 2.4(f)). It is four times as big as the primitive cell and hence contains four atoms. Using the lattice vectors of the cubic cell, the close-packed layers and the stacking direction are defined by $\{111\}$ and [111] indices, respectively.

When studying the $\{111\}$ planes, the two mentioned cells for the fcc structure may not be the best possible choices. In such a case, a cell whose vectors are either parallel or normal to the plane is usually more favored. One possible cell with this property is a prism, similar to the primitive cell of the hcp structure, whose base is a rhombus of side

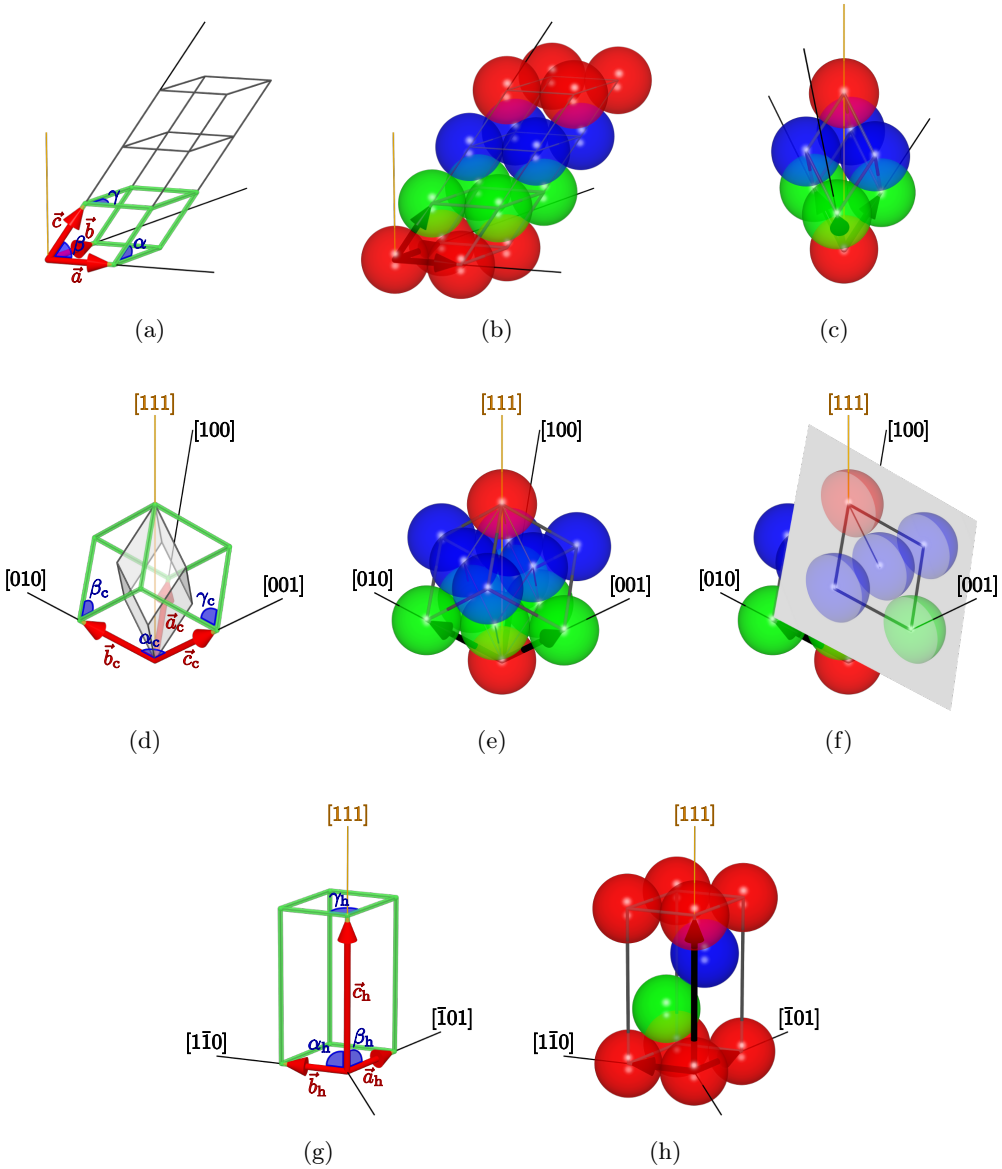

Figure 2.4: (a) The primitive cell of the fcc structure. (b) Atomic positions in the primitive cell. (c) The primitive cell is chosen so that all lattice vectors are equal along the stacking direction. (d) The conventional cubic cell of the fcc structure (highlighted by green) compared to the primitive cell (transparent rhombohedron). (e) Atomic positions in the cubic cell. The cell contains four atoms. (f) For better imagination of atomic positions in the cubic cell, the {001} plane of the cell has been highlighted. (g) Another unit cell for the fcc structure with emphasis on the stacking in [111] direction. Note that the directions shown in this hexagonal cell are based on the lattice vectors of the cubic cell. (h) Atomic positions in the hexagonal cell.

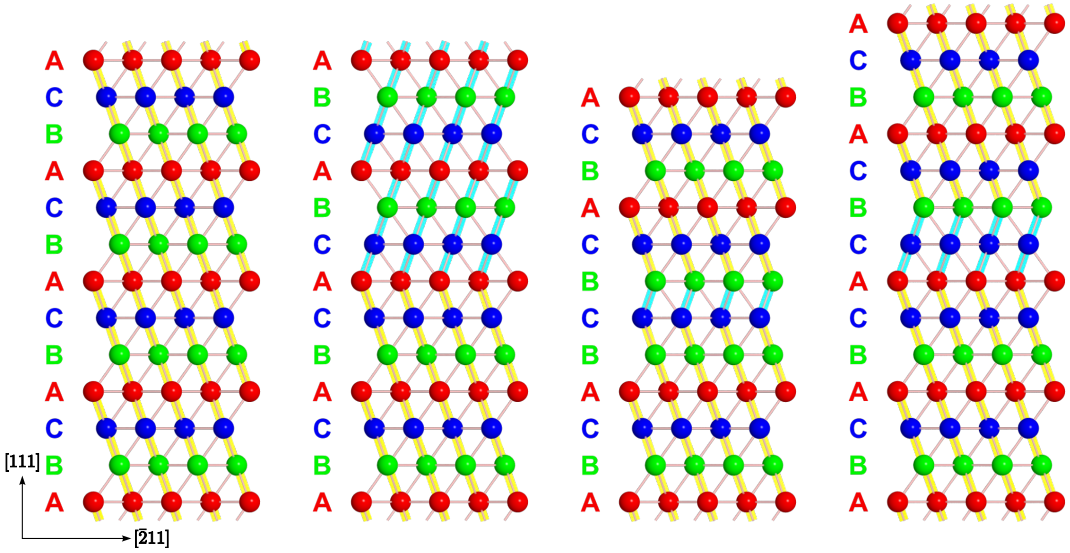

Figure 2.5: (a) The stacking sequence in a perfect fcc structure when looking along the $[0\bar{1}1]$ direction. The structure with the *perfect* stacking sequence has been highlighted by yellow color. (b) Twinning appears when the stacking order along the [111] direction is reversed. The structure with the *reversed* stacking sequence is highlighted by turquoise color. (c) An *intrinsic* SF is generated by *removing* one atomic layer from the perfect sequence. (d) An *extrinsic* SF is generated by *inserting* one atomic layer into the perfect sequence.

length a. However, the hight of this unit cell is $c = a\sqrt{6}$ which differentiates it from the primitive cell the hcp structure (see Figs. 2.4(g) and 2.4(h)). The cell is extended along the [111] direction up to three atomic layers, and hence it contains three atoms.

2.2 Geometry of the Stacking Faults in fcc Crystals

A stacking fault (SF) is a planner defect in a crystal, representing an interruption in the perfect stacking sequence of the atomic layers [52]. The SF in fcc structures is discussed in the 10th chapter of the book *Theory of Dislocations* authored by Hirth and Lothe [50]. We present only a short summary of the subject taken from this book. However, it must be noted that our discussion here focuses only on the fcc lattice, because the exact description of the SF depends on the crystal structure (for instance, see Hirth and Lothe [50] for the SF in other structures like the hcp, the body-centered cubic (bcc), and the diamond cubic lattices).

Using the lattice vectors of the cubic cell of the fcc structure, the stacking direction is indicated by [111], and consequently, the close-packed layers lie within the {111} planes. These planes are also the *glide planes* and the coherent *twin planes*. Twinning may be considered as 180° rotation of one crystal half in the {111} plane, or equivalently, as a

mirror plane reflection about the {111} plane (see Fig. 2.5(b)). Therefore, it changes the stacking of the close-packed layers to

$$\cdots ABCABC\underset{\ddagger}{\overset{\dagger}{A}}CBACBA\cdots, \tag{2.1}$$

where the dagger denotes the twin plane and also the center of the fault.

In the fcc structure, stacking faults are classified as *intrinsic* or *extrinsic*. Geometrically, an intrinsic stacking fault (ISF) simply corresponds to *removing* a layer from the perfect sequence (see Fig. 2.5(c)). Thus, the normal sequence remains unchanged on either sides of the faults right up to the fault plane. The corresponding stacking sequence can be expressed as

$$\cdots ABCABC\,|\,BCABC\cdots, \tag{2.2}$$

where the vertical lines denote the center of the fault. On the other hand, the geometry of the extrinsic stacking fault (ESF) corresponds to *inserting* one additional layer into the perfect sequence (see Fig. 2.5(d)). It generates a stacking sequence in the form of

$$\cdots ABCABC\underset{\shortparallel}{\overset{\shortparallel}{B}}ABCABC\cdots, \tag{2.3}$$

where the vertical double-line shows the inserted layer.

One may consider other faults, containing two consecutive layers of the same label, like

$$\cdots ABCABC\,|\,CABCABC\cdots. \tag{2.4}$$

Such a configuration can simply be generated by removing two consecutive layers from the perfect sequence, *i.e.*, AB here. However, the configuration breaks the close packing at the place of the fault, so it is not energetically favored. To preserve the close packing, the fault can always be converted to the ESF by deforming one of the layers in the vicinity of the fault to another type, like

$$\cdots ABCABC\,|\underset{B}{\overset{\downarrow}{C}}ABCABC\cdots \implies \cdots ABCABC\underset{\shortparallel}{\overset{\shortparallel}{B}}ABCABC\cdots \tag{2.5}$$

or

$$\cdots ABCABC\underset{A}{\overset{\downarrow}{|}}CABCABC\cdots \implies \cdots ABCAB\underset{\shortparallel}{\overset{\shortparallel}{A}}CABCABC\cdots \tag{2.6}$$

A SF can also be generated by a *shear operation* on the {111} planes [50]. Focusing on one of the {111} planes in an fcc structure, an ISF can be produced by displacing all the layers above this plane by the vector $\frac{1}{3}\mathbf{u}_{[\bar{2}11]}$. Such a displacement causes the

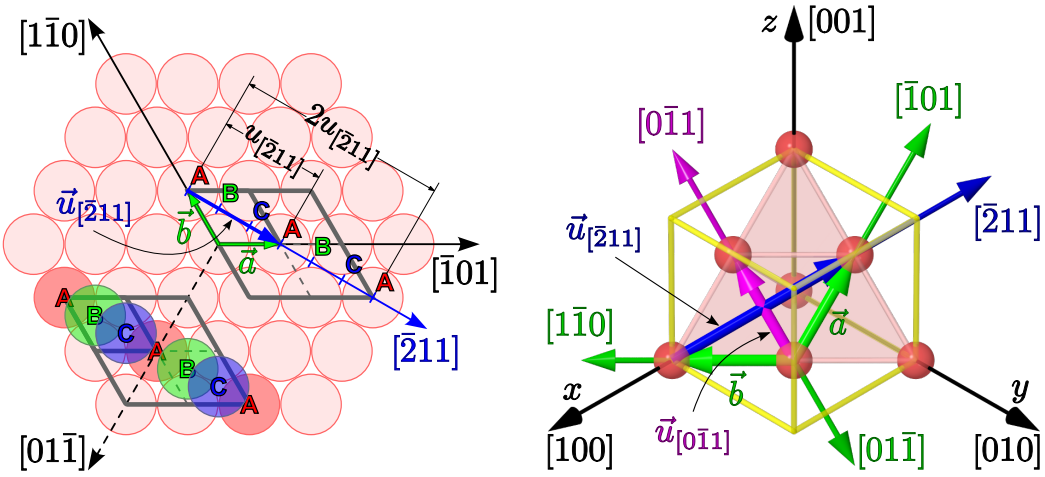

(a) (b)

Figure 2.6: (a) Projection of the atomic layers of types A, B, and C, and the displacement direction, $[\bar{2}11]$, for the transitions $A \to B$, $B \to C$, and $C \to A$ within the $\{111\}$ plane. The smaller rhombus depicts the base of the hexagonal unit cell of the fcc structure, while the larger rhombus shows the base of a 2×2 cell. (b) Definition of lattice and displacement vectors lying in the $\{111\}$ plane using the conventional unit cell.

transitions $A \to B$, $B \to C$ and $C \to A$ for all layers above the mentioned plane (see Fig. 2.6(a)). This process is expressed as

$$\cdots ABCABCABCABC\cdots \underset{BCABCA}{\downarrow\downarrow\downarrow\downarrow\downarrow\downarrow\downarrow} \quad \Longrightarrow \quad \cdots ABCABC\,|\,BCABCA\cdots. \tag{2.7}$$

Once more applying the same shear operation on this structure would produce an ESF:

$$\cdots ABCABC\,|\,BCABCAB\cdots \underset{ABCABC}{\downarrow\downarrow\downarrow\downarrow\downarrow\downarrow\downarrow} \quad \Longrightarrow \quad \cdots ABCABC\overset{\shortparallel}{B}ABCABC\cdots. \tag{2.8}$$

For further convenience, the parameter u is defined as the displacement along the $[\bar{2}11]$ direction. The periodicity of the lattice along the $[\bar{2}11]$ direction is defined as the shortest non-zero displacement which leaves the structure unchanged. The length of this displacement is denoted by $u_{[\bar{2}11]} = a\sqrt{3}$, where a is the interatomic distance (see Fig. 2.6). The required displacements corresponding to the transitions $A \to B$ and $A \to C$ are $u = \frac{1}{3}u_{[\bar{2}11]}$ and $u = \frac{2}{3}u_{[\bar{2}11]}$, respectively (see Fig. 2.6).

2.3 Stacking-fault Energy

A SF rearranges the close-packed layers in a lattice and, thus, changes the total energy of the crystal. This energy change is defined as the *stacking-fault energy* (SFE), which

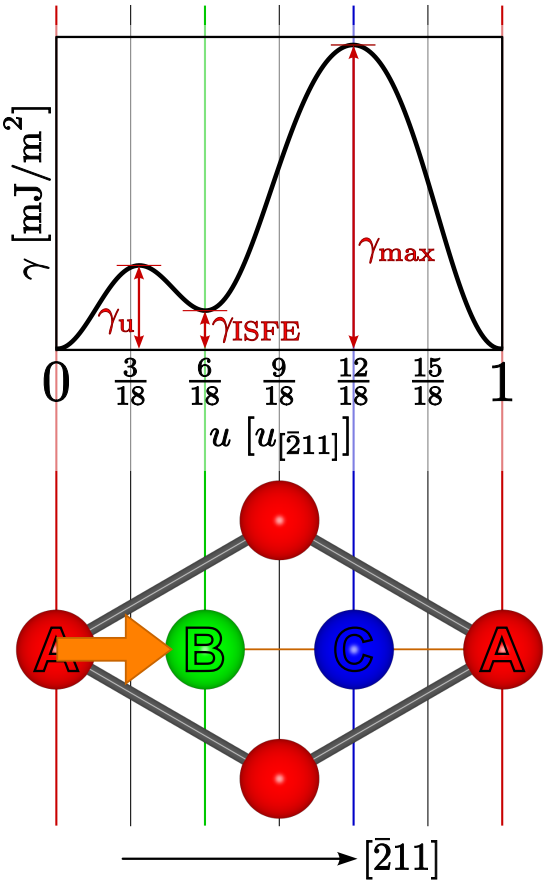

Figure 2.7: A typical γ-curve, corresponding to displacements along the $[\bar{2}11]$ direction in an fcc structure. For every point on the curve, the corresponding displacements can be found in the depicted unit cell at the bottom of the figure.

is a material property on a very small scale, in units of milli-Joules per square meter ($\mathrm{mJ/m^2}$).

While the SFE corresponds to a displacement of $u = \frac{1}{3}u_{[\bar{2}11]}$, the *generalized* stacking-fault energy (GSFE), often called the γ-curve, is defined as a function expressing the dependence of the crystal energy on all possible displacements along the $[\bar{2}11]$ direction. A typical γ-curve is presented in Fig. 2.7. The SFE is the value of the γ-curve at $u = \frac{1}{3}u_{[\bar{2}11]}$, and is a local minimum for materials with stable fcc phase. In the figure, γ_{u} denotes the barrier which must be overcome to create the ISF. γ_{max} corresponds to a transition of $A \rightarrow C$, where two consecutive layers of the same type stack on top of each other. Thus, the curve shows a pronounced maximum here.

The γ-surface is even more general, and expresses the energy dependence of the crystal on all possible displacements within the $\{111\}$ plane, disregarding their directions. It is a function of two variables, $f(x, y)$, spanning the entire $\{111\}$ plane.

The SFE is related to the preferred mechanism through which the plastic deforma-

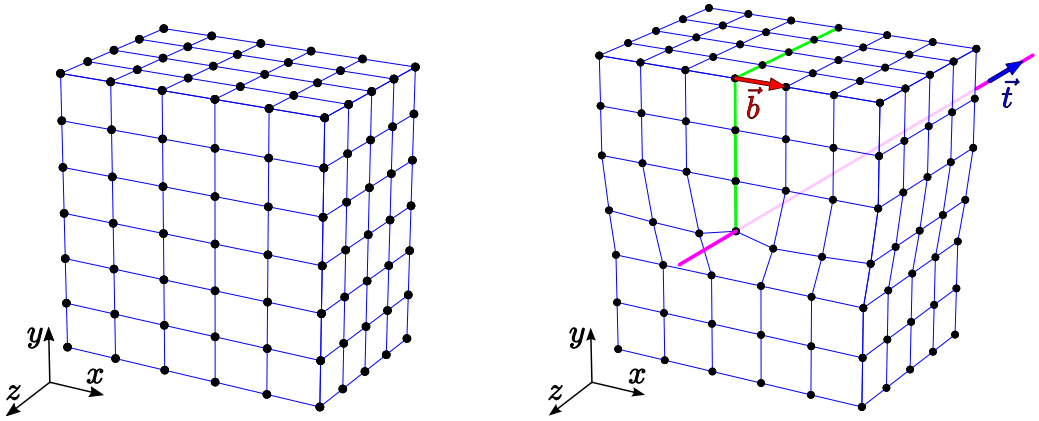

(a) (b)

Figure 2.8: (a) A perfect crystal lattice with a simple cubic unit cell. (b) Rearrangement of atomic positions around an edge dislocation, where the inserted extra layer is highlighted by the green color.

tion occurs in fcc metals [5–7]. In order to explain it, we first shortly discuss dislocations in fcc crystals. In a crystal, dislocations are linear imperfections around which the regular arrangement of the atoms is locally disturbed [52]. The direction of a dislocation is defined by the *dislocation line*, whose unit vector is usually denoted by $\hat{\mathbf{t}}$. There are two primary (basic) types of dislocations: *edge dislocations* and *screw dislocations*. For these primary dislocations, the dislocation line is a straight line resulting in a constant dislocation vector $\hat{\mathbf{t}}$. However, in more general cases, *i.e.*, common mixed dislocations combining aspects of both types, the dislocation vector may vary with position: $\hat{\mathbf{t}} = \hat{\mathbf{t}}(\mathbf{r})$. For an infinite lattice with a single dislocation of primary type, moving along the dislocation line preserves the same surrounding environment. In the core of any dislocation, atomic bonds are not in an equilibrium configuration, and thus the crystal energy and entropy change by introducing such defects.

An edge dislocation can be created by terminating one atomic plane in the middle of a crystal. Obviously, it can also be considered as insertion of an extra half-layer between other atomic layers. A schematic edge dislocation is presented in Fig. 2.8(b), where the inserted half-layer is highlighted by the green color. The surrounding planes do not remain flat, but instead, bend around the edge in order to fill the newly created vacancies, resulting in reordering the crystal structure on either side. Here, the dislocation line passes through the atomic sites at the edge of the terminated layer (pink line in the figure). Compared to a perfect crystal (Fig. 2.8(a)), the crystal lattice is distorted around the dislocation line. The direction and the magnitude of this distortion are denoted by the Burgers vector, $\mathbf{b}$, which is necessarily a lattice vector for *perfect* dislocations. The magnitude of the Burgers vector, b, is a measure for the *strength* of the dislocation, or the amount of elastic deformation in the core of the dislocation. For an edge dislocation, the Burgers vector is always perpendicular to the dislocation line

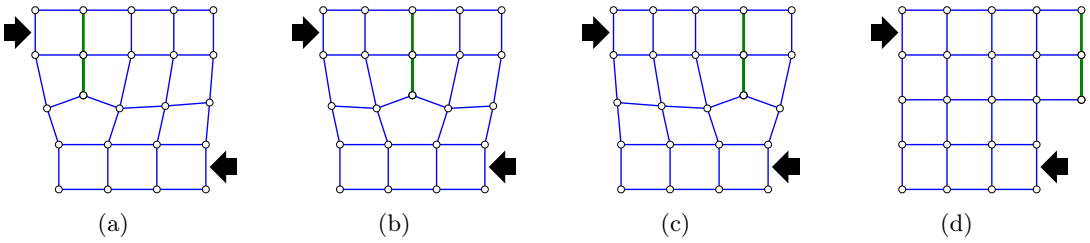

Figure 2.9: Slip movement of an edge dislocation in a simple cubic lattice. Black arrows indicate the applied shear stress.

(see Fig. 2.8(b)).

Dislocations can slip in planes containing both the line and the Burgers vector [52]. Such a plane is called *slip plane* or *glide plane*, and a dislocation able to move in this way is called *glissile* [52]. For an edge dislocation, the dislocation and the Burgers vectors are perpendicular, so there is only one plane in which the dislocation can slip. The required activation energy for dislocation slip may be provided by shear stress. In every step of a dislocation slip, around the dislocation line, atomic bonds break on one side of the defect, and new bonds form on the other side, resulting in the movement of the extra layer for one Burgers vector (see Fig. 2.9). Thus a series of single slips can move two crystal halves with respect to each other, pushing the dislocation. In fcc structures, slip occurs within the close-packed (111) planes and along the <110> directions [50], which include the the shortest lattice vectors, $a = a_c\sqrt{2}/2$, and hence the shortest Burgers vector.

As already mentioned, dislocations change the crystal energy, which is usually expressed as the energy change per length of dislocation, $E = U/L$. This energy change is the sum of two parts, *i.e.*, the elastic and the non-elastic contributions [52]. The elastic energy contribution is due to the elastically strained bonds at farther distances with respect to the dislocation line. The non-elastic energy contributions is the result of distorted atomic bonds close to the dislocation line, where elasticity theory can not be applied. The dependence of E on the magnitude of the Burgers vector may be approximately expressed as

$$E = \alpha b^2, \tag{2.9}$$

where α is almost constant with respect to b and is a property of the crystal [50, 52]. This equation shows that dislocations would energetically prefer to have the shortest possible Burgers vectors. That is why there are no dislocations with Burgers vectors larger than the smallest crystal translation vector; a dislocation with larger Burgers vector simply splits into two or more dislocations with shorter Burgers vectors.

Suppose that the close-packed layers shown in Fig. 2.10(a) correspond to two adjacent layers in an fcc structure, where the atoms in blue and red are originally in sites C and A, respectively. A perfect edge dislocation requires the translation of an atom in site A to the nearest site of the same type. In the figure, this nearest site is chosen along the $[\bar{1}01]$ direction whose corresponding Burgers vector is denoted by $\mathbf{b} = \frac{1}{\sqrt{2}} a_c \, \hat{\mathbf{e}}_{[\bar{1}01]}$,

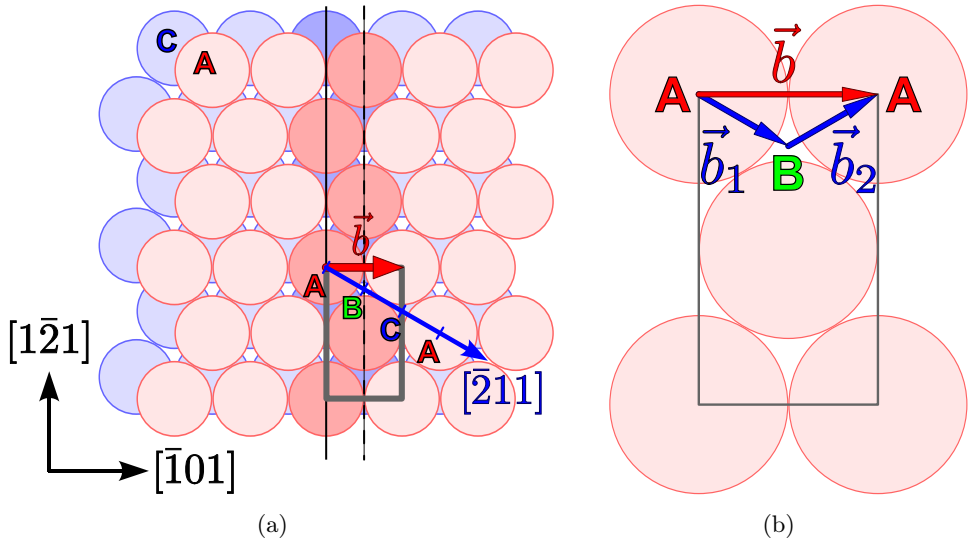

(a) (b)

Figure 2.10: (a) Top view of the {111} plane of an fcc structure, as a slip plane for an edge dislocation along the $[1\bar{2}1]$ direction. Note that a perfect edge dislocation in this lattice requires insertion of two atomic layers, which are highlighted here. (b) The Burgers vector of the perfect edge dislocation can be split into two shorter Burgers vectors, along $[\bar{2}11]$ and $[\bar{1}\bar{1}2]$ directions.

where a_c is the lattice parameter and $\hat{\mathbf{e}}_{[\bar{1}01]}$ stands for the unit vector along the $[\bar{1}01]$ direction, both defined for the cubic unit cell. As it is shown in Fig. 2.10(b), the symmetry of the {111} plane provides an alternative path for the motion: from A at origin to a site of type B along the $[\bar{2}11]$ direction with the Burgers vector $\mathbf{b}_1 = \frac{1}{\sqrt{6}} a_c \, \hat{\mathbf{e}}_{[\bar{2}11]}$, and then from B to A at destination with $\mathbf{b}_2 = \frac{1}{\sqrt{6}} a_c \, \hat{\mathbf{e}}_{[\bar{1}\bar{1}2]}$. This results in a crystal with two dislocations, separated by an area where atoms have been displaced from their original stacking positions. Regarding our discussion in the previous section, an intrinsic stacking fault occurs in this area. The Burgers vectors associated with these two dislocations, $\mathbf{b}_1$ and $\mathbf{b}_2$, are not translation vectors of the fcc lattice. Generally, such dislocations are called *partial dislocations*, and necessarily border a two-dimensional defect, usually a stacking fault [52]. Partial Burgers vectors and stacking faults thus may exist if the packing of atoms defining the crystal has additional symmetries not found in the lattice. These additional symmetries can appear where multiple atoms with proper symmetrical arrangement are placed in a lattice point.

The dissociation of a perfect dislocation to partials, as was explained here, substitutes the Burgers vector $\mathbf{b}$ with two shorter vectors $\mathbf{b}_1$ and $\mathbf{b}_2$. These two vectors are inclined at 60° to one another, hence their corresponding partials repel each other. Although the crystal restores its perfect lattice arrangement behind the partials, a ribbon of the stacking fault is created as partials move apart. These partial dislocations with Burgers vectors of length $a_c/\sqrt{6}$ along the <112> directions and glissile on the {111} planes are called *Shockley partials* [50, 52]. The procedure of dissociation of a perfect edge dislocation to extended dislocation consisting of two Shockley partials and an en-

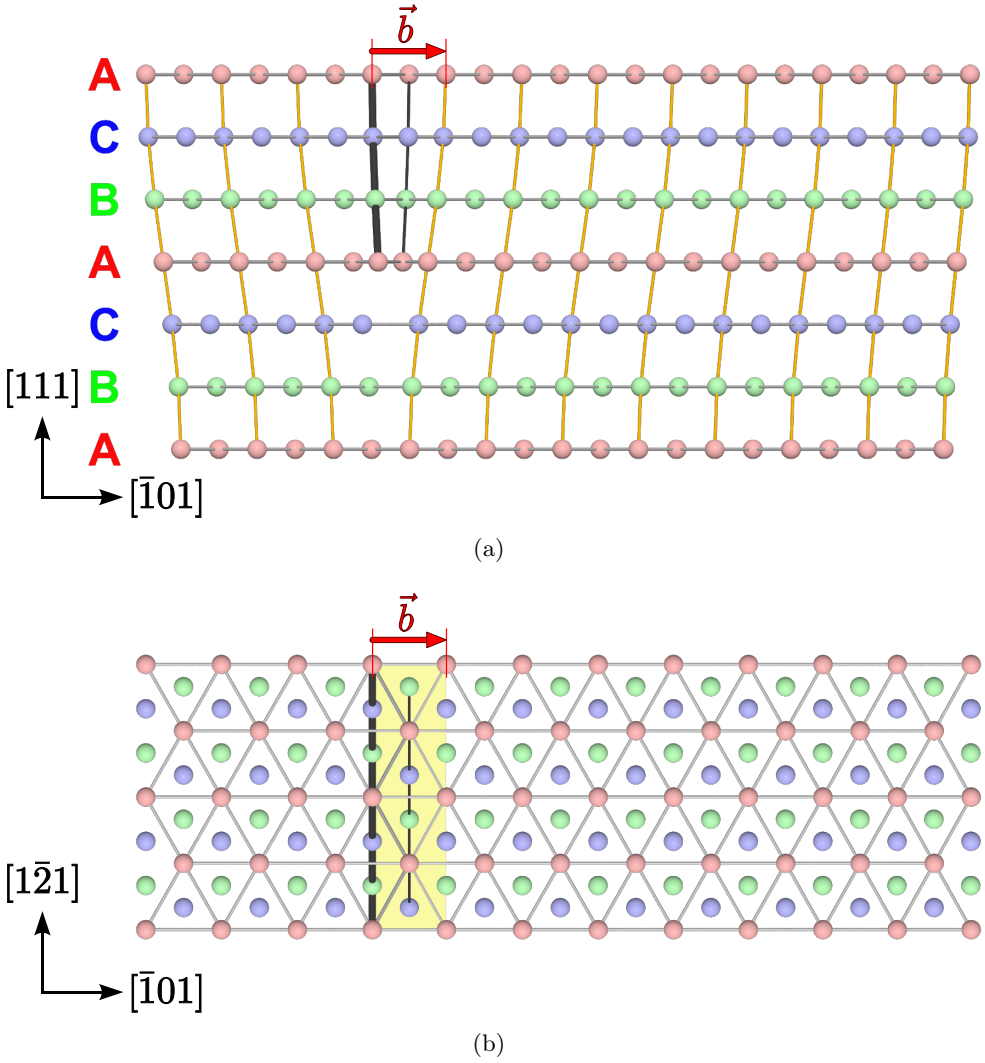

Figure 2.11: (a) Perfect edge dislocation in an fcc structure, viewed along the dislocation line. (b) The same dislocation, viewed from top.

closed stacking fault is presented in Figs. 2.11 and 2.12. Fig. 2.11 depicts the perfect edge dislocation with dislocation and Burgers vectors along [1$\bar{2}$1] and [$\bar{1}$01] directions, respectively. In the figure, all atomic sites are indicated as spheres colored according to their stacking position along the [111] direction. For better visualization of the lattice periodicity along the [$\bar{1}$01] direction, only every second atomic plane is depicted. The inserted extra atoms and their layers are highlighted. Fig. 2.12 depicts the Shockley partials separated by distance d. Here, beside the inserted extra atoms, those atomic sites which are displaced due to the SF are highlighted too. Close to the slip plane, atomic bonds which are distorted due to the SF are highlighted by the turquoise color.

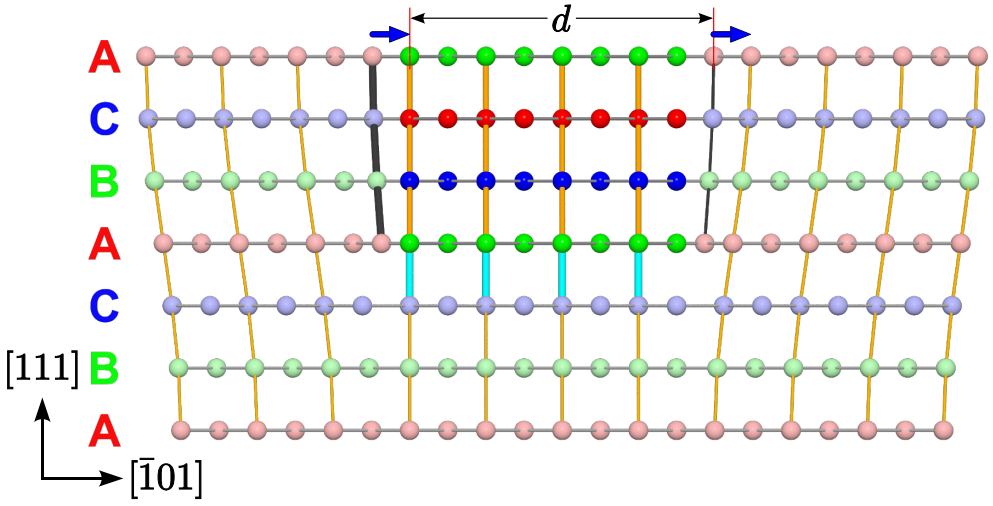

(a)

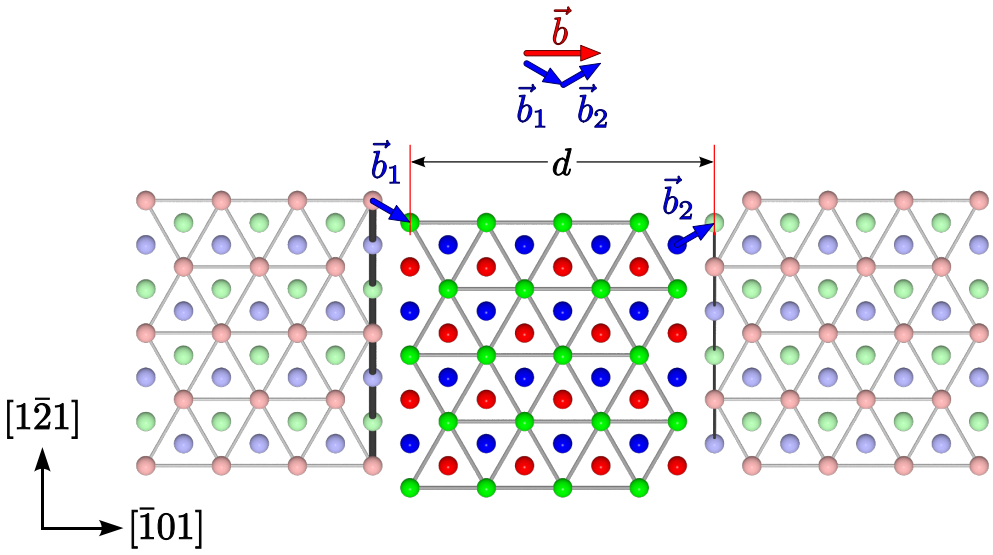

(b)

Figure 2.12: (a) Dissociation of a perfect edge dislocation into two Shockley partials, viewed along the dislocation line. (b) Top view of the Shockley partials.

The procedure of Shockley-partials separation influences the total energy of the crystal by three terms. First of all, since in the fcc lattice $b = a_c/\sqrt{2}$ and $b_1 = b_2 = a_c/\sqrt{6}$, and hence $b^2 > b_1^2 + b_2^2$, the dissociation of the Shockley partials lowers the dislocation energy (see Eq. 2.9). This energy change is not dependent on the distance d between partials. The second term is based on the interaction between two partials. Partials repel each other, and the interaction energy decreases by a factor of $1/d$. Based

on this term alone, the partial dislocations would maximize the distance d. The third term altering the total energy is the energy cost upon creating the stacking fault which is stretched out by the dissociation of partials. This term is proportional to the SFE as the energy change per area, and the total area of the SF, which increases by d. Based on this term alone, the partial dislocations would minimize the distance d. In total, the crystal energy decreases by the partial dissociation, while the distance d is determined by an equilibrium between other two terms. This equilibrium d is mainly dependent on the SFE, so that for a lower value of the SFE a larger separation between Shockley partials is expected [52].

2.4 Importance of the SFE

Plastic deformations in fcc metals may occur through different mechanisms including partial and perfect dislocation gliding, twinning (resulting in twinning-induced plasticity, TWIP), and phase transformation (resulting in transformation-induced plasticity, TRIP). The SFE is a crucial parameter for understanding plastic deformation of fcc metals, since it governs the activation of these mechanisms. Although dislocation gliding is present everywhere, it is the dominant mechanism where the SFE is quite high. The TWIP mechanism generally occurs in stable austenite where the Gibbs free energy of the martensitic transformation, $\Delta G^{\mathrm{fcc}\rightarrow\mathrm{hcp}}$, is positive and the stacking fault energy is in a moderate range. The TRIP mechanism, on the other hand, appears in metastable austenite where $\Delta G^{\mathrm{fcc}\rightarrow\mathrm{hcp}}$ is negative and the stacking fault energy is rather low, which implies preferential formation of the hcp phase [5–7].

The role of the SFE in the behavior of fcc alloys under mechanical stresses has quantitatively been studied for high-manganese steels. Frommeyer *et al.* [5] have reported the dominance of the phase transformation for SFE $\leq 16\,\mathrm{mJ/m^2}$, and twining for SFE $\approx 25\,\mathrm{mJ/m^2}$. Grässel *et al.* [6] reported the dominance of phase transformation for SFE $\leq 20\,\mathrm{mJ/m^2}$ and of twining for SFE $> 20\,\mathrm{mJ/m^2}$. Allain *et al.* [7] have reported that the martensitic transformation is the dominant mechanism at low values of the SFE, *i.e.*, SFE $\leq 18\,\mathrm{mJ/m^2}$, twining occurs for moderate values, $12 <$ SFE $\leq 18\,\mathrm{mJ/m^2}$, and for higher values dislocation gliding is favored.

2.5 Measurements of the SFE

Although there is no direct way of measuring the SFE, several indirect experimental methods have been used to determine it [53]. The most direct methods involve observation of dislocation nodes, loops, and tetrahedra by electron microscopy. Less direct methods include the measurement of x-ray texture, third-stage single-crystal work-hardening rates, and combined x-ray measurements of stacking-fault probability and dislocation density [53].

The experimental values for the SFE are highly questionable since the reported ranges are too broad. Reed and Schramm [53] have summarized the reported SFE for five fcc metals, Ag, Au, Cu, Al, and Ni. Considering only the most direct methods

Table 2.1: Measured values for the SFE, summarized by Reed and Schramm [53].

Metal	Average $[mJ/m^2]$	Range $[mJ/m^2]$	Δ [%]
Silver (Ag)	22	16 – 31	−27 – +41
Gold (Au)	50	42 – 61	−16 – +22
Copper (Cu)	62	48 – 85	−23 – +37
Aluminum (Al)	183	110 – 210	−34 – +15
Nickel (Ni)	220	160 – 300	−27 – +36

and omitting others, they came up with average SFE for every element, as presented in Tab. 2.1. As it is obvious from the table, even the most consistent measurements result in a very broad range, sometimes more than 35% variance with respect to the average value.

For plain carbon steels in the fcc phase at high temperature, Adeev and Petrov [54] have measured the SFE to lie between $70\,mJ/m^2$ and $100\,mJ/m^2$ (almost 50% deviation), based on the material grain size. Bampton et. al [19] have reported that different heat treatments applied to samples highly scatter the SFE values measured by observation of dislocation nodes. However, they show that the SFE values measured by observation of isolated dislocations are not dependent on these heat treatments. These reports emphasize the influence of both the sample preparation and the measurement method on the experimental results.

Beside the accuracy of experimental values, the measurement itself is quite complicated and difficult, since many parameters including sample quality (grain size, homogeneity, impurity, *etc.*) and picture quality must be well controlled in order to get reliable results. Because of the controversies among published results and these difficulties, a theoretical approach for evaluating the SFE is highly motivated. A systematic study based on theoretical methods would lead to a fundamental understanding of the topic, which is of great importance for designing new materials.

3

Metallurgical Background

In this chapter, a short introduction to carbon steels and iron–chromium–nickel stainless steels is presented. We shortly describe only the most prominent phases which are discussed and referred to in this thesis. For more details on these topics one can refer to books specialized in metallurgy.

3.1 Iron

Steels are alloys that mainly consist of iron, thus a good starting point for understanding steels is to recall the properties of pristine iron. At room temperature, iron is found in the body-centered cubic (bcc) lattice structure, an iron phase so-called *ferrite*, and denoted as α-iron. The ground state electron configuration of an iron atom, [Ar] $3d^6$ $4s^2$, with its four unpaired 3d electrons is mainly responsible for the magnetic properties of iron. At room temperature, the magnetic moments are aligned parallelly within ferromagnetic domains, resulting in the well known ferromagnetic properties of iron. As temperature increases, the thermal agitation of spins opposes their tendency to align, decreasing the alignment within each domain [55].

In the iron-carbon phase diagram, the phase transitions of pristine iron is presented on the vertical axis, where the carbon concentration is zero. This phase diagram is presented at different scales in Figs. 3.1 and 3.2. It demonstrates that, at ambient pressure, the ferromagnetic phase transforms to the paramagnetic phase at the Curie temperature $T_c = 1043\,\mathrm{K}$ (770 °C). In the paramagnetic phase magnetic moments are randomly oriented. The lattice structure does not change due to this magnetic phase transition. The new paramagnetic phase is historically known as β-iron. The bcc structure remains stable until the temperature reaches $T^{\beta\leftrightarrow\gamma} = 1185\,\mathrm{K}$ (912 °C), at which the structure transfers to fcc, the so-called *austenite* denoted by γ-iron. The fcc lattice of austenite is denser than the bcc lattice of ferrite and results in a higher density of austenite by 2%, indicating that the volume per atom is less in austenite [56]. At even higher temperatures, *i.e.*, $T^{\gamma\leftrightarrow\delta} = 1667\,\mathrm{K}$ (1394 °C), the fcc structure transforms back to the bcc structure, a high-temperature paramagnetic bcc phase denoted by δ-iron. Finally, at $T = 1811\,\mathrm{K}$ (1538 °C), δ-iron melts.

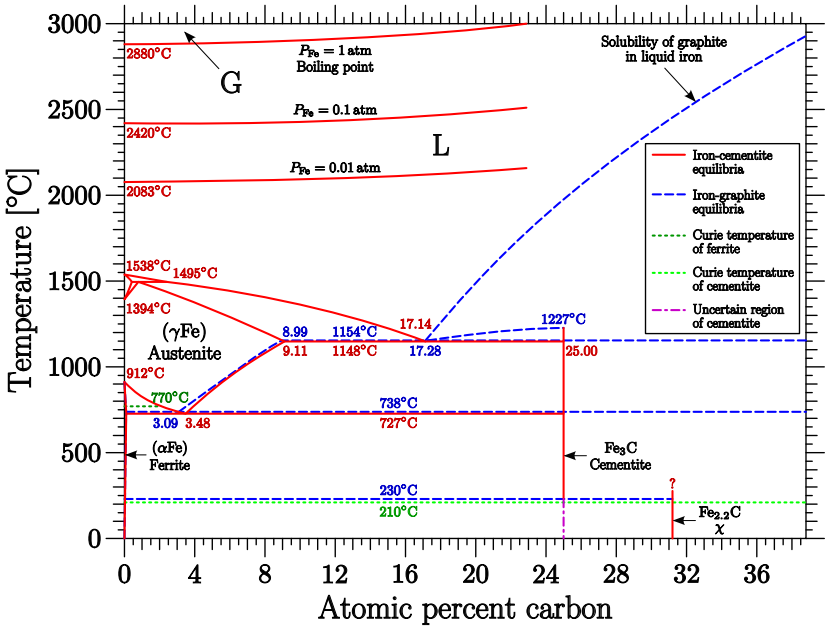

(a)

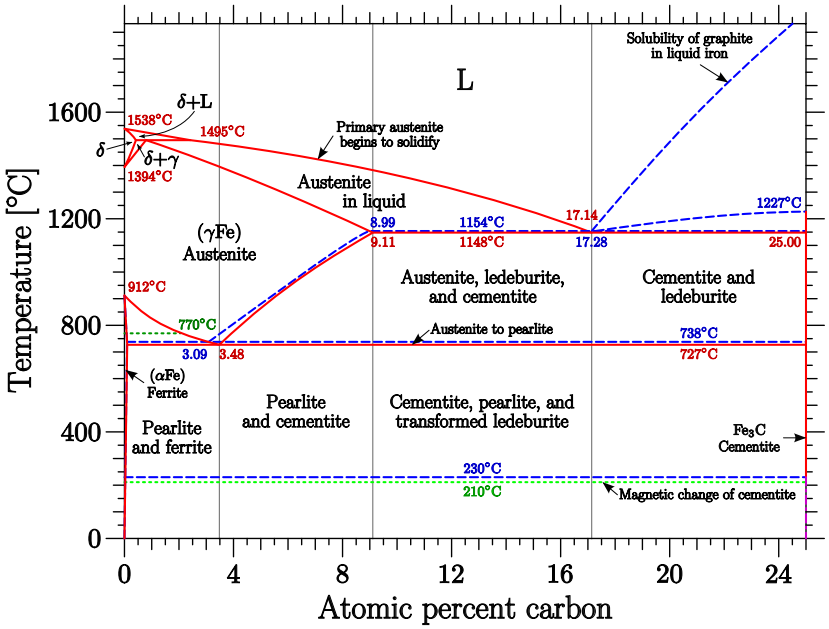

(b)

Figure 3.1: (a) Equilibrium phase diagram for the binary iron-carbon system in a wide range of concentration and temperature. The picture is a reproduction of the original diagram taken from *Binary Alloy Phase Diagrams* [57]. (b) The same phase diagram with emphasis on a range of lower carbon concentrations and lower temperatures. It was recreated using the original version taken from *Materials Science and Metallurgy* [58].

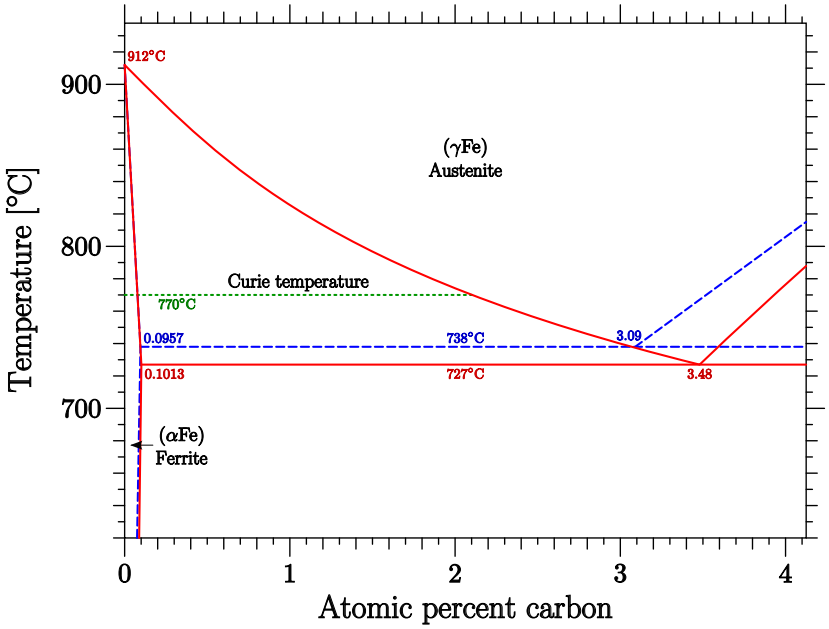

Figure 3.2: Equilibrium phase diagram for the binary iron-carbon system at low carbon contents. The picture is a reproduction of the original diagram taken from *Binary Alloy Phase Diagrams* [57].

3.2 Carbon Steels

Carbon steels are those steels in which the main interstitial alloying constituent is carbon. More precisely, the American Iron and Steel Institute (AISI) defines carbon steel as the following [59]:

> *A steel may be classified as a carbon steel if (1) the maximum content specified for alloying elements does not exceed the following: manganese 1.65%, silicon 0.60%, copper 0.60%; (2) the specified minimum for copper does not exceed 0.40%; and (3) no minimum content is specified for other elements added to obtain a desired alloying effect.*

Due to their wide range of strength, hardness, and ductility as well as their low costs, carbon steels are by far the most frequently used steels. Variations in carbon content have large effects on their mechanical properties. The addition of interstitial carbon up to 2 wt.% combined with an appropriate heat treatment increases the strength and hardness of these steels and decreases their ductility. Higher carbon concentrations, however, reduces their strength and hardness. Moreover, regardless of the heat treatment, interstitial carbon lowers the melting point of steels [2].

Generally speaking, carbon steels contain up to 2 wt.% total alloying elements and can be subdivided into low-carbon steels, medium-carbon steels, high-carbon steels, and ultrahigh-carbon steels. Beyond this limit, an alloy of iron and carbon with carbon

content within the range of 2–4 wt.% is called *cast iron*. The classification of carbon steels based on their carbon content is as the followings [60]:

- **Low-carbon steels** contain up to 0.3 wt% C. While their low carbon content disables hardening through heat treatment, it enables excellent formability in cold working.
- **Medium-carbon steels** are similar to low-carbon steels except that the carbon ranges from 0.3 to 0.6 wt%. This level of carbon content allows hardening through heat treatment. They make a balance between ductility and strength and have good wear resistance.
- **High-carbon steels** contain from 0.6 to 1 wt% C, which makes them very strong.
- **Ultrahigh-carbon steels** are experimental alloys containing 1 to 2 wt% C. They can be tempered to great hardness.

The addition of carbon significantly alters the phase stability of iron (see Fig. 3.1). In order to provide the basic knowledge which will be required in the next chapters, we present the most important phases below [56, 61].

3.2.1 Ferrite (α)

In an iron-carbon alloy, the *ferrite* phase, also known as the α-phase or the α-ferrite, is a solid solution of iron and carbon with iron atoms arranged in a bcc lattice and carbons occupying interstitial sites. In the bcc structure, there are two types of interstitial sites, octahedral sites and tetrahedral sites. An octahedral site is defined at the center of an irregular octahedron whose faces are isosceles triangles of base length a_{bcc} and equal sides of length $\frac{\sqrt{3}}{2}a_{\mathrm{bcc}}$ (see Fig. 3.3(a)). The same triangles can compromise an irregular tetrahedron including a so called tetrahedral site at its center (see Fig. 3.3(b)).

Using a hard ball representation for iron atoms, the radius of an interstitial site is defined as the radius of the largest sphere which can be placed at the site without overlapping with other atomic spheres. Taking into account that the radius of atomic spheres in a bcc structure is $\frac{\sqrt{3}}{4}a_{\mathrm{bcc}}$, the ratio between the radius of the interstitial site and the radius of iron atoms is found $2/\sqrt{3}-1 \approx 0.1547$ and $\sqrt{5/3}-1 \approx 0.2910$ for octahedral and tetrahedral sites, respectively. Although the radius of the tetrahedral site is larger than that of the octahedral site, experimental [62] and *ab-initio* [63] studies show that carbon prefers to accommodate in octahedral sites. The metallic radius of iron and the covalent radius of carbon are 1.24 Å and 0.77 Å, respectively [64], thus the radius of a carbon atom is estimated to be 0.62 of that of iron atoms. This simple consideration demonstrates that both sites, in their initial configuration, are far too small for accommodating carbon. However, it turns out that, after local lattice relaxations which expands the bcc lattice around interstitial carbons, carbon atoms prefer to stay in distorted octahedral sites where they have only two iron atoms close to them, rather than four close iron atoms as realized in the tetrahedral sites [63].

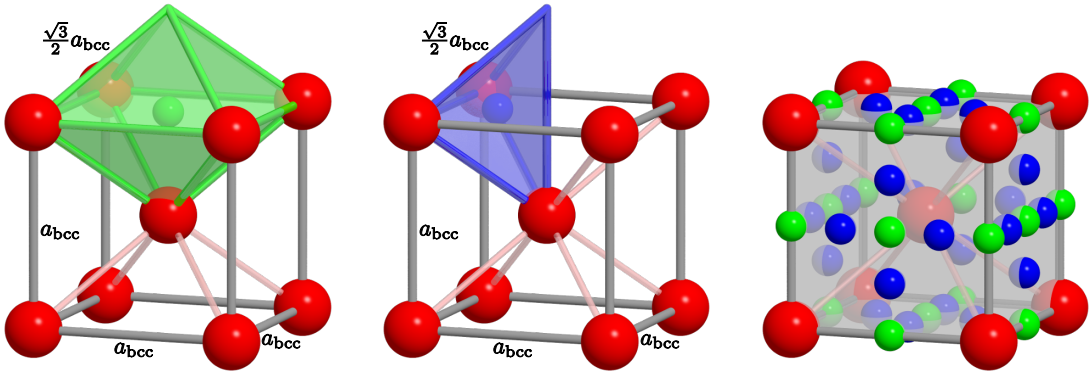

(a) (b) (c)

Figure 3.3: (a) An interstitial *octahedral* site in the bcc structure, defined at the center of an irregular octahedron. (b) An interstitial *tetrahedral* site in the bcc structure, defined at the center of an irregular tetrahedron. (c) In every cubic (conventional) unit cell of the bcc structure, there are six octahedral sites (small green spheres), three with centers lying on cell faces, and the other three with centers on the middle of the cell sides. There are also 12 tetrahedral sites (small blue spheres), all with centers on the cell faces.

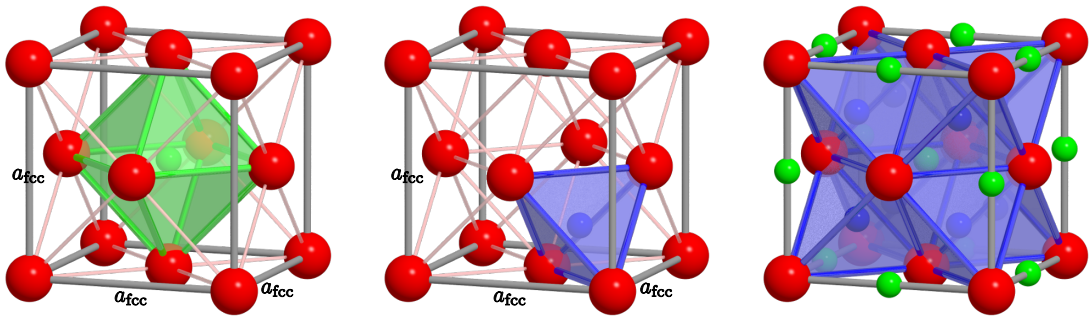

(a) (b) (c)

Figure 3.4: (a) An interstitial *octahedral* site in the fcc structure, defined at the center of a regular octahedron. (b) An interstitial *tetrahedral* site in the fcc structure, defined at the center of a regular tetrahedron. (c) In every cubic (conventional) unit cell of the fcc structure, there are four octahedral sites (small green spheres), one entirely confined at the center of cell, and others with centers on the middle of cell sides. There are also eight tetrahedral sites (small blue spheres), entirely confined in the cell.

Speaking more precisely, the tetrahedral site is neither a stable nor a metastable site, but only a transitional site on the minimum-energy path through which a carbon diffuses between two neighboring octahedral sites. *Ab-initio* simulations demonstrate that as carbon passes through this transitional site, the system's total energy reaches its maximum, resulting in a diffusion barrier of 0.86 eV [63], which is in good agreement with the experimental value of 0.87 eV [65].

The small size of the octahedral sites makes it difficult to accommodate carbon atoms, thus the solubility of carbon in α-iron is very low, with a maximum of 0.1013 at.% (0.0218 wt.%) observed at 1000 K (727 °C). This limited solubility restricts the existence of the pure α-phase of carbon steel in a very small area in the phase diagram (see Fig. 3.2). The α-ferrite is relatively soft [66] and is ferromagnetic at temperatures below 1043 K (770 °C) (see Fig. 3.2).

3.2.2 Austenite (γ)

In an iron-carbon alloy, the *austenite* phase, also known as the γ-phase or the γ-austenite, is a solid solution of iron and carbon with iron atoms arranged in an fcc lattice, and carbons occupying interstitial sites of the fcc lattice. The above-mentioned octahedral and tetrahedral sites are also present in the fcc structure, however, here both are regular bodies with sides of length $\frac{\sqrt{2}}{2}a_{\text{fcc}}$ (see Fig. 3.4). Although the packing of atoms in the fcc lattice is denser compared to that in the bcc structure, the radius of interstitial sites in the fcc lattice is larger. Taking into account that the radius of atomic spheres in an fcc structure is $\frac{\sqrt{2}}{4}a_{\text{fcc}}$, the ratio between the interstitial radius and the radius of iron atoms is given by $\sqrt{2}-1 \approx 0.4142$ and $\sqrt{3/8}-\frac{1}{2} \approx 0.1124$ for octahedral and tetrahedral sites, respectively.

Unlike the bcc lattice, in the fcc structure, carbon is accommodated in the more spacious interstitial sites. Experimental observations [67] as well as theoretical studies based on molecular dynamics [68] and *ab-initio* calculations [63] agree in the fact that, in fcc iron, interstitial carbon prefers octahedral over tetrahedral coordination. Unlike the case in ferrite, the tetrahedral site in austenite is a metastable site on the minimum-energy path through which a carbon diffuses between two neighboring octahedral sites [63]. Here, *ab-initio* calculations find diffusion barriers of 0.99 eV and 2.70 eV, respectively for the ferromagnetic high-spin and for the nonmagnetic austenite [63], which are quite different from the experimental value of ∼1.60 eV measured in the high-temperature paramagnetic austenite phase [69].

Due to the larger voids between iron atoms in the fcc structure, austenite can accommodate more carbon than ferrite. Nevertheless, the lattice has to expand around interstitial carbons. According to the phase diagrams in Figs. 3.1 and 3.2, austenite can accept a maximum of 9.11 at.% (2.11 wt.%) of carbon at 1421 K (1148 °C), which is almost 100 times greater than the maximum carbon content in ferrite. As carbon content increases further, a mixture of austenite, ledeburite, and cementite is formed.

The equilibrium phase diagram demonstrates that austenite is not stable at room temperature. However, particularly in high carbon steels, it might be found at room

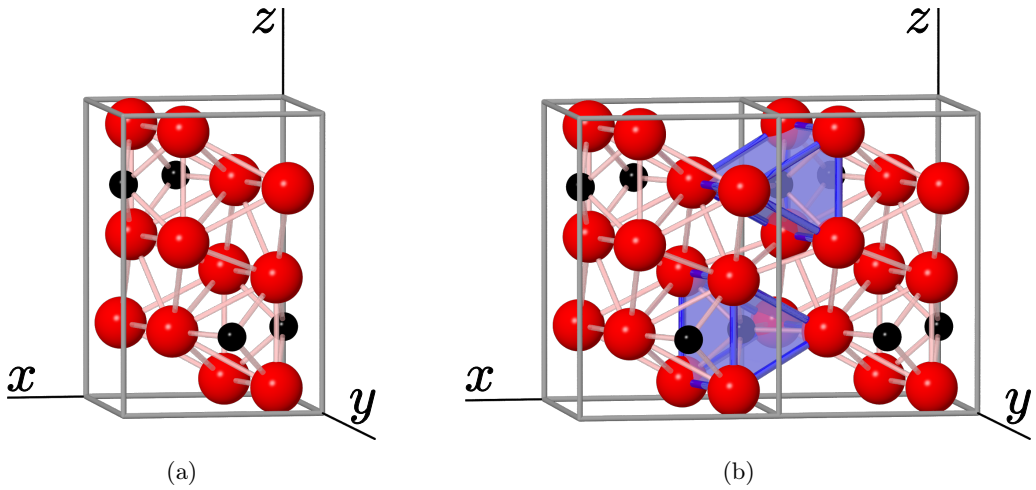

(a) (b)

Figure 3.5: (a) Unit cell of cementite with 12 iron and 4 carbon atoms. (b) Repetition of the unit cell along the x-axis shows prismatic sites occupied by carbon. Two prisms are highlighted for clarity.

temperature as a metastable phase mixed with martensite (see 3.2.4). For instance, in the Fe–1.86wt.%C steel, a significant fraction of the alloy is still in the austenite phase at room temperature [61].

3.2.3 Cementite (Fe_3C), Pearlite, and Ledeburite

As the concentration of carbon exceeds its solubility in ferrite, accumulation of the extra carbon starts forming phases which can contain a higher amount of carbon. One of these phases is *cementite*, also known as iron carbide, which is a chemical compound of iron and carbon, with the formula Fe_3C, containing 6.67 wt.% carbon. Since it is a chemical compound, unlike in solid solutions, its carbon content is always fixed. It means that, in the phase diagram, the pure cementite phase exists only in a very narrow region, more accurately a vertical line, at the carbon concentration of 25.0 at.% (6.67 wt.%). Cementite has an orthorhombic crystal structure with 12 iron and 4 carbon atoms in the unit cell (see Fig. 3.5(a)), where experimental [70] and theoretical [71] studies show that the interstitial carbons prefer to occupy prismatic sites rather than octahedral sites (see Fig. 3.5(b)). Mechanically, cementite is a very hard and brittle material, whose presence may greatly enhance the strength of some steels [66].

When the carbon content is lower than 3.48 at.% (0.77 wt.%), as indicated in Fig. 3.1(b), the extra carbon, which cannot dissolve in ferrite, results in the formation of colonies with a structure composed of alternating layers of ferrite and cementite, where the relative layer thickness is approximately 8 to 1, respectively. This layered structure is called *pearlite*, also known as eutectoid steel, and contains approximately 3.48 at.% (0.77 wt.%) carbon [66]. During slow cooling pearlite forms by a eutectoid reaction as austenite is below the eutectoid temperature, 1000 K (727 °C). At tempera-

tures below this, an iron-carbon alloy forms a mixture of ferrite and pearlite in the left side of the eutectoid point ($x_C < 3.48$ at.% $\equiv 0.77$ wt.%) and a mixture of pearlite and cementite in the right side of the point ($x_C > 3.48$ at.%). Mechanically, pearlite has properties intermediate between the soft, ductile ferrite and the hard, brittle cementite [66].

Ledeburite is a mixture of about 52% austenite and 48% cementite, and forms at temperatures below 1421 K (1148 °C) in iron-carbon alloys [72]. As temperature decreases, the austenite in the ledeburite converts into pearlite at temperatures below 1000 K (727 °C) (see Fig. 3.1(b)).

3.2.4 Martensite (α')

In carbon steels, *martensite*, also known as the α'-phase or the α'-martensite, is formed through a diffusionless transformation due to rapid cooling of austenite. The diffusionless transformation ensures that the martensite has exactly the same composition as does its parent austenite.

The equilibrium phase diagrams presented in Figs. 3.1 and 3.2 predict that as temperature decreases, depending on the carbon content, austenite may transform into a mixture of ferrite, pearlite, and cementite. Such a transformation occurs only if the cooling rate is slow enough to provide sufficient time for carbon diffusion. On the other hand, when austenite transforms to martensite by rapid cooling, for instance by quenching in water, carbon atoms do not have enough time to diffuse out of ferrite, and hence are trapped in the octahedral sites of the bcc structure. The carbon content of newly-formed ferrite is exactly the same as of the parent austenite, greatly exceeding the limit of the carbon solubility in the bcc structure of ferrite. In order to provide more space for interstitial carbons, the bcc structure is expanded along one of its sides, lets say c, resulting into a body-centered tetragonal (bct) structure. With higher carbon concentration of the martensite, more interstitial sites are filled, and the tetragonality (the tetragonal distortion characterized by the c/a ratio) increases [61].

Martensite is not present in the equilibrium phase diagrams, as its is a metastable phase. If it is heated to a temperature high enough at which carbons become movable, they would diffuse from the octahedral sites in order to form carbides. As a consequence, the martensite transforms to a mixture of ferrite and cementite, and the tetragonality is relieved [61].

3.3 Stainless Steels

Stainless steels, also known as inox steels, are generally defined as corrosion-resistant iron-based alloys with a minimum of about 10.5% (according to the European standard EN10088) [73] or 11% [74] chromium content by mass . The chromium content in these steels reacts with oxygen and forms a thin, invisible protective surface layer of chromium oxide. Due to the ability of the chromium atoms and oxide molecules to pack together tightly, such a layer with a thickness of only a few atoms protects the steel underneath

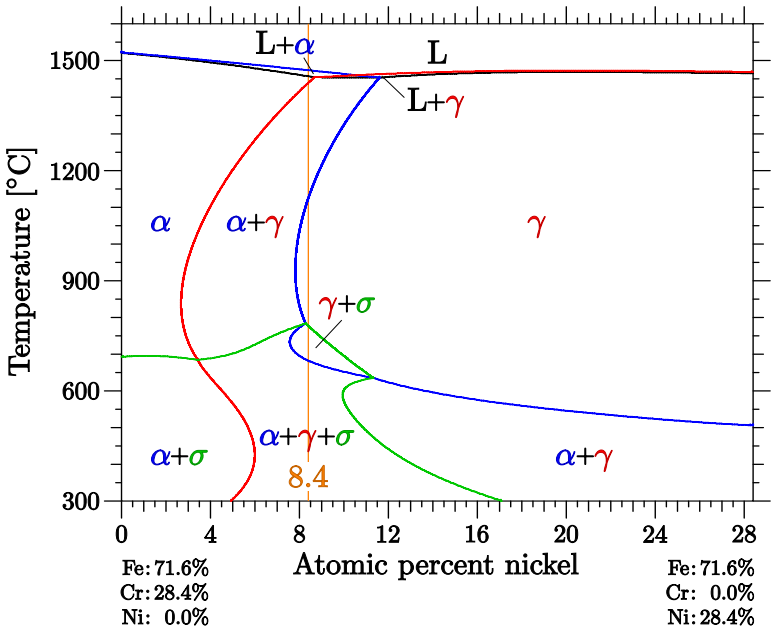

Figure 3.6: The equilibrium pseudo-binary phase diagram evaluated by the Thermo-Calc software [75, 76], where the concentration of iron has been selected according to the A607 alloy (see Chap. 6).

from further oxidation. Although stainless steel does not corrode, rust or stain with water as ordinary steel does, it is not fully stain-proof, most notably under low oxygen, high salinity, or poor circulation environments, where the *crevice corrosion* becomes a concern [74]. Stainless steels are usually used in applications where both the properties of steel, *i.e.*, strength and fabricability, and resistance to corrosion are required.

As a result of the large number of alloying elements with relatively high concentrations, stainless steels can have many stable phases concurrently. Clearly, the phase with the lowest free energy is most favored, but others may have low enough free energies that permit them to exist as metastable phase. Transition from one metastable phase to the equilibrium state, the one of the lowest energy, may require atomic rearrangements to reach the equilibrium compositions on an atomic scale. If diffusion is too slow for these rearrangements to take place, the structure may retain the prior metastable configuration indefinitely. That is why most stainless steels are used in the metastable condition [74].

The structure of the final product can be influenced by various parameters like heat treatment and mechanical working. That is why samples of the same chemical composition may be found in different phases, or they may even have different lattice parameters in the same phase. These conditions require different sets of phase diagrams according to different production processes. However, here we present only the equilibrium pseudo-binary phase digram for ternary Fe–Cr–Ni alloys, calculated by the Thermo-Calc software [75, 76] which uses experimental data bases. When evaluating the phase

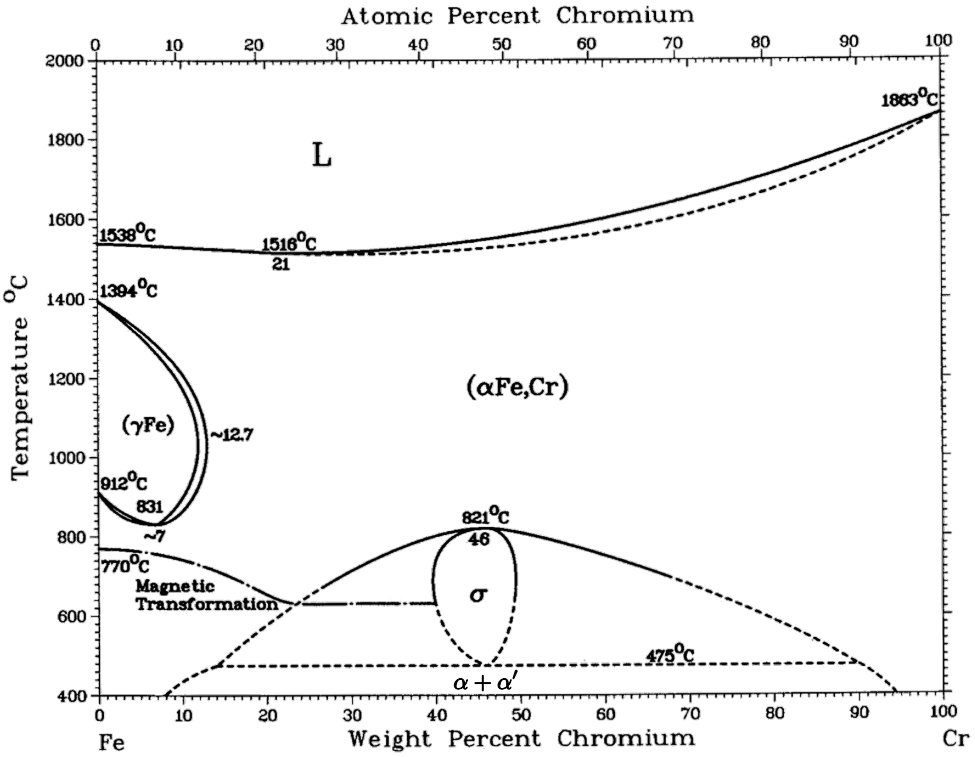

Figure 3.7: Iron-chromium phase diagram taken from *Binary Alloy Phase Diagrams* [57].

digram, we have chosen a constant iron concentration according to the simulated A607 alloy in Chap. 6.

3.3.1 Ferrite (α)

Clearly, the crystallographic structure of a solid may vary with temperature. For example, many metals, including iron, have a less-dense bcc structure at high temperature and transform to a denser fcc structure at lower temperatures. However, iron has the curious characteristic of transforming from fcc back to the low-density bcc structure at still lower temperatures (see Fig. 3.7). This is a result of the unpaired 3d electrons that give rise to ferromagnetism, causing repulsive forces between atoms and requiring a more widely spaced structure [74]. This sequence of phase transitions shows that the free energies of both structures are close to each other [74].

The base of stainless steel is iron, in which the above-mentioned sequence of phase transitions shows that the free energies of fcc and bcc structures are close to each other. Thus, alloying elements that prefer one structure over the other one can push the phase stability toward the favored structure. Among those alloying elements which are usually present in stainless steels, chromium, silicon, aluminum, molybdenum, tungsten, niobium, and titanium favor the bcc structure, and hence expand the temperature range

over which ferrite is stable. On the other hand, carbon, nitrogen, manganese, nickel, and copper are austenite-promoting alloying elements and expand the temperature range over which austenite exists. Elements which are insoluble in iron at austenite-forming temperatures, such as the impurities phosphorus, sulfur, and oxygen, have no influence on which phase is favored [57].

In order to maintain the corrosion resistance of stainless steels, a sufficient amount (at least 11 wt.%) of chromium is required, making it the main alloying element in this class of steels. Chromium has bcc structure and hence is a ferrite-stabilizing element in the alloy. Fig. 3.7 presents the equilibrium phase diagram of the iron-chromium binary alloy. The diagram shows that, as chromium is added to iron, the temperature range over which austenite is stable shrinks, and finally at about 12 wt.% chromium, ferrite becomes stable at all temperatures. By coincidence, this is the approximate level of chromium required to maintain the rust resistance under ambient conditions [74]. Therefore, in absence of significant amount of austenite-stabilizing elements, ferrite is the dominant phase of stainless steels.

Compared to austenite, ferrite has a greater thermal conductivity, lower thermal expansion, and higher stacking-fault energy. Its strength decreases with temperature more than that of austenite, but the good match in thermal expansion between the ferrite and the protective chromium-oxide still makes it an excellent high-temperature material. It has almost the same corrosion resistance as austenite [74].

3.3.2 Austenite (γ)

The second major constituent phase of stainless steels is *austenite* which exhibits fcc structure. Austenitic stainless steels, also known as *300 series*, make up the major part of the stainless steel production. In these grades, carbon is usually kept to low levels (C $<$ 0.08 wt.%), while the chromium content ranges from 16 to 28 wt.% and the nickel content ranges from 3.5 to 32 wt.%. Such a chemical composition allows them to maintain an austenitic structure from cryogenic temperatures up to the melting point of the alloy. These alloys cannot be hardened through heat treatment. The key properties of these types of stainless steel are excellent corrosion resistance, ductility and toughness [73]. The most widely used steel in this category, is the *304 grade*, containing 18–20 wt.% chromium and 8–12 wt.% nickel, which possesses an excellent combination of the above-mentioned properties.

The fcc structure is common in many transition metals to the right of iron in the periodic table. This structure should be considered normal for metals well below their melting temperature as it is a denser structure. In the case of iron, the presence of the bcc structure relates to the unpaired 3d electrons, which provide ferromagnetism. Adding elements to iron that cause pairing of the 3d electrons diminishes ferromagnetism and promotes the fcc structure. Nickel and manganese are the most prominent alloying elements that do this, but interstitial carbon and nitrogen are the most powerful austenite stabilizers on a percentage basis. However, their use is limited by their solubility and their tendency to form precipitating compounds with chromium. Manganese acts largely through its ability to promote nitrogen solubility [74].

Since all stainless steels contain principally iron and chromium, the addition of a substantial amount of austenitizing elements is necessary to transform the structure to austenite. For instance, an Fe–Cr–Ni alloy with about 17 wt.% chromium requires about 11 wt.% nickel (or its equivalents) to remain austenitic at room temperature. One weight percent nickel can be replaced by about 2 wt.% manganese as long as nitrogen is present to maintain the same phase stability. The omnipresent carbon and nitrogen have an effect 30 times that of nickel, so even in the small amounts in which they are normally present, they have a significant effect [74].

Many types of stainless steels are in metastable austenitic phase at service temperature. For example, alloys in the common grade *304* (also called 18–8 due to 18 wt.% Cr and 8 wt.% Ni) are normally used in the fully austenitic condition. Although, concerning its equilibrium, it would *rather* be partly ferritic, but the substitutional diffusion of chromium in austenite which is required to form a ferrite phase of a separate composition is so slow that it cannot occur in terrestrial time frames. However, if energy is applied by mechanical shear, the austenite can transform to the lower free-energy martensite phase without diffusion [74], as described in the next section.

Compared to ferrite, austenite has a lower thermal and electrical conductivity, greater thermal expansion, smaller stacking-fault energy, better corrosion resistance, and higher ductility. It is a paramagnetic alloy, suitable for application where a non-magnetic metal is favored [74].

3.3.3 Martensite (α' and ϵ)

We already described the formation of martensite in carbon steels. In a similar way, martensite can also form in stainless steels as a consequence of the rapid cooling of austenite which traps interstitial carbons in the octahedral sites of the final bct structure. When cooling austenite, the martensite formation starts at a certain temperature, the so-called *martensite-start* temperature, denoted by M_s. When temperature decreases, more austenite transforms to martensite, until the martensitic transformation completes as the temperature reaches the *martensite-finish* temperature, M_f. Both M_s and M_f depend on the steel composition. In the absence of mechanical stresses, M_s is estimated using the empirical equation[1] introduced by Eichelman and Hull [61]

$$\begin{aligned} M_s\ [\mathrm{K}] = 1578 - 41.67\,x_\mathrm{Cr} - 61.11\,x_\mathrm{Ni} - 33.33\,x_\mathrm{Mn} \\ -27.78\,x_\mathrm{Si} - 1667(x_\mathrm{C} + x_\mathrm{N}), \end{aligned} \tag{3.1}$$

where x_i denotes the concentration of element i in the unit of weight percent.

In stainless steels, two types of martensite form spontaneously when austenite is cooled enough: a hexagonal close-packed structure, so-called ϵ-martensite, and the

[1] As mentioned in the book *STEELS: Processing, Structure, and Performance* [61], the equation has originally been published in 1953 by Eichelman and Hull [77]. Since we did not have access to the original article, we took the equation from this book in the form of

$$M_s\ [^\circ\mathrm{F}] = 75(14.6 - x_\mathrm{Cr}) - 110(8.9 - x_\mathrm{Ni}) - 60(1.33 - x_\mathrm{Mn}) - 50(0.47 - x_\mathrm{Si}) - 3000[0.068 - (x_\mathrm{C} + x_\mathrm{N})]$$

and converted it from Fahrenheit unit (°F) to Kelvin (K).

above-mentioned α'-martensite with the bcc lattice. The ϵ-martensite forms on close-packed (111) planes in the austenite and, except for size, is morphologically very similar to deformation twins or stacking-fault clusters [78]. The nucleation of α'-martensite and its relationship to ϵ-martensite has been difficult to resolve. Evidences have been reported for two different phenomena during the formation of α'-martensite: (i) a direct transformation of austenite to α'-martensite, and also, (ii) a two-step transformation with ϵ-martensite as the intermediate phase [61]. While α'-martensite is ferromagnetic, ϵ-martensite is paramagnetic in the temperature ranges over which it exists [74].

As a unique feature of austenitic stainless steels, when mechanical stresses are applied, a *deformation-induced* martensitic transformation can occur even at temperatures higher than M_s. Deformation-induced martensite significantly enhances the strength of the alloy, and thus is desired in some types of stainless steels [61].

The martensitic transformation in austenitic stainless steels will be discussed a little further, when we will present our *ab-initio* results on the phase stability of the Fe–Cr–Ni alloy in Sec. 6.4.1.

3.3.4 Sigma Phase (σ)

In stainless steels, the *sigma* phase, denoted by σ, can form as the chromium content exceeds 18 wt.% [74]. Unlike alloys where different elements are randomly distributed trough the lattice, the sigma phase is an *intermetallic* phase, where atoms of different elements occupy certain sites in the structure. In other words, speaking about the iron–chromium system, the sigma phase is a chemical compound of these two elements. It has a complex crystal structure with a body-centered tetragonal (bct) unit cell containing 30 atoms [61]. Physically, it is very hard and brittle, and can adversely affect ductility, toughness, and corrosion resistance of stainless steels, thus its formation is not favored. The Curie temperature for the sigma phase has been reported to be below 40 K [79].

4

Theoretical Background

In condensed matter physics and chemistry, one is interested in finding the structure of materials at a microscopic scale, in which the matter is considered as a system of interacting nuclei and electrons. However, finding this structure is a difficult task because of two reasons: first, the particles must be treated using the laws of quantum mechanics, rather than classical physics, and second, the number of particles in a small (but macroscopic) piece of material is so high making it impractical to study them explicitly. Therefore, finding the microscopic structure of matter is a *quantum many-body problem*. In this chapter, a very short review is presented on the theoretical background of the computational methods that have been used in this thesis. For compiling this chapter, except the references which are explicitly cited, lecture notes presented by Roser Valentí [80] and some parts of the PhD theses written by Peter Puschnig [81], Oleg Peil [82], Tetyana Khmelevska [83], and Philip Peter Rushton [84] have been studied.

4.1 Introductory Remarks

For any non-relativistic time-independent system of nuclei and electrons, the above-mentioned quantum many-body problem can be cast in the form of a stationary Schrödinger equation [85, 86]

$$\hat{H}\Psi(\mathbf{R}_1, \mathbf{R}_2, \ldots, \mathbf{R}_M, \mathbf{r}_1, \mathbf{r}_2, \ldots, \mathbf{r}_N) = E\Psi(\mathbf{R}_1, \mathbf{R}_2, \ldots, \mathbf{R}_M, \mathbf{r}_1, \mathbf{r}_2, \ldots, \mathbf{r}_N), \quad (4.1)$$

where $\hat{H}$, $\Psi(\mathbf{R}_1, \mathbf{R}_2, \ldots, \mathbf{R}_M, \mathbf{r}_1, \mathbf{r}_2, \ldots, \mathbf{r}_N)$, and E are the Hamiltonian, the many-body wavefunction, and the total energy of the system, respectively. $\mathbf{R}_i$ and $\mathbf{r}_j$ denote, respectively, the position of the ith nucleus ($1 \leq i \leq M$) and the jth electron ($1 \leq j \leq N$), where M and N are the number of nuclei and electrons in the system, respectively. Since the particles are interacting according to the Coulomb law, the *exact* Hamiltonian

can be expressed as

$$\hat{H} = -\sum_{i=1}^{M} \frac{\hbar^2}{2m_{Z_i}} \nabla^2_{\mathbf{R}_i} - \sum_{i=1}^{N} \frac{\hbar^2}{2m_e} \nabla^2_{\mathbf{r}_i} + \frac{1}{4\pi\epsilon_0} \sum_{i=1}^{M} \sum_{j>i}^{M} \frac{Z_i Z_j e^2}{|\mathbf{R}_i - \mathbf{R}_j|} - \frac{1}{4\pi\epsilon_0} \sum_{i=1}^{N} \sum_{j=1}^{M} \frac{Z_j e^2}{|\mathbf{r}_i - \mathbf{R}_j|} + \frac{1}{4\pi\epsilon_0} \sum_{i=1}^{N} \sum_{j>i}^{N} \frac{e^2}{|\mathbf{r}_i - \mathbf{r}_j|}. \tag{4.2}$$

Here, m_e and e are the mass and the charge of an electron, $\mathbf{r}_i$ represents the position of the ith electron, and m_{Z_i}, Z_i, and $\mathbf{R}_i$ denote the mass, the charge, and the position of the ith nucleus, respectively. The first two terms in Eq. 4.2 are the kinetic energy contributions from the nuclei and the electrons, respectively. The remaining terms are the Coulomb potential energy terms arising from the ion–ion repulsion, ion–electron attraction and the electron–electron repulsion, respectively. Due to the large number of electrons and nuclei, Eq. 4.1 is simply too difficult to solve directly with this Hamiltonian in its exact form. The goal of this chapter is to introduce practical methods which allow for the solution of the many-body problem by approximating the Hamiltonian 4.2.

4.2 The Born–Oppenheimer Approximation

The electrostatic forces on both electrons and nuclei are of the same order of magnitude, thus their momentum changes are similar. Since the nuclei are of the order of $\sim 10^3$ times heavier than the electrons, their velocities must be much smaller than the velocities of the electron. Due to these vastly different dynamics, in most cases, the electronic and the nuclear degrees of freedom can be separated:

$$\Psi_{\text{total}}(\{\mathbf{R}\}, \{\mathbf{r}\}) = \Psi^{\{\mathbf{R}\}}_{\text{electronic}}(\{\mathbf{r}\}) \times \Psi_{\text{nuclear}}(\{\mathbf{R}\}). \tag{4.3}$$

Here, $\{\mathbf{R}\}$ and $\{\mathbf{r}\}$ stand for the set of all nuclear and electronic positions, respectively. The superscript $\{\mathbf{R}\}$ of the electronic wavefunction means that the positions of nuclei enter the wavefunction as parameters rather than variables [87]. This approximation is the first simplification to the mentioned many-body problem, and is known as the Born–Oppenheimer approximation [88]. Based on this approximation, nuclei are considered at fixed positions when calculating the electronic wavefunction. Therefore, their effect on the total energy of the ion–electron system is taken into account by a constant term related to the interactions among themselves, and a fixed external potential acting on electrons. This simplifies the full many-body Hamiltonian 4.2 as

$$\hat{H} = E_{\text{nuc.}} - \sum_{i=1}^{N} \frac{\hbar^2}{2m_e} \nabla^2_{\mathbf{r}_i} - \frac{1}{4\pi\epsilon_0} \sum_{i=1}^{N} \sum_{j=1}^{M} \frac{eZ_j}{|\mathbf{r}_i - \mathbf{R}_j|} + \frac{1}{4\pi\epsilon_0} \sum_{i=1}^{N} \sum_{j>i}^{N} \frac{e^2}{|\mathbf{r}_i - \mathbf{r}_j|}, \tag{4.4}$$

where $E_{\text{nuc.}}$ is the electrostatic potential energy stored in the fixed arrangement of nuclei. It must be noted that the evaluation of $E_{\text{nuc.}}$ is not required when calculating the electronic ground state. Although the Born–Oppenheimer approximation simplifies

the Hamiltonian by reducing the many-body (electrons and nuclei) problem to the many-electron problem, it is still impractical to solve the Schrödinger equation in a solid containing $N \sim 10^{23}$ electrons and consequently $3N$ variables. For simplicity, in the remaining part of this chapter we use atomic units, where $\hbar = e = m_e = 4\pi\epsilon_0 = 1$.

4.3 The Hohenberg–Kohn Theorems

Density-functional theory (DFT) is based on two simple, but extremely important, theorems known as Hohenberg–Kohn theorems [33]. Here we present these two theorems as stated in the book *Electronic Structure: Basic Theory and Practical Methods* authored by Martin [87].

- **Theorem 1.** For any system of interacting particles in an external potential $V_{\text{ext}}(\mathbf{r})$, the potential $V_{\text{ext}}(\mathbf{r})$ is determined uniquely, except for a constant, by the ground-state particle density $n_0(\mathbf{r})$.

Since the potential and consequently the Hamiltonian are determined, the many-body wavefunction can be determined for the ground state as well as all excited states. Therefore, it is then concluded from this theorem that all properties of the system are completely determined given only the ground-state density $n_0(\mathbf{r})$ [87].

- **Theorem 2.** A *universal functional* for the energy $E[n]$ in terms of the density $n(\mathbf{r})$ can be defined, valid for any external potential $V_{\text{ext}}(\mathbf{r})$. For any particular $V_{\text{ext}}(\mathbf{r})$, the exact ground-state energy of the system is the global minimum value of this functional, and the density $n(\mathbf{r})$ that minimizes the functional is the exact ground-state density $n_0(\mathbf{r})$.

From this theorem, it follows that the functional $E[n]$ suffices to determine the ground-state energy and density [87]. In fact, this functional can be considered as

$$E[n] = F[n] + \int V_{\text{ext}}(\mathbf{r})\, n(\mathbf{r})\, \mathrm{d}^3 r + E_{\text{II}}, \tag{4.5}$$

where E_{II} is the interaction energy of nuclei, and $F[n]$ is a *universal* functional of the density including all internal energies (kinetic, $T[n]$, and potential, $E_{\text{int}}[n]$) of the interacting electron system [87]:

$$F[n] = T[n] + E_{\text{int}}[n]. \tag{4.6}$$

While the Hohenberg–Kohn theorems proof the existence of an exact solution for the ground state of the system, they do not offer a practical approach for its calculation. However, in 1965, about one year after the work by Hohenberg and Kohn [33], Kohn and Sham [34] proposed a practicable method for DFT calculations which is described in the next section.

4.4 The Kohn–Sham Formalism

In this section, we shortly discuss the method proposed by Kohn and Sham [34], in order to find the ground state of the electronic system. The many-electron system is an interacting system, where the interactions originate from the Coulomb law and from the Pauli exclusion principle. However, in the Kohn–Sham formalism, this fully interacting system containing the actual interactions is mapped onto a fictitious non-interacting system, with the same ground-state density as the real system. In this non-interacting system, the electrons move within an effective single-particle potential $V_{\mathrm{KS}}(\mathbf{r})$, known as *Kohn–Sham potential*. This simplification greatly facilitates the calculation.

Kohn and Sham [34] suggested to write the universal functional 4.6 in the form of

$$F[\tilde{n}(\mathbf{r})] = T[\tilde{n}(\mathbf{r})] + \frac{1}{2}\int \frac{\tilde{n}(\mathbf{r})\,\tilde{n}(\mathbf{r}')}{|\mathbf{r}-\mathbf{r}'|}\,\mathrm{d}^3r\,\mathrm{d}^3r' + E_{\mathrm{XC}}[\tilde{n}(\mathbf{r})] \tag{4.7}$$

where $\tilde{n}(\mathbf{r})$ indicates a trial electron density for the non-interacting system, $T[\tilde{n}(\mathbf{r})]$ is the kinetic energy functional for the non-interacting electrons, the second term at the right side is the electrostatic Hartree energy, and $E_{\mathrm{XC}}[\tilde{n}(\mathbf{r})]$ is the so-called *exchange-correlation* energy functional. Note that, $F[\tilde{n}(\mathbf{r})]$ is purely related to the system of electrons, *i.e.*, it is independent of the external potential. By applying the Hohenberg–Kohn minimum principle [33], Kohn and Sham found the following system of equations, known as *Kohn–Sham equations*:

$$V_{\mathrm{KS}}(\mathbf{r}) = V_{\mathrm{ext}}(\mathbf{r}) + \int \frac{n(\mathbf{r}')}{|\mathbf{r}-\mathbf{r}'|}\,\mathrm{d}^3r' + V_{\mathrm{XC}}(\mathbf{r}), \tag{4.8}$$

$$V_{\mathrm{XC}}(\mathbf{r}) = \frac{\delta}{\delta\tilde{n}(\mathbf{r})}E_{\mathrm{XC}}[\tilde{n}(\mathbf{r})]\bigg|_{\tilde{n}(\mathbf{r})=n(\mathbf{r})}, \tag{4.9}$$

$$\left[-\frac{1}{2}\nabla^2 + V_{\mathrm{KS}}(\mathbf{r}) - \epsilon_i\right]\psi_i(\mathbf{r}) = 0, \tag{4.10}$$

$$n(\mathbf{r}) = \sum_{i=1}^{N} |\psi_i(\mathbf{r})|^2. \tag{4.11}$$

The Kohn–Sham equations are non-linear equations and thus have to be solved self-consistently, as presented in Fig. 4.1. Starting from an initial guess, which is usually obtained by a summation over atomic densities, the Kohn–Sham potential V_{KS} and consequently the Hamiltonian are obtained using Eqs. 4.8 and 4.9. By the diagonalization of this Hamiltonian, Kohn–Sham energies ϵ_i and Kohn–Sham states ψ_i are found (Eq. 4.10), resulting in a new density as expressed in Eq. 4.11. This new density, in turn, determines a new Kohn–Sham potential. This cycle is repeated until a converged ground-state density is obtained.

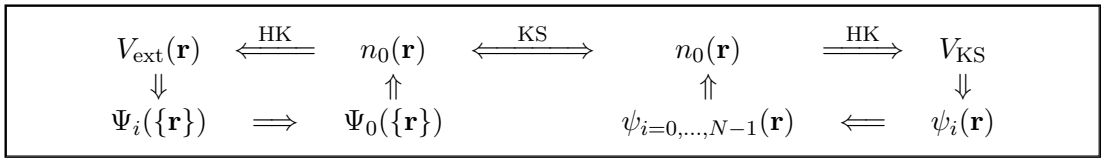

Figure 4.1: A schematic representation of the Kohn–Sham ansatz, created after Martin [87]. The left cycle depicts the real *interacting* system, where the external potential $V_{\text{ext}}(\mathbf{r})$ determines the Hamiltonian and consequently all states $\Psi_i(\{\mathbf{r}\})$, including the many-electron ground state $\Psi_0(\{\mathbf{r}\})$. The ground state then results in the ground-state density $n_0(\mathbf{r})$. The Hohenberg–Kohn theorem, indicated by an arrow with label "HK", completes the cycle by relating the external potential to the ground-state density. The right cycle depicts the fictitious *non-interacting* system, where, in a similar way, the Kohn–Sham potential determines all single-electron states $\psi_i(\{\mathbf{r}\})$. Starting from the single-electron ground state $\psi_0(\{\mathbf{r}\})$, N electrons are arranged in N states with lowest energies $\psi_{i=0,\ldots,N-1}(\{\mathbf{r}\})$, which in turn results in the ground-state density $n_0(\mathbf{r})$. Here also the Hohenberg–Kohn theorem completes the cycle by relating the Kohn–Sham potential to the ground-state density. The relation between the many-electron system and the non-interacting single-electron system is provided by the Kohn–Sham formulation, indicated by the arrow labeled with "KS".

Once the ground-state density is obtained, the ground-state energy of the electronic system is found in the form of [89]

$$E = \sum_{i=1}^{N} \epsilon_i + E_{\text{XC}}[n(\mathbf{r})] - \int V_{\text{XC}}(\mathbf{r})\, n(\mathbf{r})\, \mathrm{d}^3 r - \frac{1}{2} \int \frac{n(\mathbf{r})\, n(\mathbf{r}')}{|\mathbf{r} - \mathbf{r}'|}\, \mathrm{d}^3 r\, \mathrm{d}^3 r'. \tag{4.12}$$

All many-body effects can be taken into account in the calculation of the ground state if the exact form of $E_{\text{XC}}[n(\mathbf{r})]$ is known. Thus, the usefulness of the Kohn–Sham formalism is entirely dependent on whether good approximations of $E_{\text{XC}}[n(\mathbf{r})]$ are available. In the next section, we will discuss the most common approximations for the $E_{\text{XC}}[n(\mathbf{r})]$.

As presented here, the Kohn–Sham formalism reduces the problem of minimizing the energy functional to the problem of solving a set of single-electron Schrödinger equations. Various approaches have been developed in order to solve these single-electron equations, differing mainly in the choice of the basis set for the single-particle orbitals. As a consequence of this choice, they differ in performance as well [87]. In solid state calculations, two basic classes of methods are used: Hamiltonian methods, based on the diagonalization of the Hamiltonian; and Green's function techniques relying on the multiple-scattering formalism. Two examples of such approaches, which have been used in this thesis, will be shortly discussed in this chapter.

4.5 Exchange–Correlation Functionals

The universal exchange-correlation (XC) energy, $E_{\text{XC}}[n(\mathbf{r})]$, which appears in the universal Kohn–Sham functional for the energy (see Eqs. 4.6 and 4.7), contains (i) the

difference between the exact and the non-interacting kinetic energies and also (ii) the non-classical contribution to the electron-electron interactions

$$E_{\mathrm{XC}}[n(\mathbf{r})] = \Big(T[n(\mathbf{r})] - T_{\mathrm{NI}}[n(\mathbf{r})]\Big) + \Big(E_{\mathrm{ee}}[n(\mathbf{r})] - E_{\mathrm{ee}}^{\mathrm{H}}[n(\mathbf{r})]\Big). \tag{4.13}$$

where $T[n(\mathbf{r})]$ and $E_{\mathrm{ee}}[n(\mathbf{r})]$ are, respectively, the exact kinetic and electrostatic energies of the real *interacting* system of electrons. Similarly, $T_{\mathrm{NI}}[n(\mathbf{r})]$ and $E_{\mathrm{ee}}^{\mathrm{H}}[n(\mathbf{r})]$ are the kinetic and electrostatic energies for the *non-interacting* system. In principle, if the exact form of $E_{\mathrm{XC}}[n(\mathbf{r})]$ were known, Kohn–Sham theory would be exact. However, finding an accurate enough $E_{\mathrm{XC}}[n(\mathbf{r})]$ has shown to be extremely difficult and is currently the greatest challenge in density-functional theory [89]. The approximation to the XC energy is the main approximation entering the Kohn–Sham formalism and specifies the general accuracy and success of DFT methods.

The XC energy $E_{\mathrm{XC}}[n(\mathbf{r})]$ consists of two parts, *i.e.*, the exchange energy, $E_{\mathrm{X}}[n(\mathbf{r})]$, and the correlation energy, $E_{\mathrm{C}}[n(\mathbf{r})]$:

$$E_{\mathrm{XC}}[n(\mathbf{r})] = E_{\mathrm{X}}[n(\mathbf{r})] + E_{\mathrm{C}}[n(\mathbf{r})]. \tag{4.14}$$

In DFT, the exact exchange energy $E_{\mathrm{X}}[n(\mathbf{r})]$ is in the form of the Hartree–Fock (HF) exchange energy, $E_{\mathrm{X}}^{\mathrm{HF}}$, except that the KS orbitals are used instead of the HF orbitals [89]. However, no accurate universal expression is known for the correlation energy, giving rise to many investigations in order to find relevant approximations for it. Among many approximations proposed for the exchange-correlation functional, here we shortly introduce two most common forms.

4.5.1 The Local-density Approximation

The local-density approximation (LDA) is an approximations to the XC energy functional in DFT that depend solely upon the value of the electronic density at each point in space. The most successful forms of the LDA are those derived from the homogeneous electron gas (HEG), where, for a spin-unpolarized system, the XC energy is written as

$$E_{\mathrm{XC}}^{\mathrm{LDA}}[n(\mathbf{r})] = \int \epsilon_{\mathrm{XC}}(n(\mathbf{r}))\, n(\mathbf{r})\, \mathrm{d}^3 r. \tag{4.15}$$

Here, $\epsilon_{\mathrm{XC}}(n(\mathbf{r}))$ is the XC energy per electron (XC-energy density) of a uniform electron gas of density $n(\mathbf{r})$ [34]. In order to use the HEG results for approximating the XC energy in a system where the density in not homogeneous, an integration over space is performed in which the inhomogeneous system is locally approximated with a HEG of the same density.

The homogeneous electron gas is considered as a system of interacting electrons placed in a volume with a relevant positive background charge so that keeps the system neutral. In such a system without a net charge, the total energy consists of only two contributions: the kinetic energy and the XC energy:

$$\epsilon_{\mathrm{tot}}^{\mathrm{HEG}}(n) = \tau^{\mathrm{HEG}}(n) + \epsilon_{\mathrm{XC}}(n). \tag{4.16}$$

The kinetic energy per electron, τ^{HEG}, is obtained as [90]

$$\tau^{\mathrm{HEG}}(n) = \frac{3}{5}\epsilon_{\mathrm{F}}(n) = \frac{3}{10}\Big(\frac{9\pi}{4}\Big)^{\frac{2}{3}}\frac{1}{r_s^2} \approx \frac{1.10}{r_s^2}\ \mathrm{Ha}, \tag{4.17}$$

where the energy unit, Ha, stands for *Hartree*: $1\,\mathrm{Ha} = 2\,\mathrm{Ry} \approx 27.211\,\mathrm{eV}$. Here, $\epsilon_{\mathrm{F}}(n)$ indicate the Fermi energy per electron, and r_s is the radius of a sphere containing one electron, given as [36, 87]

$$\frac{4\pi}{3}r_s^3 = \frac{1}{n} \qquad \Longrightarrow \qquad r_s = \Big(\frac{3}{4\pi}\frac{1}{n}\Big)^{\frac{1}{3}}. \tag{4.18}$$

The XC-energy density $\epsilon_{\mathrm{XC}}(n)$ is decomposed into two parts, *i.e.*, the exchange- and the correlation-energy densities:

$$\epsilon_{\mathrm{XC}}(n) = \epsilon_{\mathrm{X}}(n) + \epsilon_{\mathrm{C}}(n). \tag{4.19}$$

For a spin-unpolarized HEG with *constant* density n, the exact exchange-energy density is obtained as [36, 87, 90]

$$\epsilon_{\mathrm{X}}(n) \equiv \epsilon_{\mathrm{X}}^{\uparrow}(n) = \epsilon_{\mathrm{X}}^{\downarrow}(n) = -\frac{3}{4\pi}\Big(\frac{9\pi}{4}\Big)^{\frac{1}{3}}\frac{1}{r_s}\ \mathrm{Ha} = -\frac{0.458}{r_s}\ \mathrm{Ha}, \tag{4.20}$$

As mentioned earlier, there is no general analytical expression for the correlation energy. The nearly exact correlation-energy density for the HEG can be calculated only for high- and low-density limits, corresponding to infinitely-weak and infinitely-strong correlations. For a spin-unpolarized HEG with *constant* density n, the correlation-energy density at these two limits is obtained as [89]

$$\epsilon_{\mathrm{C}}(n) \equiv \epsilon_{\mathrm{C}}^{\uparrow}(n) = \epsilon_{\mathrm{C}}^{\downarrow}(n) = \begin{cases} 0.0311\ln r_s - 0.048 + r_s(A\ln r + C) & r_s \ll 1 \\ \dfrac{1}{2}\Big(\dfrac{g_0}{r_s} + \dfrac{g_1}{r_s^{3/2}} + \dfrac{g_2}{r_s^2} + \dots\Big) & r_s \gg 1 \end{cases} \tag{4.21}$$

In general, using Eqs. 4.16 and 4.19, $\epsilon_{\mathrm{C}}(n)$ can be defined as the remaining contribution to the total energy:

$$\epsilon_{\mathrm{C}}(n) = \epsilon_{\mathrm{tot}}^{\mathrm{HEG}}(n) - \tau^{\mathrm{HEG}}(n) - \epsilon_{\mathrm{X}}(n). \tag{4.22}$$

This equation suggest a way for evaluating the correlation-energy density by calculating the total energy of the HEG [90]. Accurate total energies have been obtained for intermediate values of density using quantum Monte-Carlo simulations [91, 92]. An interpolation is performed over the results of these simulations in order to find a general expression for $\epsilon_{\mathrm{C}}(n)$ as a function of density. When both $\epsilon_{\mathrm{X}}(n)$ and $\epsilon_{\mathrm{C}}(n)$ are found, the $\epsilon_{\mathrm{XC}}(n)$ and consequently the $E_{\mathrm{XC}}^{\mathrm{LDA}}[n(\mathbf{r})]$ are obtained.

Based on its derivation, the LDA is obviously exact for the homogeneous electron gas [36]. Moreover, it was initially expected to give reasonable results in solids close to a homogeneous gas, where the density is slowly varying on the scale of the local

Fermi wavelength $\lambda_F = 2\pi/k_F = h/\sqrt{2mE_F}$. However, it turned out that the LDA gives reasonable results even for atoms and molecules where the condition of slowly varying densities is not satisfied [36, 87]. A great number of calculations have shown that the LDA gives ionization energies of atoms, dissociation energies of molecules and cohesive energies with a fair accuracy of typically 10–20%. Structural properties such as bond lengths and the geometries of molecules and solids are obtained typically with an astonishing accuracy of ∼1% [36]. The LDA (and the LSDA, its extension to system with unpaired spins) can fail in systems, like heavy fermion systems, so dominated by electron–electron interaction effects that they lack any resemblance to noninteracting electron gases [36].

4.5.2 The Generalized Gradient Approximation

The first step beyond the local approximation was a functional of the density $n(\mathbf{r})$, as well as the magnitude of its gradient, $|\nabla n(\mathbf{r})|$. Such a *gradient-expansion approximation* (GEA) was first suggested in the original paper of Kohn and Sham [34]. However, the GEA did not result in consistent improvement over the LSDA; indeed it often leads to worse results. The basic problem is that the gradients in real materials are so large that the expansion diverges [87].

In order to modify the behavior of functionals at large gradients and thus to preserve the desired properties, a variety of solutions were suggested resulting in different *generalized-gradient approximations* (GGA's). The expression of the XC energy presented in Eq. 4.15 can be generalized in the form of

$$E_{XC}^{GGA}[n(\mathbf{r})] = \int \epsilon_{XC}\big(n(\mathbf{r}), |\nabla n(\mathbf{r})|\big)\, n(\mathbf{r})\, \mathrm{d}^3 r, \tag{4.23}$$

where $\epsilon_{XC}\big(n(\mathbf{r}), |\nabla n(\mathbf{r})|\big)$ is the XC-energy density as a function of two variables: (i) the electron density $n(\mathbf{r})$ and (ii) the magnitude of the electron-density gradient, $|\nabla n(\mathbf{r})|$. Currently, the most widely used GGA is the one proposed by Perdew, Burke, and Enzerhof, known as GGA-PBE [93].

The GGA's improve the description of structural properties of systems which considerably differ from the HEG. For instance, the use of the GGA's reduces the errors of atomization energies of standard sets of small molecules consist of light atoms by factors of typically 3–5 [36].

4.6 The Hamiltonian Methods

In order to solve the Kohn–Sham equations for an electronic system, the wavefunction is expanded using an appropriate basis set. Generally, a good basis set must be simultaneously *unbiased*, *simple*, and *efficient*. Unbiased means that the basis set must not assume any preconceptions of the form of the problem. Simplicity means the ease of implementation, which would require less technical efforts. And finally, the efficiency is determined by the number of the basis functions which are required in order to get

an accurate enough representation of the expanded wavefunction. This section aims to give a short introduction to theoretical approaches which help to understand the mixed LAPW+LO and APW+lo basis sets used in the thesis. We follow closely the review published by Madsen *et al.* [94].

4.6.1 The Augmented Planewave (APW) Method

When studying periodic crystals, plane waves $e^{\imath(\mathbf{k}+\mathbf{G})\cdot\mathbf{r}}$ are a natural choice of basis functions, as they are compatible with the periodic boundary conditions. Here, $\mathbf{k}$ denotes a vector in the first Brillouin zone, and $\mathbf{G}$ is a reciprocal lattice vector. Moreover, plane waves are unbiased and technically very simple to implement. Using a planewave basis set, any eigenfunction of a periodic Hamiltonian can be expanded as

$$\psi_{n,\mathbf{k}}(\mathbf{r}) = \sum_{\mathbf{G}} c_{n,\mathbf{k},\mathbf{G}}\, e^{\imath(\mathbf{k}+\mathbf{G})\cdot\mathbf{r}}. \tag{4.24}$$

Despite the above mentioned advantages of the plane waves, they are not efficient, particularly when trying to reproduce the rapid oscillations of the wavefunction near the nuclei. In order to describe the nodal structure of the wavefunction in these regions, a large number of planewave basis functions is needed which increases the computational burdens significantly.

One solution to this problem is using pseudopotentials. In pseudopotential approaches, in order to reduce the number of required basis functions, the steep real Coulombic potential in a region close to a nucleus, the *inner* region, is approximated with a smooth virtual potential which results in a nodeless pseudo-wavefunction [95–97]. As the distance from the nucleus increases, the pseudopotential continuously evolves into the real potential in *outer* regions. In pseudopotential approaches, while the valance states are explicitly calculated, the core states are considered rigid regardless the various surrounding environments (molecules, solids, *etc.*). Therefore, despite their efficiency, pseudopotential approaches are not a relevant choice for studying material properties in systems where the core states can significantly change.

The augmented planewave (APW) [94, 98, 99] method is another solution to the efficiency problems associated with the planewave basis set. In this approach, the unit cell is partitioned into two regions: the *muffin-tin* (MT) region which consists of non-overlapping spheres of radius R_{MT} centered at the atomic nuclei, and the remaining space which is called *interstitial* region (I) and is generally known as the spaces far from the nuclei. In the interstitial region, the potential and consequently the wavefunction vary smoothly. Therefore, plane waves are a good basis set in order to expand the wavefunction in this part of the unit cell. On the other hand, in the regions near the nuclei, the potential and consequently the wavefunction are similar to those of an isolated atom. Thus, in the muffin-tin region, the wavefunction can be described well using the atomic orbitals. The crystal wavefunction is expanded in terms of the APW basis functions $\phi^{\mathrm{APW}}_{\mathbf{k}+\mathbf{G}}$

$$\psi_{n,\mathbf{k}}(\mathbf{r}) = \sum_{\mathbf{G}} c_{n,\mathbf{k},\mathbf{G}}\, \phi^{\mathrm{APW}}_{\mathbf{k}+\mathbf{G}}(\mathbf{r}, E), \tag{4.25}$$

where [80, 87, 94]

$$\phi^{\mathrm{APW}}_{\mathbf{k}+\mathbf{G}}(\mathbf{r},E) = \begin{cases} \displaystyle\sum_{l=0}^{l_{\max}} \sum_{m=-l}^{l} A^{\alpha}_{lm}(\mathbf{k}+\mathbf{G})\, u^{\alpha}_{l}(r',E)\, Y_{lm}(\hat{\mathbf{r}}') & r' < R^{\alpha}_{\mathrm{MT}} \\ \dfrac{1}{\sqrt{\Omega}} e^{\imath(\mathbf{k}+\mathbf{G})\cdot\mathbf{r}} & r \in I \end{cases} \tag{4.26}$$

Here, Ω is the unit-cell volume, and $\mathbf{r}' = \mathbf{r} - \mathbf{R}^{\alpha}$ where $\mathbf{R}^{\alpha}$ is the atomic position of atom α within the unit cell. $u^{\alpha}_{l}(r',E)$ is the numerical solution to the radial Schrödinger equation at the energy E. The coefficients $A^{\alpha}_{lm}(\mathbf{k}+\mathbf{G})$ are chosen so that the atomic orbitals match the plane waves over the complete surface of the muffin-tin sphere [80, 94].

Inside the muffin-tin sphere, an accurate description of the Kohn–Sham orbital $\psi_i(\mathbf{r})$ requires the coefficient E to be selected equal to the energy eigenvalue ϵ_i of $\psi_i(\mathbf{r})$. Therefore, for every energy eigenvalue ϵ_i a different energy-dependent set of APW basis functions must be found. On the other hand, ϵ_i is not known; in fact, ϵ_i is exactly the quantity which is desired to be determined. This leads to a nonlinear eigenvalue problem, and must be solved using root determination algorithms. Such a solution is computationally very demanding, and hence known as the main drawback of the APW method [80, 94].

4.6.2 The Linearized Augmented Planewave (LAPW) Method

A successful attempt to improve the APW method is the linearization proposed by Andersen [100], leading to the first implementation of the linearized augmented planewave (LAPW) method [101]. In the LAPW method, the energy dependence of the radial functions inside each sphere is linearized by adding a second term to the radial part of the basis functions [94]

$$\phi^{\mathrm{LAPW}}_{\mathbf{k}+\mathbf{G}}(\mathbf{r}) = \begin{cases} \displaystyle\sum_{l=0}^{l_{\max}} \sum_{m=-l}^{l} \Big[A^{\alpha}_{lm}(\mathbf{k}+\mathbf{G})\, u^{\alpha}_{l}(r',E_l) \\ \qquad + B^{\alpha}_{lm}(\mathbf{k}+\mathbf{G})\, \dot{u}^{\alpha}_{l}(r',E_l) \Big] Y_{lm}(\hat{\mathbf{r}}') & r' < R^{\alpha}_{\mathrm{MT}} \\ \dfrac{1}{\sqrt{\Omega}} e^{\imath(\mathbf{k}+\mathbf{G})\cdot\mathbf{r}} & r \in I \end{cases} \tag{4.27}$$

Here, u_l is the solution to the radial Schrödinger equation at a fixed linearization energy E_l, and $\dot{u}_l$ is its derivative with respect to energy, calculated at E_l. The two groups of coefficients $A^{\alpha}_{lm}(\mathbf{k}+\mathbf{G})$ and $B^{\alpha}_{lm}(\mathbf{k}+\mathbf{G})$ are chosen so that the function inside the muffin-tin sphere matches the plane waves both in value and slope at the sphere boundary [80, 94]. The LAPW's, as defined above, are a sufficiently flexible basis which can describe eigenfunctions with energy eigenvalues around the linearization energy. Therefore, the E_l values can be kept fixed and all energy eigenvalues can be obtained

with a single diagonalization, resulting in a significant improvement in terms of efficiency [94].

However, LAPW's are not suited for treating states that lie far from the linearization energy. Furthermore, the linearization is not sufficiently accurate for broad valence bands, if the partial wave shows a large energy variation inside the muffin-tin sphere [94]. For instance, bcc Fe has two valence states with the same value of $l = 1$: 4p and 3p states, respectively at 0.2 Ry and 4.3 Ry below the Fermi level E_{F}. Both states are valence states as they are not confined in the muffin-tin sphere. In such a situation, the problem is how to choose the linearization energy $E_{l=1}$ [80]. A solution to this problem is presented in the next subsection.

4.6.3 The LAPW+LO Method

As mentioned above, in some cases there might be more than one valence (or semicore) state with the same value of l, making it difficult to choose a relevant linearization energy E_l. In order to solve such a problem and improve the linearization, Singh [102] introduced local orbitals (LO's) which augment the LAPW basis set for certain l values. This method is known as LAPW+LO, where the LO's are defined as

$$\phi_{lm}^{\alpha',\mathrm{LO}}(\mathbf{r}) = \begin{cases} \Big[A_{lm}^{\alpha',\mathrm{LO}}\, u_l^{\alpha'}(r', E_{1,l}^{\alpha'}) \\ + B_{lm}^{\alpha',\mathrm{LO}}\, \dot{u}_l^{\alpha'}(r', E_{1,l}^{\alpha'}) \\ + C_{lm}^{\alpha',\mathrm{LO}}\, u_l^{\alpha'}(r', E_{2,l}^{\alpha'}) \Big] Y_{lm}(\hat{\mathbf{r}}') & r' < R_{\mathrm{MT}}^{\alpha'} \\ 0 & r \in I \end{cases} . \tag{4.28}$$

Here, $E_{1,l}^{\alpha'}$ and $E_{2,l}^{\alpha'}$ are linearization energies suitable for the highest and the lowest states, respectively [80]. In other words, an LO, $\phi_{lm}^{\alpha',\mathrm{LO}}(\mathbf{r})$, is constructed from the LAPW radial functions at the energy $E_{1,l}$ and a third radial function $u_l^{\alpha'}(r', E_{2,l}^{\alpha'})$ at a second energy $E_{2,l}$, chosen to most efficiently improve the linearization. Since LO's are not connected to plane waves in the interstitial region, they have no $\mathbf{k}$ or $\mathbf{G}$ dependence. The three coefficients $A_{lm}^{\alpha',\mathrm{LO}}$, $B_{lm}^{\alpha',\mathrm{LO}}$, and $C_{lm}^{\alpha',\mathrm{LO}}$ are determined by the requirements that the LO's should be normalized and also should have zero value and slope at the muffin-tin sphere boundary [80, 94]. Finally, it must be noted that the index α' in the above expression indicates that the LO's are added for *all* (not only non-equivalent) atoms in the unit cell. For instance, adding the LO's for p and d states of all atoms in a unit cell with N_{atom} atoms increases the basis set by $(3+5) \times N_{\mathrm{atom}} = 8N_{\mathrm{atom}}$, which is not a big number compared to the size of a typical basis set [80]. LO's were found to be more efficient in improving the linearization than alternative methods with APW's having continuous second and third derivatives [102].

4.6.4 The APW+lo Method

As mentioned earlier, the main drawback of the APW method is the energy dependence of its basis set. In order to overcome this difficulty, the LAPW+LO method was developed, where the energy dependence is removed at the cost of enlarging the basis set size (through linearization and introduction of local orbitals). Later, Sjöstedt *et al.* [103] suggested a modification of the LAPW method, where they combine the advantages of the APW and LAPW methods by finding an energy-independent basis set that does not demand a noticeable higher planewave cutoff than the original APW basis functions. In their approach, the original APW's, Eq. 4.26, are evaluated at a fixed energy and the variational freedom is improved by adding local orbitals for physically important l-quantum numbers, *i.e.*, for $l \leq 3$. These local orbitals put no extra condition on the APW basis set, and the number of plane waves in the interstitial region is therefore unaffected. These local orbitals, which are completely different than those introduced in the LAPW method (LO's), are denoted by "lo". Therefore, the approach is known as APW+lo, where lo's are defined as [80]

$$\phi_{lm}^{\alpha',\mathrm{lo}}(\mathbf{r}) = \begin{cases} \left[A_{lm}^{\alpha',\mathrm{lo}}\, u_l^{\alpha'}(r', E_l^{\alpha'}) + B_{lm}^{\alpha',\mathrm{lo}}\, \dot{u}_l^{\alpha'}(r', E_l^{\alpha'})\right] Y_{lm}(\hat{\mathbf{r}}) & r' < R_{\mathrm{MT}}^{\alpha'} \\ 0 & r \in I \end{cases} \tag{4.29}$$

Here, also, index α' indicates all atoms. The lo's are evaluated at the same fixed energy as the corresponding APW's. The two coefficients $A_{lm}^{\alpha',\mathrm{lo}}$ and $B_{lm}^{\alpha',\mathrm{lo}}$ are determined by normalization and by the condition that $\phi_{lm}^{\alpha',\mathrm{lo}}$ has zero value at the muffin-tin sphere boundary. Both the APW's and lo's are continuous at the sphere boundary, but their first derivatives are discontinuous [80].

The full-potential LAPW+LO (FP-LAPW+LO) and the FP-APW+lo methods are among the most accurate *ab-initio* methods [42]. These two methods have been implemented in the WIEN2k code [42, 104]. We use the version 8.3 of this code in order to investigate the iron–carbon system (see Chap. 5). In particular, the WIEN2k code is capable of calculating the local lattice relaxations, which are crucial when interstitial sites are occupied.

4.7 Green's Function Methods

Beside the Hamiltonian approaches, methods based on Green's function provide another class of techniques for solving the Kohn–Sham equations. Green's function methods are much less efficient than the Hamiltonian methods in the total-energy calculations, as well as in finding relaxed geometries of solids and molecules. However, the Green's function formalism is the basis of first-principles alloy theory, making it particularly useful when studying properties of disordered alloys [105]. This section aims to shortly introduce the Green's function formalism, and also the *exact muffin-tin orbital* (EMTO) method based on it. Here, we closely follow the review published by Ruban and Abrikosov

[105]. Moreover, some parts of the PhD theses written by Oleg Peil [82] and Tetyana Khmelevska [83] have been studied when compiling the text.

4.7.1 The Green's Function or Multiple-scattering Formalism

Generally, the Green's function method operates with the single-particle Green's function $G(\mathbf{r}, \mathbf{r}', \epsilon)$, which describes the propagation of an independent particle from point $\mathbf{r}$ to point $\mathbf{r}'$ at energy ϵ. When applied to a system of electrons, this single-particle (single-electron) Green's function is a solution of the Kohn–Sham equation 4.10 for energy ϵ with a source at a point $\mathbf{r}'$ [105]

$$\left[-\frac{1}{2}\nabla^2 + V_{\mathrm{KS}}(\mathbf{r}) - \epsilon \right] G(\mathbf{r}, \mathbf{r}', \epsilon) = -\delta(\mathbf{r} - \mathbf{r}'), \tag{4.30}$$

where $V_{\mathrm{KS}}(\mathbf{r})$ is the Kohn–Sham single-electron effective potential, as presented in Eq. 4.8. The Green's function can be explicitly represented in terms of the corresponding single-electron wavefunctions of the original Kohn–Sham equation as [105]

$$G(\mathbf{r}, \mathbf{r}', \epsilon + \imath\xi) = \sum_i \frac{\psi_i(\mathbf{r}, \epsilon)\, \psi_i^*(\mathbf{r}', \epsilon)}{\epsilon + \imath\xi - \epsilon_i}, \tag{4.31}$$

where the summation is performed over all occupied states. Once the Green's function is given, different quantities can be calculated. For instance, the electron density is obtained as [105]

$$n(\mathbf{r}) = -\frac{2}{\pi} \int^{E_{\mathrm{F}}} \mathrm{Im}\big(G(\mathbf{r}, \mathbf{r}, \epsilon)\big)\, \mathrm{d}\epsilon, \tag{4.32}$$

where the upper limit of the integral is specified by the Fermi energy E_{F}.

In principle, it is possible to obtain the Green's function in the framework of any Hamiltonian method which can calculate the single-electron wavefunctions $\psi_j(\mathbf{r}, \epsilon)$ (see Eq. 4.31). However, the next subsection introduces a method which naturally suits the Green's function formalism.

4.7.2 Korringa–Kohn–Rostocker (KKR) method

The Korringa–Kohn–Rostocker (KKR) method [106, 107] provides a very efficient way of calculating the Green's function using the multiple-scattering formalism [108]. The main idea of the KKR method is to consider atoms as scattering centers, whose properties are given by a scattering matrix t, and then to solve the electronic structure problem by demanding that the incident wave at each center is equal to the sum of the outgoing waves from all the other centers. In order to do so, the space is divided into non-overlapping muffin-tin (MT) spheres (or cells), centered at the nuclei positions. The solutions of the Schrödinger equation inside the cells are treated as outgoing waves. Then, the self-consistent scattering implies that the outgoing wave for a given site cancels all the waves incoming from other sites [82, 105].

In the original and in many modern implementations of the KKR method, the full potential is approximated by a so-called muffin-tin potential, representing a sum of spherical potentials within spheres of radius R_{MT} (muffin-tin radius) centered at atomic sites, and a constant potential in the remaining space [107]. The cancellation of scattering waves at the boundary of the muffin-tin spheres results in a smooth solution of the Schrödinger equation in the entire space. The muffin-tin potential is very well justified on physical grounds in homogeneous systems with close-packed structures, but can give erroneous results in open structures with anisotropic distortions, where the full potential must be considered. A general formulation of the KKR for the case of potentials of arbitrary shape is possible within the full-potential (FP) KKR scheme [108–112]. Calculations with FP-KKR are quite demanding, although affordable with modern computers [82].

Here, we consider the basic notions of the KKR formalism within the muffin-tin approximation. Scattering within the muffin-tin spheres is described by the scattering matrix $t(\epsilon)$, whose angular components can be written as

$$t_l(\epsilon) = -\frac{1}{\kappa}\, e^{\imath\eta_l(\epsilon)}\, \sin[\eta_l(\epsilon)], \tag{4.33}$$

where $\kappa = \sqrt{\epsilon}$, and the phase shifts $\eta_l(\epsilon)$ are determined from the solution of the radial Schrödinger equation for angular momentum l and energy ϵ inside the corresponding muffin-tin sphere [82, 105].

The propagation of states between scattering centers in the free space is given by the structure constant matrix,

$$S^{ij}_{lm,l'm'}(\epsilon) = -4\pi\kappa \sum_{l''m''} i^{l''} C^{lm}_{l'm',l''m''}\, h_{l''}(\kappa|\mathbf{R}_i - \mathbf{R}_j|)\, Y_{l''m''}(\widehat{\mathbf{R}_i - \mathbf{R}_j}), \tag{4.34}$$

where l and m indicate the angular-momentum quantum numbers, Y_{lm} denote the spherical harmonics, h_l stand for the Hankel functions, and $C^{lm}_{l'm',l''m''}$ are the Gaunt coefficients [82, 105].

The core of the KKR method is the KKR equation, expressing the above-mentioned cancellation of outgoing and incoming waves in terms of the on-site scattering matrices, t_i , and the structure constant matrix,

$$\det\left|t_{i,l}(\epsilon)^{-1} - S^{ij}_{lm,l'm'}(\epsilon)\right| = 0, \tag{4.35}$$

which gives the eigenvalues ϵ of the original Schrödinger equation for the entire system. The energies can be obtained as poles of the scattering path operator, $g^{ij}_{lm,l'm'}(\epsilon)$, defined in a periodic system as

$$g^{ij}_{lm,l'm'}(\epsilon) = \frac{1}{\Omega_{\mathrm{BZ}}} \int_{\mathrm{BZ}} \mathrm{d}^3k \left[t_{i,l}(\epsilon)^{-1} - S_{lm,l'm'}(\mathbf{k},\epsilon)\right]^{-1} e^{\imath\mathbf{k}(\mathbf{R}_i - \mathbf{R}_j)} \tag{4.36}$$

where the integration is performed over the Brillouin zone (BZ), and $S_{lm,l'm'}(\mathbf{k},\epsilon)$ is the Fourier transform of the structure constant matrix $S^{ij}_{lm,l'm'}(\epsilon)$ [82, 105].

The path operator provides all information about scattering at the lattice sites. For instance, $g^{ij}_{lm,l'm'}(\epsilon)$ describes the propagation of the states with energy ϵ between sites i and j of the lattice. In order to get the full Green's function defined in the entire space, the path operator must be properly normalized. The Green's function can be represented in the form

$$\begin{aligned} G(\mathbf{r}+\mathbf{R}_i, \mathbf{r}'+\mathbf{R}'_j, \epsilon) &= \sum_{lm}\sum_{l'm'} R_{il}(\mathbf{r},\epsilon)\, g^{ij}_{lm,l'm'}(\epsilon)\, R_{jl'}(\mathbf{r}',\epsilon) \\ &- \delta_{ij}\sum_{lm} R_{il}(\mathbf{r},\epsilon)\, H_{jl}(\mathbf{r}',\epsilon). \end{aligned} \tag{4.37}$$

Here, $\mathbf{r}$ and $\mathbf{r}'$ are defined within the muffin-tin spheres centered at $\mathbf{R}_i$ and $\mathbf{R}'_j$, respectively. l and m are the angular-momentum quantum numbers, and ϵ is the energy with respect to the constant potential in the interstitial region. Finally, R_{il} and H_{il} are the regular and irregular solutions to the Schrödinger equation in the atomic sphere i for orbital moment l and energy ϵ [82, 105].

Generally, the mathematical form of g, t and S, as well as relations between g and $G(\mathbf{r},\mathbf{r}',\epsilon)$, depend on a particular space division and on the used basis functions. However, the atomic part, given by the scattering matrix, t, and the structural part, given by structure constants S, are independent of each other and separated in the equation of the scattering path operator (see Eq. 4.36). This separation is a very important feature of the method, making the multiple-scattering theory a very powerful tool, which can be applied to systems with reduced or no symmetry that lie outside the realm of applicability of conventional methods [105].

4.7.3 The Exact Muffin-tin Orbital (EMTO) Method

The exact muffin-tin orbital (EMTO) method [47] belongs to the family of KKR methods. The main idea of the EMTO approach is to use large overlapping muffin-tin spheres instead of non-overlapping ones, which results in an accurate representation of the exact single-electron potential [47].

The EMTO method allows one to calculate the Green's function of a system with a periodic potential. However, disordered alloys are not translationally invariant and thus the method is not directly applicable. In order to represent a disordered alloy, a very large supercell with randomly distributed atoms has to be considered [113, 114]. On the other hand, one can use the single-electron Green's function, which is a self-averaging quantity, and find an average Green's function of an alloy considered as a one-component effective medium having the translational symmetry of the underlying lattice [105].

The simplest and the most accurate consistent method of performing configurational averaging of the Green's function is the coherent potential approximation (CPA) [43–45] which reduces a multi-component disordered alloy to a translationally invariant system with a single component representing an effective medium. Such an invariant system will have the translational symmetry of the underlying lattice. The main idea of the

CPA is to define an effective medium whose scattering properties are the same as those of the original alloy components on average. Such an effective medium is defined by a coherent potential function, $\tilde{P}$, and the on-site coherent path operator, $\tilde{g}$, is determined by an equation analogous to Eq. 4.36 [45],

$$\tilde{g}(\epsilon) = \frac{1}{\Omega_{\mathrm{BZ}}} \int_{\mathrm{BZ}} \mathrm{d}^3k \, \frac{1}{\tilde{P}(\epsilon) - S(\mathbf{k}, \epsilon)}. \tag{4.38}$$

According to the CPA condition, this coherent on-site path operator should be equal to the average on-site path operator of the alloy components embedded in the effective medium, *i.e.*,

$$\tilde{g}(\epsilon) = \sum_{\alpha} C_\alpha \, g_\alpha(\epsilon), \tag{4.39}$$

where α indicates all components in the alloy, and the on-site path operators of the alloy components, $g_\alpha(\epsilon)$, are obtained from a single-site Dyson equation,

$$\tilde{g}_\alpha(\epsilon) = \frac{1}{1 + \tilde{g}(\epsilon)[P_\alpha(\epsilon) - \tilde{P}]} \tilde{g}(\epsilon). \tag{4.40}$$

Here, P_α are the potential function matrices of alloy components.

The non-linear equations 4.38, 4.39, 4.40 must be solved self-consistently for every energy. The electron density of each alloy component can then be determined from g_α using Eq. 4.32.

Since, in the single-site approximation, the electron density of each alloy component is known only inside its atomic spheres, the lack of information about the true (non-averaged) electron density around such an atomic sphere results in a net charge for the whole system, which is incorrect [105]. The solution of the problem can be found only beyond the single-site approximation [115, 116], where the contribution of the corresponding screened Coulomb interaction to single-electron potential and total energy is determined based on the screening parameters defined for every alloy component. We will refer to these screening parameters in Section 6.3.3, where we will calculate the total energy of an random Fe–Cr–Ni alloy in the paramagnetic state.

Studying the paramagnetic state of an alloy requires the simulation of a system of local magnetic moments with random orientations. In order to calculate the effects of magnetic disorder on the electronic structure, a mean-field like approximation called disordered local moment (DLM) [46] approach can be applied. The idea of the DLM formalism is to represent magnetic disorder within the CPA by treating magnetic metals as a pseudo-binary alloy, $\mathrm{M}^{\uparrow}_{1-x}\mathrm{M}^{\downarrow}_{x}$, where $1-x$ is the concentration of atoms of sort M with positive spin moment $\mathrm{M}^{\uparrow}$ and x of those with negative moment $\mathrm{M}^{\downarrow}$. The case of $x = 0$ describes a ferromagnetic solution, while $x = 0.5$ represents a state with positive and negative local moments equipartitionally distributed on all magnetic sites (DLM state), thus modeling the paramagnetic state of a magnetic metal in an alloy analogy [83].

The EMTO method, in combination with the CPA and the DLM approaches, provides an excellent tool to investigate random alloys with arbitrary compositions in the

paramagnetic state. However, this approach does not allow to relax the atomic forces which can be introduced to the system due to atomic size mismatch. Although such forces are often not significant in the case of substitutional alloys composed of atoms of similar sizes, they become extremely important in the case of interstitial atoms, where the lattice around the interstitial atom is significantly distorted.

5

The Fe–C System

As mentioned in Chap. 3, carbon steels have numerous applications in different fields of industry, giving rise to a great interest to shed light on the mechanisms relevant for their plastic deformation behavior. The plastic deformation of fcc materials, as explained in Sec. 2.4, is strongly governed by the stacking-fault energy (SFE). The SFE and its generalizations to the quantities known as the γ-curve and the γ-surface were introduced in Sec. 2.3. The current chapter is dedicated to the evaluation of the SFE and the γ-surface in austenitic carbon steels.

5.1 Introduction

The phase stability of carbon steels was discussed in Sec. 3.2. At temperatures higher than 1000 K (727 °C), the paramagnetic austenite, γ-iron with fcc structure, becomes stable and the dominant phase of pure iron and carbon steels. At room temperature, austenite can be stabilized by alloying with a relevant amount of metals like Mn and Ni (see Sec. 3.3). However, these substitutional elements hardly affect the SFE of iron. For instance, measurements in a variety of Fe–Cr–Ni stainless steels have shown that the addition of Ni increases the SFE by a rate of 1.4–2.4 $\mathrm{mJ/m^2}$ per wt.%, while Cr decreases it by of 0.2–1.2 $\mathrm{mJ/m^2}$ per wt.% [117]. In the case of Fe–Mn alloys, although measurements have reported a non-monotonic dependence of the SFE on the Mn content [22, 118, 119], the changes of the SFE are found to be less than 3 $\mathrm{mJ/m^2}$ per wt.% of Mn. These small rates suggest that, the simple Fe–C system in its fcc phase can be a good representative of the more complicated and disordered Fe–Cr–Ni–C and Fe–Mn–C alloys.

Experimental observations [67] as well as theoretical studies based on molecular dynamics [68] and *ab-initio* calculations [63] agree that, in fcc iron, carbon occupies interstitial sites, preferring octahedral over tetrahedral coordination (see Sec. 3.2.2). However, concerning the influence of carbon on the SFE in austenitic steels, experimental studies give controversial answers. An early work by Schramm and Reed [117] suggests a linear dependence of the SFE on the elemental compositions of Ni, Cr, and

C in the form of

$$\text{SFE}\ [\text{mJ/m}^2] = 4 + 1.8\,x_{\text{Ni}} - 0.2\,x_{\text{Cr}} + 410\,x_{\text{C}}, \tag{5.1}$$

where x denotes the concentration of the respective element in weight percent. This result, exhibiting a strong dependence of the SFE on x_{C}, was based on measurements performed on samples with a maximum of 0.036% carbon concentration. Later, Brofman and Ansell [120] included newer experimental data related to samples with carbon concentrations up to 0.29% and came up with the following modification,

$$\text{SFE}\ [\text{mJ/m}^2] = 16.7 + 2.1\,x_{\text{Ni}} - 0.9\,x_{\text{Cr}} + 26\,x_{\text{C}}, \tag{5.2}$$

indicating a carbon dependence which is 15 times smaller. Considering that, in this class of steels, we deal with carbon concentrations of the order of 0.1, and that the typical magnitude of the SFE is 15–60 mJ/m^2, the influence of carbon on the SFE lies within the typical experimental accuracy of $\pm$15–20 mJ/m^2 [11]. In other words, the latter measurements suggest that the SFE is very small and its dependence on the carbon concentration is very weak. The diversity of experimental results does not only exist for the magnitude of the SFE, but it is also found in the behavior of this quantity when carbon is added. For instance, while above-mentioned works predict a linear increase, Petrov [25] reported that the SFE decreases for small carbon content, while it increases for higher concentrations. This controversy in the existing literature suggests that presently the influence of carbon on the SFE is difficult to determine experimentally, and insight from theory, in particular from first principles, is highly desirable.

A strong influence on the SFE of fcc iron in the presence of interstitial atoms has already been shown by earlier theoretical studies. For instance, Kibey and coworkers [39] have found nitrogen to significantly alter the γ-surface. Moreover, for carbon concentrations up to 1.33 wt.%, Abbasi *et al.* [40] have reported the SFE to linearly increase with a slope of 340 mJ/m^2 per weight-percent carbon. However, the γ-surface has not been computed for the iron–carbon system so far.

In this chapter, we present the generalized stacking-fault energy evaluated by means of *ab-initio* calculations within the framework of density functional theory (DFT) [33, 34], applying the all-electron FP-LAPW+LO and FP-APW+lo methods (see Sec. 4.6) as implemented in the WIEN2k package [121].

5.2 Methodology

In this work, all stacking faults are *explicitly* simulated by utilizing the supercell technique. Compared to the axial next-nearest-neighbor Ising (ANNNI) model [48, 49], where the SFE is expanded in terms of the free energies of fcc, hcp, and double-hcp (dhcp) phases, the supercell approach facilitates the calculation of the full γ-surface by comparing the energy of structures with a fault to the energy of an undistorted reference structure (see Sec. 6.2 for an introduction to the ANNNI model). Moreover, the

supercell approach allows for the relaxation of the atomic positions around the interstitial atoms and the fault. Such relaxations are crucial in the Fe–C system, since the interstitial atoms introduce significant local lattice deformations which must be taken into account.

Despite the mentioned advantages, chemical and magnetic disorder can not easily be accounted for in the supercell approach. The former restriction is not severe in this case since experimental [122] and *ab-initio* [63] studies show that the carbon–carbon interaction for interstitial carbons in fcc iron is repulsive, supporting the implicit assumption of a homogeneous carbon distribution by the supercell approach. Concerning magnetic effects, we note that a comparison between magnetic (ferromagnetic) and non-magnetic calculations resulted in only small differences in terms of relative changes of the SFE as a function of carbon concentration [40]. We therefore consider the Fe–C model system in the non-magnetic state. Nevertheless, it must be noted that for the accurate computation of the absolute values of the SFE, the paramagnetic state must be taken into account [37, 38]. However, the treatment of magnetic disorder in combination with (i) large supercells and (ii) the need for local lattice relaxations, is, unfortunately, out of reach within present-day *ab-initio* methodologies.

As mentioned above, for each carbon concentration, our SF simulations require finding the energy difference between structures with a relevant displacement and the reference structure with undistorted bulk configuration. Every point on the γ-surface corresponds to a specific displacement in the crystal lattice, thus this approach requires many supercells in order to calculate the entire γ-surface. These supercells are constructed by gliding blocks of bulk with respect to each other (see Sec. 2.2). The bulk itself requires finding the optimized lattice parameters and atomic positions. Once the energy differences are calculated, an appropriate two-dimensional function is fitted to them in order to evaluate the entire γ-surface. In this section, these steps are explained in more detail.

5.2.1 Bulk Crystal Structures

Experimental data for the lattice parameter of austenite are available only for temperature ranges in which the phase becomes stable, *i.e.*, well above room temperature. However, the DFT calculations are performed for 0 K; thus we use the equilibrium lattice parameters in our simulations. We calculate the equilibrium lattice parameters and atomic positions for austenite with different carbon concentrations, *i.e.*, pure iron, $Fe_{24}C$, and Fe_3C, corresponding to 0.00, 0.89, and 6.67 weight percent of interstitial carbon, respectively. The equilibrium volume for pure iron is calculated in the primitive unit cell of the fcc structure where no force relaxation is required. For Fe_3C and $Fe_{24}C$, however, hexagonal unit cells are utilized, where both parameters a and c are optimized independently. Moreover, since there are variable internal positions in these two cells, all atomic forces are relaxed in every step of the cell optimization. More technical details are found in the following:

- **Fe:** The structure of this element is fcc with only one atom in the unit cell,

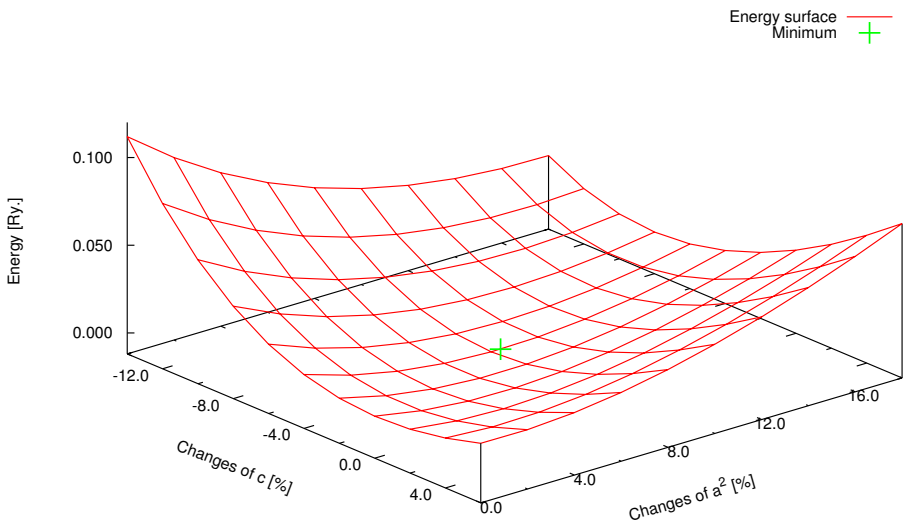

Figure 5.1: Optimization of cell dimensions for Fe_3C.

and hence no freedom for internal positions. The equilibrium lattice parameter is found using the Murnaghan equation of state [123].

- **$Fe_{24}C$**: This compound has a hexagonal unit cell containing six nonequivalent iron atoms and one carbon atom (see Fig. 5.2(c)). There are eight degrees of freedom for the unit-cell shape and the internal positions: the lattice parameters a and c, and the internal positions of the six nonequivalent iron atoms (carbons are considered at the cell vertices). In order to find the equilibrium configuration, we construct a number of unit cells, where the cell parameters a and c are changed independently. The total energy is calculated for these structures after the relaxation of atomic forces. The equilibrium parameters a and c are then found by fitting a two-dimensional polynomial, $f(x, y)$, to the calculated points, (a, c, E).

- **Fe_3C:** This compound has a hexagonal unit cell containing two nonequivalent iron atoms (see Fig. 5.2(b)). It has three degrees of freedom: the unit-cell dimensions, a and c, and the internal position of the iron atoms which are placed inside the unit cell with equal distances from the carbon atom. The equilibrium parameters a and c are found in the same way as explained for $Fe_{24}C$. Fig. 5.1 presents the total energy of the bulk of Fe_3C as a function of a^2 and c.

A summary of the results is presented in Tab. 5.1.

5.2.2 Supercells for the Stacking-fault Simulations

The principles of supercell construction for the γ-surface simulations was explained in Chap. 2: In an fcc structure, an ISF can be created by fixing the atomic layers below the

Table 5.1: Equilibrium bulk structures of different compounds investigated in this work. V_{cell} denotes the unit-cell volume, V_{atom} stands for the volume per iron atom, and ΔV shows the change in the volume by adding carbon, compared to the volume for pure iron; $\Delta V = \frac{(V_{\text{atom}})_{\text{composite}} - (V_{\text{atom}})_{\text{Fe}}}{(V_{\text{atom}})_{\text{Fe}}} \times 100$, in %.

Compound	lattice type	atoms Fe	atoms C	a [a.u.]	c [a.u.]	V_{cell} [a.u.^{3}]	V_{atom} [a.u.^{3}]	ΔV %
Fe	fcc	1	0	6.524	—	69.42	69.42	0.00
$Fe_{24}C$	hexagonal	24	1	9.351	22.905	1734.40	72.27	4.10
Fe_3C	hexagonal	3	1	4.955	11.810	251.11	83.70	20.57

fault, and sliding all upper layers along the $[\bar{2}11]$ direction with the displacement vector $\mathbf{u}_{\text{ISF}} = \frac{1}{3}\mathbf{u}_{[\bar{2}11]}$ (see Fig. 2.6(a)). However, in order to evaluate the entire γ-surface, the displacement vector must span every point in the {111} plane. Among different available approaches, we construct our supercells in a special way by considering two facts: (i) For reducing the probability of occurring errors, it is highly recommended to use the same basis set in all calculations. (ii) In the WIEN2k package, relaxing the atomic forces in the direction of lattice vectors is more straightforward than in other directions. In this subsection, we explain our method and compare it with other often used approaches.

Fig. 5.2 shows the perfect bulk unit cells for different carbon concentrations. In Fig. 5.3, we present three possible ways in which a supercell with the ISF can be constructed out of the bulk unit cells. The smallest possible supercell, denoted by us as *tilted* supercell, is presented in Fig. 5.3(a). This supercell contains only one bulk slice. Since the cell vector **c** is tilted, a displacement appears between the bulk layers of the cell and those of its periodic image. In Fig. 5.3(b), another possible supercell is depicted containing two bulk slice which are slided with respect to each other. In order to ensure periodic boundary conditions in z-direction, sufficient vacuum has to be added to prevent any interaction between the slices and their periodic images. We call it here *single-shift* supercell. Figs. 5.3(c) and 5.3(d) depict a third possibility for choosing a supercell. It is a supercell with three bulk slices containing three SFs with displacement vectors of identical magnitude but different directions, namely $[\bar{2}11]$, $[1\bar{2}1]$, and $[11\bar{2}]$, respectively. Thus, the resulting displacement vector adds up to zero, ensuring periodic boundary conditions. We call it here *triple-shift* supercell. Unlike the two former supercells where only one SF is associated with every cell, the *triple-shift* supercell contains three SFs per unit cell (see Fig. 5.3(c)).

Tab. 5.2 summarizes the main features of these supercells. The *tilted* supercell exhibits the smallest cell, *i.e.*, its volume is three times smaller than that of the other two supercells, which clearly reduces the computational cost. However, when constructing structures with different displacements along the fault plane, the cell shape and consequently the basis set changes for the *tilted* supercell, while the other two supercells have

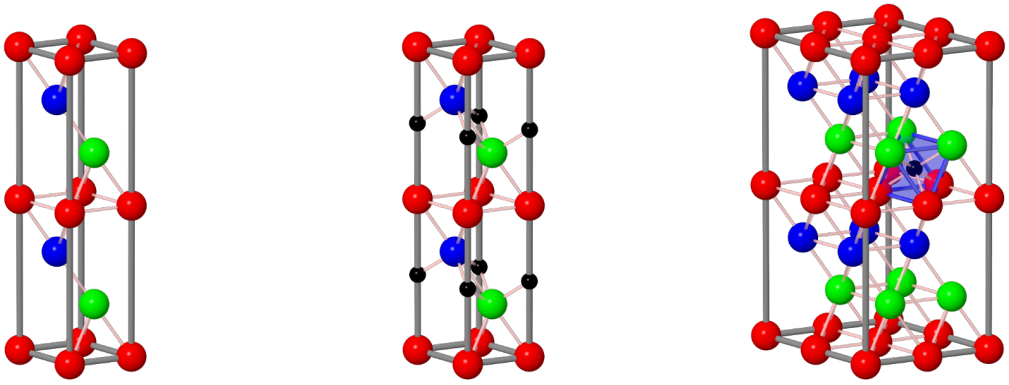

(a) (b) (c)

Figure 5.2: Bulk unit cells which are used for constructing supercells with an ISF; (a) shows the bulk unit cell for pure iron, and (b) for Fe_3C. (c) depicts the unit cell for $Fe_{24}C$ with highlighted octahedral sites for better imagination.

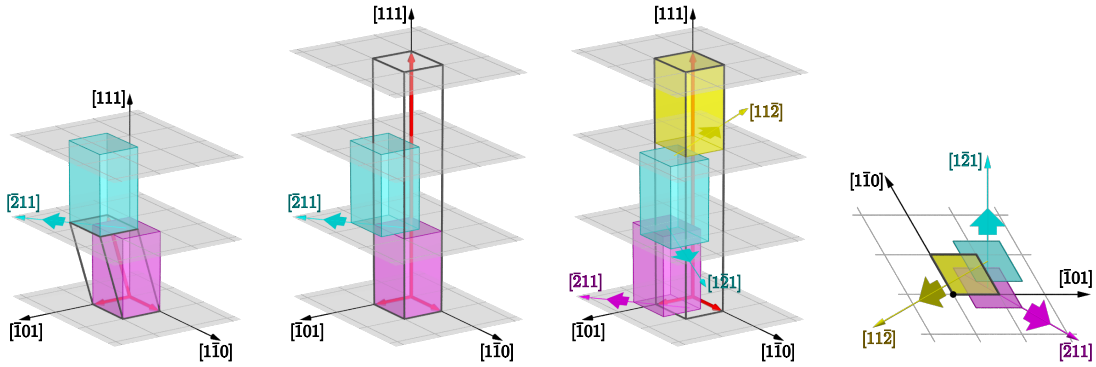

(a) (b) (c) (d)

Figure 5.3: Schematic representation of three possible supercells for the γ-surface calculations. (a) depicts the *tilted*, (b) the *single-shift* supercell, and (c) and (d) show side and top views of the *triple-shift* supercell, respectively. The gray cages show the supercells including one ((a) and (b)) or three ((c)) SFs, while the boxes in different colors represent building blocks of the bulk structure.

fixed shape and dimensions. Thus, the *tilted* supercell requires higher energy cutoffs and denser k-meshes to ensure convergence of results. Moreover, since in the *tilted* supercell the cell vector **c** is not perpendicular to the fault plane, atomic-force relaxations with the constraint that only the component perpendicular to the SF plane is relaxed, is not straightforward. These two drawbacks led us to discard the *tilted* supercell for our studies of the γ-surface. Concerning the *single-shift* supercell, it requires a vacuum layer which introduces surface effects, and also decreases the symmetry. The *triple-shift*

Table 5.2: Comparison of possible supercells

property	*tilted* supercell	*single-shift* supercell	*triple-shift* supercell
supercell height	L	$2L + l_{\text{vacuum}}$	$3L$
symmetry	very low	low	high
fixed supercell shape	×	✓	✓
straightforward relaxation	×	✓	✓

supercell does not suffer from any of these difficulties. In fact, for $Fe_{24}C$, the *single-shift* supercell has 50 non-equivalent atoms, while the *triple-shift* supercell has only 25. Thus, we chose the *triple-shift* supercell for all our computations.

5.2.3 Interstitial Carbon

We use the scheme $\cdots AcBaCbAcBaCb \cdots$ for labeling the position of octahedral interstitial sites with respect to the atomic layers. Here, capital letters denote atomic positions and lowercase letters mark octahedral sites. The usage of the same letter in upper and lower case (for instance A and a) indicates that their corresponding sites are on top of each other when viewed along the <111> direction (see Fig. 5.4). While in the perfect fcc structure all octahedral sites are naturally identical, in the presence of a fault they must be differentiated according to their distance from the fault plane. We indicate this distance by the parameter d (see Fig. 5.4). For instance, $d = 0$ represents an octahedral site positioned within the fault plane. Similarly, $d = 1$ denotes such a site separated from the fault plane by one atomic layer, and so on.

A carbon atom has different effects on the γ-curve, when positioned at octahedral sites with different values of d, while all possible octahedral sites with the same d have identical effect due to translational symmetry. Thus, the ideal supercell for computing the γ-curve for a homogeneous distribution of interstitial carbons should simultaneously include carbon atoms at all *different* octahedral sites. Such a supercell requires extending along the $\{111\}$ plane, so that the single-layer concentration of carbon, θ, is fixed for all layers. The supercell concentration of carbon, x, is then found equal to θ, since $x = \sum_d \theta_d / \sum_d$ (see Fig. 5.5(a)). This ideal supercell would, however, be huge and computationally impractical for low carbon concentrations. By assuming that carbon atoms influence the γ-curves independently from each other, one can investigate their impact within smaller cells, each of which including only one or a few carbon atoms (see Fig. 5.5(b)). The γ-curve is then calculated for every such small cell, and finally

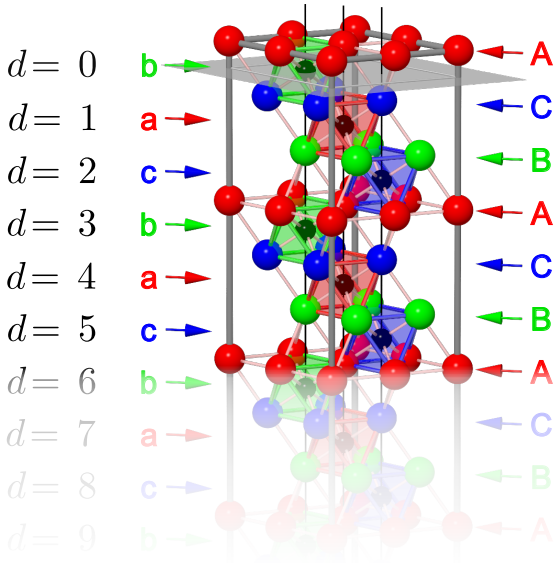

Figure 5.4: Labeling the octahedral sites with respect to atomic layers and the fault plane (gray plane). Large spheres and capital letters denote the stacking of the atomic layers in a perfect fcc lattice, while small black spheres and lower-case letters indicate the interstitial sites at the center of octahedra. For better imagination, every octahedron is highlighted such that its color corresponds to the stacking position of its site. The distance between an interstitial site and the fault plane is indicated by the parameter d.

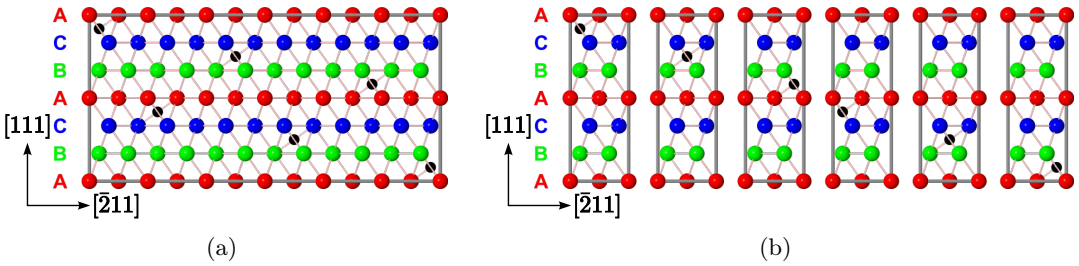

Figure 5.5: (a) A supercell, where carbon atoms are distributed as homogeneously as possible among all layers. (b) The supercell is split into smaller cells, each containing only one carbon atom.

an average over all individual γ-curves is taken according to

$$\gamma_{\text{av}} = \frac{\sum_{d=0}^{d_{\max}} \gamma_d}{d_{\max}+1}, \tag{5.3}$$

where γ_d denotes the γ-curve obtained for a cell with an octahedral carbon at a distance d from the fault plane, and $d_{\max}$ is the maximum distance considered. In fact, $d_{\max}$ is obtained based on the supercell dimensions. For instance, using a 2×2 supercell for $Fe_{24}C$, every layer contains 4 iron atoms, and thus the maximum height of the supercell equals to $24/4 = 6$ atomic layers, leading to $d_{\max} = 5$.

When calculating γ-surfaces, iron atoms within two atomic layers next to the fault plane are allowed to move perpendicular to the plane. Moreover, carbon atoms in this region are fully relaxed in all directions.

5.2.4 Interpolation of the γ-surface

The complete γ-surface requires the evaluation of the energy differences for a two-dimensional grid of points in the $\{111\}$ plane. However, by considering the symmetry of the surface, the problem can be reduced to the evaluation of the so-called γ-curve, which depicts the energy changes versus displacements in $[\bar{2}11]$ direction. The energy differences between the perfect structure and structures with faults are calculated for displacement vectors of different sizes between 0 and $u_{[\bar{2}11]}$, along the $[\bar{2}11]$ direction (see Fig. 2.6(a)). The γ-curve and, consequently, the γ-surface are then interpolated using a Fourier series taking into account the symmetry properties of the surface, thereby recovering the full two-dimensional dependence of the γ-surface.

The general form of the two-dimensional Fourier expansion for a function $f(x, y)$ is given by

$$f(x,y) = \sum_{m,n \in \mathbb{Z}} C_{mn}\, e^{\imath \frac{2\pi x}{a} m}\, e^{\imath \frac{2\pi y}{b} n}, \tag{5.4}$$

where m and n are integer numbers, C_{mn} denote expansion coefficients, and a and b are the periodicities along the x- and y-axes, respectively. For expanding the γ-surface in the $\{111\}$ plane of an fcc structure, we select the x- and y-axes along $[\bar{2}11]$ and $[0\bar{1}1]$, respectively. This choice requires $a = b\sqrt{3}$. Since the γ-surface is a real function and obeys the symmetry of the structure, the expansion should have the following features:

- a three-fold rotational symmetry of the $\{111\}$ plane,

  $$\hat{R}_{[111]}(240^\circ) f(x,y) = \hat{R}_{[111]}(120^\circ) f(x,y) = f(x,y),$$

  where $\hat{R}_{[111]}(\alpha)$ is the rotation operator with angle α around an axis normal to in the $\{111\}$ plane;

- reflection symmetry with respect to the x-axis,

  $$f(x,-y) = f(x,y),$$

- and real value,

$$f^*(x,y) = f(x,y).$$

By applying these criteria to Eq. 5.4, $f(x,y)$ is obtained as

$$\begin{aligned} f(x,y) = & \sum_{\substack{n\in Z \\ n\geq 0 \\ n=2l}}{}' \left\{ p_{0n} \left[\cos(\frac{2\pi y}{b}n) + 2\cos(\frac{2\pi x}{a}\cdot\frac{3n}{2})\cos(\frac{2\pi y}{b}\cdot\frac{n}{2}) \right] \right\} \\ & + \sum_{\substack{m,n\in Z \\ m>0 \\ n\geq 0 \\ m+n=2l}}{}' \left\{ p_{mn} \left[\cos(\frac{2\pi x}{a}m)\cos(\frac{2\pi y}{b}n) \right.\right. \\ & \qquad + \cos(\frac{2\pi x}{a}\cdot\frac{m+3n}{2})\cos(\frac{2\pi y}{b}\cdot\frac{m-n}{2}) \\ & \qquad \left.\left. + \cos(\frac{2\pi x}{a}\cdot\frac{m-3n}{2})\cos(\frac{2\pi y}{b}\cdot\frac{m+n}{2}) \right] \right. \\ & \left. + q_{mn} \left[\sin(\frac{2\pi x}{a}m)\cos(\frac{2\pi y}{b}n) \right.\right. \\ & \qquad + \sin(\frac{2\pi x}{a}\cdot\frac{m+3n}{2})\cos(\frac{2\pi y}{b}\cdot\frac{m-n}{2}) \\ & \qquad \left.\left. + \sin(\frac{2\pi x}{a}\cdot\frac{m-3n}{2})\cos(\frac{2\pi y}{b}\cdot\frac{m+n}{2}) \right] \right\} \end{aligned} \tag{5.5}$$

where p_{mn} and q_{mn} are constant. The prime sign of $\sum'$ means that every pair of integer numbers (m,n) can appear in the arguments of sin and cos only once. In other words, once m and n have values m_0 and n_0, they will not take any of the values $\frac{m_0+3n_0}{2}$, $\frac{m_0-n_0}{2}$, $\frac{m_0-3n_0}{2}$, and $\frac{m_0+n_0}{2}$. p_{mn} and q_{mn} are found by fitting the function f to a number of total energies obtained by DFT calculations. For more details of the derivation of this equation, see Appendix 6.5.

5.3 Computational Details

As it was already mentioned, our *ab-initio* calculations are performed using the WIEN2k package [121] (see Sec. 4.6). The exchange-correlation effects are treated within the generalized-gradient approximation according to Perdew, Burke and Ernzerhof (GGA-PBA) [93] (see Sec. 4.5).

In *ab-initio* electronic-structure methods, there is a set of computational parameters (usually referred as convergence parameters) which can affect the accuracy of the calculation on one hand, and of course, the computational costs on the other hand. Therefore they should be selected carefully to assure accurate enough results, and also to minimize

the computational effort as much as possible. To achieve these two purposes, convergence tests are required before starting the actual simulations. The aim of this section is to explain the optimizations which are applied in this part of the work. However, for a quick reference, all computational parameters are summarized in Tab. 5.3.

Table 5.3: Cell dimensions together with convergence parameters as used in our calculations. In all cases, muffin-tin radii R_{MT} of 1.6 and 1.4 a.u. were chosen for Fe and C, respectively.

			Lattice parameters							
		lattice type	a [a.u.]	b [a.u.]	c [a.u.]	cell volume [a.u.^{3}]	$RK_{\max}$	$R_{\mathrm{MT}}^{\min}$	matrix size	k-mesh $k_x \times k_y \times k_z$
Bulk	Fe	fcc	4.613	4.613	4.613	69.42	9.00	2.0	125	$15 \times 15 \times 15$
	Fe_3C	hexag.	4.955	4.955	11.810	251.11	7.00	1.4	580	$15 \times 15 \times 5$
	Fe_4C	cubic	6.520	6.520	6.520	277.11	7.00	1.4	811	$15 \times 15 \times 15$
	$Fe_{24}C$	hexag.	9.351	9.351	22.905	1734.40	7.00	1.4	2604	$8 \times 8 \times 2$
γ-curve	Fe	hexag.	4.613	4.613	67.799	1249.46	8.00	1.6	2921	$11 \times 11 \times 1$
	Fe_3C	hexag.	4.955	4.955	70.860	1506.67	7.00	1.4	3377	$10 \times 10 \times 1$
	$Fe_{24}C$	hexag.	9.351	9.351	68.714	5203.46	6.50	1.4	9596	$4 \times 4 \times 1$

5.3.1 Number of k-points

The Kohn–Sham equation (Eq. 4.10) must be independently solved for a set of k-points in the Brillouin zone. Solving this equation is usually the most time-consuming part of the DFT calculations, so the computational cost of the calculations scales linearly with the total number of k-points. On the other hand, reducing the number of k-points affects the accuracy of results. Therefore, a compromise between the accuracy and the number of k-points becomes important. This is usually done by finding the least dense mesh of k-points which can guarantee the required accuracy of results.

The required accuracy is usually defined corresponding to the goals of the calculations. Moreover, the system specifications (unit-cell shape and size, symmetry, atoms, *cte.*) and calculation type (magnetic state, desired properties, *cte.*) can influence the optimized k-mesh. We perform some tests for Fe_4C in order to find an optimum k-mesh for the bulk calculations. We evaluate the dependence of the total energy on the number of k-points as plotted in Fig. 5.6. For this cubic system, a k-mesh of $15 \times 15 \times 15$ guaranties the required accuracy. For other concentrations, the commensurate k-mesh is selected by comparing the unit-cell shape and size to those of Fe_4C.

5.3.2 Number of Basis Functions

In the LAPW method, the unit cell is divided into non-overlapping atomic spheres centered at the atomic sites (muffin-tin spheres), and the interstitial region (see Sec. 4.6). Technically, the expansion 4.25 must be truncated at a certain $\mathbf{G}_{\max}$. A bigger basis

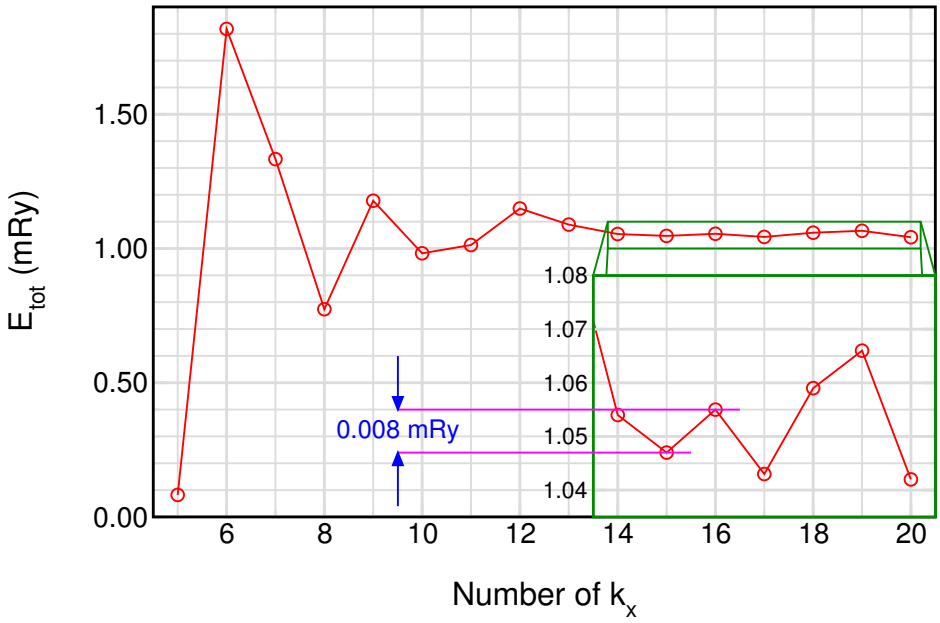

Figure 5.6: Total energy versus the number of the k-points for Fe_4C. A homogeneous k-mesh in all directions has been used. The inset depicts a zoom into a larger scale.

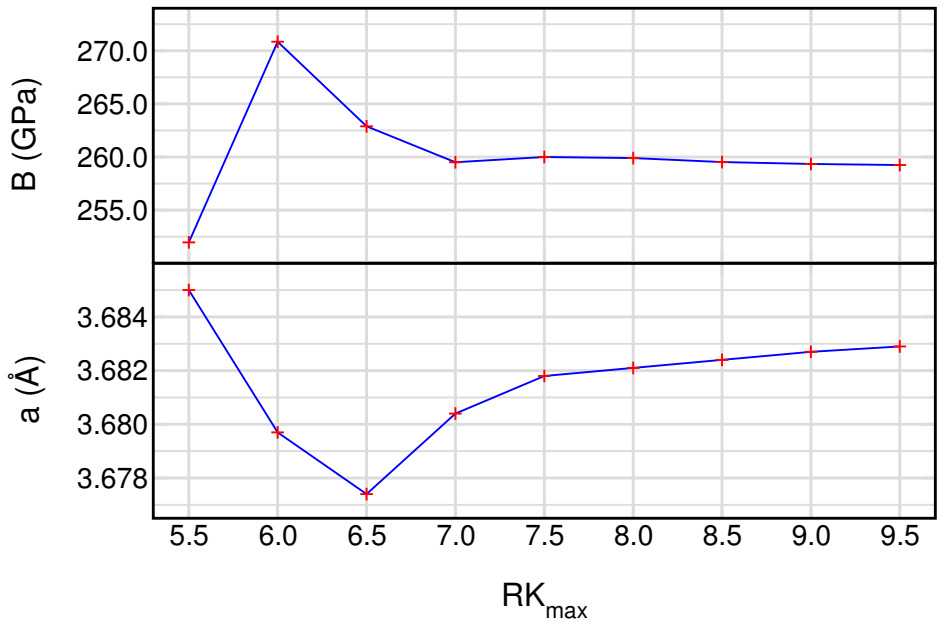

Figure 5.7: The dependence of the Lattice parameter, a, and bulk modulus, B, of Fe_4C on the values of $RK_{\max}$. Here $RK_{\max} = 7.0$ is enough for required accuracy.

set (with higher number of terms) produces more accurate results at the cost of extra computational resources. Therefore selecting a reasonable upper bound for the expansion to keep a compromise between the accuracy and efficiency becomes important. In the WIEN2k package, this upper bound is controlled by the cutoff parameter $RK_{\max}$, where R is the smallest atomic-sphere radius in the unit cell and $K_{\max}$ is the magnitude of the largest $\mathbf{G}$ vector in the expansion.

The applied optimization method is explained in the following:

- **Bulk:** The lattice parameter and the bulk modulus are calculated for Fe_4C bulk using different values of $RK_{\max}$. The results are shown in Fig. 5.7. Any $RK_{\max}$ larger than or equal to 7.00 gives required accuracy for both desired parameters (see Table 5.3).
- **Slice, Fe_3C:** For this structure, the k-mesh and $RK_{\max}$ are optimized simultaneously. Some points on the γ-curve are calculated using a k-mesh of $10 \times 10 \times 1$ and $RK_{\max} = 7.0$. The calculations are repeated using a $15 \times 15 \times 1$ k-mesh and $RK_{\max} = 8.0$. Since no significant difference in the γ-curve is observed the smaller values are selected (see Fig. 5.8 and also Table 5.3).
- **Slice, $Fe_{24}C$:** For this concentration which has a larger unit cell, the effect of $RK_{\max}$ on the atomic forces in the slab is investigated. The results are shown in Fig. 5.9 (see also Table 5.3). Here $RK_{\max} = 6.5$ leads to reasonable results.

5.3.3 Number of Layers in the Slice

A fault is created by displacing two slices of bulk with respect to each other (see Sec. 5.2.2). While using slices with small number of atomic layers, L, is computationally favored, for keeping the accuracy of the results, L must be big enough so that the layer in the center of slice would feel an environment quite similar to that of the perfect bulk. A compromise between accuracy and performance can be found by investigating the influence of the number of layers on the γ-curve. Some points on the γ-curve are calculated using slices with different number of layers, *i.e.*, $L = 3, 6, 9, 12$, as shown in Fig. 5.10. Since no significant change is found in the results going from $L = 6$ to 9 or 12, we select $L = 6$.

5.4 Results

5.4.1 The γ-curve of Fe

For non-magnetic pure iron at 0 K, DFT predicts the hcp phase to be energetically more stable than fcc [124]. Therefore, an fcc structure exhibiting an ISF is energetically more favorable than a perfect fcc structure since the $\cdots ABCAB|ABC\cdots$ stacking sequence of the former resembles an hcp-like stacking ($ABAB$) which appears close to the fault plane. This is reflected in our results which produce negative values of the γ-curve around $u = \frac{6}{18} u_{[\bar{2}11]}$ (see Fig. 5.11(c)). Our SFE of $-450\,\mathrm{mJ/m^2}$ is in

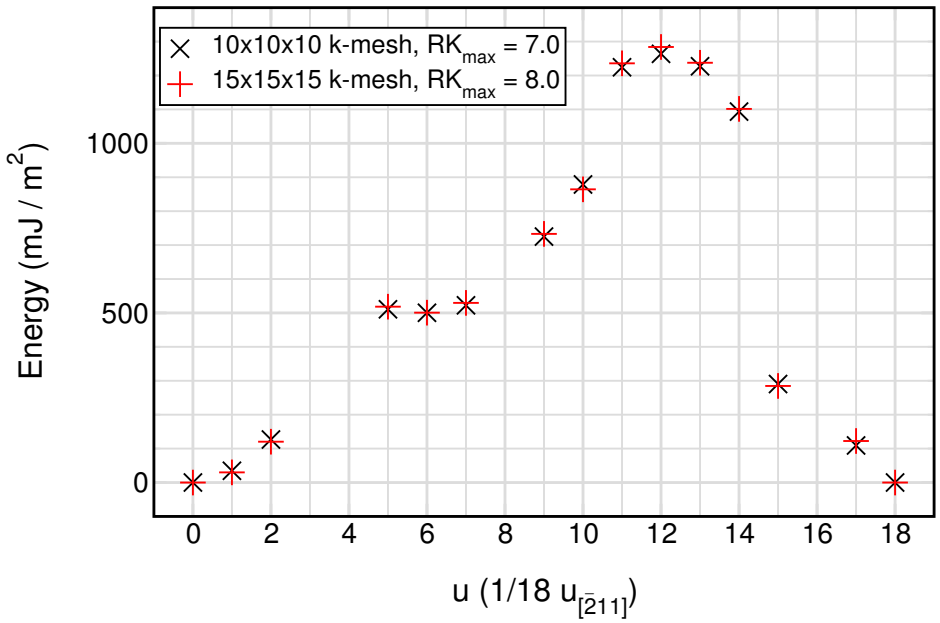

Figure 5.8: γ-curve in Fe_3C for two different sets of k-mesh and RK_{max}.

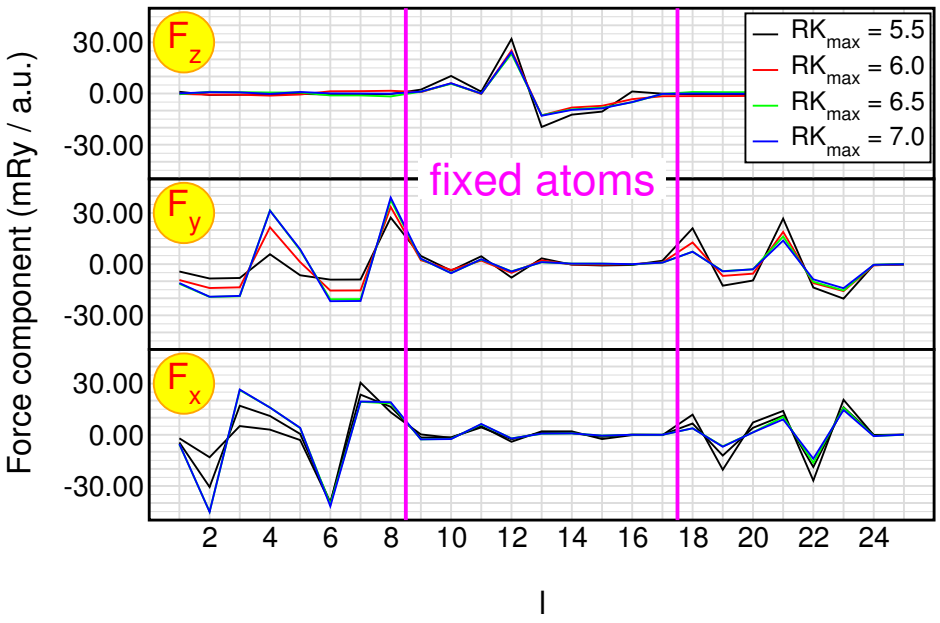

Figure 5.9: The dependence of the atomic forces on the value of RK_{max} for the $Fe_{24}C$ slab. l denotes the index of non-equivalent atoms in the unit cell. The atoms in the middle layers (*i.e.* far away from the SF) are not allowed to relax. The results for $RK_{max} = 6.50$ (green) and $RK_{max} = 7.00$ (blue) are almost the same.

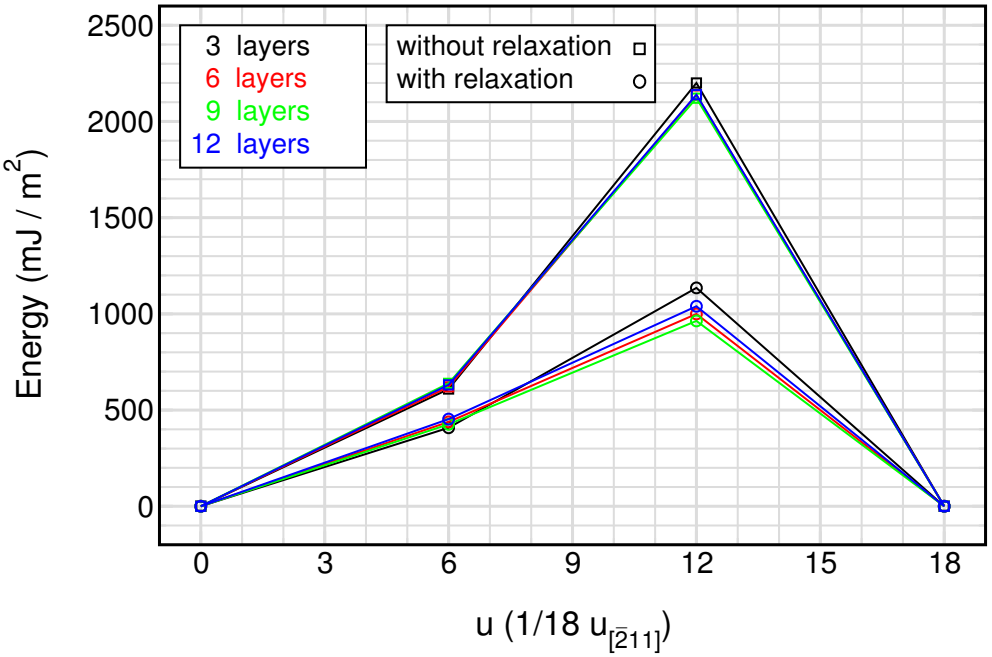

Figure 5.10: Dependence of the γ-curve on the number of atomic layers, L, between two consecutive faults.

good agreement with the work of Abbasi and coworkers [40], who found values between -452 and $-464\,\mathrm{mJ/m^2}$ for different unit-cell choices. The first peak in the curve, *i.e.*, at $u \approx \frac{3}{18}u_{[\bar{2}11]}$, describes the energy barrier which must be overcome in order to create an ISF. The second peak at $u = \frac{12}{18}u_{[\bar{2}11]}$ corresponds to a configuration with an $\cdots ABCAB|BCAB\cdots$ stacking sequence, which strongly violates the close-packing and, thus, is energetically very unfavorable. To preserve the close-packed stacking, the displacement can transform to an *extrinsic* SF by shearing one layer with respect to the entire crystal [50].

5.4.2 The γ-surface of $Fe_{24}C$

The supercell of $Fe_{24}C$ along the $[\bar{2}11]$ direction is twice as long as that of Fe and Fe_3C (see Fig. 2.6(a)). Hence, differences in the γ-curve between the first and the second half of this periodicity may arise due to the presence of carbon. However, when analyzing the γ-curve along the full doubled unit cell, our calculations show that the second half of the curve, *i.e.*, $u_{[\bar{2}11]} < u < 2u_{[\bar{2}11]}$, is only slightly different than its first half, *i.e.*, $0 < u < u_{[\bar{2}11]}$, particularly when carbon is not placed in the fault plane. For this reason we present only the first half of the γ-curve here. This has the advantage that the horizontal axes in all presented γ-curves are of the same length and scale.

In Fig. 5.11(a), we present the γ-curves for carbon atoms positioned at various octahedral vacancies, corresponding to distances from the fault plane $0 \leq d \leq 3$. The results for $d = 0$ (dashed black curve) yield a very large energy for $u = \frac{6}{18}u_{[\bar{2}11]}$ since

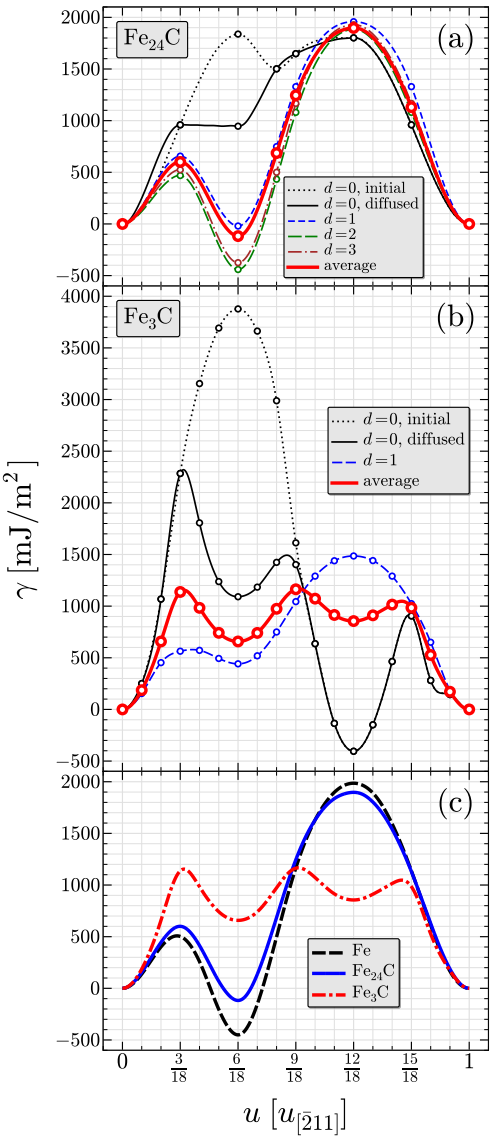

Figure 5.11: (a) The γ-curve for different positions of carbon with respect to the fault plane and their average, all calculated for $Fe_{24}C$. (b) The same for Fe_3C. (c) Comparison of the averages with pure Fe.

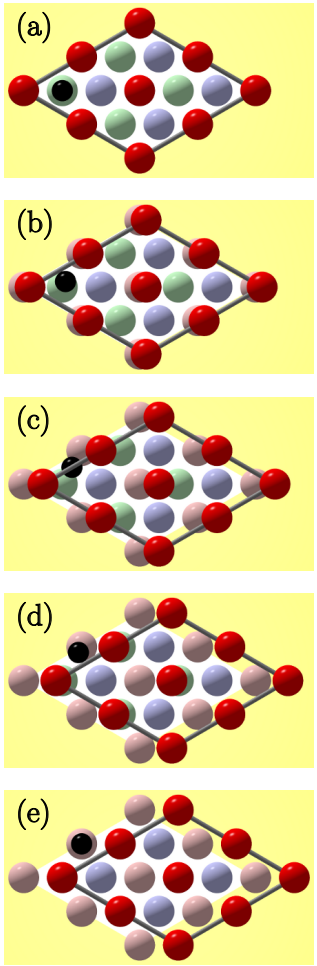

Figure 5.12: Carbon diffusion in $Fe_{24}C$ along the {111} plane. Spheres with pale and deep colors denote atomic layers belonging to fixed and shifted crystal halves, respectively. When a carbon atom is located in the fault plane, shifting the atomic layers requires an iron atom to pass on top of the carbon. The resulting configuration is highly unstable, thus the carbon diffuses to a new vacancy, which has just been created due to the shift.

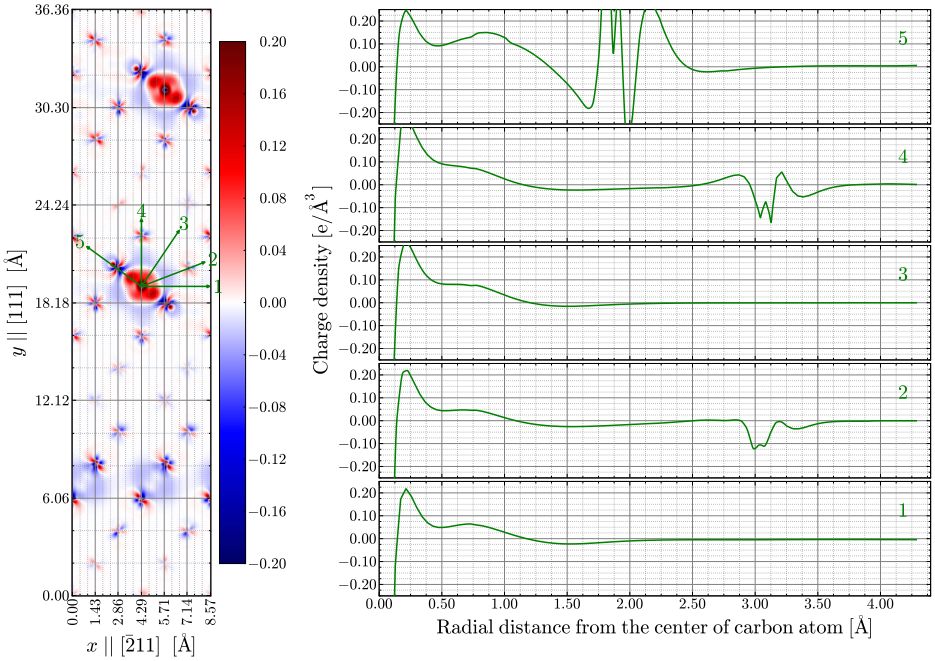

Figure 5.13: The difference in the charge density due to doping a carbon atom in $d = 2$ positions.

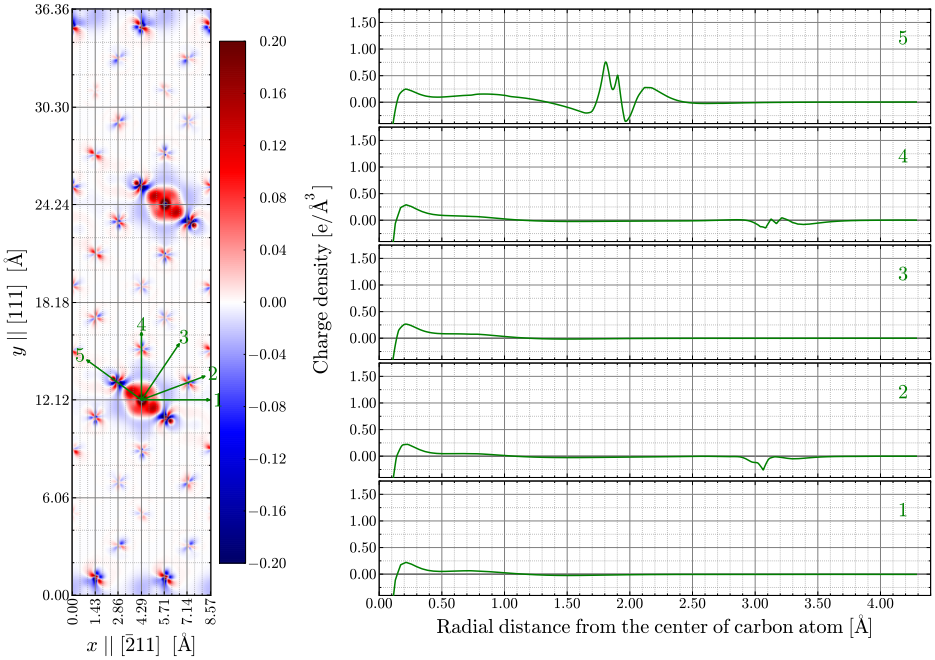

Figure 5.14: The difference in the charge density due to doping a carbon atom in $d = 3$ positions.

this point corresponds to an unfavorable configuration in which an iron atom sits on top of the interstitial carbon. The creation of the SF, on the other hand, leads to new octahedral sites, which can be occupied by small interstitial atoms like carbon (see Fig. 5.12). Thus, the diffusion of carbon into such new interstitial sites at the fault plane decreases the energy considerably, as indicated by the solid black curve. We further observe that the second peak in the curve with $d = 0$, is somewhat lower than the corresponding peak in the other curves. This can be explained by considering the fact that this peak is due to repulsion between iron atoms in two consecutive atomic layers, which is reduced when the distance between iron layers is increased through the presence of carbon. Focusing on the d-dependence at $u = \frac{6}{18}u_{[\bar{2}11]}$, *i.e.*, the ISF, we observe a monotonic behavior when increasing the carbon distance from $d = 0$ to $d = 2$, so that the curve corresponding to $d = 2$ is similar to the γ-curve for pure iron. However, the curve for $d = 3$ breaks this monotonicity which was assigned to Friedel-like oscillations [40]. Such oscillations appear in the charge density when an impurity is doped in a cloud of electrical charges. Here, the cloud is the body of the metal, and the impurity is the carbon atom. In order to visualize these oscillations, we calculate the charge densities for three supercells, including iron, carbon, and iron–carbon systems. The changes in the charge density is found by subtracting the charge densities of iron and carbon systems from the charge density of the iron–carbon system. These differences are presented in Figs. 5.13 and 5.14, for the two mentioned structures, *i.e.*, $d = 2$ and $d = 3$, respectively. The dependence of the SFE on the distance of the carbon atom from the fault plane is summarized in Fig. 5.15. It demonstrates that, the closer the carbon atom is positioned with respect to the fault plane, the higher is its influence on the SFE.

As explained in Sec. 5.2.3, we are interested in the γ-curve for a homogeneous carbon distribution. Therefore, we have to average over the results for various carbon positions characterized by their distances d from the fault plane in an appropriate manner. The $Fe_{24}C$ supercell, which has been utilized in this work, contains six types of interstitial octahedral sites, *i.e.*, $0 \leq d \leq 5$, while the γ-curve is calculated explicitly only for four sites with d up to 3. The effect of the other two layers, *i.e.*, $d = 4, 5$, on the γ-curve is taken into account by approximating their contribution by the mean value of the curves for $d = 2$ and $d = 3$. Using this mean value, we simulate the environment far from the fault plane, smearing out the above mentioned oscillations. In short, using $\gamma_4 = \gamma_5 = (\gamma_2 + \gamma_3)/2$, the general behavior of the γ-curve for $Fe_{24}C$ is found from the following expression

$$\gamma_{\mathrm{av}}^{\mathrm{Fe_{24}C_1}} = \frac{\gamma_0 + \gamma_1 + 2(\gamma_2 + \gamma_3)}{6}. \tag{5.6}$$

Using the approach described in Sec. 5.2.2, we can reconstruct the full two-dimensional γ-surface by making use of the symmetry properties of the crystal. It is presented in Fig. 5.16 for a rectangular area within the {111}-plane.

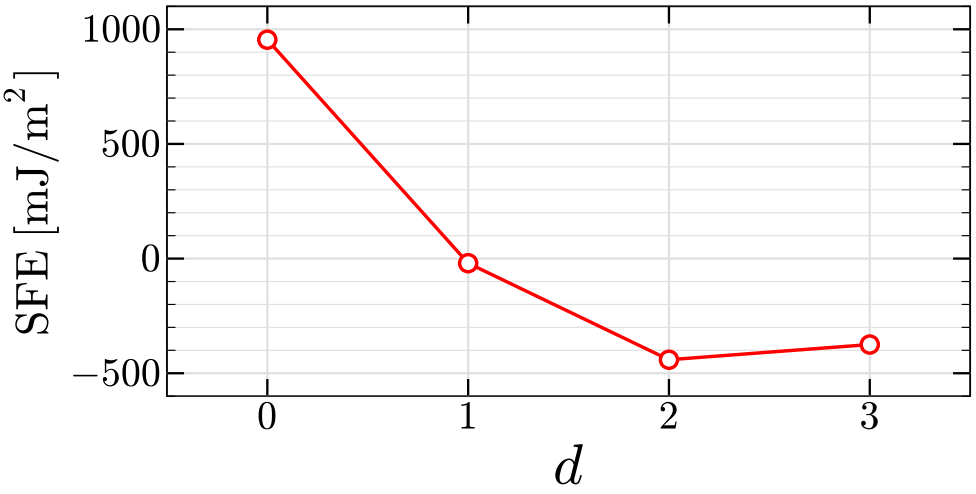

Figure 5.15: Dependence of the SFE on the distance of carbon from the fault plane for $Fe_{24}C$. For definition of d, see Sec. 5.2.3.

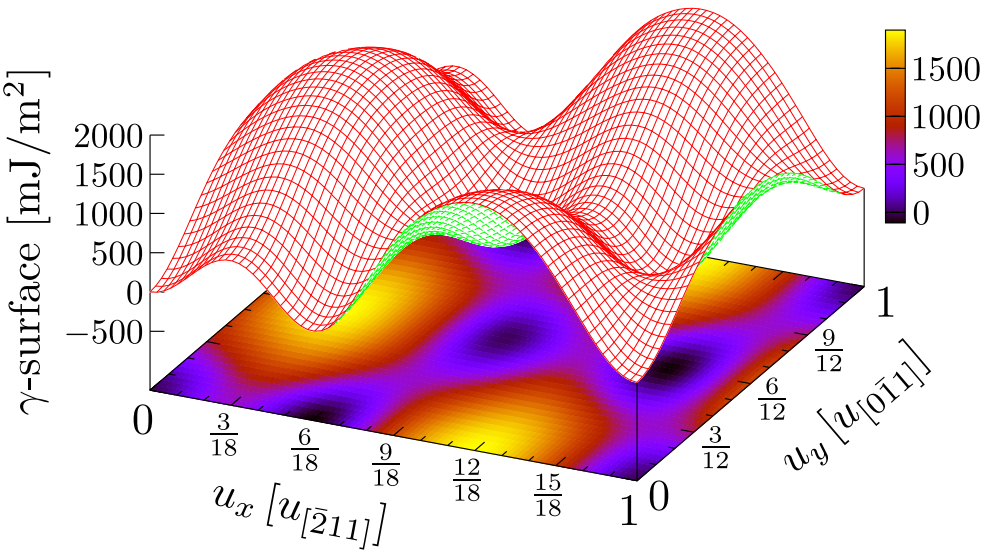

Figure 5.16: The γ-surface for $Fe_{24}C$.

5.4.3 The γ-curve of Fe_3C

Fe_3C, or iron carbide, is a chemical compound of iron and 6.67 w% of carbon. At low temperatures, it is found in an orthorhombic crystal structure, known as cementite. It contains two kinds of vacancies, with octahedral and prismatic environment. A prismatic vacancy is formed by six iron atoms which are located at the vertices of a triangular prism. DFT calculations show that carbon prefers to occupy the prismatic vacancy rather than the octahedral one [71].

As we are interested in the austenitic phase, our approach to calculate the γ-curve for Fe_3C is, like the case of $Fe_{24}C$, based on an fcc structure where carbon occupies octahedral sites. When introducing a staking fault, two possible interstitial carbon sites must be distinguished which we characterize by the distance from the fault plane as $d = 0$ and $d = 1$. For $d = 0$, we calculate a value of 3877 mJ/m^2 at $u = \frac{6}{18}u_{[\bar{2}11]}$, as shown in Fig. 5.11(b). Diffusion of interstitial carbon along the {111}-plane into another possible interstitial site decreases this value to 1091 mJ/m^2. In contrast to all other curves, the case of $d = 0$ at $u = \frac{12}{18}u_{[\bar{2}11]}$ has a deep minimum instead of a high maximum. The reason is that in the corresponding configuration, $\cdots ABCAB|BCAB\cdots$, iron atoms around the SF are all located at vertices of triangular prisms with bases parallel to the fault plane. Every second prism contains a carbon atom in its center, providing six Fe-C bonds. Thus, the observed deep minimum results from the fact that for Fe_3C the cementite structure, described above, is more stable than austenite.

The average SFE for Fe_3C is presented by the red solid curve in Fig. 5.11(b). It shows a positive SFE, indicating that for this concentration the fcc structure is more stable than the hcp structure.

5.5 Discussion

In Fig. 5.17, our results about the influence of carbon on the SFE in fcc iron are summarized and confronted with available experimental and other theoretical results. As already mentioned in Sec. 5.1, experimental data are controversial: While a common behavior is that the SFE increases with carbon concentration, there is a large spread in the magnitude of the effect. Our calculations show that the SFE increases from -450 mJ/m^2 for pure iron to -116 mJ/m^2 for $Fe_{24}C$ with 0.89 w% of carbon. Thus, for carbon concentrations between 0 and 0.89 w%, the SFE dependence on the carbon concentration can be approximated by 376 mJ/m^2 per weight percent of carbon. This value is in good agreement with recently published results by Abbasi *et al.* [40] and also compares well with experiments by Schramm and Reed [117]. Our results for Fe_3C, *i.e.*, in the limit of very large carbon concentrations, show that the dependence of the SFE on the carbon concentration levels off at large carbon content. Although our calculations have been performed for zero Kelvin, we expect the fcc phase to become stable for carbonic steels with about 2 w% of carbon.

The barrier height at $u \approx \frac{3}{18}u_{[\bar{2}11]}$ increases with the carbon content. In contrast, at $u = \frac{12}{18}u_{[\bar{2}11]}$ the curves for $Fe_{24}C$ and Fe_3C show different behavior. There are two

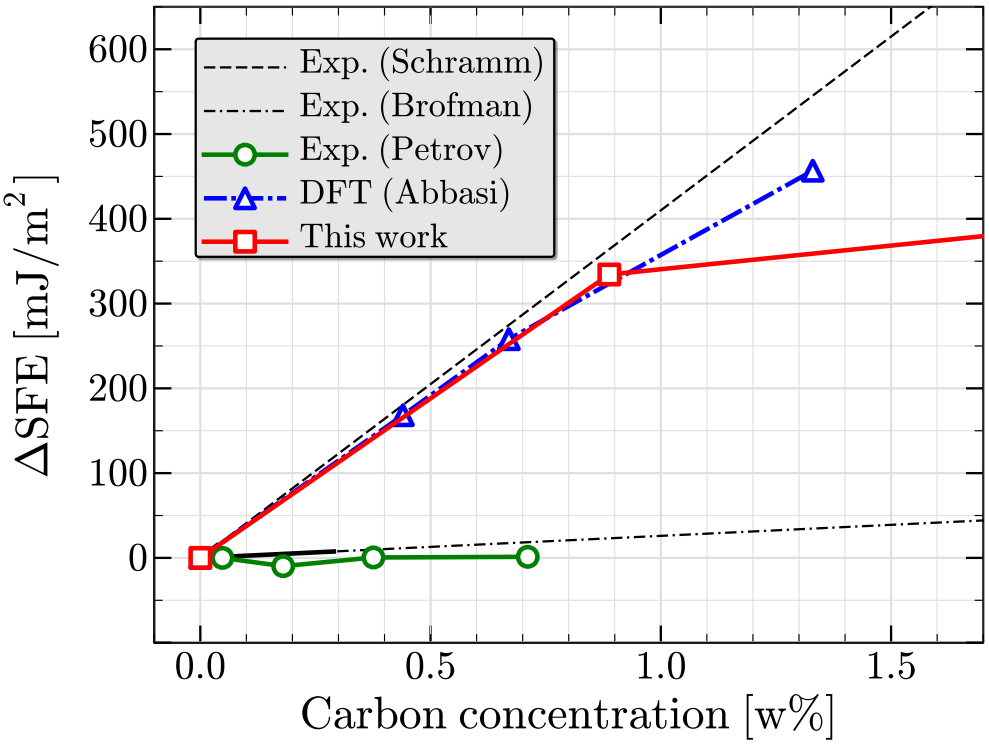

Figure 5.17: Carbon-induced change in the intrinsic SFE, ΔSFE, as a function of carbon concentration. Note that the values are normalized to the value of the intrinsic SFE for pure iron. Our calculations are compared to experimental data [25, 117, 120] and DFT [40] results.

competing phenomena affecting the total energy at this point: the distance between iron layers and the presence of a carbon at a prismatic site. For all values of d, the small inter-layer distance around the fault plane increases the total energy. Since the increase in cell volume per iron atom upon adding carbon is 4.1 % and 20.6 % for $Fe_{24}C$ and Fe_3C, respectively (see Tab. 5.3), $Fe_{24}C$ is more affected than Fe_3C. Occupation of prismatic sites by carbon decreases the energy. The possibility of occupying such site, which only occurs for $d = 0$, is $\frac{1}{12}$ and $\frac{1}{6}$ for $Fe_{24}C$ and Fe_3C, respectively. This confirms its more significant influence on the γ-curve of Fe_3C. As a result of these counteracting effects, we observe a high maximum for $Fe_{24}C$ and a local minimum for Fe_3C at $u = \frac{12}{18} u_{[\bar{2}11]}$.

6

The Fe–Cr–Ni System

Stainless steels, their classifications, and their properties were introduced in Chap. 3. The importance of this class of steels in many applications motivates investigations for finding efficient production and shaping methods. Shaping steels under shear stresses involves plastic deformation, a process where the stacking-fault energy (SFE) has a well-known influence [5–7]. The SFE, in turn, depends on temperature and on the composition of the alloy (see Appendix A for experimental reports, and [37, 125, 126] for theoretical references), making it particularly important when considering the thermal treatments and shaping of the metal at high temperatures. Therefore, this chapter is dedicated to the evaluation of the SFE as a function of temperature in austenitic Fe–Cr–Ni stainless steel.

6.1 Introduction

As discussed in Sec. 3.3, provided a sufficient amount of Ni and a relevant heat treatment, an Fe–Cr–Ni alloy can be found in the austenite phase over a broad range of temperature, including room temperature. In such an alloy with fcc structure, the SFE becomes a crucial parameter when studying plastic deformations under shear stress (see Secs. 2.3 and 2.4). Therefore, there have been many experimental investigations where the SFE has been measured as a function of temperature and also chemical composition (see Appendix A). Based on such studies, the main part of our present understanding about the SFE and its empirical connection to the physical properties of materials has been formed. On the other hand, the SFE is related to the material structure on the atomic scale, and thus is relevant to be investigated using *ab-initio* techniques. Such systematic investigations based on theories capable of describing materials on the atomic scale provide an important tool for intelligent design of materials. However, in Fe–Cr–Ni alloys, the SFE has not widely been studied using first-principles methods.

To the best of our knowledge, the SFE for a disordered Fe–Cr–Ni alloy in its paramagnetic state has been calculated only by Vitos *et al.* [37, 125, 126]. They have investigated the SFE as a function of temperature and chemical composition, emphasizing the role of thermal magnetic excitations in the SFE. However, the thermal lattice

Table 6.1: The atomic and mass concentrations of the commercial alloy, Böhler A607, compared to their simplified equivalents used in our simulations.

alloy	unit	Cr	Ni	Mn	Mo	C	Fe
Böhler A607	wt. %	18.00	9.00	≤2.00	—	≤0.03	70.17
	at. %	19.97	8.47	≤2.01	—	≤0.14	69.41
Simulated A607	wt. %	18.80	8.91	—	—	—	72.29
	at. %	20.00	8.40	—	—	—	71.60

expansion has not fully been taken into account in their work, since they evaluate the magnetic entropy for equilibrium volume calculated at 0 K. As we will show in this chapter, one must account for the thermal lattice expansion in order to obtain the accurate behavior of the SFE versus temperature.

In this chapter, we study the influence of temperature on the SFE of a ternary alloy with $Fe_{0.716}Cr_{0.200}Ni_{0.084}$ composition. Moreover, the effect of different parameters, approximations, and computational techniques on the final results are intensively investigated. The EMTO method described in Sec. 4.7 is employed in order to calculate the SFE in the temperature range of 298–1273 K (25–1000 °C). The chromium and nickel contents in this alloy are similar to those in the commercial product known as Böhler[1] A607. However, as shown in Tab. 6.1, this commercial alloy contains small amounts of additional elements which are not taken into account in our calculations. For brevity, in this document, *A607* is used in order to point to the simulated composition, while the corresponding alloy with real composition is referred by its full name, *Böhler A607* (see Tab. 6.1). The fcc structure of Böhler A607 over the entire temperature range has been proven through the X-ray diffraction (XRD) measurements.

Our simulations are performed for the random alloy in the paramagnetic austenitic phase in the above-mentioned temperature range. Briefly speaking, we use the axial next-nearest-neighbor Ising (ANNNI) model [48, 49] in order to expand the SFE in terms of the free energies of bulk with fcc, hcp, and double-hcp (dhcp) crystal structures (see Fig. 6.1 and Sec. 6.2). These free energies depend on the lattice parameter which is obtained from experimental thermal expansion data measured using the XRD technique, and on the thermal excitation of the local magnetic moments which is evaluated by running a Monte-Carlo simulation on the system energy maps calculated using DFT techniques (see Sec. 6.4.2). The DFT calculations are performed using the exact muffin-tin orbitals (EMTO) method [127] and the locally self-consistent Green's function (LSGF) method [128], where the random alloy and the paramagnetic state are modeled using the coherent potential approximation (CPA) [45] and the disordered local moment (DLM) [46], respectively.

[1] *Böhler Special Steels*, A-8605 Kapfenberg, Austria

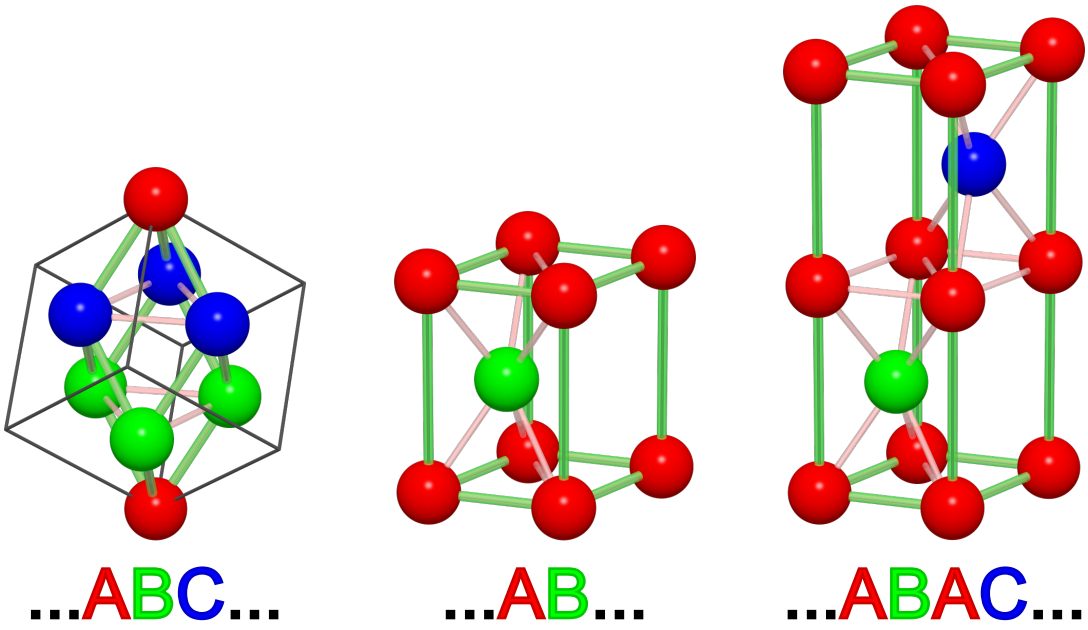

(a) (b) (c)

Figure 6.1: Primitive cells of three crystal structures used in the ANNNI model. Atoms are colored according to their stacking position along the [111] direction. (a) depicts the primitive cell of the fcc structure with only one atomic site. The cubic cell is shown for a better imagination of the lattice. (b) shows the primitive cell of the hcp structure containing two non-equivalent atoms (two atomic sites). (c) represents the primitive cell of the dhcp structure with four non-equivalent atoms.

6.2 Methodology

This section aims to explain the relation between the SFE as a result of a fault, and the free energies of a variety of undistorted phases. The free energies, in turn, depend on different entropy contributions, which are discussed in more detail.

6.2.1 The ANNNI Model

An intrinsic stacking fault (ISF) changes the total energy of a crystal by introducing an irregularity in the sequence of atomic layers. Since the close packing is preserved, these changes are generally very small compared to the crystal total energy. While the SFE can be accurately and explicitly calculated using the first-principles supercell techniques [39–41], these methods are quite cumbersome, since they require large cells. A more efficient solution, which is going to be explained here, is to expand the SFE in terms of the free energies of bulk unit-cells with fcc, hcp, and double-hcp (dhcp) structures (see Fig. 6.1).

In the fcc lattice, an ISF, which corresponds to the removing of one atomic layer

from the perfect $ABCABCABC\cdots$ structure, may be represented as the arrangement of atomic layers with the repeat unit of $ABCBC(ABC)^n$ $(n = 0, 1, 2, \cdots)$, consisting of N layers $(N = 5, 8, 11, 14, \cdots)$ in the limit $N \to \infty$. We can now apply the axial next-nearest-neighbor Ising (ANNNI) model [48, 49] to this representation, where the analogue of the Ising spin S_i for layer i, has a value $+1$ (-1) if the next layer with index $i+1$ does (not) conform the ideal stacking sequence. This idea results in the following expression for the Helmholtz free energy of any arbitrary stacking sequence [49]:

$$\mathcal{F} = \mathcal{F}_0 - J_1 \sum_i S_i S_{i+1} - J_2 \sum_i S_i S_{i+2} - J_3 \sum_i S_i S_{i+3} - \cdots , \tag{6.1}$$

where $\mathcal{F}_0$ is the energy contribution disregarding all interactions between layers, and thus is the same for any arbitrary stacking sequence. The parameters $J_n (n = 1, 2, 3, \cdots)$ may be interpreted as interaction energies between two layers that are nearest neighbors (J_1), next-nearest neighbors (J_2), ... It is expected that the magnitude of J_n decreases for increasing n. In the ANNNI model, by definition, all J_n with $n \geq 3$ are neglected [48].

In the limit of large N, the above equation suggests the following expressions for the Helmholtz free energies of the stacking sequences with different repeat units [49]:

$$\begin{array}{lllllll} ABC & \mathcal{F}^{\mathrm{fcc}} = J_0 & -J_1 & -J_2 & -J_3 & -J_4 - \cdots , \\ AB & \mathcal{F}^{\mathrm{hcp}} = J_0 & +J_1 & -J_2 & +J_3 & -J_4 + \cdots , \\ ABAC & \mathcal{F}^{\mathrm{dhcp}} = J_0 & & +J_2 & & -J_4 + \cdots , \\ ABCBC(ABC)^n & \mathcal{F}^{\mathrm{ISF}} = J_0 & -\frac{N-4}{N} J_1 & -\frac{N-4}{N} J_2 & -\frac{N-4}{N} J_3 & -\frac{N-4}{N} J_4 - \cdots , \end{array} \tag{6.2}$$

where the energies are normalized to a unit cell in one layer, and J_0 is the energy per unit cell in one layer if the interactions between layers are disregarded. Using the first three equations, J_0 is found as

$$J_0 = \frac{\mathcal{F}^{\mathrm{fcc}} + \mathcal{F}^{\mathrm{hcp}} + 2\mathcal{F}^{\mathrm{dhcp}}}{4} + O(J_4). \tag{6.3}$$

The energy difference between a structure with an ISF and the fcc bulk structure, both of the same thickness equal to N layers, is defined as

$$\begin{aligned} \lim_{N\to\infty} N\{\mathcal{F}^{\mathrm{ISF}} - \mathcal{F}^{\mathrm{fcc}}\} &= 4\{J_1 + J_2 + J_3 + J_4 + \cdots\} \\ &= -4\{\mathcal{F}^{\mathrm{fcc}} - J_0\} \\ &= \mathcal{F}^{\mathrm{hcp}} + 2\mathcal{F}^{\mathrm{dhcp}} - 3\mathcal{F}^{\mathrm{fcc}} + O(J_4). \end{aligned} \tag{6.4}$$

Since the number of atomic sites per volume is equal in ideal fcc, hcp, and dhcp structures (see Fig. 6.1), we can easily rewrite the above equation in terms of the Helmholtz free energies per atomic site, F. Finally, by neglecting all J_n with $n \geq 4$ according to the definition of ANNNI model, and by considering the dependence of the Helmholtz free energies on temperature, the SFE is expressed as

$$\mathrm{SFE}(T) \approx \frac{F^{\mathrm{hcp}}(T) + 2F^{\mathrm{dhcp}}(T) - 3F^{\mathrm{fcc}}(T)}{A}, \tag{6.5}$$

where A is the area in a close-packed layer occupied by a single atomic site, and its value can simply be obtained in terms of the fcc lattice parameter: $A = \frac{\sqrt{3}}{4} a_{\mathrm{fcc}}^2$.

6.2.2 Temperature Dependence of the Free Energy

When studying molecules and solids, the stable structure is the one with the lowest Gibbs free energy. At temperature T and pressure p, the Gibbs free energy is defined as

$$G(p,T) = E(p,T) + pV(p,T) - TS(p,T), \tag{6.6}$$

where E denotes the total energy (internal energy), and V and S are the volume and the entropy, respectively.

In solids, volume changes are usually very small, and thus, at ambient conditions with constant pressure, the contribution of the term $p\Delta V$ to the Gibbs free-energy differences, ΔG, becomes negligible. In such cases, the Helmholtz free energy can be used instead of the Gibbs free energy. At temperature T, the Helmholtz free energy is defined as

$$F(T) = E(T) - TS(T). \tag{6.7}$$

It must be noted here that we calculate all quantities in the above equation, *i.e.*, F, E, and S, for a single site in the lattice.

The total energy $E(T)$ is calculated using DFT. Using the Mermin functional [129], finite-temperature DFT calculations can account for the temperature dependence of the distribution of electrons over states [87]. However, this is not enough for calculating the total energy as a function of temperature, since a major part of the temperature dependence of $E(T)$ comes through the lattice parameter, $a(T)$, and also through all average local magnetic moments, $\{m_s(T)\}$ (here $s \in \{\text{Fe, Cr, Ni}\}$):

$$E(T) = E\big(a(T), \{m_s(T)\}\big). \tag{6.8}$$

Since the first-principles calculation of the lattice parameter as a function of temperature would require the calculation of vibrational excitations for the random alloy in the paramagnetic state, we resort to measurements at different temperatures. Therefore, we obtain the temperature dependence of the lattice parameter using the thermal lattice expansion data measured through the XRD technique.

The temperature dependence of the local magnetic moments is difficult to be measured. However, considering the thermal excitation of the individual moments through statistical methods, it is possible to calculate the average magnetic moments for every element in the paramagnetic DLM state at different temperatures. This approach is discussed in more detail in the next subsection.

6.2.3 Longitudinal Spin Fluctuations

In order to describe the thermal excitation of the local magnetic moments in the paramagnetic DLM state, we use a simple model based on the unified itinerant magnetism theory [130]. While the theory includes both transverse and longitudinal spin fluctuations on equal footing, we assume in our simplified model that the transverse spin fluctuations, *i.e.*, the fluctuations in the orientations of the magnetic moments, always

follow the completely disordered configuration, as described in the DLM state. For evaluating the longitudinal spin fluctuations (LSF), *i.e.*, the fluctuations in the size of the magnetic moments, a classical Monte-Carlo simulation is performed over a mapping of the system energetics, calculated for relevant configurations using the EMTO method.

6.2.3.1 Magnetic Hamiltonian

Ruban *et al.* [131] have introduced a magnetic Hamiltonian which, taking into account the LSF, can give a quite accurate representation of the energy of the classical magnetic state, as well as the values of the magnetic moments in the state. For a system consist of identical atoms, the Hamiltonian is defined as

$$H_{\text{mag.}} = \sum_i J^{(0)}(\bar{M}) + \sum_i J^{(1)}(\bar{M}, M_i) + \sum_{ij} J_{ij}^{(2)}(\bar{M}, M_i, M_j)\, \mathbf{M}_i \cdot \mathbf{M}_j, \tag{6.9}$$

where the vector $\mathbf{M}_i$ is the local spin moment of an atom at site i, whose length M_i can have any positive value. $\bar{M} = \langle M_i \rangle = \frac{1}{N}\sum_i M_i$ denotes the average value of the local magnetic moments in the system. $J^{(0)}(\bar{M})$ is the zeroth-order term defined as the energy of a homogeneous DLM state representing a system of randomly oriented spins with a fixed value of the magnetic moments $\bar{M}$. $J^{(1)}(\bar{M}, M_i)$ is the on-site term, the LSF energy, which is the energy required to change the size of the magnetic moment of the atom in position i, from the corresponding DLM value $\bar{M}$ to M_i. Finally, $J_{ij}^{(2)}(\bar{M}, M_i, M_j)$ is the pair exchange interaction parameter, which describes the magnetic interaction between atoms at sites i and j, with local magnetic moments M_i and M_j embedded in the DLM effective medium.

Using a similar approach, Reyes-Huamantinco *et al.* have recently calculated the single-site LSF for a paramagnetic iron-manganese binary alloy [38]. However, they assume that the free energy is dominated by single-site magnetic fluctuations in the paramagnetic DLM state, thus they define a Hamiltonian which includes only the first term of Eq. 6.9. Following their approach, we can rewrite the Hamiltonian for an alloy as

$$H_{\text{mag.}} = \sum_s c_s J_s(m_s), \tag{6.10}$$

where s stands for the species (elements) in the alloy (s = Fe, Cr, and Ni here), c_s is the concentration of element s, m_s is the *spatially-averaged* local magnetic moments of element s, and, finally, $J_s(m_s)$ is the energy required to excite these averaged moments from 0 to the value m_s in the DLM paramagnetic state. In fact, $J_s(m_s)$ in Eq. 6.10 corresponds to $J^{(0)}(\bar{M})$ in Eq. 6.9. Note that, while the Eq. 6.9 includes terms related to all individual atoms in the system (expressed by the summation $\sum_i$), Eq. 6.10 contains only single-site terms, which may be considered as an average over all atoms. That is why the summation $\sum_i$ has disappeared in the Eq. 6.10. We will present this approach in Sec. 6.4.2. In order to calculate $J_s(m_s)$ for our ternary system, we extend the methodology developed by Reyes-Huamantinco *et al.* [38] to include the thermal lattice expansion of the alloy. Computational details and results are presented in Sec. 6.4.2.

6.2.3.2 Monte-Carlo Technique

In order to obtain the temperature-dependence of the local magnetic moments, a Metropolis Monte-Carlo technique is used. In this approach, a system of randomly oriented spins is considered whose configuration is progressively altered by changing the size of its individual spins in a random manner. After a change applied, the total energy is calculated using the Hamiltonian 6.10, where the dependence of the total energy on the size of the magnetic moments has been defined using the energetics of the paramagnetic random alloy, $J_s(m_s)$, calculated using the EMTO method. A change in the system configuration is always permitted, if it lowers the system total energy, *i.e.*, it results in a negative ΔE, defined as $\Delta E = E_{\text{after}} - E_{\text{before}} < 0$, where E_{after} and E_{before} are the system total energies after and before the change, respectively. Otherwise, when $\Delta E > 0$, the changed configuration is accepted depending on the excitation probability, which is defined as $e^{-\Delta E/k_{\text{B}}T}$. As it is obvious from this definition, when $\Delta E > 0$, a configuration with larger $\Delta E/k_{\text{B}}T$ has lower chance to be accepted. The process is repeated many times, so that the changes in total energy, ΔE, become smaller than a given convergence criteria, showing that the current configuration is already very close to the equilibrium configuration with the lowest energy. Once these conditions are satisfied, the *spatial average* of the magnetic moments is calculated.

The algorithm starts with the highest temperature in the desired range, and while decreasing the temperature step by step, tries to find the equilibrium configuration of the magnetic moments.

6.2.4 Entropy contributions

The entropy is calculated by accounting for all available excitations which may occur in the microscopic configuration (microstate) of the system. The microstate might change due to various excitations: *configurational excitations*, considered as the interchange of positions between atoms of different types, *vibrational excitations*, defined as small displacements of atoms around their lattice sites, *magnetic excitations*, which are fluctuations in the size or the orientation of the atomic magnetic moments, and, finally, *electronic excitations*, which are changes in the electronic structure of the metal as electrons are excited to levels higher then the Fermi level. Depending on the diffusion rate, for very fast diffusion in solids, configurational excitations occur at a time scale of 10^{-5} or 10^{-4} seconds, while the atomic vibrations are at time scale of 10^{-11} or 10^{-10} seconds. The magnetic excitations are even faster than the vibrations, and the electronic excitations are the fastest in the list. The large differences between these time scales allow to apply a course-graining method in order to calculate the excitations independently, which finally results in their separate contributions to the total entropy of the crystal [105, 132]:

$$S = S_{\text{vib.}} + S_{\text{conf.}} + S_{\text{mag.}} + S_{\text{el.}}, \tag{6.11}$$

where all terms are related to a single site in the lattice. In the following, these four terms are discussed in more detail.

6.2.4.1 Vibrational Entropy

Currently, there are no available theoretical tools to accurately determine the vibrational entropy in paramagnetic random alloys. However, Vitos *et al.* [37] have estimated the error which might be introduced to the SFE as a result of excluding the vibrational entropy. By assuming similar vibrational free energies for fcc and dhcp lattices, they approximate the vibrational free energy as $\Delta F_{\text{vib.}} \approx F_{\text{vib.}}^{\text{hcp}} - F_{\text{vib.}}^{\text{fcc}}$. Using the high-temperature expansion of the phonon entropy [133], for two solids with similar Debye temperature (θ), they conclude $\Delta F_{\text{vib.}} \approx 3k_{\text{B}}T\frac{\Delta\theta}{\theta}$ [134]. Finally, considering the Debye temperature ratios between the bcc α-iron and the hcp ϵ-iron ($\theta_{\text{bcc}}/\theta_{\text{hcp}} \approx 0.96$) [135] and also between the bcc α-iron and the fcc γ-iron ($\theta_{\text{bcc}}/\theta_{\text{fcc}} \approx 0.97$) [134, 136], at $T = 300\,\text{K}$, they obtain $\Delta F_{\text{vib.}} \approx 0.75\,\text{meV/atom}$. This free energy corresponds to a contribution of $\Delta\text{SFE} \approx 2\,\text{mJ/m}^2$ to the SFE, which is rather small.

6.2.4.2 Configurational Entropy

Considering totally random alloys, the configurational entropy depends only on the chemical composition [137]:

$$S_{\text{conf.}} = -k_{\text{B}} \sum_{s\in\{\text{species}\}} c_s \ln(c_s), \tag{6.12}$$

where c_s denotes the atomic concentration of element s. In our calculations, we approximate the alloy as a fully random configuration of atoms. Such an assumption results in equal configurational entropies for all phases with the same chemical compositions, canceling each other out in Eq. 6.5.

However, it must be noted here that the assumption of the random distribution of all atoms on a sublattice is best in situations when (i) the temperature is very high, so the atoms are indeed randomly distributed on the sublattice; (ii) the temperature is very low, and only a few antisite atoms are present [137]. For other situations, particularly when temperature is not very high or when chemical compositions of elements in an alloy are not very small, this assumption is not entirely correct, since atoms show certain preferences when interacting with their neighbors. In a solid solution, these atomic interactions can express the local tendency for preferences of like or unlike neighbor pairs, which is known as *short-range order* (SRO) [137]. The SRO might be better understood compared to the *long-range order* (LRO), a crystal character which precisely specifies the properties (the position and the type) of atoms in the entire lattice by knowing them at a single lattice point. This term might also be pointed as the chemical or the atomic SRO (LRO) for the sake of distinguishing from its analogue in magnetism, *i.e.* the magnetic SRO (LRO).

In an ordered alloy, the SRO can change with some independence of the LRO, resulting in changes in the configurational entropy. Particularly at high temperatures, where the LRO vanishes, considerable SRO exists, increasing its importance in the entropy calculations [137]. Additional to the entropy, the total energy $E(T)$ also changes due to the SRO, resulting in further changes in the free energy. In order to take the

SRO into account, some corrections to the CPA approximation and the configurational entropy equation, Eq. 6.12, are required.

6.2.4.3 Magnetic Entropy

In a system of localized magnetic moments of the same size and completely disordered orientations, *i.e.*, the ideal paramagnetic state, the magnetic entropy is evaluated using the mean-field expression [133]

$$S_{\text{mag.}} = k_{\text{B}} \sum_{s\in\{\text{species}\}} c_s \ln\big(m_s(T)+1\big). \tag{6.13}$$

Here, $m_s(T)$ denotes the average (over time and space) local magnetic moment of element s, and is obtained using statistical approaches where the thermal excitations of magnetic moments are taken into account (see Sec. 6.4.2). Similar to the existence of the atomic SRO even at temperatures where the atomic LRO has already vanished, magnetic SRO might exist in a paramagnetic state.

6.2.4.4 Electronic Entropy

The electronic entropy can be calculated as [47]

$$S_{\text{el.}}(T) = -2k_{\text{B}} \int \Big\{ f(\epsilon)\ln\big(f(\epsilon)\big) + \big(1-f(\epsilon)\big)\ln\big(1-f(\epsilon)\big) \Big\} D(\epsilon)\,\mathrm{d}\epsilon, \tag{6.14}$$

where, $D(\epsilon)$ and $f(\epsilon)$ denote the density of states and the finite-temperature Fermi function [138], respectively. The Fermi function is a consequence of the Fermi-Dirac statistics [138, 139] and gives the probability of occupation of a state with energy ϵ at temperature T. The Fermi function is defined as

$$f(\epsilon) = \frac{1}{e^{(\epsilon-\mu)/k_{\text{B}}T}+1}, \tag{6.15}$$

where μ indicates the chemical potential. This approach is already available in the EMTO code, and we use it in order to calculate the electronic entropy. However, as we will present in Sec. 6.4.6.1, the influence of the electronic entropy on the final SFE in Fe–Cr–Ni alloy is very small, and hence can be safely neglected.

6.2.5 The SFE Calculations

Once the temperature dependence of the lattice parameter (through the XRD measurements) and of the local magnetic moments (through the Monte-Carlo step of the LSF calculations) are known, we perform a set of *constrained* DFT calculations to find the free energy of every phase as a function of temperature. These calculations are called constrained because the magnetic moments of all atom types are fixed to their corresponding values evaluated using the Monte-Carlo method. The SFE is then evaluated using these free energies, as expressed in the Eq. 6.5.

As a summary of our methodology, the necessary steps for evaluating the SFE are as follows:

- **Magnetic moments calculations:** In this step, for every element in every phase, we calculate the average magnetic moments as a function of temperature (see Sec. 6.4.2 for details). The calculations are broken into two major parts:

  1. **DFT calculations with fixed spins for one element:** In this part the dependence of the total energy of the system on the local magnetic moments of every element is obtained (see Sec. 6.4.2.1).
  2. **The Monte-Carlo calculations:** A set of simulations with magnetic Hamiltonians are performed on the system energy maps calculated in part 1, and the temperature dependence of the average magnetic moments is found (see Sec. 6.4.2.2).

- **Constrained DFT calculations:** In this step, according to Eq. 6.8, for different temperatures, the experimental lattice parameter and the magnetic moments from the previous step are used in DFT calculations in order to find the total energy as a function of temperature. These calculations are called *constrained*, because all magnetic moments are fixed (see Sec. 6.4.3 for details).

- **Free energy evaluation:** Using the results of the previous steps, according to Eqs. 6.7 and 6.13, the Helmholtz free energy is evaluated for all phases at different temperatures by subtracting the magnetic entropy from the total energy. Finally, using these free energies in the ANNNI model gives the SFE as a function of temperature (see Sec. 6.4.3 for details).

6.3 Computational Details

In a simulation, the accuracy of the final results is influenced by two major choices: the physical model, and the computational method. The physical model, using available theories, tries to approximate the real interactions between the individual parts of a system. In order to get a correct physical description of the system, these approximations must be as sophisticated as possible. In other words, the more detailed interactions are considered in the model, the more accurate results can *potentially* be obtained. However, it is possible, especially when investigating the difference between properties of two systems, that the shortcomings of the applied physical model remain hidden since the errors in calculations cancel each other out. Very often in practice, when developing a physical model, a compromise is necessary between the importance of the existing interactions and the complexities of their accounting. In fact, by such a compromise, the physical model defines the limit of accuracy and the reliability of the final results. In previous section, we already introduced our physical model and discussed applied approximations in detail.

Assuming the chosen physical model to be sufficiently accurate, the computational method calculates the system properties in the frame of this model. In the computational method, also, by setting proper computational parameters, a compromise is achieved between the desired accuracy and the required numerical efforts. The subject of this section is to discuss the most important computational parameters we have in our simulations.

The SFE is usually expressed in the unit of $\mathrm{mJ/m^2}$, and its value has been reported in the range of 10–50 for stainless steels with composition close to A607 (for a summary of experimental values, see Appendix A and Fig. 6.19). Considering the geometry of the {111} surface of an fcc structure, we find that

$$1\ \mathrm{mJ/m^2} = 1.98641346 \times 10^{-6} a_{\mathrm{fcc}}^2\ \mathrm{Ry/site}, \tag{6.16}$$

where a_{fcc} stands for the fcc lattice parameter in the unit of Angstrom (Å). Considering $a_{\mathrm{fcc}} \approx 3.6\,\text{Å}$ (see Fig. 6.8), the equation results in

$$1\ \mathrm{mJ/m^2} \approx 2.6 \times 10^{-5}\ \mathrm{Ry/site}. \tag{6.17}$$

The equation suggests that, in order to get the SFE with an accuracy of $1\,\mathrm{mJ/m^2}$, the differences between the free energies of the three phases must be calculated with an accuracy higher than $10^{-5}\,\mathrm{Ry/site}$. Using the Eq. 6.13, the influence of an error in the local magnetic moments on the final SFE can be estimated as

$$\Delta F(T) = T\Delta S_{\mathrm{mag.}}(T) = Tk_{\mathrm{B}} \sum_{s\in\{\mathrm{species}\}} c_s \frac{1}{m_s(T)+1}\,\Delta m_s(T). \tag{6.18}$$

Considering $(c_{\mathrm{Fe}}, c_{\mathrm{Cr}}, c_{\mathrm{Ni}}) = (0.716, 0.200, 0.084)$ and $(m_{\mathrm{Fe}}, m_{\mathrm{Cr}}, m_{\mathrm{Ni}}) \approx (1.3, 0.6, 0.3)$ at 300 K and $(m_{\mathrm{Fe}}, m_{\mathrm{Cr}}, m_{\mathrm{Ni}}) \approx (1.7, 1.2, 0.6)$ at 1300 K (see Fig. 6.17), the equation results in

$$\Delta F(300\,\mathrm{K}) \approx 1 \times 10^{-3}\,\Delta m_s, \tag{6.19}$$

$$\Delta F(1300\,\mathrm{K}) \approx 3 \times 10^{-3}\,\Delta m_s. \tag{6.20}$$

Here, this equation suggests that in order to preserve the accuracy of $10^{-5}\,\mathrm{Ry/site}$ in the SFE, the m_s must be calculated with an accuracy higher than $10^{-2}\,\mu_{\mathrm{B}}$. In our simulations, we go one order of magnitude beyond these values, *i.e.*, we calculate the total energy and the local magnetic moments with the accuracy of $10^{-6}\,\mathrm{Ry/site}$ and $10^{-3}\,\mu_{\mathrm{B}}$, respectively.

6.3.1 k-point Convergence

The number of k-points is one of the parameters affecting the accuracy of results, and hence must be selected carefully. We calculate the total energy and the local magnetic moments for different k-meshes to obtain the least dense k-mesh which guaranties the desired accuracy. As presented in Fig. 6.2, for the A607 alloy with the fcc structure, a k-mesh of $31 \times 31 \times 31$ results in converged values for both energy and magnetic moments. Using these informations, the commensurate sets of k-meshes for hcp and dhcp are found $30 \times 30 \times 16$ and $30 \times 30 \times 8$, respectively.

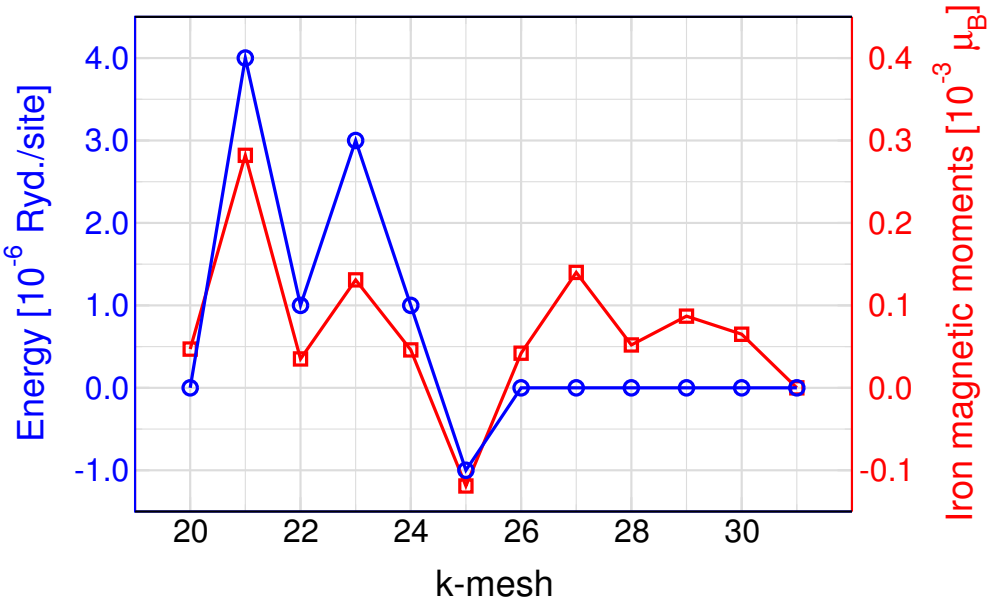

Figure 6.2: k-mesh optimization for the fcc structure of A607 alloy

6.3.2 Treatment of Core-electrons

There are two possible treatments for core electrons, the *soft-core* approach versus the simplified *frozen-core* approximation. In the frozen-core approximation, the wave functions of the core electrons are assumed not to be affected by different surrounding environments. Based on this assumption, the atomic orbitals with lower energies are kept exactly as they are in isolated atoms, and are constrained to remain doubly-occupied by the inner-shell electrons. Unlike this, in the soft-core approximation, all electrons (including both core and valance electrons) are calculated through the self-consistent approach. Tab. 6.2 presents the electronic configurations of iron, chromium, and nickel atoms, where core states are indicated by gray background. Note that, these are the default values defined in the EMTO code we use in this work, and might be changed by user. In the table, electronic states are characterized according their *relativistic* quantum number, κ, which is derived using the *azimuthal* and *spin* quantum numbers, *i.e.* l and s respectively (see Tab. 6.3).

The frozen-core approach might speed up the calculation, but at the price of losing accuracy, as it approximates the core orbitals with atomic orbitals. This simplification affects the physical description of the system, as it neglects all changes which might appear in the core states. Moreover, it has already been reported that when atoms are brought together to form molecules or solids the change in the kinetic energy of the core electrons can be an order of magnitude larger than the change in total energy [141]. Generally, if no sufficient corrections are applied, it is recommended to avoid this approximation where an accuracy higher than 0.1 eV is desired [141]. We apply the soft-core approach in order to get a better description of interactions between atoms

Table 6.2: The electronic configuration of elements iron, chromium, and nickel, according to the default definitions in the EMTO code. n indicates the principle quantum number, and κ denotes the relativistic quantum number (see Tab. 6.3). For better readability, core states have been highlighted by the gray background.

^{26}Fe: $1s^2$ $2s^2$ $2p^6$ $3s^2$ $3p^6$ $4s^2$ $3d^6$										
n	1	2	2	2	3	3	3	3	3	4
κ	−1	−1	1	−2	−1	1	−2	2	−3	−1
occupation	2	2	2	4	2	2	4	4	3	1

^{24}Cr: $1s^2$ $2s^2$ $2p^6$ $3s^2$ $3p^6$ $4s^1$ $3d^5$									
n	1	2	2	2	3	3	3	3	4
κ	−1	−1	1	−2	−1	1	−2	2	−1
occupation	2	2	2	4	2	2	4	4	2

^{28}Ni: $1s^2$ $2s^2$ $2p^6$ $3s^2$ $3p^6$ $4s^2$ $3d^8$										
n	1	2	2	2	3	3	3	3	3	4
κ	−1	−1	1	−2	−1	1	−2	2	−3	−1
occupation	2	2	2	4	2	2	4	4	4	2

Table 6.3: The derivation of the relativistic quantum number and the maximum occupations of electronic states per spin. Indicating the *principle*, the *azimuthal*, and the *spin* quantum numbers respectively by n, $0 \leq l < n$ and $s = \pm 1$, the *orbital* and the *relativistic* quantum numbers are defined as $j = l + s/2$ and $\kappa = -s(j + 1/2)$, respectively [140].

orbital	l	$j = l + s/2$		$\kappa = -s(j + 1/2)$		max. occupation	
		$s = -1$	$s = +1$	$s = -1$	$s = +1$	$s = -1$	$s = +1$
s	0		1/2		−1		2
p	1	1/2	3/2	1	−2	2	4
d	2	3/2	5/2	2	−3	4	6
f	3	5/2	7/2	3	−4	6	8

in the alloy. However, no efficiency improvement was observed in our test calculations with the frozen-core approximation (see Sec. 6.4.6.3).

6.3.3 Screening Parameters

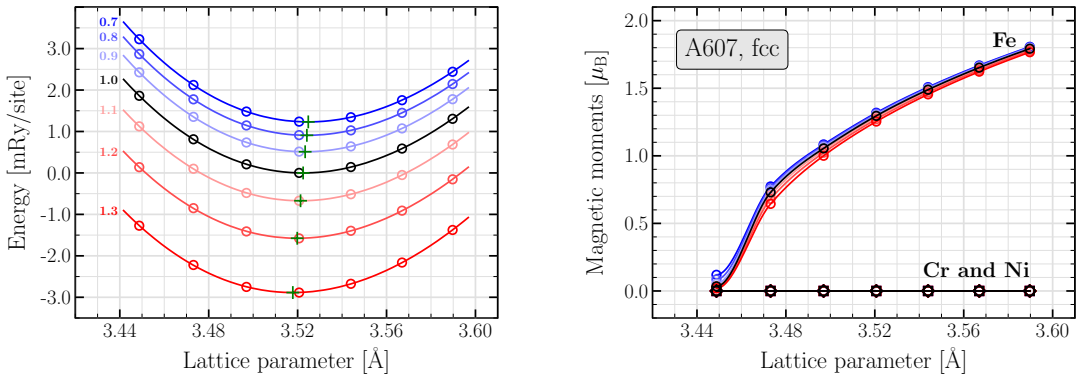

(a) (b)

Figure 6.3: For the fcc phase of A607 alloy, (a) and (b) show the effect of uniform scaling of all screening parameters on the E-V curve, and on the local magnetic moments, respectively.

For every element in the system, a pair of screening parameters must be given: a_{scr} which is related to charge transfers in the system, and b_{scr} which is related to the electrostatic energy. The influence of b_{scr} is small compared to that of a_{scr} [citation], thus we investigate the effect of a_{scr} only. While in the new LSGF-EMTO method they are calculated self consistently, in the version of the EMTO code we use in this work they must be given as input parameters. Since it could be time-consuming to calculate them, we used values suggested by Prof. Andrei Ruban, the developer of the code.

As a convergence test, we calculate the influence of the screening parameters on the equilibrium volume and the magnetic moments of the A607 alloy in the fcc phase. The results of these tests are presented in Fig. 6.3. Our calculations show that scaling all screening parameters uniformly shifts the entire E-V curve along the energy axis, where a set of larger screenings results in the lower total energy, and vise versa. The equilibrium volume has reverse relation with the uniformly scaled screenings: it increases 0.06% for scaling factor of 0.7, and decreases 0.13% for scaling factor of 1.3. Such small changes might be considered as negligible. Moreover, the local magnetic moments presented in Fig. 6.3(b) show only small changes due to the uniform scaling of the screening parameters. Further investigations by calculating the same quantities for the hcp and dhcp phases, show that the total-energy shifts are equal for all three phases. As presented in Fig. 6.4, when evaluating the SFE, these changes cancel each other out, leaving the SFE unchanged.

The behavior of the E-V curve and the magnetic moments versus the non-uniform scaling of the screening parameters is presented in Fig. 6.5, where these two quantities

are plotted for scaling factors of 0.8, 1.0, and 1.2. Similar to the case of the uniform scaling, the changes in the equilibrium volume are negligible. For the magnetic moments, although our results show an increase of up to 0.2 μ_B in the local magnetic moments of iron at smaller lattice volumes, changes at equilibrium volume are negligible. The interesting result which is found by analyzing the equilibrium energy E_0 is the fact that, despite of their concentrations, the total energy is mainly affected by the screening parameter of chromium, followed by nickel, and finally iron. This result is plotted in Fig. 6.6, where scaling factor are distinguished by different colors. The curly brackets and their labels in the figure indicate categories of calculations with the same screening for the specified atom type.

We can finally conclude that, as long as the screening parameters are not selected too far from their correct values, they are not affecting the accuracy of the SFE significantly. A set of screenings with less than ±10% errors might be consider accurate enough for the SFE calculations.

6.4 Results

6.4.1 Volume Effects

In order to investigate the properties of bulk materials, we evaluate the dependence of the total energy and the local magnetic moments on the volume. By using the ideal c/a ratio for the hcp and dhcp phases, and selecting a according to the lattice parameter of the fcc phase, we ensure equal inter-atomic distances and also the same volume per site for all of them.

6.4.1.1 Equilibrium Volume

The equilibrium lattice parameter is obtained by fitting the Murnaghan equation of state [123] to a number of total energies calculated for different volumes, as presented in Fig. 6.7(a). Our results show, for the A607 alloy in the paramagnetic state at 0 K equilibrium, that hcp is found as the most stable phase among the three studied phases, followed by dhcp and finally fcc. It is also found that the equilibrium volume is smaller for the more stable phases. As the volume increases from the equilibrium, the phase stability in the paramagnetic state changes so that the fcc phase first overtakes the dhcp phase, and later overtakes the hcp phase, resulting in an hcp→fcc phase transition.

6.4.1.2 Experimental Evidences

In metallurgy, the higher stability of the hcp phase at low temperatures, with respect to the fcc phase, is a well-known fact which results in the cryogenic transition of γ-austenite to the ϵ-martensite (a paramagnetic [17] hcp phase) on cooling [61]. The ϵ-martensite is usually considered as an intermediate phase which transforms to the more stable α'-martensite with ferromagnetic body-centered tetragonal (bct) structure [17, 32, 142–145]. The overall $\gamma \rightarrow \epsilon \rightarrow \alpha'$ transition is called *martensitic transformation*. The

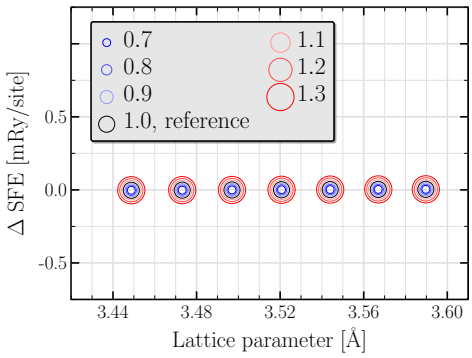

Figure 6.4: The influence of uniform scaling of the screening parameters on the SFE, calculated for A607 alloy.

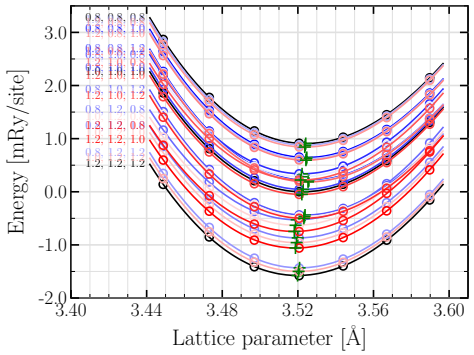

(a)

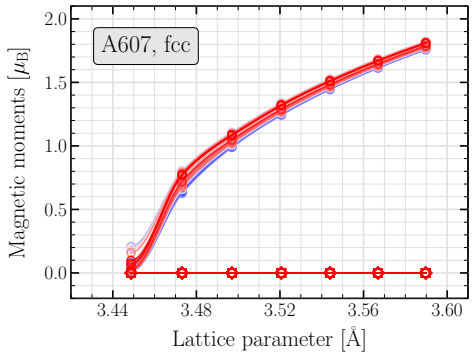

(b)

Figure 6.5: For the fcc phase of A607 alloy, (a) and (b) show the effect of non-uniform scaling of all screening parameters on the E-V curve, and on the local magnetic moments, respectively.

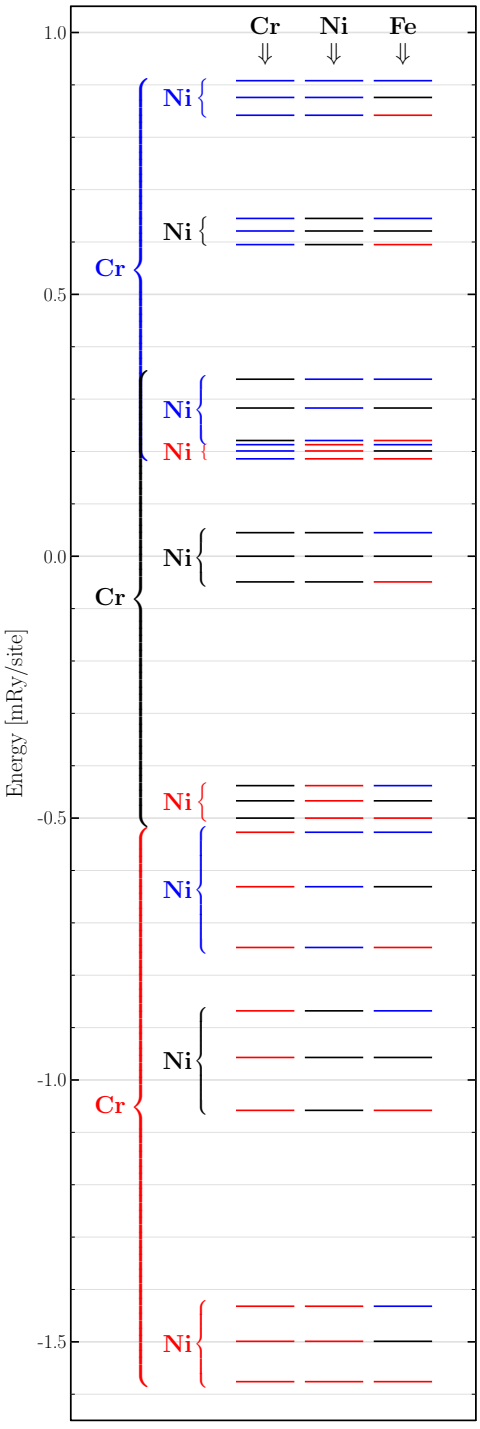

Figure 6.6: The effect of non-uniform scaling of the screening parameters on the total energy of fcc phase. Blue, black, and red lines depict the scaling factors of 0.8, 1.0, and 1.2, respectively.

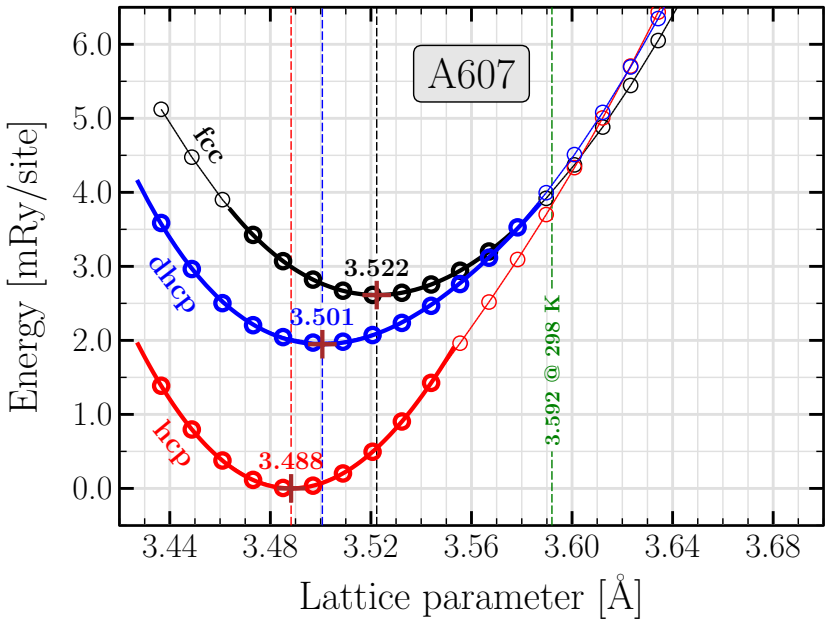

(a)

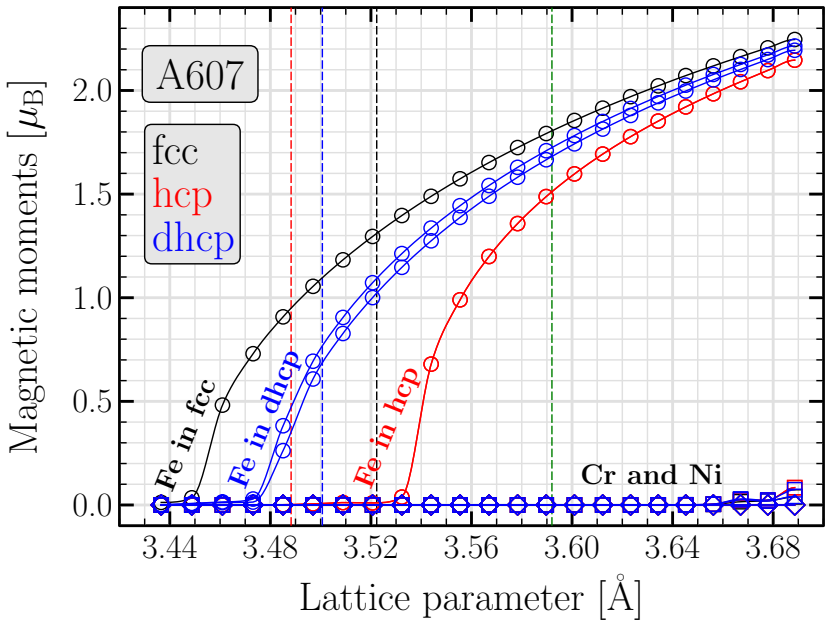

(b)

Figure 6.7: (a) Total energy versus the lattice parameter, calculated for the A607 alloy using the *soft-core* approach and the GGA-PBE functional. The green vertical line indicates the measured fcc lattice parameter at room temperature, as presented in Fig. 6.8. (b) depicts the behavior of the local magnetic moment of all elements.

formation of α'-martensite is a consequence of the presence of interstitial carbon. In fact, at very low temperatures, the most stable phase of the high-purity Fe–Cr–Ni alloys is the α-ferrite with ferromagnetic bcc structure. Since the carbon solubility in the bcc phase is very low, the unit cell is expanded along one of its sides, resulting in body-centered tetragonal structure. With higher carbon concentrations, more interstitial sites are filled, and the tetragonality increases [61].

When cooling austenite, the martensitic transformation starts as temperature reaches the *martensite start temperature*, M_s. In the absence of these mechanical stresses, M_s may be estimated using Eichelman and Hull empirical equation[1] [61]

$$\begin{aligned} M_s\ [\mathrm{K}] = 1578 - 41.67\, x_{\mathrm{Cr}} - 61.11\, x_{\mathrm{Ni}} - 33.33\, x_{\mathrm{Mn}} \\ -27.78\, x_{\mathrm{Si}} - 1667(x_{\mathrm{C}} + x_{\mathrm{N}}), \end{aligned} \tag{6.21}$$

where x_i denotes the concentration of element i in the unit of weight percent. Substituting the chromium and nickel concentrations in the equation, M_s is estimated about 250 K (−23 °C) for the A607 alloy, explaining its fcc structure at room temperature and its hcp structure at low temperatures. This agrees with the results of our ground-state DFT calculations, where, at 0 K, the paramagnetic hcp phase is found more stable than the paramagnetic fcc phase.

Experimental data shows that stainless steels with composition close to A607 may have a mixture of different phases, depending on their production conditions like cooling rate. The equilibrium phase diagram predicts that this alloy may contain γ, α, and σ phases at room temperature (see Fig. 3.6). However, because the alloy is found in austenite phase at high temperatures, the full austenite phase can be maintained by rapid cooling to room temperature (for instance, by quenching in water) [56]. These statements emphasizes the importance of the production process. As a direct experimental evidence, we can refer to our XRD measurements on samples of Böhler A607, where only the presence of fcc phase was observed. We can compare our *ab-initio* lattice parameter with its corresponding experimental value measured for the fcc lattice at 298 K (25 °C), presented in Fig. 6.8. Our theoretical value, $a_{\mathrm{A607}}^{\mathrm{fcc,DFT}} = 3.522$ Å, agrees with the measured value, $a_{\mathrm{A607}}^{\mathrm{fcc,EXP}}(T = 298\,\mathrm{K}) = 3.592$ Å, within 2%.

6.4.1.3 Local Magnetic Moments

In Fig. 6.7(b), the magnetic moments in the DLM state are plotted versus the lattice parameter for all elements in the three phases. The plot shows that, in all three phases, chromium and nickel remain nonmagnetic in the entire range of the lattice parameter. However, the magnetic moment of iron shows a direct dependence on the lattice spacing,

[1] As mentioned in the book *STEELS: Processing, Structure, and Performance* [61], the equation has originally been published in 1953 by Eichelman and Hull [77]. Since we did not have access to the original article, we took the equation from this book in the form of

$$M_s\ [^\circ\mathrm{F}] = 75(14.6 - x_{\mathrm{Cr}}) - 110(8.9 - x_{\mathrm{Ni}}) - 60(1.33 - x_{\mathrm{Mn}}) - 50(0.47 - x_{\mathrm{Si}}) - 3000[0.068 - (x_{\mathrm{C}} + x_{\mathrm{N}})]$$

and converted it from Fahrenheit unit (°F) to Kelvin (K).

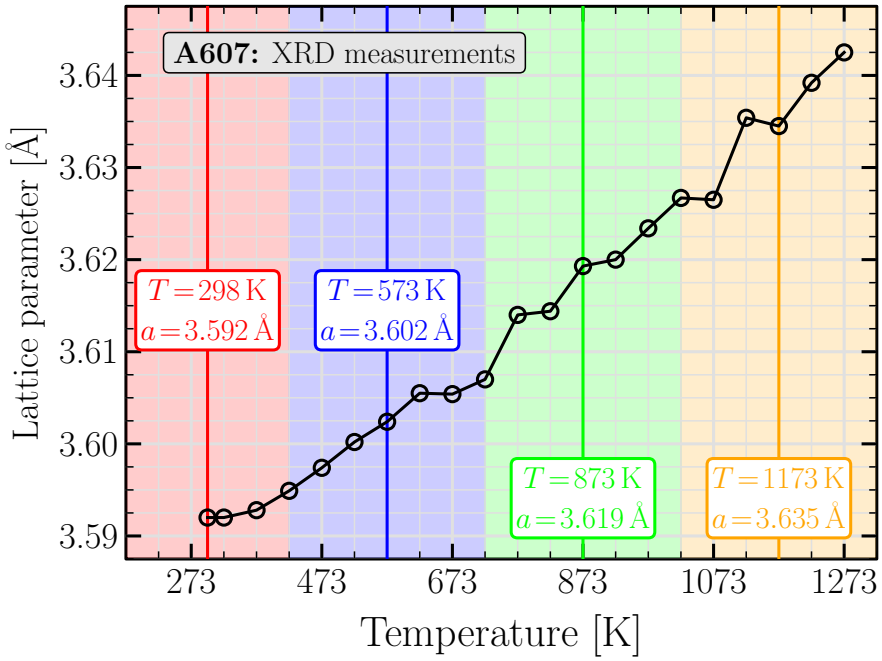

Figure 6.8: Lattice parameter of the A607 alloy as a function of temperature, as determined from high temperature XRD through the heating process. Shaded areas denote four temperature ranges where the lattice parameter at the middle of every interval is used in the LSF calculations.

so that while it remains negligible for smaller volumes, it increases significantly with the lattice parameter, introducing a low-spin to high-spin magnetic transition. In different phases, this transition occurs at different volumes, so that at a certain lattice parameter, an iron atom has quite different magnetic moments in different phases. As a result of this behavior, iron is already magnetic at the equilibrium volume of the fcc and dhcp phases, while it is still nonmagnetic at the equilibrium volume of the hcp phase. In the limit of large volumes, however, all three phases exhibit the same magnetic behavior. In all three phases, unlike their equilibrium volumes, iron atoms have significant magnetic moments between $1.55\,\mu_B$ and $1.85\,\mu_B$ at the lattice parameter measured at room temperature. It shows that the usage of the theoretical lattice parameter can lead to an unrealistic description of the magnetic configuration of the alloy, resulting in wrong values for the SFE.

6.4.1.4 Frozen-core approximation

Delczeg *et al.* have recently calculated the equilibrium lattice parameters for the paramagnetic state of Fe–Cr–Ni alloys using a method similar to what we use here, *i.e.*, the EMTO approach [146]. For $Fe_{74}Cr_{18}Ni_8$ alloy, they have reported 3.605 Å for the fcc lattice parameter at 0 K equilibrium, which, compared to our result, is closer to the room-temperature experimental value.

The difference between this value and our result comes from the different treatments applied for core electrons. While we use the soft-core approach, they have used frozen-core approximation, a simplified description of core electrons that results in larger equilibrium lattice parameters at 0 K which are closer to experimental data [146–148], but can not be justified theoretically. A comparison between the soft- and the frozen-core approaches is presented in Fig. 6.9, where the equilibrium volume and the local magnetic moments are plotted for the fcc phase of A607 alloy. More detailed informations, including the experimental values for the room-temperature lattice parameter and the bulk modulus are given in Tab. 6.4. Our results show that the equilibrium volume and the bulk modulus calculated using the soft-core approach are respectively smaller and larger then those coming through the frozen-core approximation. This suggest that the frozen-core approximation, compared to the soft-core approach, underestimate the strength of atomic interactions in the metal.

Despite significant difference in the equilibrium volumes calculated using the two core-electron treatments, Fig. 6.9(b) shows that both approaches result in very similar values calculated for the magnetic moments. At first glance, it might point to the dominance of the valence states in the magnetization of elements, as these states are calculated in both approaches on equal footing. However, unless it is proven using other methods, a question rises here: If the frozen-core approximation describes the magnetic structure of the system in similar manner as the soft-core approach, why does it result in different equilibrium volume. To answer this question, whether the magnetic behavior is correctly and mainly characterized by valence states, or the mentioned match is just an accident, or it is a bug in the implementation of the frozen-core approximation in the code, further investigations are required.

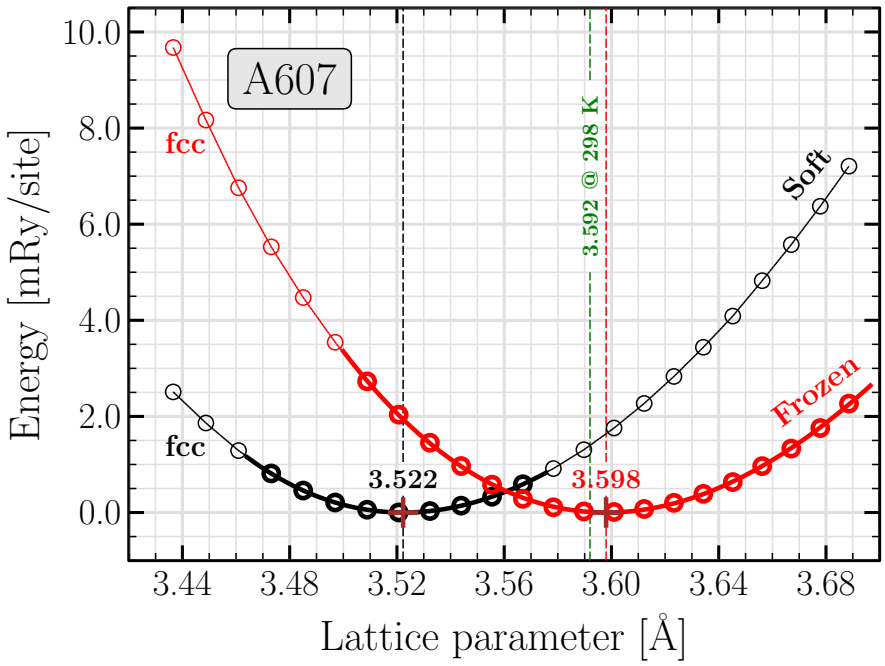

(a)

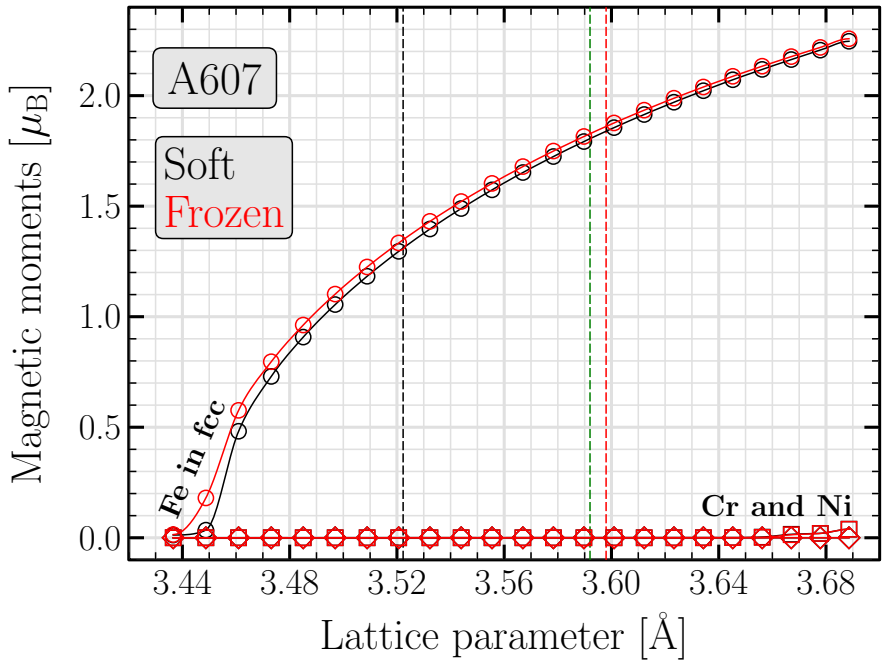

(b)

Figure 6.9: Comparison of the physical properties of the A607 alloy, calculated using the soft-core and the frozen-core approaches. As the lattice parameter increases, (a) presents the changes in the total energy, while (b) shows the behavior of the local magnetic moments.

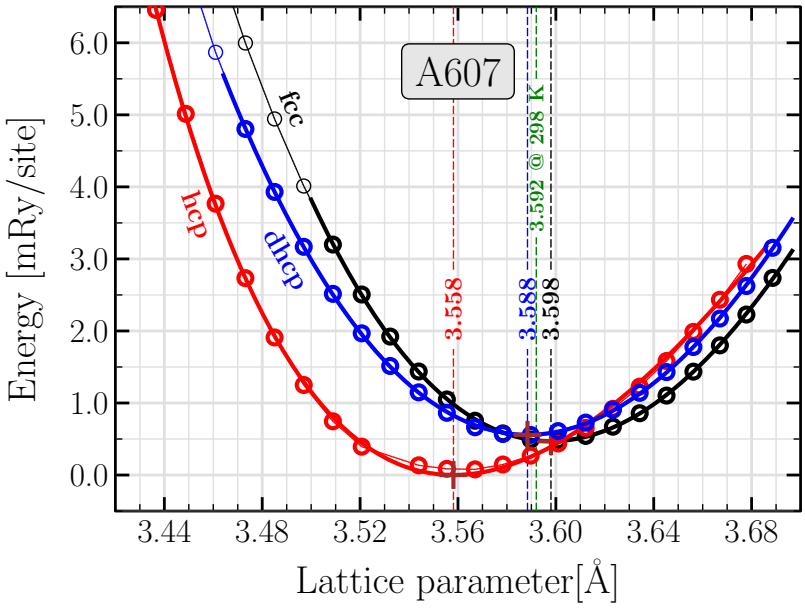

(a)

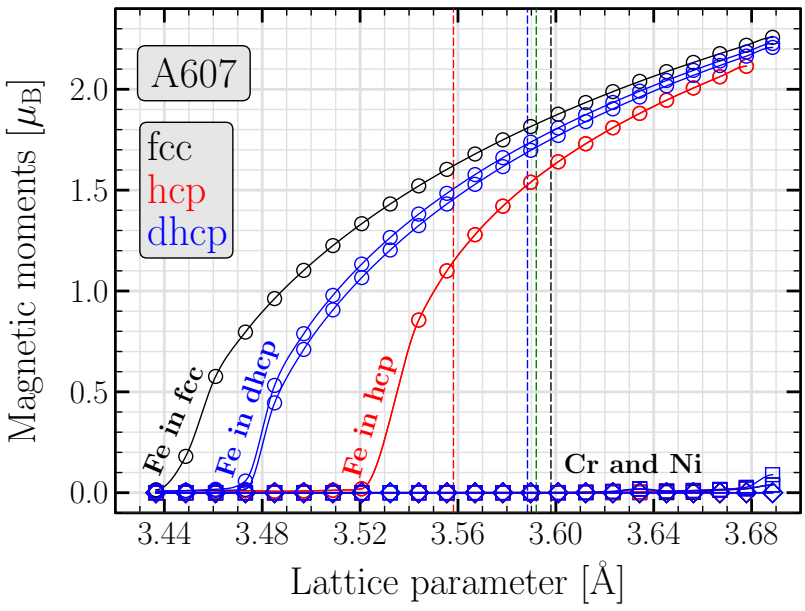

(b)

Figure 6.10: (a) Total energy versus the lattice parameter, calculated for the A607 alloy using the *frozen-core* approximation and the GGA-PBE functional. The green vertical line indicates the measured fcc lattice parameter at room temperature, as presented in Fig. 6.8. (b) depicts the behavior of the local magnetic moment of all elements. Compared to Fig. 6.7, this approximation results in a significant shift in the equilibrium lattice parameter, while the behavior of the magnetic moments remain almost unchanged.

Table 6.4: The calculated equilibrium lattice parameter and the bulk modulus of the fcc, hcp, and dhcp structures, compared to available experimental data. Note that the fcc lattice parameter a_{fcc}, is derived using the equilibrium volume of every phase.

phase	a_{fcc} [Å]			B [GPa]		
	soft-core	frozen-core	experiment	soft-core	frozen-core	experiment
fcc	3.522	3.598	3.592*	172.2	164.9	∼160.0 [21]
hcp	3.488	3.558	—	271.5	152.2	—
dhcp	3.501	3.588	—	178.2	153.0	—

* Our XRD measurements

The E-V curves calculated for all three considered phases using the frozen-core approximation are presented in 6.10. These results show that, in this approximation, the most stable phase at 0 K equilibrium is hcp, followed by fcc and dhcp. This is different than the order we found using the soft-core approach: hcp, dhcp, and fcc (see Fig. 6.7). Moreover, compared to Fig. 6.7, Fig. 6.10 shows that, at 0 K equilibrium, the energy differences between the three phases become smaller when the frozen-core approximation is applied. These differences become of particular importance when investigating the SFE which, in the absence of the entropy at 0 K, is calculated as

$$\text{SFE}(T = 0\,\text{K}) = \frac{E^{\text{hcp}} + 2E^{\text{dhcp}} - 3E^{\text{fcc}}}{A}, \tag{6.22}$$

resulting in values of $-126\,\text{mJ/m}^2$ and $6\,\text{mJ/m}^2$ for soft- and frozen core approaches, respectively. Finally, in the hcp phase, Fig. 6.10 shows a kink in the E-V curve at $a_{\text{fcc}} \approx 3.53\,\text{Å}$, which can be related to a low-spin to high-spin magnetic transition of iron atoms. Although the same transition is observed in all phases in Figs. 6.7(b) and 6.10(b), except the hcp phase with frozen-core approximation, it never results in a visible change in the corresponding E-V curves.

6.4.2 Longitudinal Spin Fluctuations

Our methodology for calculating the longitudinal spin fluctuations (LSF) was explained in Sec. 6.2.3. In this section, we present computational details and results.

6.4.2.1 Determination of $J_s(m_s)$ from DFT

To this end, the cell volumes are adjusted based on the experimental lattice parameters measured for Böhler A607 alloy. In order to do so, taking only the heating branch of the lattice thermal expansion curve, the desired temperature range 273 K–1273 K (0 °C–1000 °C) is divided into four intervals, whose middle values are selected for our calculations (see Fig. 6.8). The total energy is evaluated via the self-consistent DFT calculations, where one magnetic moment out of $s \in \{\text{Fe}, \text{Cr}, \text{Ni}\}$ is fixed to the set

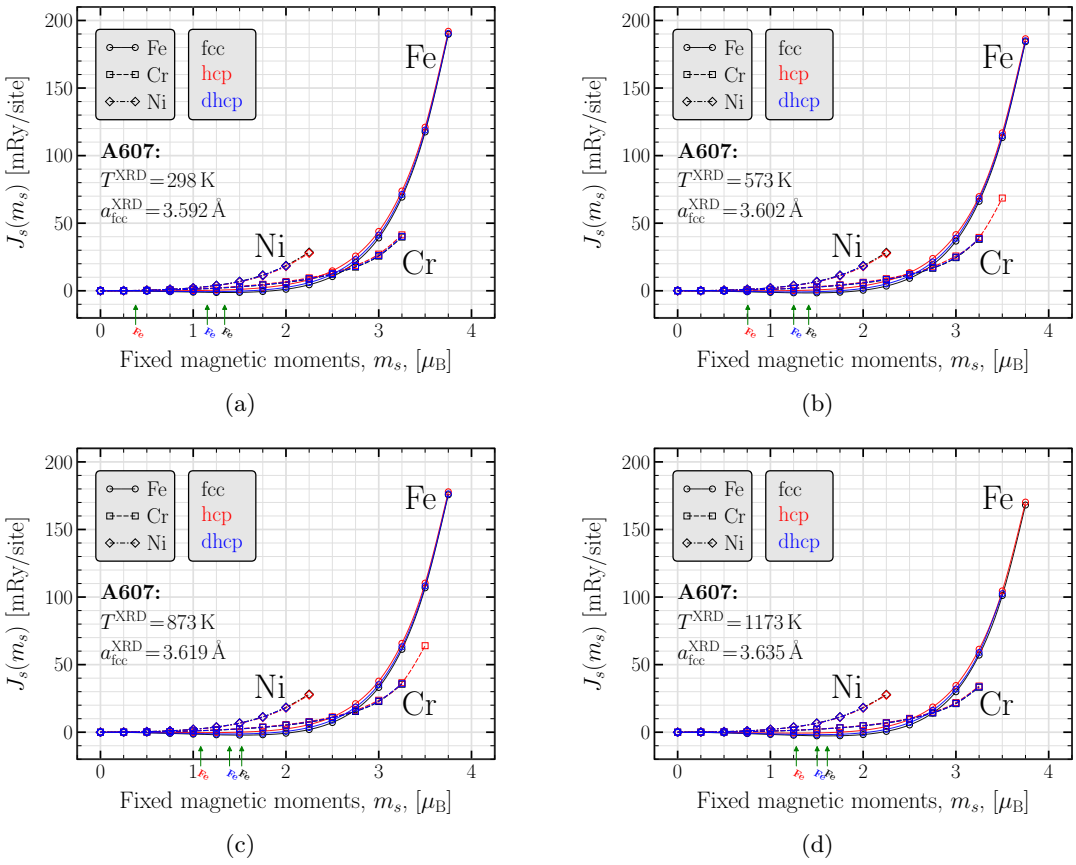

Figure 6.11: The overall behavior of the Hamiltonian parameters $J_s(m_s)$ versus the size of the magnetic moments m_s, as calculated using four experimental lattice parameters in the A607 alloy. For a closer view of the region around the horizontal axis, see Fig. 6.12.

of values $m_s \in \{0.00, 0.25, 0.50, \cdots, 4.00\ \mu_{\mathrm{B}}\}$, while the other moments are allowed to relax. In these calculations, the exchange–correlation (XC) effects are approximated using the local spin density approximation (LSDA) [149], since it has been reported in the cases of bcc iron [150] and bcc chromium [151] to result in more realistic magnetic moments compared to the generalized gradient approximation (GGA) [93]. This approach gives the total energy of system $E_s(m_s)$ as a function of the magnetic moments of element s. The Hamiltonian parameters are obtained by normalizing these energies to the energy of nonmagnetic state: $J_s(m_s) = E_s(m_s) - E_s(0)$.

For the A607 alloy, we present the overall behavior of $J_s(m_s)$ in Fig. 6.11, while a more detailed presentation with focus on an enlarged region around the horizontal axis is available in Fig. 6.12. For each of chromium and nickel, the total energy monotonically increases with the magnetic moments. This suggests that chromium and nickel are nonmagnetic at the equilibrium DLM state, as it was also mentioned when discussing the volume effects in Sec. 6.4.1. Moreover, it evidences the thermal excitations of their

Table 6.5: Comparison of the magnetic moments of iron, calculated in the DLM paramagnetic state of the A607 alloy using the LSDA and the GGA functionals. The LSF-LSDA and the LSF-GGA magnetic moments have been obtained according to the minimum total energy of the system, normalized to the total energy of the corresponding nonmagnetic state, $\Delta E_{\mathrm{Fe}} = E_{\mathrm{Fe}}(m_{\mathrm{Fe}}) - E_{\mathrm{Fe}}(0)$(see Fig. 6.12).

			GGA	LSF-LSDA		LSF-GGA	
T^{XRD}	$a_{\mathrm{fcc}}^{\mathrm{XRD}}$	phase	m_{Fe}	m_{Fe}	ΔE_{Fe}	m_{Fe}	ΔE_{Fe}
[K]	[Å]		[μ_{B}]	[μ_{B}]	[mRy]	[μ_{B}]	[mRy]
		fcc	1.805	1.339	−1.288	1.709	−3.671
298	3.592	hcp	1.512	0.379	−0.004	1.449	−1.223
		dhcp	1.725	1.152	−0.616	1.617	−2.619
		fcc	1.863	1.413	−1.597	—	—
573	3.602	hcp	1.610	0.756	−0.066	—	—
		dhcp	1.792	1.251	−0.855	—	—
		fcc	1.951	1.523	−2.154	—	—
873	3.619	hcp	1.748	1.081	−0.305	—	—
		dhcp	1.891	1.392	−1.316	—	—
		fcc	2.023	1.613	−2.724	—	—
1173	3.634	hcp	1.854	1.279	−0.647	—	—
		dhcp	1.972	1.504	−1.809	—	—

magnetic moments at higher temperatures. This behavior demonstrates the itinerant nature of the electron magnetism in chromium and nickel. The steeper curve of nickel results in the fact that there are less states available with a smaller variety of magnetic moments for nickel than for chromium.

In the case of iron, unlike chromium and nickel, the energy curve always passes through a shallow minimum as the magnetic moments increase from zero. These minima and their corresponding magnetic moments are presented in Tab. 6.5, and are also indicated on the horizontal axes in the figures. A minimum in the energy curve means that iron exhibits a magnetic equilibrium DLM state, indicating the Heisenberg nature of its electron magnetism. Moreover, the small depth of this minimum indicates that spin fluctuations with a large variety of the magnetic moments are accessible because of their low excitation energy. This reflects the itinerant nature of the magnetism in this element. Although both Heisenberg and itinerant types of magnetism are present in iron, later we will see that the Heisenberg type is dominant.

We can also compare these curves with E-V curves, presented in Fig. 6.7. For an easier comparison, see the GGA and the LSF-LSDA magnetic moments in Tab. 6.5. We find that the energy minima in J_{Fe} occur at magnetic moments which are smaller

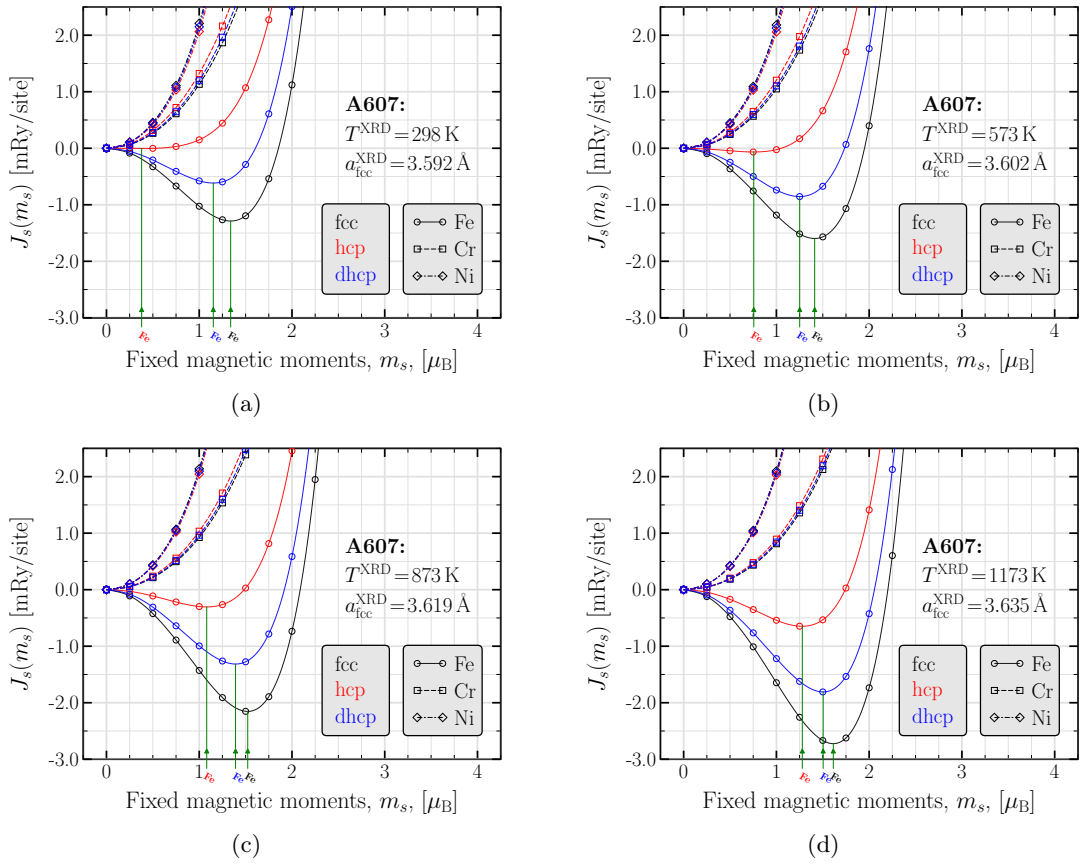

Figure 6.12: Same as Fig. 6.11, but with a zoomed-in energy scale to unveil the minima of $J_{\mathrm{Fe}}(m_{\mathrm{Fe}})$ curves.

then their corresponding values calculated in Sec. 6.4.1. These differences are mainly due to the different exchange–correlation approximations applied in the two series of calculations, *i.e.*, the GGA-PBE functional used in the calculations of volume effects, while the LSDA functional was selected for the LSF calculations. The results of an LSF calculation with the GGA-PBE functional are presented under the title GGA-LSF in Tab. 6.5. In every phase, the GGA-LSF magnetic moments are approximately $0.1\,\mu_{\mathrm{B}}$ smaller than their corresponding values obtained from the E-V calculations. Further investigations are required to unveil the source of these small differences.

With increasing volume (for instance, by moving from Figs. 6.12(a) to Figs. 6.12(d)), we observe two trends. First, the position of the minima get more similar when comparing fcc, hcp, and dhcp. Second, the depths of the minima grow. Generally, a deeper minimum means that the magnetic moments of the system are more localized, and hence thermal excitation becomes more difficult, indicating the weak itinerant nature of the system. Based on the same argument, in our Fe–Cr–Ni alloy, the fcc and the hcp phases demonstrate the weakest and the strongest itinerant magnetism, respectively.

Finally, the relatively small slope of all energy curves around their minima emphasizes that the spin fluctuations are highly available in this alloy, which are necessary to be taken into account in order to get an accurate physical description of the system.

Figs. 6.13 – 6.16 demonstrate the correlations between the magnetic moments of different elements in the alloy. In all cases, the magnetic moments of chromium (red curves) and nickel (blue curves) remain unchanged as the moments of any other element increase. On the other hand, magnetic moments of iron (black curves) exhibit only a week correlation with moments of other elements, where they increase with chromium moments, but decrease as nickel moments increase. This indicates that the magnetic interactions among different species are generally weak.

6.4.2.2 Monte Carlo Calculations

The outputs of Monte-Carlo calculations related to the four selected experimental lattice parameters are presented in Fig. 6.17, where different phases are distinguished with their corresponding colors. For the DLM paramagnetic state, our results predict that, in all three phases, iron holds significant magnetic moments at 0 K, evidencing the contribution of localized *d*-electrons to its magnetism. This behavior is a characteristic of systems which follow the Heisenberg model of magnetism. However, as temperature rises, the magnetic moments of iron grow, which is a characteristic of the itinerant magnetism [131]. So we can conclude that, the electron magnetism in iron can be described as a mixture of both Heisenberg and itinerant types. The itinerant nature of magnetism is stronger in the hcp phase, followed by dhcp and fcc, as determined by the slope of their corresponding curves, particularly at lower temperatures. In the entire temperature range, the fcc phase has the largest magnetic moments, followed by dhcp and hcp. A similar finding has been reported for iron in Fe–Mn alloys [38]. Chromium and nickel, on the other hand, obtain significant magnetic moments only due to the thermal excitation of their spins, indicating the pure itinerant nature of their electron magnetism.

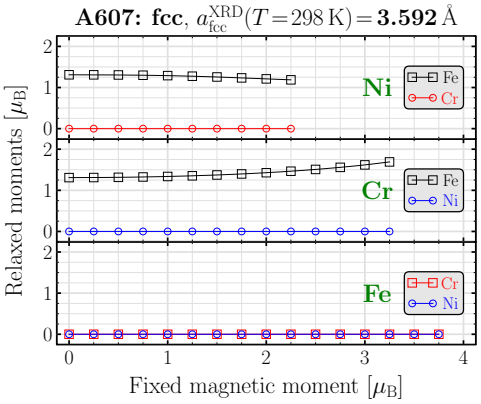

(a)

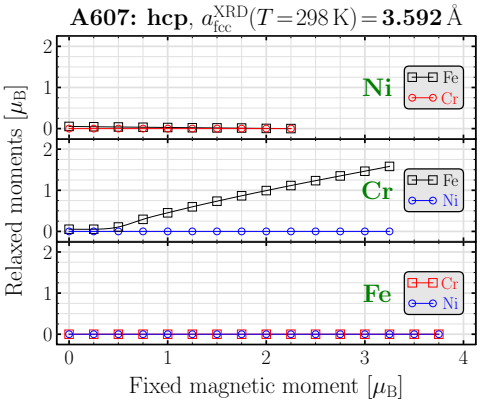

(b)

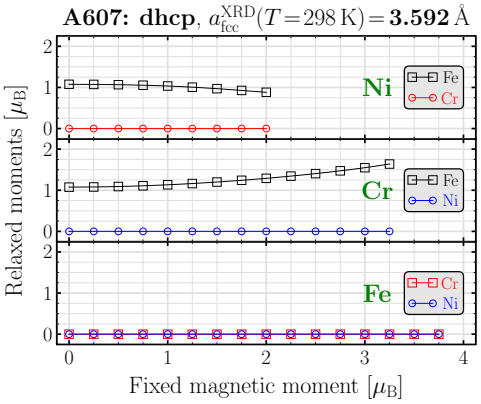

(c)

Figure 6.13: The correlation between magnetic moments in A607 alloy, using the lattice parameter at 298 K.

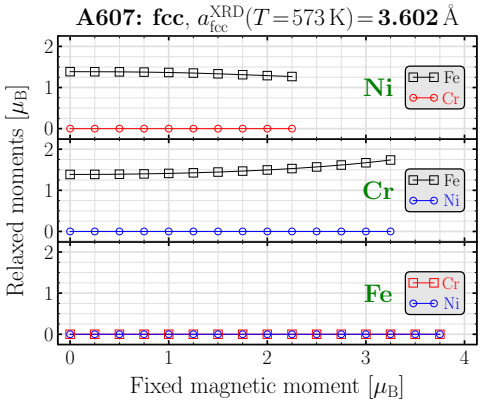

(a)

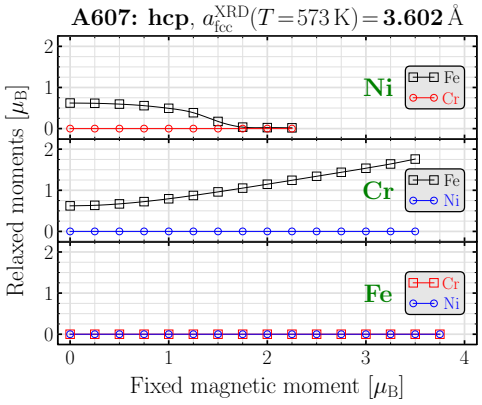

(b)

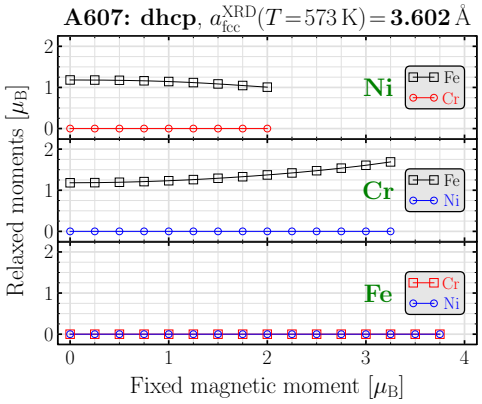

(c)

Figure 6.14: The correlation between magnetic moments in A607 alloy, using the lattice parameter at 573 K.

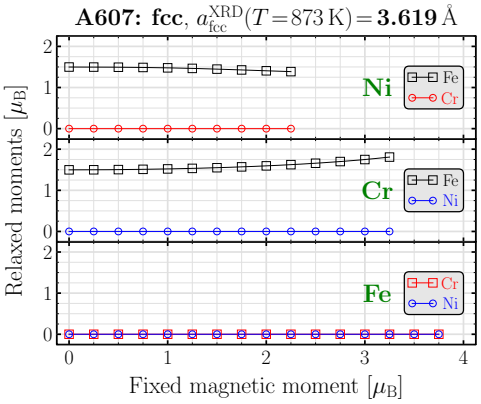

(a)

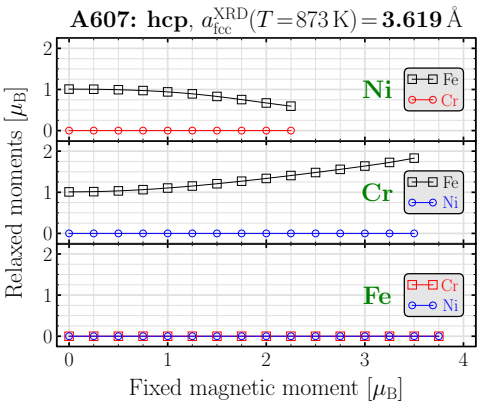

(b)

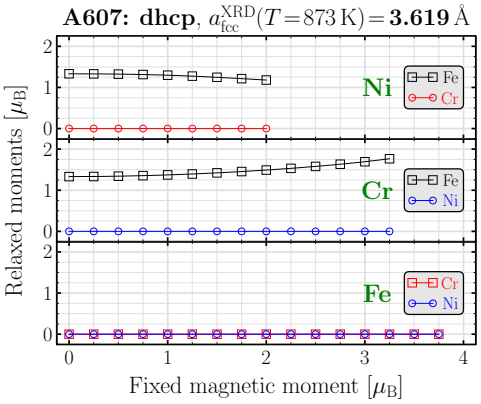

(c)

Figure 6.15: The correlation between magnetic moments in A607 alloy, using the lattice parameter at 873 K.

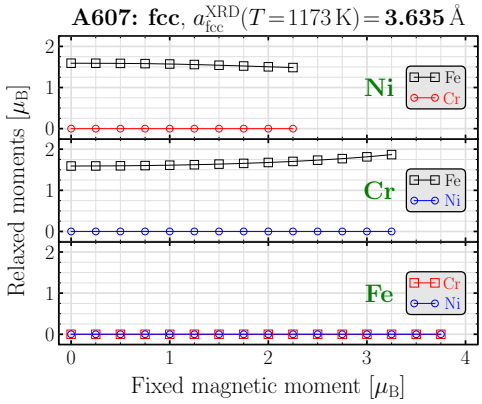

(a)

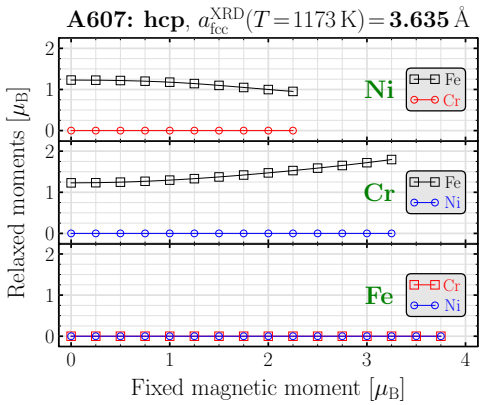

(b)

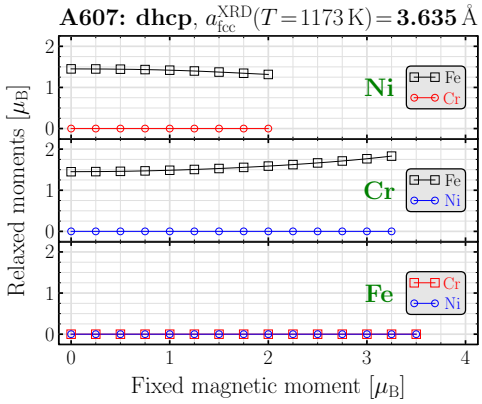

(c)

Figure 6.16: The correlation between magnetic moments in A607 alloy, using the lattice parameter at 1173 K.

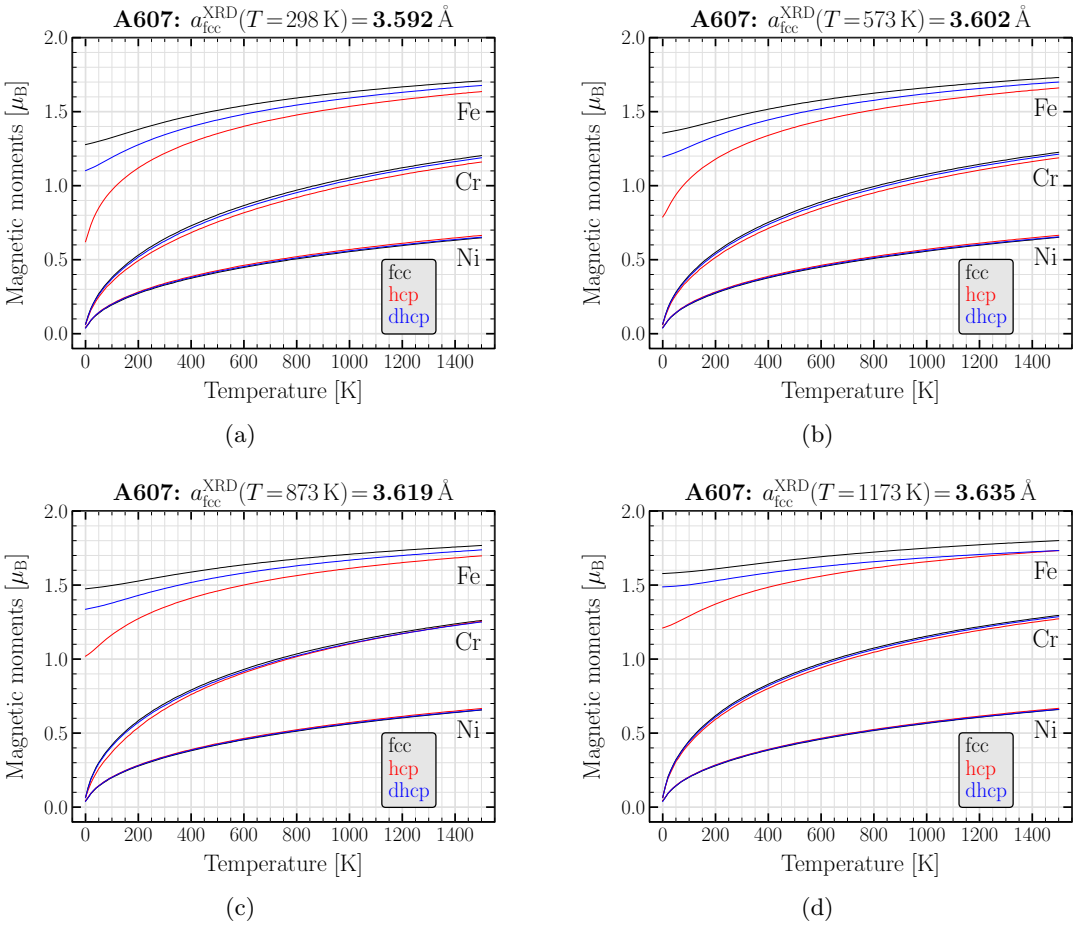

Figure 6.17: The dependence of the magnetic moments on temperature, calculated for the A607 alloy, at four different experimental lattice parameters.

6.4.3 The SFE Calculations

In Fig. 6.18(a), the SFE results based on five different sets of the LSF calculations are presented. The first set uses the theoretical equilibrium volume, while the other four sets utilize the measured lattice parameters at 298, 573, 873, and 1173 K (25, 300, 600, and 900 °C, respectively). For every set, a third order polynomial is fitted to the calculated points. All results exhibit an increase of the SFE with temperature. Moreover, it is found that larger volumes result in larger SFE's. The colored curves are more reliable in a temperature range around the point at which their corresponding lattice parameters have been measured. These ranges and their corresponding data points are highlighted in Fig. 6.18(b). The overall temperature dependence of the SFE can be found by fitting a third order polynomial to these highlighted points. We find that, for the A607 alloy, the SFE almost linearly increases with the temperature:

$$\mathrm{SFE}^{\mathrm{A607}}(T) = -3.530{\times}10^{1} + 1.006{\times}10^{-1}\,T - 3.924{\times}10^{-5}\,T^2 + 1.296{\times}10^{-8}\,T^3, \quad (6.23)$$

where T and $\mathrm{SFE}^{\mathrm{A607}}$ are in Kelvin and $\mathrm{mJ/m^2}$, respectively.

6.4.3.1 Comparison with Other Works

Among the most direct and also the most frequently used methods for measuring the SFE is the observation of the extended dislocation nodes, loops, and tetrahedra by transmission electron microscopy (TEM). Depending on the restrictions in the resolution of TEM images, this method is usually considered accurate for cases where the SFE is below $50\,\mathrm{mJ/m^2}$. For materials with larger SFE, investigating the XRD profiles by Fourier analysis can be applied [53, 117].

Generally, finding trusted experimental values for the stacking-fault energy is quite challenging. As presented in Tab. 2.1, uncertainties up to 30% have been reported in the case of pure metals, making it difficult to fully rely on an individual experimental value. One must also take into account that, when measuring the SFE in alloys, the problem becomes even more elaborate due to complexities which are a part of the nature of the composition compared to a pure material. Particularly for steels, comparing the calculated SFE's with experimental values is not a straightforward task, since experimental samples always contain small fractions of other elements, making them different from the simulated systems. Moreover, the process of sample preparation alters its final microstructure, a property which highly governs the SFE measurements, and hence significantly changes the measured results, even for samples with equal chemical compositions. For instance, for plain carbon steels in the γ-phase at high temperature, the SFE has been measured between $70\,\mathrm{mJ/m^2}$ and $100\,\mathrm{mJ/m^2}$ (almost 50% deviation), depending on the material grain size [54]. Especially when the temperature dependence of the SFE is of interest, some irreversible changes may be introduced in samples as they are heated up and cooled down again (see the references of the reported experimental results).

Experimental SFE values, which have been extracted from relevant publications, are presented in Appendix A. In order to compare our results with available experimental

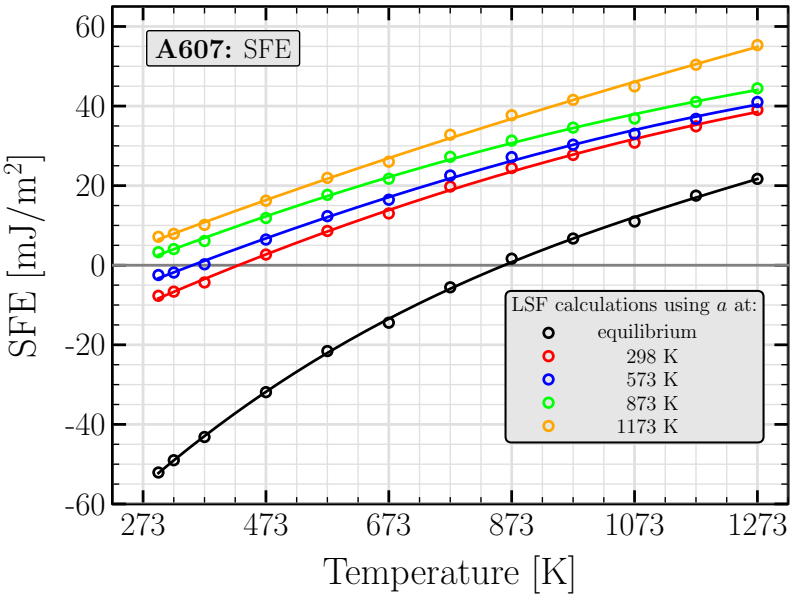

(a)

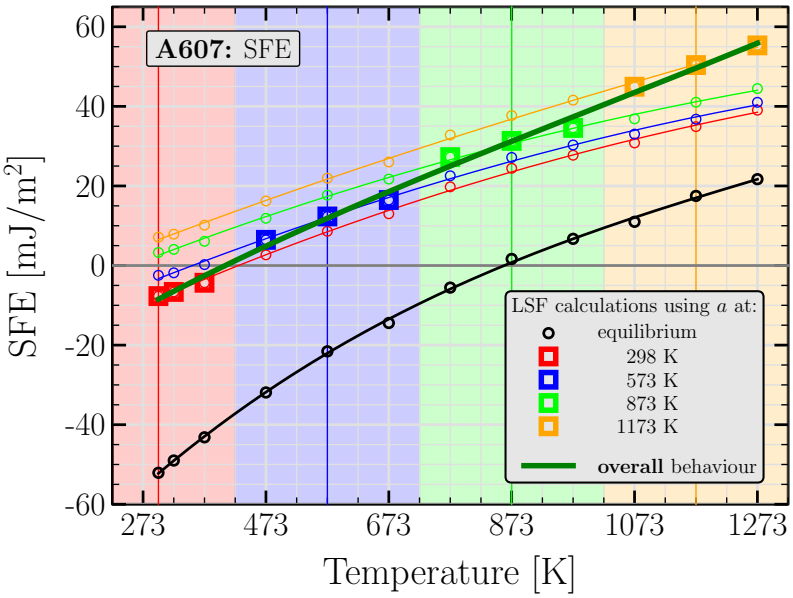

(b)

Figure 6.18: (a) The temperature dependence of the SFE, evaluated for the A607 alloy. Different curves correspond to different volumes used in the LSF calculations. Using the experimental lattice parameter (colored curves) instead of the equilibrium value (black curve) increases the SFE significantly. (b) The temperature interval is divided into 4 regions (see Fig. 6.8), where the most relevant points of every curve is selected. The overall behavior of the SFE is found by fitting a third order polynomial to the selected points.

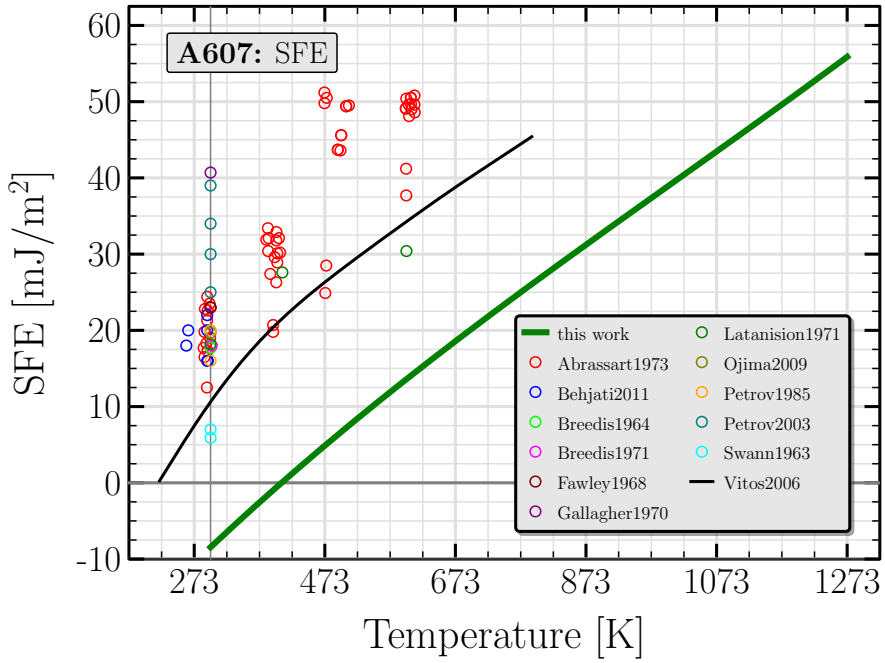

Figure 6.19: Comparison between our results and available experimental and theoretical SFE's for the A607 alloy. Experimental data are presented for alloys where the deviation of the chemical composition from our A607 is in the range of ±4 at.%, ±2 at.%, and ±2 at.%, respectively for iron, chromium, and nickel. However, the accurate composition of these alloys are presented in Appendix A. The black curve presents the temperature dependence of the SFE, calculated for $Fe_{74}Cr_{18}Ni_8$ [37]. Room temperature has been indicated by a vertical line at 298 K (25 °C).

values, we select only those alloys for which the deviation of the chemical composition from our A607 is in the range of ±4 at.% for iron and ±2 at.% for chromium and nickel. Although we ignore the presence of any other elements, we omit alloys where the sum of all additional elemental concentrations exceeds the limit of ±2 at.%. Our calculated SFE and the measured values for these selected alloys are presented in Fig. 6.19. The black curve in the figure is the theoretical result published by Vitos *et al.* [37]; they have calculated the temperature and composition dependence of the SFE using an approach similar to ours. However, their applied approximations and some computational details are different than ours. For instance, they have not accounted for the thermal lattice expansion. Moreover, they have applied the frozen-core approximation and the SC-LSF scheme. These differences will later be discussed in this section. Our results and Vitos's results agree in the prediction of the direct temperature dependence of the SFE, especially at higher temperatures where both curves increase with almost the same slope. At lower temperatures, including room temperature, the curve calculated by Vitos has larger slope. However, the main difference between these two theoretical results comes from their different SFE-intercept, a constant which shifts the entire curve along the vertical axis, *i.e.*, SFE-axis. While Vitos *et al.* have found a positive SFE at

room temperature which agrees with the experimental values, our calculations result in a negative SFE at room temperature, which is approximately 15 mJ/m^2 lower than the lowest measured value.

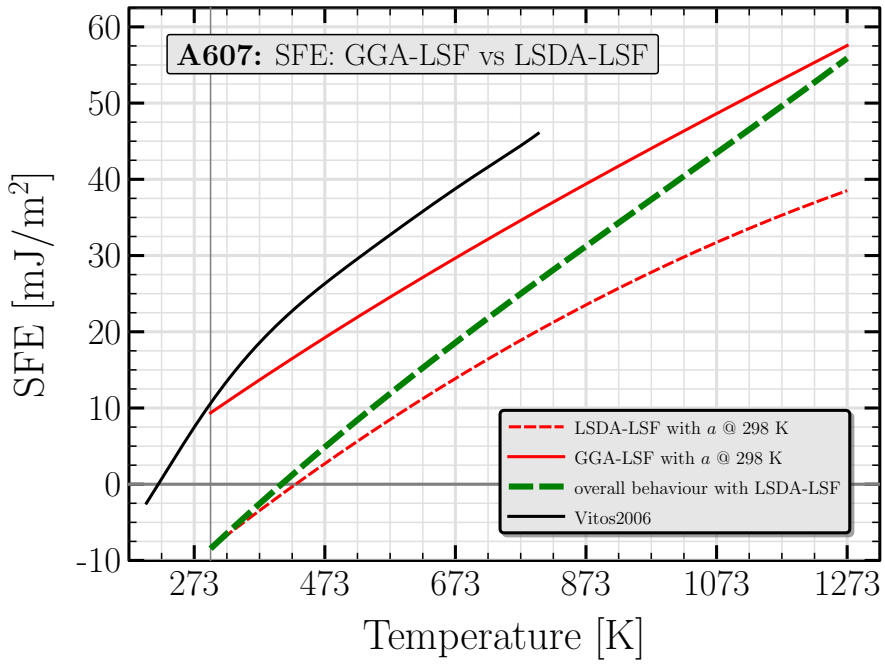

Figure 6.20: Comparison between the SFE results, as the LSF calculations are performed using the LSDA (dashed curves) or the GGA (solid curves) functional. Like in the Fig. 6.18(a), red curves correspond to a set of calculations where the lattice parameter measured at 298 K (25 °C) is utilized in the LSF evaluation.

Vitos *et al.* have applied the GGA functional in order to approximate the exchange–correlation effects in the free energy calculations, as well as in the evaluation of the thermal excitation of the magnetic moments. In fact, the applied self-consistent scheme of the LSF calculations evaluates these thermal excitations and the free energy simultaneously, making it impossible to use different exchange–correlation terms in them. Unlike their approach, we calculate the LSF prior to the free-energy calculations, which allows us to chose different computational parameters for these separated tasks. As it was already mentioned in Sec. 6.4.2.1, we use the LSDA functional in the LSF calculations, while utilizing the GGA functional in the free-energy calculations.

In order to find the origin of the difference between our results and Vitos's report, we recalculate the thermal excitation of the magnetic moments using the GGA functional. Our SFE results for both functionals are presented in Fig. 6.20, where the dashed and solid curves indicate the usage of the LSDA and GGA functionals in the LSF calculations, respectively. Compared to graphs if Fig. 6.18(a), we have recalculated the LSF only for the lattice parameter measured at 298 K (25 °C). Using the GGA functional in the LSF calculations introduces a significant shift of almost 20 mJ/m^2 toward higher

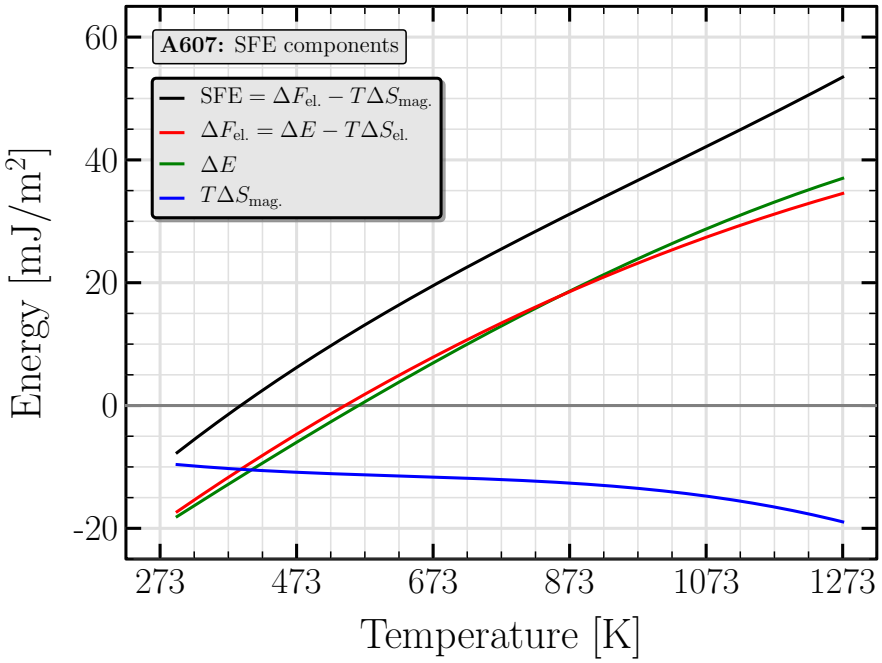

Figure 6.21: The main components of the SFE, calculated for A607. The thermal excitation of the magnetic moments are taken into account using the LSDA exchange–correlation functional in the LSF calculations.

values to the entire curve. At room temperature, this results in very good agreement with experimental data and Vitos's report. For higher temperatures, as presented in Fig. 6.18(b), further calculations using relevant lattice parameters in the LSF step are required. However, comparing the enhanced slope of the overall curve to the slope of the curve utilizing $a\,@\,298\,\text{K}$ (green dashed curve compared to the red dashed curve in Fig. 6.20), we expect that the same improvement will occur here.

6.4.4 Various Contributions to the SFE

As a result of the ANNNI model, the SFE is affected by various contributions to the free energies, which are in turn derived by subtracting different entropy contributions from the total energy (see Eqs. 6.7 and 6.11). In Fig. 6.21, we disentangle the three main components of the SFE, *i.e.*, the differences in the total energies

$$\Delta E = E^{\text{hcp}} + 2E^{\text{dhcp}} - 3E^{\text{fcc}}, \tag{6.24}$$

the differences in the electronic free energies

$$\Delta F_{\text{el.}} = \Delta E - T\Delta S_{\text{el.}} = \Delta E - T(S^{\text{hcp}}_{\text{el.}} + 2S^{\text{dhcp}}_{\text{el.}} - 3S^{\text{fcc}}_{\text{el.}}), \tag{6.25}$$

and the differences in the magnetic entropies

$$T\Delta S_{\text{mag.}} = T(S^{\text{hcp}}_{\text{mag.}} + 2S^{\text{dhcp}}_{\text{mag.}} - 3S^{\text{fcc}}_{\text{mag.}}). \tag{6.26}$$

By increasing from $-18\,\mathrm{mJ/m^2}$ at 298 K (25 °C) to $37\,\mathrm{mJ/m^2}$ at 1273 K (1000 °C), the total-energy contribution, ΔE plotted in green, governs both the value and the temperature dependence of the SFE. The effect of the electronic-entropy contribution can be analyzed by comparing the electronic-free energy, $\Delta F_{\mathrm{el.}}$ plotted in red, to the total energy. The small difference between these two curves indicates the tiny effect of the electronic-entropy contribution on the SFE, which might safely be ignored. The magnetic-entropy contribution, $T\Delta S_{\mathrm{mag.}}$ plotted in blue, changes from $-9.6\,\mathrm{mJ/m^2}$ at 298 K (25 °C) to $-18.9\,\mathrm{mJ/m^2}$ at 1273 K (1000 °C). By changing less than $3\,\mathrm{mJ/m^2}$ within a range of 600 K, it forms almost a plateau at the first half of the temperature range. Including this term in our calculations, shifts the entire SFE curve toward higher values. Although it slightly increases the slope of the SFE curve, the main influence of the magnetic-entropy contribution must be considered as an improvement in the SFE value rather than in the SFE temperature dependence.

However, the contribution of the magnetic entropy to the free energy is not the only way through which the local magnetic moments influence the final results. Via the thermal lattice expansion, the local magnetic moments are also altered, resulting in further changes in the total energy. These effect even appears even when the electronic structure is calculated for the ground state of the system according to 0 K, at which no thermal excitation exists.

In order to investigate this effect, we calculate ΔE for the A607 alloy in two different conditions: (i) in the DLM state at 0 K, where no thermal excitation of the magnetic moments exists, and (ii) in the DLM state at finite temperatures, where the thermal excitations of the magnetic moments are taken into account by calculating the fluctuation of spins. The only difference between these two scenarios is the different size of the local magnetic moments, coming from the itinerant nature of electronic magnetism in the Fe–Cr–Ni alloy.

Fig. 6.8 demonstrates that in the temperature range of 298 K to 1273 K (25 °C to 1000 °C), the fcc lattice parameter, a_{fcc}, falls between 3.5920 Å and 3.6425 Å. Our ground state calculations for 0 K shows that, in this range of the lattice parameter, chromium and nickel preserve their nonmagnetic state, while the finite magnetic moments of iron grow with volume (see Fig. 6.7(b)). The thermal excitations of the magnetic moments in this temperature range have been presented in Fig. 6.17. The magnetic moments of iron atoms in this figure are almost equal to their corresponding values calculated at 0 K (see Fig. 6.7(b)) which shows the dominance of the Heisenberg nature of its electron magnetism. However, despite to their nonmagnetic state at 0 K, chromium and nickel exhibit significant spin polarization in this temperature range ($m_{\mathrm{Cr}} \sim 0.6 - 0.7\,\mu_{\mathrm{B}}$ and $m_{\mathrm{Ni}} \sim 0.3\,\mu_{\mathrm{B}}$), showing the dominance of the itinerant nature of their electron magnetism. These excited magnetic moments are responsible for the difference between two curves in Fig. 6.22. Despite this difference, both curves show quite similar temperature dependence of ΔE, emphasizing the larger influence of the lattice expansion compared to the thermal excitations of the magnetic moments.

A further analysis of the magnetic moments in Fig. 6.23 shows that the magnetic moments of iron have larger influence compared to those of chromium and nickel. Com-

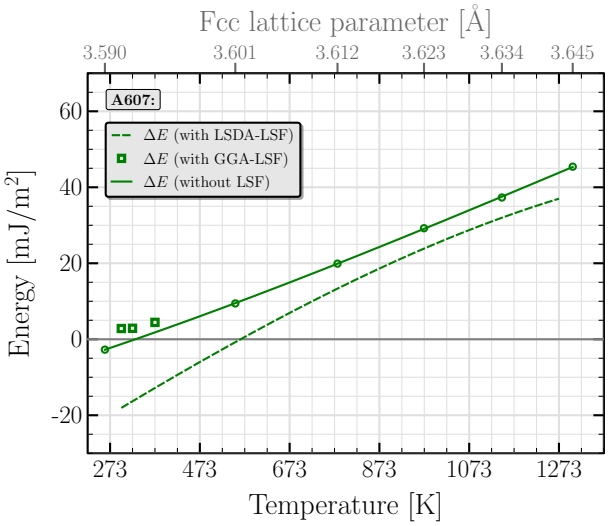

Figure 6.22: The main contributions to the SFE, calculated for A607. The dashed curve demonstrates our results where the thermal excitation of the magnetic moments are taken into account using the LSDA exchange–correlation functional in the LSF calculations. Square symbols represent the results of a similar approach, where the GGA functional is applied instead of the LSDA in the LSF calculations. The solid curve corresponds to the 0 K ground-state calculation for different lattice parameters, using the GGA exchange–correlation functional. Using the thermal lattice expansion date presented in Fig. 6.8, these lattice parameters are mapped into temperature axis and indicated on the second horizontal axis.

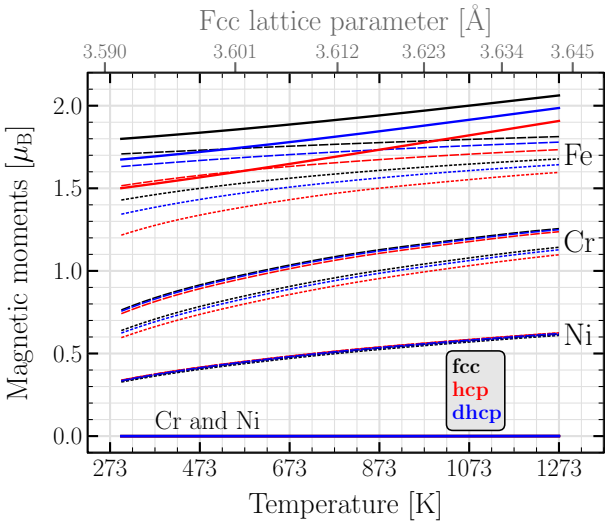

Figure 6.23: The temperature dependence of the magnetic moments, calculated for A607 using different approaches. The dotted and the dashed curves demonstrate the thermal excitation of the magnetic moments evaluated using the LSDA and GGA functional in the LSF calculations, respectively. Both calculations are based on the lattice parameter $a_{\mathrm{fcc}} = 3.5920$ Å measured at 298 K (25 °C). The solid curves, presents the ground-state magnetic moments at 0 K, calculated using the GGA functional for different lattice parameters.

paring the LSDA-LSF and GGA-LSF results it is found that nickel magnetic moments are not affected by the exchange–correlation functional. However, iron and chromium obtain larger moments when the GGA functional is used instead of the LSDA. This increase is more pronounced at lower temperatures, resulting in a larger split between the room-temperature results (see Fig. 6.22). At 0 K, nickel and chromium remain nonmagnetic regardless of the lattice parameter. However, the magnetic moments of iron are found larger then their corresponding values using the GGA-LSF. As the volume increases, they grow faster than the GGA-LSF moments grow with temperature, making the split between two class of results larger at higher temperature (volumes). Despite the nonmagnetic state of chromium and nickel, the ΔE values obtained from the ground-state calculations are in good agreement with the GGA-LSF results. This suggests that the behavior of ΔE is mainly driven by the magnetic moments of iron. On the other hand, we may conclude that, at least for Fe–Cr–Ni alloys, the evaluation of the thermal excitation of the magnetic moments is not the crucial part of the SFE calculation, since the temperature dependence of iron magnetic moments as the main contributers can simply be accounted for by the lattice thermal expansion data. These results can provide a solution for applications where a simplified treatment of the SFE is sufficient.

As a summary of the above discussion, we present the two main contribution to the SFE, *i.e.*, ΔE, $T\Delta S_{\text{mag.}}$, in Fig. 6.24. Here, the dashed curves and square symbols indicate the implementation of the LSDA and GGA in the LSF calculations, respectively, and the solid curves correspond to the 0 K ground state calculations. First of all, comparing the SFE's calculated using the LSDA-LSF and the GGA-LSF, we found that the latter results in very good agreement with the experimental results, which is due to the larger magnetic moments resulting from the GGA. All three levels of approximations demonstrate that the SFE is dominantly governed by the total energy difference, ΔE, which is in turn highly dependent on the lattice parameter. Moreover, comparing the two magnetic phenomena, *i.e.*, (i) the change in the magnetic moments due to a pure lattice expansion, and (ii) the change in the magnetic moments due to the thermal excitations (magnetic-entropy contribution), we found that they are almost equally important in the SFE calculations. Considering the significant effort required for evaluating these thermal excitations, it might be omitted when approximate values of the SFE are sufficient.

These findings about the magnetic effects are clearly in contrast with earlier results published by Vitos *et al.*, where the temperature dependence of the SFE in Fe–Cr–Ni alloys is solely determined by the magnetic-entropy contribution [37, 47, 125]. As mentioned in their papers, they perform all calculations using 0 K equilibrium volume. Supported by a recent publication by Reyes-Huamantinco *et al.* who have recently calculated the influence of different contributions on the temperature dependence of the SFE for Fe–Mn alloys, we conclude that the thermal expansion must be taken into account as the crucial effect. Of second order of importance, is the contribution of the magnetic moments in the total energy and also the magnetic-entropy contribution to the free energy. Finally, the electronic entropy may be safely omitted.

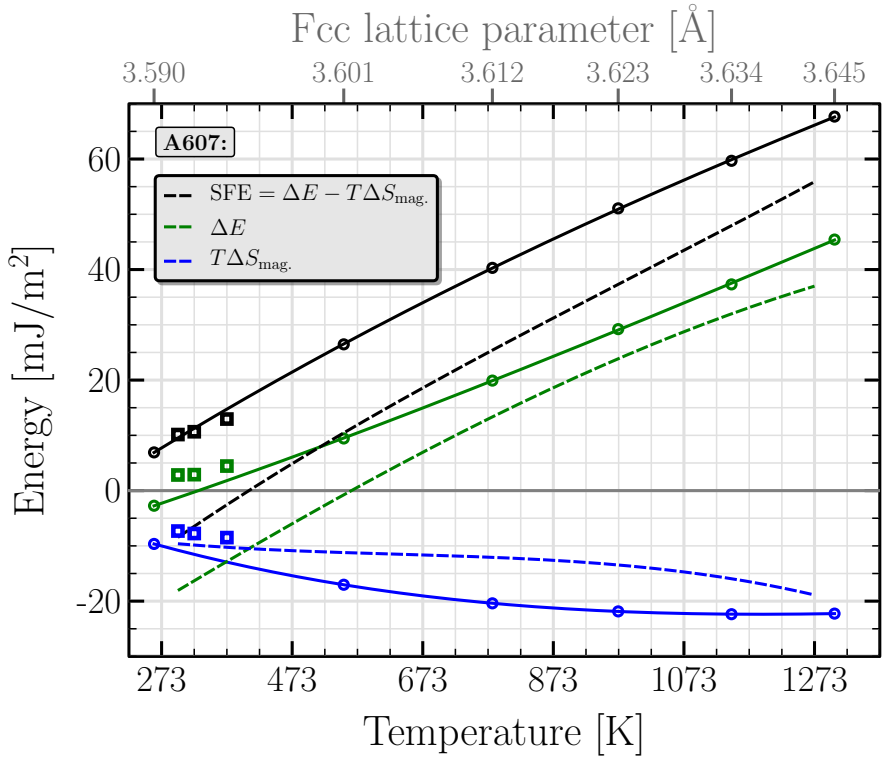

Figure 6.24: The main contribution to the SFE, calculated for A607. In the dashed curves, thermal excitations of the magnetic moments are taken into account using the LSDA exchange–correlation functional in the LSF calculations. Square symbols represent the same approach, except the implementation of the GGA functional instead of the LSDA in the LSF calculations. Solid curves correspond to the ground-state calculation at 0 K, using the GGA exchange–correlation functional.

6.4.5 The hcp→fcc Driving Force

Now that the free energies are available for both fcc and hcp phases, we can also evaluate the driving force for the hcp→fcc transformations, which is a measure for the tendency of the system to transform from one phase to the other. Generally, this parameter is defined as the difference between the free energies of the two phases, thus

$$\Delta F^{\mathrm{hcp}\to\mathrm{fcc}} = F^{\mathrm{hcp}} - F^{\mathrm{fcc}}. \tag{6.27}$$

In Fig. 6.25, we present these differences for both hcp and dhcp phases, *i.e.*, $\Delta F^{\mathrm{hcp}\to\mathrm{fcc}}$ (the red curve) and $\Delta F^{\mathrm{dhcp}\to\mathrm{fcc}} = F^{\mathrm{dhcp}} - F^{\mathrm{fcc}}$ (the blue curve). A positive $\Delta F^{\mathrm{hcp}\to\mathrm{fcc}}$ indicates that the system would prefer the fcc phase over the hcp, and vice versa.

The thermodynamical equilibrium occurs at a temperature indicated by $T_0^{\mathrm{fcc,hcp}}$, where the free energies of the two phases become equal, and consequently $\Delta F^{\mathrm{hcp}\to\mathrm{fcc}} = \Delta F^{\mathrm{fcc}\to\mathrm{hcp}} = 0$. However, in the real world, due to the existence of non-chemical energy barriers such as interfacial and elastic energy, these transformations occur when their

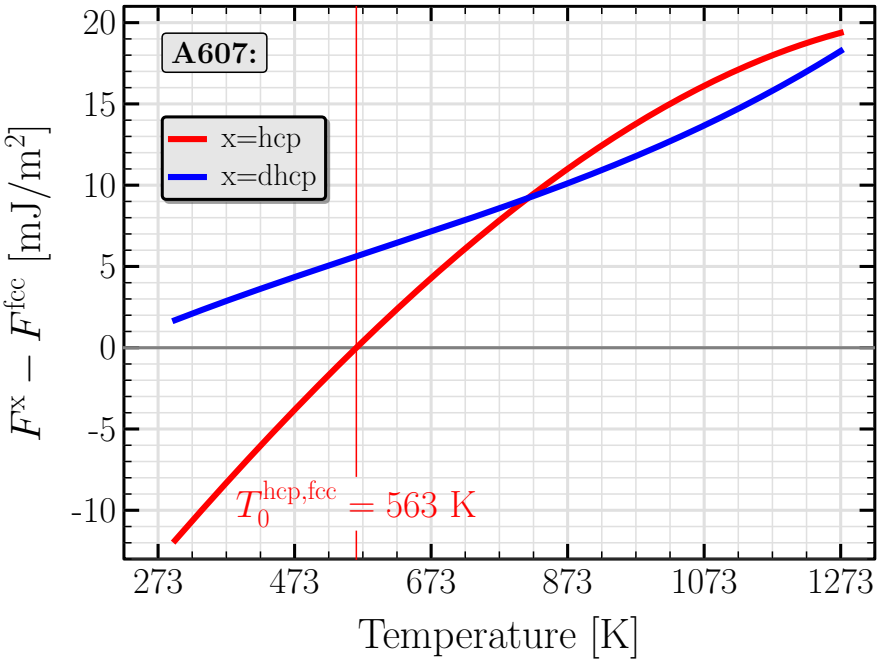

Figure 6.25: The differences between the free energies of the hcp and dhcp phases with respect to the free energy of the fcc phase, calculated for A607 alloy.

corresponding driving forces find certain positive values [28]. That is why a significant hysteresis is observed between the starting points of the austenite-to-martensite transformation during cooling, and its reversed form, *i.e.*, the martensite-to-austenite transformation during heating.

The experimental measurements for the α'-martensite start temperature, $M_s^{\gamma\to\alpha'}$, and the austenite start temperature, $A_s^{\alpha'\to\gamma}$, are presented in Tab. 6.6 for alloys with chemical compositions close to that of A607. The averages values in the table are in good agreement with the empirical formula presented in Eq. 3.1, which estimates the $M_s^{\gamma\to\alpha'}$ temperature about 250 K (−23 °C) for A607. For Fe–18.8wt.%Cr–11.5wt.%Ni, which has a slightly higher amount of nickel, Singh has observed that the ϵ and α'-martensites are stable up to 473 K (200 °C) and 673 K (400 °C), respectively [23]. Summarizing these data, and keeping in mind that the hcp ϵ-phase is an intermediate phase in $\gamma \leftrightarrow \alpha'$ transformations, one can conclude that the temperature at which the free energies of ϵ and γ phases become equal, $T_0^{\gamma,\epsilon}$, is somewhere between $M_s^{\gamma\to\alpha'}$ and $A_s^{\alpha'\to\gamma}$. Using the average values in Tab. 6.6, the middle point of the $[M_s^{\gamma\to\alpha'}, A_s^{\alpha'\to\gamma}]$ temperature interval is 487 K (214 °C). Based on our calculations, $T_0^{\text{fcc,hcp}} = 563$ K (290 °C) (see Fig. 6.25). This value is in reasonable agreement with the discussed experimental values, and also with the γ–ϵ equilibrium temperature of 521 K (248 °C), calculated using Thermo-Calc.

Table 6.6: Experimental values of $M_s^{\gamma\to\alpha'}$ and $A_s^{\alpha'\to\gamma}$, measured for alloys with chemical composition similar to A607. For accurate composition of other elements, see Appendix A.

Cr	Ni	$M_s^{\gamma\to\alpha'}$		$A_s^{\alpha'\to\gamma}$		notes and reference
[wt%]	[wt%]	[K]	[°C]	[K]	[°C]	
18.00	7.00	193	−80	—	—	Abrassart1973 [17]
20.00	8.00	294	21	—	—	Behjati2011 [32]
18.00	10.00	264	−9	—	—	Behjati2011 [32]
20.00	10.00	261	−12	—	—	Behjati2011 [32]
17.30	11.00	223	−50	—	—	Breedis1964 [9]
18.03	7.94	—	—	813	540	Guy1983 [20]
17.55	7.67	—	—	723	450	Knutsson2008 [30]
18.34	8.53	—	—	710	437	average over five measurements, Tavares2000 [27]
Average:		**247**	**−26**	**727**	**454**	

6.4.6 Approximations and Approaches

Here we present a systematic study of the influence of various approximations and physical effects on the SFE results. For brevity and clarity, first we explain all terms appearing in plot labels and legends:

- **Analytical LSF:** The default approach for evaluating the magnetic free energy, where the magnetic fluctuations are accounted for by using the Monte-Carlo results as described in Subsec. 6.4.2.2. This is our default approach of LSF calculations, if nothing else is mentioned explicitly.
- **Self-consistent LSF (SC-LSF):** The magnetic free energy is computed from the self-consistent magnetic fluctuations.
- **Constant a:** Without the addition of SC-LSF, it means that the DFT calculations in the latest step have been performed with fixed lattice spacing for the entire temperature range, omitting the thermal expansion. However, it must be noted that the thermal expansion has been considered when evaluating the temperature dependence of magnetic moments using the analytical LSF. When used in combination with SC-LSF, is omitted completely, using the experimental fcc lattice parameter measured at 298 K.
- **Variable a:** The thermal expansion has been taken into account every where in calculations. This is our default method, if nothing else is mentioned explicitly.
- **Frozen core:** The frozen-core approximation is applied only in the DFT calculations in the latest step. In this approximation, the core states in a crystal are approximated with their atomic equivalents in an isolated atom, and remain unchanged while valence states are calculated through the self-consistent approach.
- **Soft core:** All electronic states, including core and valence states, have been calculated self-consistently. This is our default choice.
- **Electronic entropy ($S_{\text{el.}}$):** The contribution of the electronic entropy has been accounted when calculating the free energy. By default, this contribution is not taken into account, unless explicitly mentioned.

6.4.6.1 The Electronic Entropy

In Fig. 6.26 we present the contribution of the electronic entropy to the temperature dependent SFE, where the dashed and solid lines, respectively, indicate our final results without and with accounting for this effect. As shown in the figure, the electronic entropy has a very small effect, $\sim 2\,\text{mJ/m}^2$, when the SFE is calculated using the analytical approach for the LSF. More accurately speaking, including the electronic entropy increases the SFE at the first half of the temperature range, while decreasing it at the other half. Given the overall accuracy, the electronic entropy might be safely omitted.

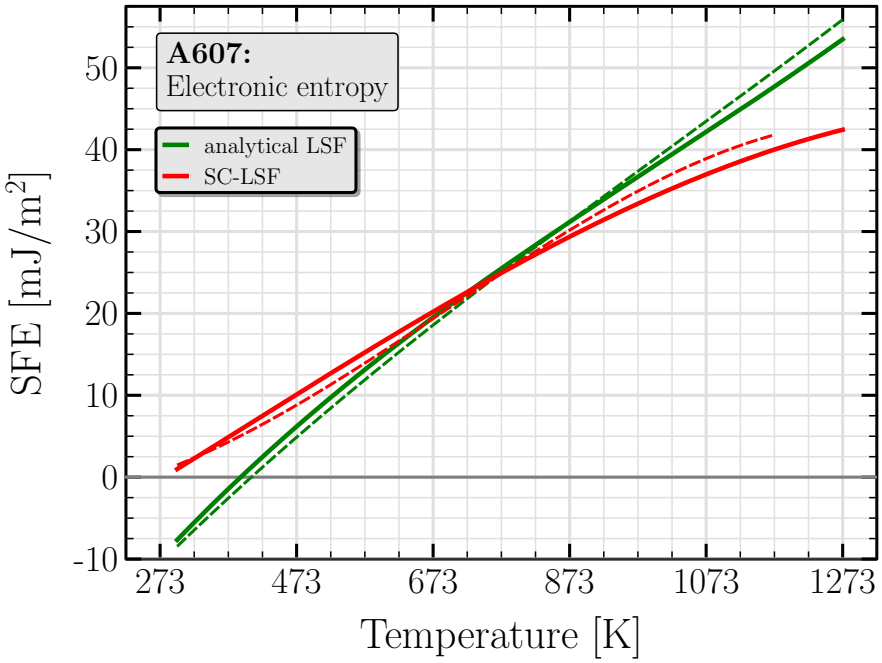

Figure 6.26: Changes introduced in the SFE, as the electronic entropy is taken into account in the free energy calculation. The dashed and the solid lines indicate the results without and with accounting for the electronic entropy, respectively. The curves show that the electronic entropy does not significantly affect the final results.

On the other hand, when the SC-LSF approach is applied for evaluating the magnetic excitations, the electronic entropy has a more pronounced effect, $\sim 5\,\mathrm{mJ/m^2}$ at its maximum, on the final results.

In a similar way, the contribution of the electronic entropy to the temperature dependent DF is presented for two cases: calculations with default settings (Fig. 6.27(a)), and with SC-LSF (Fig. 6.27(b)). Our results show that $T_0^{\mathrm{fcc,hcp}}$ is shifted toward higher temperatures, as the electronic entropy is included in the free-energy calculations. Like the case of the SFE, the shift is larger when the SC-LSF approach is applied.

6.4.6.2 The Thermal Expansion

In Fig. 6.28, we present the influence of the thermal expansion on the temperature dependence of the SFE in A607 alloy. The influence of the thermal expansion on differences between the free energies of three phases is presented in Fig. 6.29. In the SC-LSF approach, a single computation involves a given lattice parameter and temperature. The local magnetic moments, and consequently, the magnetic entropy and the free energy are calculated self-consistently. When lattice expansion is omitted, the only difference between systems at two different temperatures is their magnetic state. Since the effect of magnetic excitations on the temperature dependence of the SFE is relatively small, it results in a very weak temperature dependence of the SFE, which is presented

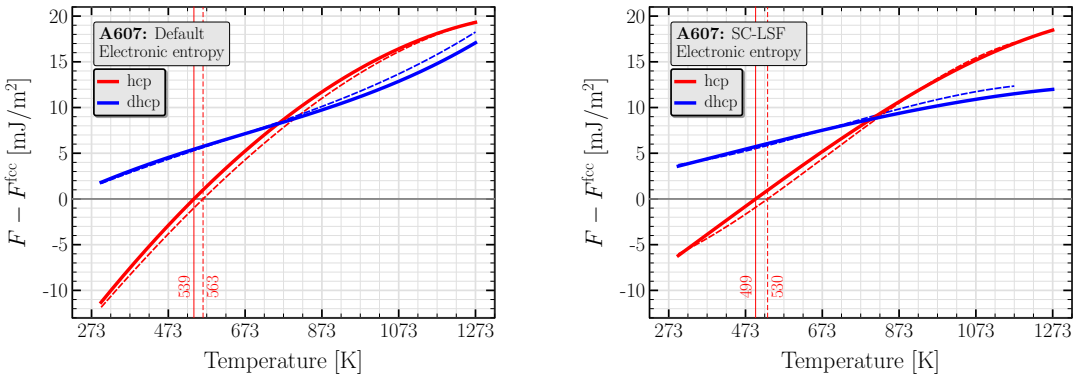

Figure 6.27: Changes introduced in the differences between free energies of hcp and dhcp phases with respect to the free energy of the fcc phase, as the electronic entropy is taken into account. In every plot, the dashed and the solid lines indicate the results without and with accounting the electronic entropy, respectively. (a) Calculations with default settings. (b) Calculations with SC-LSF approximation.

by the small slope of corresponding curves in Figs. 6.28 and 6.29(c).

When calculating using the analytical LSF approach (see Sec. 6.4.2), the thermal expansion must be considered in two steps, first when calculating the LSF, and second when calculating the total energy (see Sec.6.4.3). Here we present the influence of the thermal expansion on the second step only, as it has already been taken into account when evaluating the fluctuation of magnetic moments. We found that the thermal expansion is equally important for both soft- and frozen-core treatments, as it leads to significant increase in the slope of the SFE curve (see Fig. 6.28), or results in big shifts in the fcc–hcp equilibrium temperature, $T_0^{\mathrm{fcc,hcp}}$ (see Figs. 6.29(a) and 6.29(b)). Thus we conclude that the thermal expansion is a crucial effect which must be taken into account in order to understand the correct electronic structure and physical properties of an alloy at finite temperatures, particularly its phase stability, transformation temperatures, and the temperature dependence of the SFE.

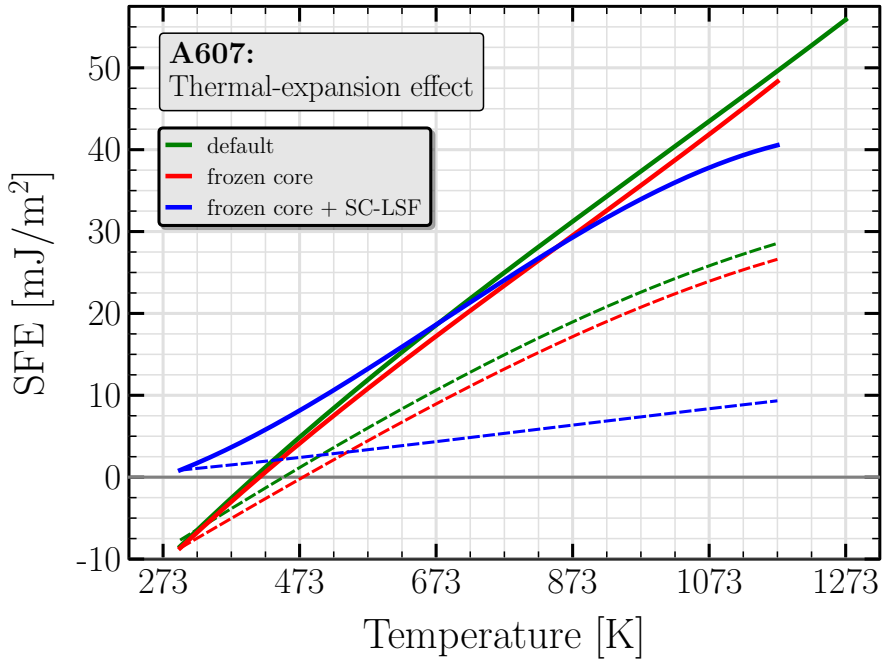

Figure 6.28: Changes introduced in the SFE, as the thermal lattice expansion is taken into account in the free energy calculation. The dashed and the solid lines indicate the results without and with accounting for the thermal expansion, respectively. The curves show that the thermal expansion is an essential effect which must be considered in order to find the correct temperature dependence of the SFE.

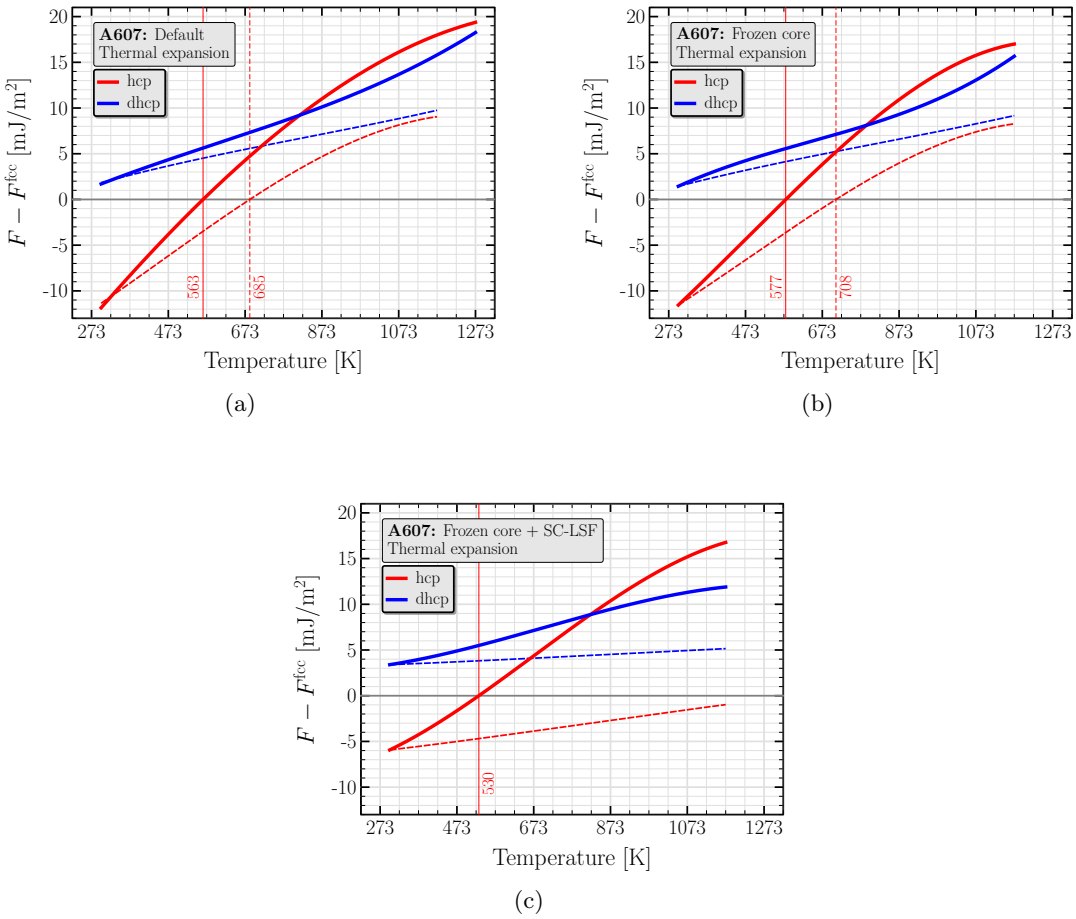

Figure 6.29: Changes introduced in the differences between free energies of hcp and dhcp phases with respect to the free energy of the fcc phase, as the thermal expansion is taken into account. In every plot, the dashed and the solid lines indicate the results without and with accounting for the thermal expansion, respectively. (a) Calculations with default settings. (b) Calculations with frozen-core approximation. (c) Calculations with frozen-core approximation and SC-LSF.

6.4.6.3 The Frozen-core Approximation

In order to investigate the influence of the frozen-core approximation, we recalculate our results by applying this approximation. The SFE and the free energies are presented in Figs. 6.30 and 6.31, respectively. In all figures, the dashed curves indicate the results of calculation with default settings (soft core, here), while the solid curves show the outputs of with the frozen-core approximation. We conclude that the frozen-core approximation has only a small influence on the final results. On the other hand, we found that the application of this approximation does not improve the performance. Thus, we did not find any motivation for using this approximation.

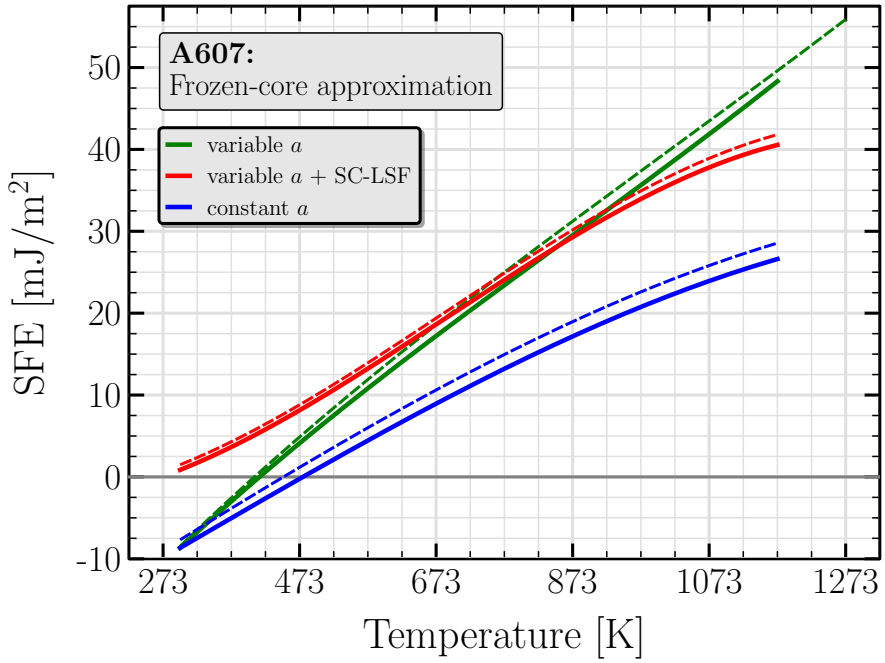

Figure 6.30: The influence of the frozen-core approximation on the SFE, calculated for two systems, including and excluding the thermal expansion (green and red curves, respectively). The dashed and the solid lines indicate the results with soft- and frozen-core approximations, respectively. The curves show just a slight change in the SFE introduced by the approximation.

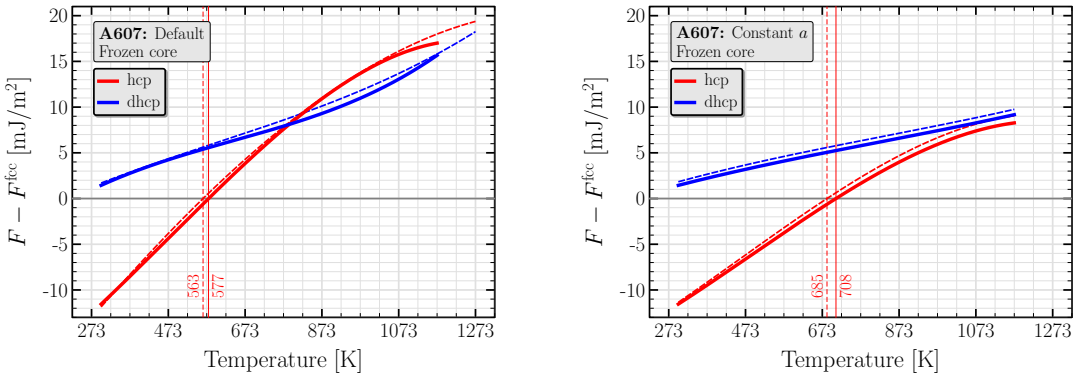

Figure 6.31: Changes introduced in the differences between free energies of hcp and dhcp phases with respect to the free energy of the fcc phase, as the frozen-core approximation is applied. The dashed and the solid lines indicate the results with soft- and frozen-core approximations, respectively. (a) Calculations with default settings. (b) Calculations with constant spacing.

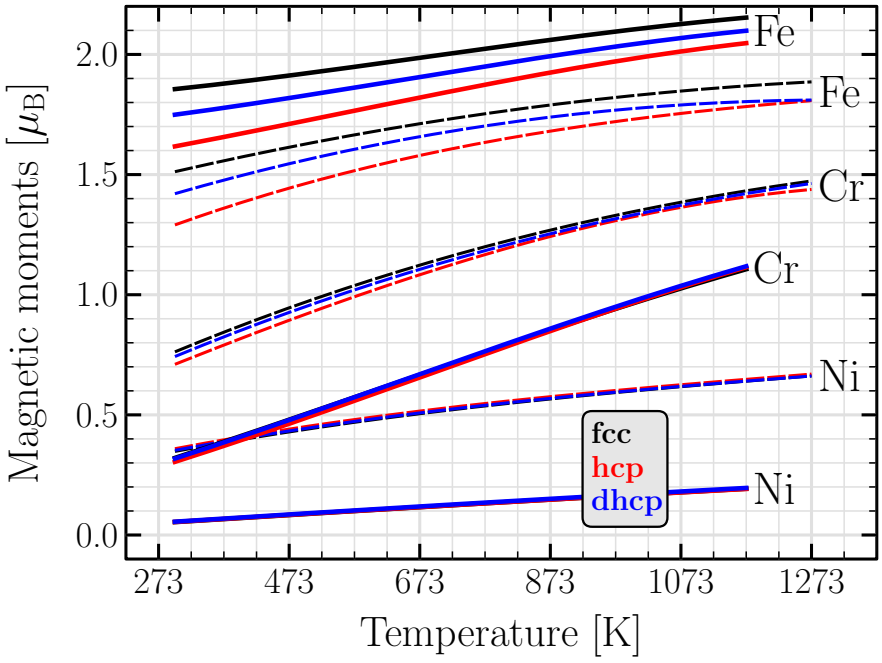

Figure 6.32: The temperature dependence of the magnetic moments, calculated for A607 using different approaches. The dashed curves show the thermal excitation of the magnetic moments evaluated using the analytical approach, where the solid curves present the results of SC-LSF approach.

6.4.6.4 The Self-consistent LSF

In our default approach, analytical LSF, the itinerant nature of the chromium and nickel electronic magnetism is accounted for, and hence a significant temperature-induced increase in the local magnetic moments of these two elements is captured. In the self-consistent LSF approach, the magnetic entropy is obtained using the magnetic moments calculated through the ground-state DFT calculations. In Fig. 6.32, we present a comparison between the temperature dependence of the magnetic moments, calculated using the two mentioned methods.

Evidently, the SC-LSF approach does not correctly account for the thermal excitation of the magnetic moments of chromium and nickel. Therefore, they maintain their 0 K nonmagnetic state even at high temperatures, resulting to an underestimated magnetic entropy. This underestimation is reflected in a too weak temperature dependence of the SFE presented in Fig. 6.33.

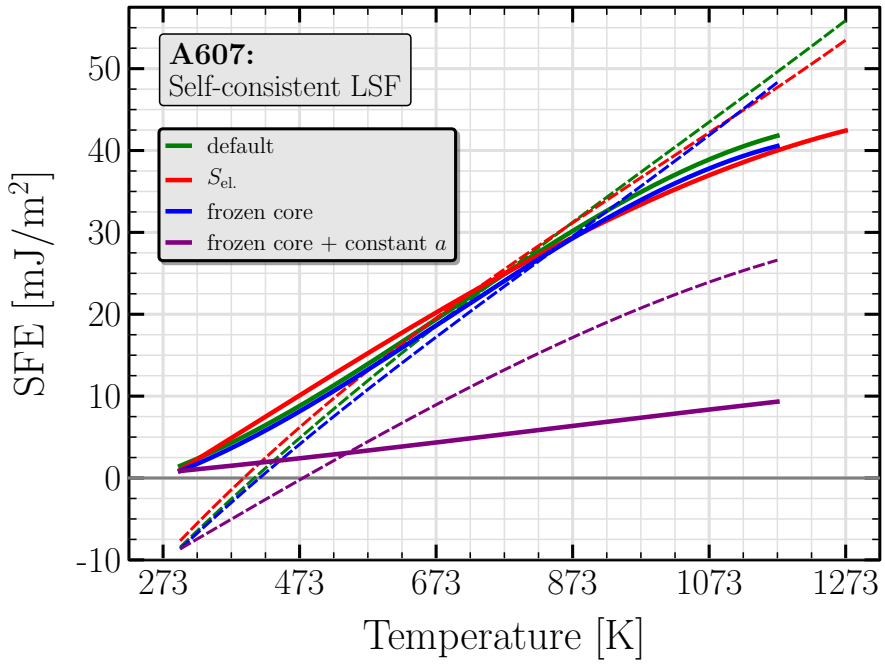

Figure 6.33: Comparison of the SFE's, as the LSF is considered using the analytical (dashed lines) or self-consistent (solid lines) approaches.

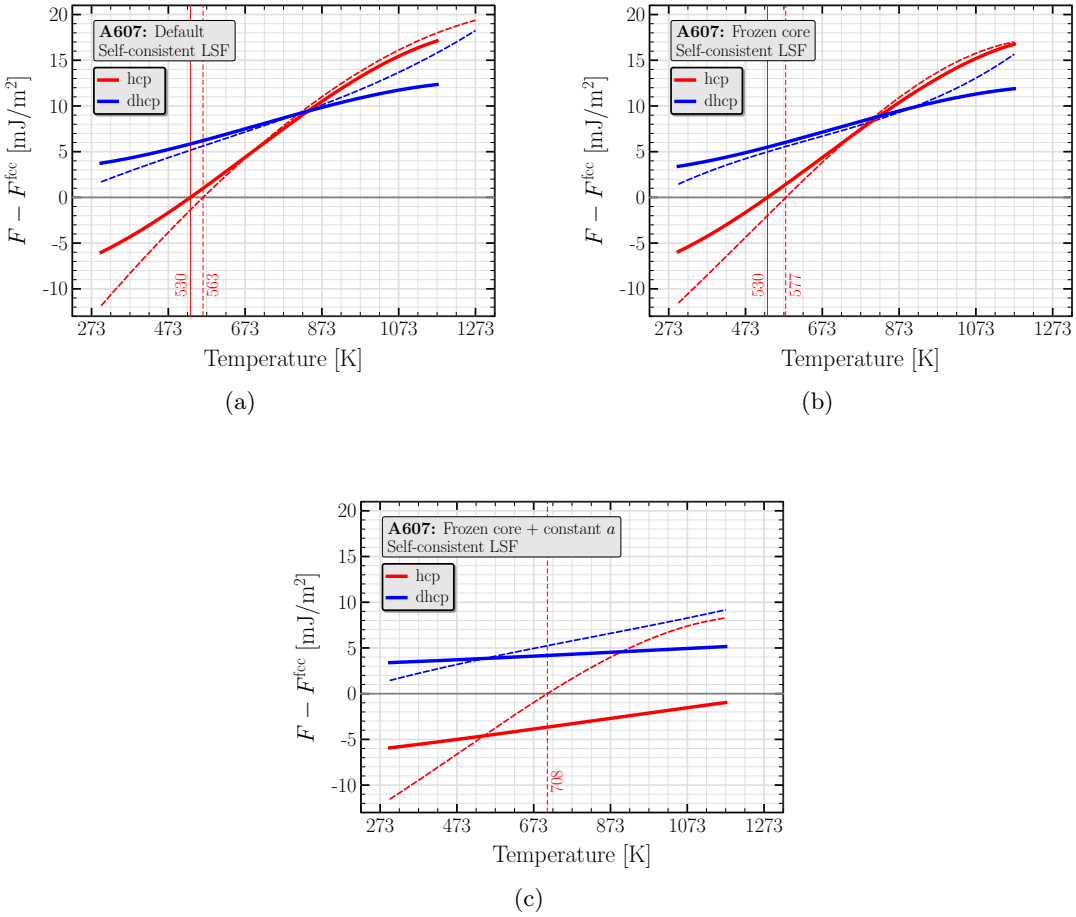

Figure 6.34: Changes introduced in the differences between free energies of hcp and dhcp phases with respect to the free energy of the fcc phase, as the magnetic fluctuations are accounted through the self-consistently. In every plot, the dashed lines indicate the results with analytical LSF evaluation. (a) Calculations with default settings. (b) Calculations with frozen-core approximation. (c) Calculations with frozen-core approximation and constant spacing.

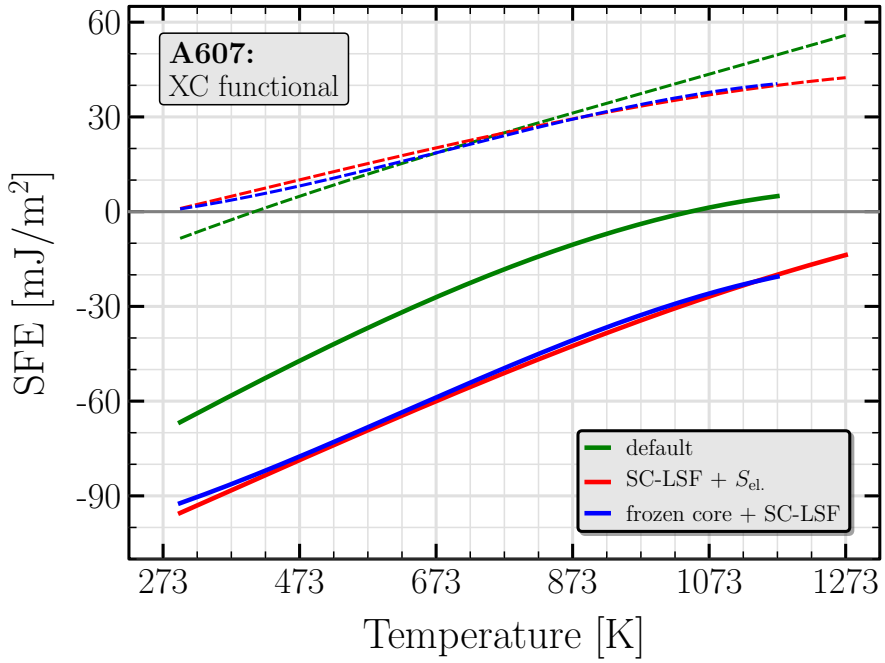

Figure 6.35: The dependence of the SFE on the exchange–correlation functional applied in the free energy calculations. The SFE's evaluated using the LSDA-LSF+GGA-FE (dashed curves) combination agree with experimental results better than those calculated using LSDA-LSF+LSDA-FE (solid curves).

6.4.6.5 The Exchange–Correlation Functional

In our default approach, we use the LSDA exchange–correlation functional when calculating the thermal excitation of magnetic moments (see 6.4.2.1), while we use the GGA functional when evaluating the free energies through the constrained DFT calculations (see 6.4.3). Beside this LSDA-LSF+GGA-FE combination, we have performed tests with other choices like LSDA-LSF+LSDA-FE and GGA-LSF+GGA-FE. The SFE and the driving forces are respectively presented in Fig. 6.35, where dashed and solid curves indicate the LSDA-LSF+GGA-FE and the LSDA-LSF+LSDA-FE combinations, respectively. The SFE curves show that a better agreement with experimental results is obtained when the GGA functional is used in the free energy calculations. This difference is also observed in the driving force curves, presented in Fig. 6.36, where using the LSDA functional underestimates the free energies of the hcp and the dhcp phases with respect to the fcc phase, resulting in wrong phase stabilities in a wide temperature range.

A further investigation on the main contribution to the SFE, *i.e.* ΔE and $T\Delta S_{\text{mag.}}$ can unveil the origin of the difference. As presented in Fig.6.37, the values of $T\Delta S_{\text{mag.}}$ are found very similar when calculated using the both XC functionals (compare blue curves with blue symbols in the figure). On the other hand, the differences between total energies, ΔE, are strongly dependent of the XC functional applied in the final DFT

calculations. In summary, we can say that the best agreement with experimental results is obtained when the GGA functional is applied in both the LSF and the total-energy calculations.

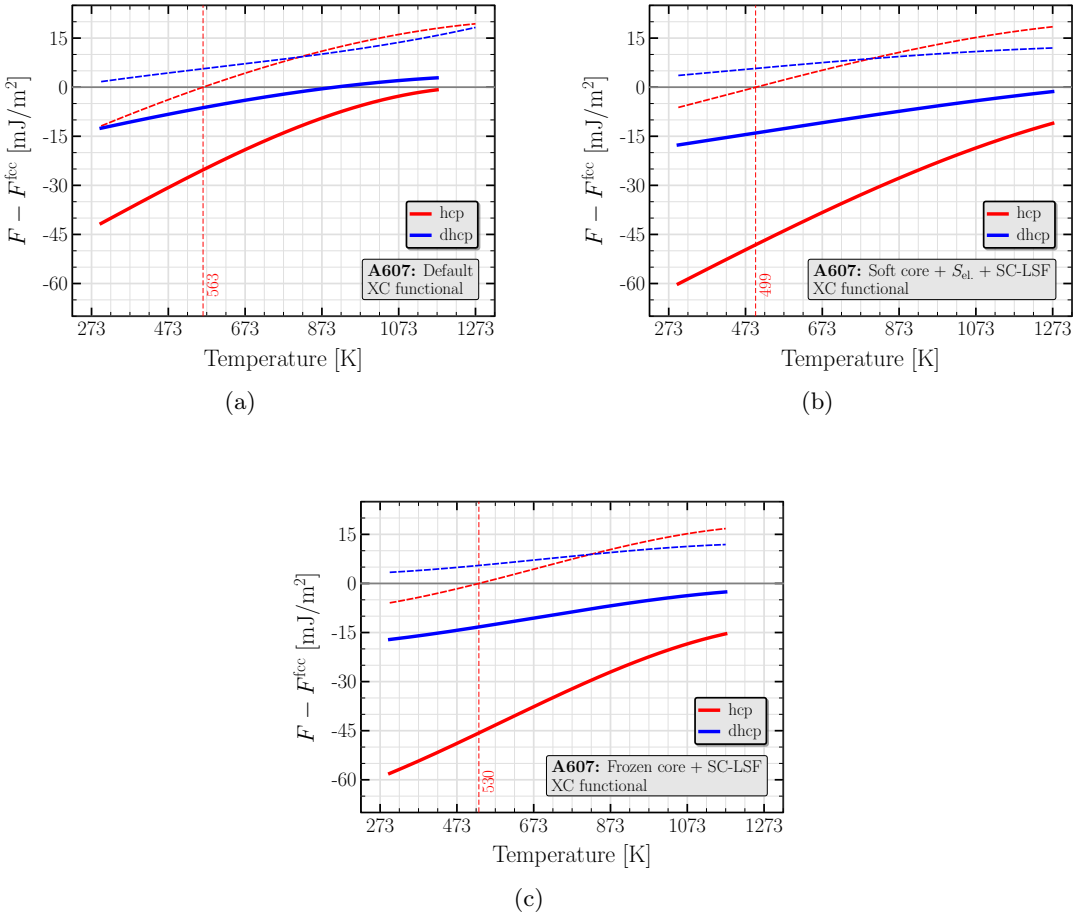

Figure 6.36: Changes introduced in the differences between free energies of hcp and dhcp phases with respect to the free energy of the fcc phase, as the exchange–correlation effects in the final DFT step are approximated using the LSDA functional, instead of the GGA. In every plot, the dashed lines indicate the results with the LSDA-LSF+GGA-FE combination, while the solid lines present the LSDA-LSF+LSDA-FE results. (a) Calculations with default settings. (b) Calculations including the electronic entropy, using the SC-LSF approach. (c) Calculations with frozen-core approximation and the SC-LSF approach.

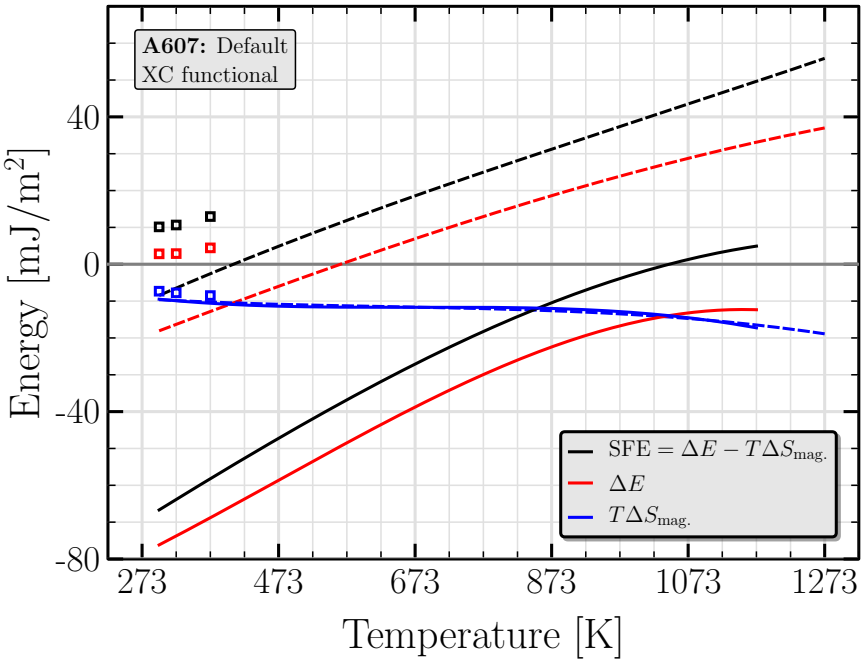

Figure 6.37: The dependence of the contribution to the SFE on the exchange–correlation functional applied in the calculations. Here, dashed curves present the LSDA-LSF+GGA-FE results, while solid curves have been calculated using the LSDA-LSF+LSDA-FE combinations. Squared symbols indicate GGA-LSF+GGA-FE results.

6.5 Conclusion

Here, we would like to draw conclusions from our results.

- When calculating the SFE using the ANNNI model, our results for the Fe–Cr–Ni alloy show that a deviation of maximal ±10% in the value of the screening parameters still result in reasonable results.
- The frozen-core approximation, compared to the soft-core approach, underestimates the strength of the atomic interactions in the metal, resulting in larger equilibrium volumes and smaller bulk moduli. However, the magnetic moments are found very similar in both approaches.
- Thermal excitation of magnetic moments reveal that, at 0 K, iron exhibits a magnetic moment, while chromium and nickel are nonmagnetic. As temperature rises, all three elements increase their moments. It shows the dominance of the itinerant nature of the electron magnetisms in chromium and nickel, and the dominance of the Heisenberg nature of the electron magnetisms in iron.
- We found that, for the A607 alloy in the range of 298 K–1273 K (25 °C–1000 °C), the SFE almost linearly increases with temperature with the slope of 0.1 $\mathrm{mJ/m^2/K}$.
- The thermal lattice expansion is by far the main parameter influencing the temperature dependence of the SFE. The electronic entropy is very small, and hence can be neglected. The main contribution of the magnetic entropy to the SFE is shifting the entire curve toward larger values.
- For the applications where approximate values of the SFE suffice, the thermal excitation of the magnetic moments can be neglected, by taking the magnetic moments calculated versus the volume.
- The SC-LSF approach might be used in order to include the thermal excitation of the magnetic moments. While its results are similar to the analytical approach, it requires less computational effort.
- The LSDA functional predicts the phase stability of the steel incorrectly, resulting in significantly underestimated SFE. It also underestimates the magnetic moments, resulting in too small magnetic entropy contribution. In order to find better agreement with experimental results, the use of the GGA functional in the entire calculations is recommended.

In this appendix, we derive a two-dimensional Fourier expansion which obeys the symmetry properties of the {111} plane in the fcc structure. Such an expansion can be fitted to a number of points calculated on the γ-curve in order to interpolate the entire γ-surface.

A Three-fold Rotational Symmetry

Using the Cartesian coordinate system, the most general form of the Fourier expansion in two dimensions is given by

$$f(x,y) = \sum_{m,n\,\in\,\mathbb{Z}} C_{mn}\, e^{\imath \frac{2\pi x}{a} m}\, e^{\imath \frac{2\pi y}{b} n}, \tag{28}$$

where m and n are integer numbers, C_{mn} denote expansion coefficients, and a and b are the periodicities along the x and y axes, respectively. When studying the {111} plane of the fcc structure, we select the x and y axes lying in the plane, and thus the z axis becomes normal to the plane along the [111] crystallographic direction. Here, we call this z axis as the [111] axis. The {111} plane has a 3-fold rotational symmetry around the [111] axis. Mathematically, it means that any function $f(x,y)$ which obeys the symmetries of such plane must remain unchanged under a rotation by any angle of an integer factor of $\frac{2\pi}{3} = 120^\circ$ about the [111] axis. It requires that, for any arbitrary point (x,y) in the {111} plane, $f(x,y)$ must fulfill the condition

$$f(x',y') = f(x'',y'') = f(x,y), \tag{29}$$

where (x',y') and (x'',y'') are the images of point (x,y) under rotations by angles 120° and -120°, respectively.

A rotation by angle θ around the [111] axis is characterized by the operator $\hat{R}_{[111]}(\theta)$ as

$$\hat{R}_{[111]}(\theta) = \begin{pmatrix} \cos(\theta) & -\sin(\theta) \\ \sin(\theta) & \cos(\theta) \end{pmatrix}. \tag{30}$$

Applying $\hat{R}_{[111]}(120^\circ)$ and $\hat{R}_{[111]}(-120^\circ) = \hat{R}_{[111]}(240^\circ)$ to a point (x,y) results in

$$\begin{pmatrix} x' \\ y' \end{pmatrix} = \hat{R}_{[111]}(120^\circ) \begin{pmatrix} x \\ y \end{pmatrix} = \begin{pmatrix} -\frac{1}{2}x - \frac{\sqrt{3}}{2}y \\ \frac{\sqrt{3}}{2}x - \frac{1}{2}y \end{pmatrix} \tag{31}$$

and

$$\begin{pmatrix} x'' \\ y'' \end{pmatrix} = \hat{R}_{[111]}(-120^\circ) \begin{pmatrix} x \\ y \end{pmatrix} = \begin{pmatrix} -\frac{1}{2}x + \frac{\sqrt{3}}{2}y \\ -\frac{\sqrt{3}}{2}x - \frac{1}{2}y \end{pmatrix}. \tag{32}$$

Substituting Eq. 31 into the Eq. 28 leads to

$$\begin{aligned} f(x',y') &= \sum_{m',n'\in\mathbb{Z}} C_{m'n'}\, e^{\imath\frac{2\pi x'}{a}m'}\, e^{\imath\frac{2\pi y'}{b}n'} \\ &= \sum_{m',n'\in\mathbb{Z}} C_{m'n'}\, e^{\imath\frac{2\pi}{a}(-\frac{1}{2}x-\frac{\sqrt{3}}{2}y)m'}\, e^{\imath\frac{2\pi}{b}(\frac{\sqrt{3}}{2}x-\frac{1}{2}y)n'} \\ &= \sum_{m',n'\in\mathbb{Z}} C_{m'n'}\, e^{\imath\frac{2\pi}{a}(-\frac{m'}{2}+\frac{a\sqrt{3}n'}{2b})x}\, e^{\imath\frac{2\pi}{b}(-\frac{b\sqrt{3}m'}{2a}-\frac{n'}{2})y}. \end{aligned} \tag{33}$$

The condition 29 necessitates that the expansions on the right side of Eqs. 28 and 33 must be equal for all points (x, y) in the $\{111\}$ plane. Such a requirement is fulfilled only when the coefficients of the plane waves with the same arguments are equal:

$$C_{m'n'} = C_{mn}, \quad \text{if} \begin{cases} m = \frac{1}{2}(-m' + \frac{a\sqrt{3}}{b}n') \\ n = \frac{1}{2}(-\frac{b\sqrt{3}}{a}m' - n') \end{cases} \Leftrightarrow \begin{cases} m' = \frac{1}{2}(-m - \frac{a\sqrt{3}}{b}n) \\ n' = \frac{1}{2}(\frac{b\sqrt{3}}{a}m - n) \end{cases}. \tag{34}$$

In a similar way, substituting Eq. 32 into the Eq. 28 leads to

$$C_{m''n''} = C_{mn}, \quad \text{if} \begin{cases} m = \frac{1}{2}(-m'' - \frac{a\sqrt{3}}{b}n'') \\ n = \frac{1}{2}(\frac{b\sqrt{3}}{a}m'' - n'') \end{cases} \Leftrightarrow \begin{cases} m'' = \frac{1}{2}(-m + \frac{a\sqrt{3}}{b}n) \\ n'' = \frac{1}{2}(-\frac{b\sqrt{3}}{a}m - n) \end{cases}. \tag{35}$$

Since m', n', m'', and n'' are all integers, both $m \pm \frac{a\sqrt{3}}{b}n$ and $\frac{b\sqrt{3}}{a}m \mp n$ have to be even numbers. Satisfying this condition for any arbitrary m and n requires that $\frac{a\sqrt{3}}{b}, \frac{b\sqrt{3}}{a} \in \mathbb{Z}$. Assuming these two integer numbers to be equal to k and l leads to

$$\left.\begin{aligned} \frac{a\sqrt{3}}{b} = k, \quad k\in\mathbb{Z} \quad &\Rightarrow \quad a = \frac{k}{\sqrt{3}}b \\ \frac{b\sqrt{3}}{a} = l, \quad l\in\mathbb{Z} \quad &\Rightarrow \quad a = \frac{\sqrt{3}}{l}b \end{aligned}\right\} \Rightarrow \frac{k}{\sqrt{3}}b = \frac{\sqrt{3}}{l}b \Rightarrow kl = 3. \tag{36}$$

There is only one pair of integer numbers which satisfies the final equation: $k = 3, l = 1$, or vise versa. The choice of $k = 3, l = 1$ results in

$$a = \sqrt{3}b, \tag{37}$$

which gives exactly the dimensions of the smallest octahedral unit cell of the fcc structure, as presented in Fig. 38. In fact, we have proven here that all lattice points in the close-packed $\{111\}$ plane can be produced just by combining the translational and the 3-fold rotational symmetries.

Substituting the Eq. 37 in Eqs. 34 and 35 leads to

$$C_{m'n'} = C_{mn}, \quad \text{if} \begin{cases} m' = \dfrac{-m-3n}{2} \\ n' = \dfrac{m-n}{2} \end{cases}, \tag{38}$$

and

$$C_{m''n''} = C_{mn}, \quad \text{if} \begin{cases} m'' = \dfrac{-m+3n}{2} \\ n'' = \dfrac{-m-n}{2} \end{cases}, \tag{39}$$

with the restriction of

$$m+n = 2l, \quad l \in \mathbb{Z} \tag{40}$$

in order to assure integer values for m', n', m'', and n''.

At this point, the most general form of the 2-dimensional Fourier expansion with 3-fold rotational symmetry is obtained by applying the above results to the original equation 28:

$$\begin{aligned} f(x,y) = \sum_{\substack{m,n\in\mathbb{Z} \\ m+n=2l}}{}' C_{mn} \Big\{ & e^{\imath\frac{2\pi x}{a}m} e^{\imath\frac{2\pi y}{b}n} \\ & + e^{\imath\frac{2\pi x}{a}\left(\frac{-m-3n}{2}\right)} e^{\imath\frac{2\pi y}{b}\left(\frac{m-n}{2}\right)} \\ & + e^{\imath\frac{2\pi x}{a}\left(\frac{-m+3n}{2}\right)} e^{\imath\frac{2\pi y}{b}\left(\frac{-m-n}{2}\right)} \Big\}. \end{aligned} \tag{41}$$

The prime sign of $\sum'$ means that every pair of integer numbers (m,n) can appear in the arguments of the exponential functions only once. In other words, once m and n have values m_0 and n_0, they will not take any of the values $\frac{m_0+3n_0}{2}$, $\frac{m_0-n_0}{2}$, $\frac{m_0-3n_0}{2}$, and $\frac{m_0+n_0}{2}$.

B Reflection Symmetry

In the fcc structure, the $\{0\bar{1}1\}$ plane is a mirror plane (see Fig. 38). The intersection of this plane and the $\{111\}$ plane is a line along the $[\bar{2}11]$ direction, here selected as x axis. Therefore, the $\{111\}$ plane has a reflection symmetry with respect to the x axis. Such a symmetry must be present in any function obeying the symmetry properties of the $\{111\}$ plane.

Considering our choice for the x and y axes, the reflection symmetry requires the function $f(x,y)$ to have equal values at y and $-y$:

$$f(x,-y) = f(x,y). \tag{42}$$

It is easy to show that such a condition necessitates

$$C_{m,-n} = C_{m,n}, \tag{43}$$

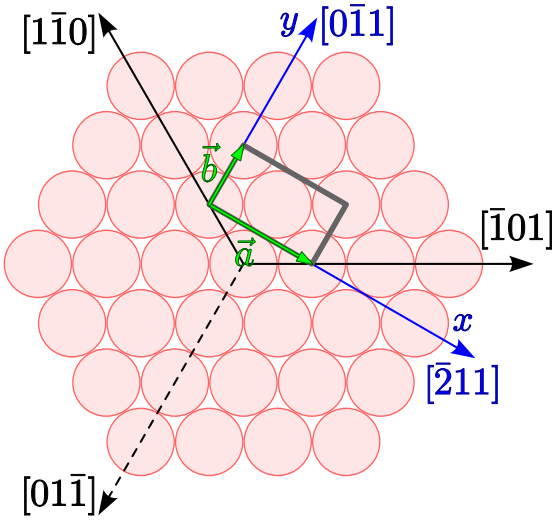

Figure 38: The top view of the {111} plane of the fcc structure, where the base of an orthorhombic unit cell is indicated by the gray rectangle. In such a unit cell, $a = \sqrt{3}b$.

leading to

$$f(x,y) = \sum_{\substack{m,n\in\mathbb{Z}\\ m+n=2l}}{}' C_{mn}\Big\{ e^{\imath\frac{2\pi x}{a}m} e^{\imath\frac{2\pi y}{b}n} + e^{\imath\frac{2\pi x}{a}(\frac{-m-3n}{2})} e^{\imath\frac{2\pi y}{b}(\frac{m-n}{2})} + e^{\imath\frac{2\pi x}{a}(\frac{-m+3n}{2})} e^{\imath\frac{2\pi y}{b}(\frac{-m-n}{2})}\Big\}. \tag{44}$$

Using Euler's formula $e^{\imath x} = \cos x + \imath \sin x$, the equation is rewritten as

$$f(x,y) = \sum_{\substack{m,n\in\mathbb{Z}\\ n\geq 0\\ m+n=2l}}{}' C_{mn}\Big\{ e^{\imath\frac{2\pi x}{a}m} \cos(\frac{2\pi y}{b}n) + e^{\imath\frac{2\pi x}{a}(\frac{-m-3n}{2})} \cos(\frac{2\pi y}{b}\cdot\frac{m-n}{2}) + e^{\imath\frac{2\pi x}{a}(\frac{-m+3n}{2})} \cos(\frac{2\pi y}{b}\cdot\frac{-m-n}{2})\Big\}. \tag{45}$$

C Real Function $f(x, y)$

We are interested in functions with *real* values: $f(x, y) \in \mathbb{R}$. In the most general case, C_{mn} are complex numbers:

$$C_{mn} = p_{mn} - \imath q_{mn}, \qquad p_{mn}, q_{mn} \in \mathbb{R}. \tag{46}$$

By substituting this equation into Eq. 45, and using Euler's formula, we find

$$f(x,y) = f^*(x,y) \quad \Rightarrow \quad C_{-m,n} = C^*_{m,n}. \tag{47}$$

For $m = 0$, the above equation results in $C_{0n} = C_{0n}^*$, which means that C_{0n} is real, thus $q_{0n} = 0$.

Finally, the desired Fourier expansion, which obeys the symmetry of the fcc {111} plane and results in real values is obtained as

$$
\begin{aligned}
f(x,y) \;=\; & \sum_{\substack{n\in Z\\ n\geq 0\\ n=2l}}{}' \left\{ p_{0n} \left[\cos(\frac{2\pi y}{b}n) + 2\cos(\frac{2\pi x}{a}\cdot\frac{3n}{2})\cos(\frac{2\pi y}{b}\cdot\frac{n}{2}) \right] \right\} \\
& + \sum_{\substack{m,n\in Z\\ m>0\\ n\geq 0\\ m+n=2l}}{}' \left\{ p_{mn} \left[\cos(\frac{2\pi x}{a}m)\cos(\frac{2\pi y}{b}n) \right.\right. \\
& \qquad + \cos(\frac{2\pi x}{a}\cdot\frac{m+3n}{2})\cos(\frac{2\pi y}{b}\cdot\frac{m-n}{2}) \\
& \qquad \left.\left. + \cos(\frac{2\pi x}{a}\cdot\frac{m-3n}{2})\cos(\frac{2\pi y}{b}\cdot\frac{m+n}{2}) \right] \right. \\
& \qquad + q_{mn} \left[\sin(\frac{2\pi x}{a}m)\cos(\frac{2\pi y}{b}n) \right. \\
& \qquad\qquad + \sin(\frac{2\pi x}{a}\cdot\frac{m+3n}{2})\cos(\frac{2\pi y}{b}\cdot\frac{m-n}{2}) \\
& \qquad\qquad \left. \left. + \sin(\frac{2\pi x}{a}\cdot\frac{m-3n}{2})\cos(\frac{2\pi y}{b}\cdot\frac{m+n}{2}) \right] \right\}
\end{aligned}
\tag{48}
$$

Appendix A

Experimental Data

Table A.1: Abrassart1973 [17]: Fe-Cr-Ni

name	method	Fe	Cr	Ni	C	Al	Si	Mn	Nb	Mo	M_s	T	SFE	M_d
Steel 1	exp	74.82	18	7	0.18	—	—	—	—	—	193.15 ± 5	287.55	17.7	$353.15 < x < 363.15$
Steel 1	exp	74.82	18	7	0.18	—	—	—	—	—	—	288.85	16.5	—
Steel 1	exp	74.82	18	7	0.18	—	—	—	—	—	—	288.85	19.8	—
Steel 1	exp	74.82	18	7	0.18	—	—	—	—	—	—	289.55	22.8	—
Steel 1	exp	74.82	18	7	0.18	—	—	—	—	—	—	291.75	18.3	—
Steel 1	exp	74.82	18	7	0.18	—	—	—	—	—	—	292.65	12.5	—
Steel 1	exp	74.82	18	7	0.18	—	—	—	—	—	—	292.95	21.3	—
Steel 1	exp	74.82	18	7	0.18	—	—	—	—	—	—	293.15	24.4	—
Steel 1	exp	74.82	18	7	0.18	—	—	—	—	—	—	293.45	17.3	—
Steel 1	exp	74.82	18	7	0.18	—	—	—	—	—	—	293.65	22.6	—
Steel 1	exp	74.82	18	7	0.18	—	—	—	—	—	—	296.75	23.5	—
Steel 1	exp	74.82	18	7	0.18	—	—	—	—	—	—	297.45	19	—
Steel 1	exp	74.82	18	7	0.18	—	—	—	—	—	—	383.55	31.9	—
Steel 1	exp	74.82	18	7	0.18	—	—	—	—	—	—	385.95	33.4	—
Steel 1	exp	74.82	18	7	0.18	—	—	—	—	—	—	386.35	30.4	—
Steel 1	exp	74.82	18	7	0.18	—	—	—	—	—	—	387.15	32.1	—
Steel 1	exp	74.82	18	7	0.18	—	—	—	—	—	—	389.65	27.4	—
Steel 1	exp	74.82	18	7	0.18	—	—	—	—	—	—	393.95	19.8	—
Steel 1	exp	74.82	18	7	0.18	—	—	—	—	—	—	393.95	20.7	—
Steel 1	exp	74.82	18	7	0.18	—	—	—	—	—	—	396.35	29.6	—
Steel 1	exp	74.82	18	7	0.18	—	—	—	—	—	—	398.75	26.3	—
Steel 1	exp	74.82	18	7	0.18	—	—	—	—	—	—	398.85	31.8	—
Steel 1	exp	74.82	18	7	0.18	—	—	—	—	—	—	399.05	32.9	—
Steel 1	exp	74.82	18	7	0.18	—	—	—	—	—	—	400.35	28.9	—

Continued on next page

Table A.1 – continued from previous page

name	method	Fe	Cr	Ni	C	Al	Si	Mn	Nb	Mo	M_s	T	SFE	M_d
Steel 1	exp	74.82	18	7	0.18	—	—	—	—	—	—	400.45	30.1	—
Steel 1	exp	74.82	18	7	0.18	—	—	—	—	—	—	402.95	32.1	—
Steel 1	exp	74.82	18	7	0.18	—	—	—	—	—	—	404.65	30.2	—
Steel 1	exp	74.82	18	7	0.18	—	—	—	—	—	—	472.55	51.2	—
Steel 1	exp	74.82	18	7	0.18	—	—	—	—	—	—	472.65	49.8	—
Steel 1	exp	74.82	18	7	0.18	—	—	—	—	—	—	473.85	24.9	—
Steel 1	exp	74.82	18	7	0.18	—	—	—	—	—	—	475.35	28.5	—
Steel 1	exp	74.82	18	7	0.18	—	—	—	—	—	—	476.15	50.5	—
Steel 1	exp	74.82	18	7	0.18	—	—	—	—	—	—	493.05	43.7	—
Steel 1	exp	74.82	18	7	0.18	—	—	—	—	—	—	493.05	43.7	—
Steel 1	exp	74.82	18	7	0.18	—	—	—	—	—	—	497.15	43.6	—
Steel 1	exp	74.82	18	7	0.18	—	—	—	—	—	—	498.25	45.6	—
Steel 1	exp	74.82	18	7	0.18	—	—	—	—	—	—	498.25	45.6	—
Steel 1	exp	74.82	18	7	0.18	—	—	—	—	—	—	505.85	49.4	—
Steel 1	exp	74.82	18	7	0.18	—	—	—	—	—	—	505.85	49.4	—
Steel 1	exp	74.82	18	7	0.18	—	—	—	—	—	—	510.05	49.5	—
Steel 1	exp	74.82	18	7	0.18	—	—	—	—	—	—	597.25	49.1	—
Steel 1	exp	74.82	18	7	0.18	—	—	—	—	—	—	597.25	49.1	—
Steel 1	exp	74.82	18	7	0.18	—	—	—	—	—	—	597.65	41.2	—
Steel 1	exp	74.82	18	7	0.18	—	—	—	—	—	—	597.85	37.7	—
Steel 1	exp	74.82	18	7	0.18	—	—	—	—	—	—	597.95	50.4	—
Steel 1	exp	74.82	18	7	0.18	—	—	—	—	—	—	601.55	49.6	—
Steel 1	exp	74.82	18	7	0.18	—	—	—	—	—	—	602.15	48.1	—
Steel 1	exp	74.82	18	7	0.18	—	—	—	—	—	—	604.95	50.5	—

Continued on next page

Table A.1 – continued from previous page

name	method	Fe	Cr	Ni	C	Al	Si	Mn	Nb	Mo	M_s	T	SFE	M_d
Steel 1	exp	74.82	18	7	0.18	—	—	—	—	—	—	604.95	50.5	—
Steel 1	exp	74.82	18	7	0.18	—	—	—	—	—	—	605.05	49.7	—
Steel 1	exp	74.82	18	7	0.18	—	—	—	—	—	—	605.85	49	—
Steel 1	exp	74.82	18	7	0.18	—	—	—	—	—	—	610.35	49.6	—
Steel 1	exp	74.82	18	7	0.18	—	—	—	—	—	—	610.45	50.8	—
Steel 1	exp	74.82	18	7	0.18	—	—	—	—	—	—	610.85	48.6	—
Steel 2	exp	75.84	15.5	4.2	0.13	0.17	0.16	1.2	0.1	2.7	$273.15 < x < 283.15 \pm 5$	—	—	393.15

Table A.2: Bampton1978 [19]: Fe-Cr-Ni

name	method	Fe	Cr	Ni	C	Si	Mn	Mo	T	SFE
16/14	exp	69.67	16.2	14	0.02	0.01	0.08	0.02	298.15	23 ± 5
16/22	exp	62.9	16.21	20.77	0.01	0.01	0.08	0.02	298.15	31 ± 5
21/14	exp	64.97	21.1	13.8	0.02	0.01	0.08	0.02	298.15	18 ± 4
21/22	exp	56.89	21	22	0.01	0.01	0.07	0.02	298.15	33 ± 5
26/22	exp	52.96	25.85	21.07	0.01	0.01	0.08	0.02	298.15	35 ± 5

Table A.3: Behjati2011 [32]: Fe-Cr-Ni

name	method	Fe	Cr	Ni	C	N	O	Si	P	S	Mn	Mo	M_s	T	$DF^{\epsilon\rightarrow\gamma}$	T	SFE	$T_0^{\gamma,\alpha'}$	T	$DF^{\alpha'\rightarrow\gamma}$
16/12	exp	71.9942	16	12	0.0004	0.001	0.001	0.002	0.0001	0.0001	0.001	0.0002	—	—	—	—	—	—	77.1	891.6
16/12	exp	71.9942	16	12	0.0004	0.001	0.001	0.002	0.0001	0.0001	0.001	0.0002	—	—	—	—	—	—	123.3	947.9
16/12	exp	71.9942	16	12	0.0004	0.001	0.001	0.002	0.0001	0.0001	0.001	0.0002	—	—	—	—	—	—	203.1	1029.1
16/12	exp	71.9942	16	12	0.0004	0.001	0.001	0.002	0.0001	0.0001	0.001	0.0002	—	—	—	—	—	—	213.2	1110
16/12	exp	71.9942	16	12	0.0004	0.001	0.001	0.002	0.0001	0.0001	0.001	0.0002	—	—	—	—	—	—	223.2	1155.9
16/12	exp	71.9942	16	12	0.0004	0.001	0.001	0.002	0.0001	0.0001	0.001	0.0002	—	—	—	—	—	—	232.9	1172
20/10	exp	69.9942	20	10	0.0004	0.001	0.001	0.002	0.0001	0.0001	0.001	0.0002	—	—	—	—	—	—	4.1	645.8
20/10	exp	69.9942	20	10	0.0004	0.001	0.001	0.002	0.0001	0.0001	0.001	0.0002	—	—	—	—	—	—	77.2	689.6
20/10	exp	69.9942	20	10	0.0004	0.001	0.001	0.002	0.0001	0.0001	0.001	0.0002	—	—	—	—	—	—	203.1	778.1
20/10	exp	69.9942	20	10	0.0004	0.001	0.001	0.002	0.0001	0.0001	0.001	0.0002	—	—	—	—	—	—	233.2	857.4
20/10	exp	69.9942	20	10	0.0004	0.001	0.001	0.002	0.0001	0.0001	0.001	0.0002	—	—	—	—	—	—	253	903.8
20/10	exp	69.9942	20	10	0.0004	0.001	0.001	0.002	0.0001	0.0001	0.001	0.0002	—	—	—	—	—	—	293.2	921
20/12	exp	67.9942	20	12	0.0004	0.001	0.001	0.002	0.0001	0.0001	0.001	0.0002	—	—	—	—	—	—	4.1	532.5
20/12	exp	67.9942	20	12	0.0004	0.001	0.001	0.002	0.0001	0.0001	0.001	0.0002	—	—	—	—	—	—	133	576.8
20/12	exp	67.9942	20	12	0.0004	0.001	0.001	0.002	0.0001	0.0001	0.001	0.0002	—	—	—	—	—	—	203.1	692
20/12	exp	67.9942	20	12	0.0004	0.001	0.001	0.002	0.0001	0.0001	0.001	0.0002	—	—	—	—	—	—	223.2	720
20/08	exp	71.9942	20	8	0.0004	0.001	0.001	0.002	0.0001	0.0001	0.001	0.0002	294	294	2346	293	16 ± 1.9	634	294	1130
20/08	exp	71.9942	20	8	0.0004	0.001	0.001	0.002	0.0001	0.0001	0.001	0.0002	—	—	—	294	16	—	—	—
18/10	exp	71.9942	18	10	0.0004	0.001	0.001	0.002	0.0001	0.0001	0.001	0.0002	264	294	2379	293	22 ± 2.3	587	294	1130
18/10	exp	71.9942	18	10	0.0004	0.001	0.001	0.002	0.0001	0.0001	0.001	0.0002	—	—	—	264	20	—	—	—
20/10	exp	69.9942	20	10	0.0004	0.001	0.001	0.002	0.0001	0.0001	0.001	0.0002	261	294	2426	293	20 ± 2.1	550	294	921
20/10	exp	69.9942	20	10	0.0004	0.001	0.001	0.002	0.0001	0.0001	0.001	0.0002	—	—	—	261	18	—	—	—
16/12	exp	71.9942	16	12	0.0004	0.001	0.001	0.002	0.0001	0.0001	0.001	0.0002	231	294	2432	293	28 ± 2.9	552	294	1172
16/12	exp	71.9942	16	12	0.0004	0.001	0.001	0.002	0.0001	0.0001	0.001	0.0002	—	—	—	231	24	—	—	—
18/12	exp	69.9942	18	12	0.0004	0.001	0.001	0.002	0.0001	0.0001	0.001	0.0002	220	294	2479	293	26 ± 2.9	510	294	950
18/12	exp	69.9942	18	12	0.0004	0.001	0.001	0.002	0.0001	0.0001	0.001	0.0002	—	—	—	220	21	—	—	—
20/12	exp	67.9942	20	12	0.0004	0.001	0.001	0.002	0.0001	0.0001	0.001	0.0002	216	294	2508	293	24 ± 2.7	464	294	720
20/12	exp	67.9942	20	12	0.0004	0.001	0.001	0.002	0.0001	0.0001	0.001	0.0002	—	—	—	216	19	—	—	—

Table A.4: Breedis1964 [9]: Fe-Cr-Ni

name	method	Fe	Cr	Ni	M_s	T	SFE
Fe-19Cr-11Ni	exp	69.5	19.3	11.2	225.15	298.15	12.7
Fe-17Cr-11Ni	exp	71.7	17.3	11	223.15	298.15	17.7
Fe-16Cr-12Ni	exp	71.9	16	12.1	214.15	298.15	22.2
Fe-13Cr-14Ni	exp	72.8	13	14.2	183.15	298.15	33.1
Fe-11.5Cr-15Ni	exp	73.4	11.5	15.1	173.15	—	—
Fe-11.5Cr-16Ni	exp	72.4	11.5	16.1	$77.15 < x < 143.15$	—	—
Fe-10Cr-16Ni	exp	73.4	10.4	16.2	208.15	298.15	42.6
Fe-10Cr-16Ni	exp	73.4	10.4	16.2	$77.15 < x < 143.15$	—	—
Fe-7.5Cr-19Ni	exp	73.2	7.5	19.3	238.15	—	—
Fe-5Cr-23Ni	exp	71.9	4.8	23.3	258.15	—	—
Fe-3Cr-27Ni	exp	70.2	2.8	27	$77.15 < x < 143.15$	—	—
Fe-2Cr-30Ni	exp	68	1.9	30.1	$77.15 < x < 143.15$	—	—
Fe-33Ni	exp	66.9	—	33.1	173.15	—	—

Table A.5: Breedis1971 [14]: Fe-Cr-Ni

name	method	Fe	Cr	Ni	T	SFE
1	exp	69.5063	19.2551	11.2387	300	13

Continued on next page

Table A.5 – continued from previous page

name	method	Fe	Cr	Ni	T	SFE
2	exp	71.7291	17.2592	11.0117	300	18
3	exp	71.9295	16.0171	12.0534	300	22
4	exp	72.5882	12.9756	14.4362	300	33
5	exp	73.39	10.4267	16.1833	300	43

Table A.6: Fawley1968 [11]: Fe-Cr-Ni

name	method	Fe	Cr	Ni	C	N	T	SFE
1	exp	69.989	20	10	0.006	0.005	298.15	23 $\pm$ 4.025
2	exp	64.979	20	15	0.018	0.003	298.15	32 $\pm$ 5.6
3	exp	59.979	20	20	0.015	0.006	298.15	40 $\pm$ 7
4	exp	54.985	20	25	0.009	0.006	298.15	38 $\pm$ 6.65
5	exp	49.983	20	30	0.011	0.006	298.15	34 $\pm$ 5.95
6	exp	69.984	10	20	0.012	0.004	298.15	53 $\pm$ 9.275
7	exp	64.976	15	20	0.019	0.005	298.15	40 $\pm$ 7
8	exp	54.973	25	20	0.022	0.005	298.15	45 $\pm$ 7.875
9	exp	49.959	30	20	0.036	0.005	298.15	57 $\pm$ 9.975
10	exp	69.944	20	10	0.012	0.044	298.15	23 $\pm$ 4.025

Continued on next page

Table A.6 – continued from previous page

name	method	Fe	Cr	Ni	C	N	T	SFE
11	exp	64.955	20	15	0.01	0.035	298.15	34 $\pm$ 5.95
12	exp	59.931	20	20	0.018	0.051	298.15	38 $\pm$ 6.65
13	exp	54.958	20	25	0.009	0.033	298.15	38 $\pm$ 6.65
14	exp	49.961	20	30	0.01	0.029	298.15	34 $\pm$ 5.95
15	exp	69.975	10	20	0.012	0.013	298.15	48 $\pm$ 8.4
16	exp	64.977	15	20	0.012	0.011	298.15	44 $\pm$ 7.7
17	exp	54.936	25	20	0.017	0.047	298.15	47 $\pm$ 8.225
19	exp	59.97	20	20	0.027	0.003	298.15	43 $\pm$ 7.525
20	exp	49.94	20	30	0.05	0.01	298.15	47 $\pm$ 8.225

Table A.7: Gallagher1970 [12]: Fe-Cr-Ni

name	method	Fe	Cr	Ni	T	SFE
	exp	72.4	18	9.6	298.15	40.7
	exp	67.9	18	14.1	298.15	40.9
	exp	62.8	18	19.2	298.15	48.8

Table A.8: Guy1983 [20]: Fe-Cr-Ni

name	method	Fe	Cr	Ni	C	N	Si	P	S	Ti	V	Mn	Co	Mo	$A_s^{\alpha' \to \gamma}$	$A_f^{\alpha' \to \gamma}$
18/8	exp	72.524	18.03	7.94	0.039	0.011	0.2	0.01	0.006	0.1	0.04	1.08	0.01	0.01	813.15 ± 10	923.15 ± 10
18/12	exp	68.588	17.97	11.9	0.013	0.01	0.32	0.009	0.005	0.1	0.04	1.03	0.01	0.005	743.15 ± 10	883.15 ± 10

Table A.9: Knutsson2008 [30]: Fe-Cr-Ni

name	method	Fe	Cr	Ni	C	N	Si	Mn	Co	Cu	Nb	Mo	$A_s^{\alpha' \to \gamma}$	$A_f^{\alpha' \to \gamma}$
AISI 301	exp	72.215	17.55	7.67	0.095	0.022	0.55	1.23	0.1	0.25	0.008	0.31	723.15	873.15

Table A.10: Latanision1971 [15]: Fe-Cr-Ni

name	method	Fe	Cr	Ni	C	T	SFE
18.3Cr-10.7Ni	exp	70.995	18.3	10.7	0.005	298.15	18.2 ± 1
18.3Cr-10.7Ni	exp	70.995	18.3	10.7	0.005	408.15	27.6 ± 1.2
18.3Cr-10.7Ni	exp	70.995	18.3	10.7	0.005	598.15	30.4 ± 1.6
18.7Cr-15.9Ni	exp	65.395	18.7	15.9	0.005	298.15	24.9 ± 1
18.7Cr-15.9Ni	exp	65.395	18.7	15.9	0.005	408.15	28.8 ± 1.1
18.7Cr-15.9Ni	exp	65.395	18.7	15.9	0.005	598.15	31.8 ± 1.4

Table A.11: Lecroisey1970 [13]: Fe-Cr-Ni

name	method	Fe	Cr	Ni	C	M_s	T	SFE	M_d
1	exp	68.09	17.8	14.1	0.01	< 4.15	298.15	45	223.15
2	exp	71.59	15.9	12.5	0.01	< 178.15	298.15	24	273.15

Table A.12: Lecroisey1972 [16]: Fe-Cr-Ni

name	method	Fe	Cr	Ni	C	M_s	T	SFE	M_d
0-31	exp	69.18	—	30.8	0.02	248.15	—	—	278.15
0-31C	exp	69.06	—	30.8	0.14	228.15	—	—	273.15
0-25	exp	75	—	25	—	383.15	—	—	—
7-20	exp	73.296	6.7	20	0.004	$4.15 < x < 77.15$	—	—	> 298.15
7-19	exp	73.494	6.9	19.6	0.006	248.15	—	—	> 333.15
7-18C	exp	74.65	7.2	18	0.15	$77.15 < x < 183.15$	—	—	268.15
5-17C	exp	77.95	4.5	17.3	0.25	183.15	—	—	323.15
16-13	exp	71.59	15.9	12.5	0.01	178.15	298.15	22	353.15
16-11	exp	73.296	15.5	11.2	0.004	253.15	—	—	423.15
16-11B	exp	73.397	15.6	11	0.003	263.15	—	—	423.15
16-11C	exp	73	15.7	11.2	0.1	4.15	—	—	333.15
18-12	exp	70.192	17.8	12	0.008	208.15	298.15	30	323.15

Table A.13: Ledbetter1984 [21]: Fe-Cr-Ni

name	method	Fe	Cr	Ni	Mn	B_{fcc}
monocrystal	exp	71	19	10	—	160
polycrystal	exp	70.8	18.6	9.3	1.3	158.2

Table A.14: Li2000 [26]: Fe-Cr-Ni

name	method	Fe	Cr	Ni	C	M_s	$M_d^{\gamma\to\epsilon}$	$M_d^{\gamma\to\alpha'}$
	exp	74.82	18	7	0.18	356.15	420.15	360.15

Table A.15: Martinez1992 [24]: Fe-Cr-Ni

name	method	Fe	Cr	Ni	C	N	Al	Si	P	S	Mn	Cu	As	Nb	Mo	Sn	T	SFE
A	exp	69.2916	14.4	15.1	0.02	0.0084	0.005	0.59	0.006	0.013	0.53	0.02	0.002	0.002	0.01	0.002	298.15	45.5 $\pm$ 7.5
B	exp	68.7459	14.7	15.1	0.02	0.0081	0.005	0.48	0.006	0.012	0.43	0.04	0.001	0.44	0.01	0.002	298.15	27.5 $\pm$ 4.5
C	exp	68.7869	15.1	14.1	0.02	0.0071	0.005	0.53	0.006	0.012	0.52	0.01	0.002	0.89	0.01	0.001	298.15	23 $\pm$ 4
D	exp	67.7459	14.6	14.8	0.02	0.0081	0.005	0.57	0.006	0.012	0.47	0.01	0.002	1.74	0.01	0.001	298.15	21.5 $\pm$ 3.5

Table A.16: Ojima2009 [31]: Fe-Cr-Ni

name	method	Fe	Cr	Ni	C	N	Si	Mn	Mo	T	SFE
316L	exp	65.6457	17.35	12.95	0.015	0.0193	0.43	1.3	2.29	298.15	14.2
SUS310S	exp	53.899	25.1	19.8	0.048	0.023	0.33	0.8	—	298.15	30.9
SUS310S-N	exp	52.377	25	21.1	0.048	0.325	0.31	0.84	—	298.15	42.9
HNS	exp	69.731	23.09	4.16	0.019	1	—	—	2	298.15	22.3
10Cr-20Ni	exp	70.15	10	19.81	0.01	—	0.01	0.01	0.01	298.15	35.6
15Cr-10Ni	exp	75	14.98	9.98	0.01	—	0.01	0.01	0.01	298.15	15.2
15Cr-15Ni	exp	69.72	15.15	15.09	0.01	—	0.01	0.01	0.01	298.15	27.8
15Cr-20Ni	exp	65.05	15.06	19.85	0.01	—	0.01	0.01	0.01	298.15	31.4
15Cr-25Ni	exp	60.37	15.13	24.46	0.01	—	0.01	0.01	0.01	298.15	36.9
18Cr-12Ni	exp	70.65	18.13	11.18	0.01	—	0.01	0.01	0.01	298.15	19.3
20Cr-10Ni	exp	70.87	19.13	9.96	0.01	—	0.01	0.01	0.01	298.15	19.7
20Cr-15Ni	exp	64.81	20.06	15.09	0.01	—	0.01	0.01	0.01	298.15	21.8
20Cr-20Ni	exp	60.37	19.7	19.89	0.01	—	0.01	0.01	0.01	298.15	27.5
20Cr-25Ni	exp	55.45	20.09	24.42	0.01	—	0.01	0.01	0.01	298.15	36
25Cr-15Ni	exp	59.93	25.07	14.96	0.01	—	0.01	0.01	0.01	298.15	26
25Cr-19Ni	exp	56.62	24.56	18.78	0.01	—	0.01	0.01	0.01	298.15	28
25Cr-25Ni	exp	51.61	24.84	23.5	0.01	—	0.01	0.01	0.02	298.15	30.1

Table A.17: Olson1976 [18]: Fe-Cr-Ni

name	method	Fe	Cr	Ni	C	T	SFE
Fe16Cr13Ni	exp	71.59	15.9	12.5	0.01	158.6	13.7
Fe16Cr13Ni	exp	71.59	15.9	12.5	0.01	159.1	9.4
Fe16Cr13Ni	exp	71.59	15.9	12.5	0.01	166.2	9.6
Fe16Cr13Ni	exp	71.59	15.9	12.5	0.01	181.3	14.8
Fe16Cr13Ni	exp	71.59	15.9	12.5	0.01	183.6	10.8
Fe16Cr13Ni	exp	71.59	15.9	12.5	0.01	185.3	12.5
Fe16Cr13Ni	exp	71.59	15.9	12.5	0.01	215.9	18.3
Fe16Cr13Ni	exp	71.59	15.9	12.5	0.01	216.6	17.1
Fe16Cr13Ni	exp	71.59	15.9	12.5	0.01	225	18.2
Fe16Cr13Ni	exp	71.59	15.9	12.5	0.01	225.4	16.1
Fe16Cr13Ni	exp	71.59	15.9	12.5	0.01	264.9	20.3
Fe16Cr13Ni	exp	71.59	15.9	12.5	0.01	266	19.2
Fe16Cr13Ni	exp	71.59	15.9	12.5	0.01	266.2	20.8
Fe16Cr13Ni	exp	71.59	15.9	12.5	0.01	273.8	25.5
Fe16Cr13Ni	exp	71.59	15.9	12.5	0.01	297	19.6
Fe16Cr13Ni	exp	71.59	15.9	12.5	0.01	297.7	21.6
Fe16Cr13Ni	exp	71.59	15.9	12.5	0.01	297.9	20.7
Fe16Cr13Ni	exp	71.59	15.9	12.5	0.01	297.9	24.4

Continued on next page

Table A.17 – continued from previous page

name	method	Fe	Cr	Ni	C	T	SFE
Fe16Cr13Ni	exp	71.59	15.9	12.5	0.01	298	20.1
Fe16Cr13Ni	exp	71.59	15.9	12.5	0.01	298	26.1
Fe16Cr13Ni	exp	71.59	15.9	12.5	0.01	298.4	23.4
Fe16Cr13Ni	exp	71.59	15.9	12.5	0.01	329	31.1
Fe16Cr13Ni	exp	71.59	15.9	12.5	0.01	333.8	25
Fe16Cr13Ni	exp	71.59	15.9	12.5	0.01	334	24
Fe16Cr13Ni	exp	71.59	15.9	12.5	0.01	335.2	20.5
Fe16Cr13Ni	exp	71.59	15.9	12.5	0.01	373	25.2
Fe16Cr13Ni	exp	71.59	15.9	12.5	0.01	373.6	26.3
Fe18Cr12Ni	exp	70.192	17.8	12	0.008	94.3	10.8
Fe18Cr12Ni	exp	70.192	17.8	12	0.008	94.3	11.9
Fe18Cr12Ni	exp	70.192	17.8	12	0.008	181.3	16.1
Fe18Cr12Ni	exp	70.192	17.8	12	0.008	182.5	17.3
Fe18Cr12Ni	exp	70.192	17.8	12	0.008	220.5	20.6
Fe18Cr12Ni	exp	70.192	17.8	12	0.008	223.1	18.8
Fe18Cr12Ni	exp	70.192	17.8	12	0.008	235.2	23.4
Fe18Cr12Ni	exp	70.192	17.8	12	0.008	236.5	17.4
Fe18Cr12Ni	exp	70.192	17.8	12	0.008	275.1	20.5

Continued on next page

Table A.17 – continued from previous page

name	method	Fe	Cr	Ni	C	T	SFE
Fe18Cr12Ni	exp	70.192	17.8	12	0.008	275.3	25.3
Fe18Cr12Ni	exp	70.192	17.8	12	0.008	291.1	28.9
Fe18Cr12Ni	exp	70.192	17.8	12	0.008	291.1	30
Fe18Cr12Ni	exp	70.192	17.8	12	0.008	291.2	28.2
Fe18Cr12Ni	exp	70.192	17.8	12	0.008	292.4	19.5
Fe18Cr12Ni	exp	70.192	17.8	12	0.008	292.9	22.8
Fe18Cr12Ni	exp	70.192	17.8	12	0.008	293	24.5
Fe18Cr12Ni	exp	70.192	17.8	12	0.008	333.6	28.1
Fe18Cr12Ni	exp	70.192	17.8	12	0.008	334.2	33.2
Fe18Cr14Ni	exp	68	18	14	—	107.9	23.3
Fe18Cr14Ni	exp	68	18	14	—	118.6	23.3
Fe18Cr14Ni	exp	68	18	14	—	152.9	25.7
Fe18Cr14Ni	exp	68	18	14	—	157.7	27.8
Fe18Cr14Ni	exp	68	18	14	—	157.7	28.8
Fe18Cr14Ni	exp	68	18	14	—	184.2	26
Fe18Cr14Ni	exp	68	18	14	—	184.2	26.8
Fe18Cr14Ni	exp	68	18	14	—	216.1	29.7
Fe18Cr14Ni	exp	68	18	14	—	216.8	28.5

Continued on next page

Table A.17 – continued from previous page

name	method	Fe	Cr	Ni	C	T	SFE
Fe18Cr14Ni	exp	68	18	14	—	241.3	32.3
Fe18Cr14Ni	exp	68	18	14	—	261.2	35
Fe18Cr14Ni	exp	68	18	14	—	298.5	35.2
Fe18Cr14Ni	exp	68	18	14	—	298.7	42.1
Fe18Cr14Ni	exp	68	18	14	—	299.2	34

Table A.18: Petrov1985 [22]: Fe-Cr-Ni

name	method	Fe	Cr	Ni	T	SFE
	exp	72.5298	16.8828	10.5874	298.15	16
	exp	67.3201	16.8395	15.8404	298.15	28
	exp	62.137	16.7965	21.0666	298.15	35
	exp	75.3949	14.0397	10.5654	298.15	16
	exp	70.6132	18.7847	10.6021	298.15	20
	exp	65.7981	23.5628	10.6391	298.15	25
	exp	69.7691	9.28008	20.9508	298.15	60
	exp	65.0089	13.9681	21.023	298.15	40
	exp	60.2158	18.6885	21.0957	298.15	35
	exp	55.3893	23.4417	21.1689	298.15	45

Table A.19: Petrov1985 [22]: Fe-Mn

name	method	Fe	Mn	T	SFE
	exp	85.2076	14.7924	298.15	25
	exp	80.2607	19.7393	298.15	28
	exp	75.3058	24.6942	298.15	27
	exp	70.3427	29.6573	298.15	42

Table A.20: Petrov1993 [25]: Fe-Mn

name	method	Fe	Mn	C	T	SFE
	exp	77.78	22	0.22	298.15	32.4
	exp	77.17	22	0.83	298.15	22.6
	exp	76.28	22	1.72	298.15	32.8
	exp	74.79	22	3.21	298.15	33.6

Table A.21: Petrov2003 [29]: Fe-Cr-Mn

name	method	Fe	Cr	Mn	N	T	SFE
Fe-15Cr-17Mn	exp	67.94	15	17	0.06	298.15	24 $\pm$ 1.2
Fe-15Cr-17Mn-0.2N	exp	67.77	15	17	0.23	298.15	25.1 $\pm$ 1.2
Fe-15Cr-17Mn-0.5N	exp	67.52	15	17	0.48	298.15	21.1 $\pm$ 1.1
Fe-15Cr-17Mn-0.9N	exp	67.11	15	17	0.89	298.15	41.6 $\pm$ 2

Table A.22: Petrov2003 [29]: Fe-Cr-Ni

name	method	Fe	Cr	Ni	C	N	Mn	T	SFE
Fe-18Cr-10Ni	exp	70.4	17.8	10.6	—	—	1.2	298.15	25 $\pm$ 1.2
Fe-18Cr-10Ni-0.05C	exp	70.64	17.9	10.5	0.06	—	0.9	298.15	30 $\pm$ 1.4
Fe-18Cr-10Ni-0.1C	exp	71.11	18.1	10.1	0.09	—	0.6	298.15	34 $\pm$ 1.5
Fe-18Cr-10Ni-0.15C	exp	70.69	18.1	10.6	0.11	—	0.5	298.15	39 $\pm$ 1.8
Fe-18Cr-16Ni-10Mn	exp	55.79	18.5	16.1	—	0.01	9.6	298.15	44 $\pm$ 2
Fe-18Cr-16Ni-10Mn-0.1N	exp	55.73	18.5	16.1	—	0.07	9.6	298.15	47 $\pm$ 2.3
Fe-18Cr-16Ni-10Mn-0.2N	exp	55.59	18.5	16.1	—	0.21	9.6	298.15	55 $\pm$ 2.7
Fe-18Cr-16Ni-10Mn-0.3N	exp	55.49	18.5	16.1	—	0.31	9.6	298.15	62 $\pm$ 3
Fe-18Cr-16Ni-10Mn-0.4N	exp	55.4	18.5	16.1	—	0.4	9.6	298.15	65 $\pm$ 3.2
Fe-18Cr-16Ni-10Mn-0.5N	exp	55.26	18.5	16.1	—	0.54	9.6	298.15	53 $\pm$ 2.6

Table A.23: Petrov2003 [29]: Fe-Mn

name	method	Fe	Mn	C	T	SFE
Fe-22Mn	exp	77.97	22	0.03	298.15	29 $\pm$ 1.4
Fe-22Mn-0.1C	exp	77.87	22	0.13	298.15	23 $\pm$ 1.2
Fe-22Mn-0.3C	exp	77.67	22	0.33	298.15	26 $\pm$ 1.3
Fe-22Mn-0.7C	exp	77.31	22	0.69	298.15	29 $\pm$ 1.5

Table A.24: Shin2001 [28]: Fe-Cr-Ni

name	method	Fe	Cr	Ni	C	N	Si	P	S	Mn	Mo	M_d
304	exp	71.524	18.07	8.5	0.05	0.037	0.56	0.025	0.004	1.05	0.18	322

Table A.25: Silcock1966 [10]: Fe-Cr-Ni

name	method	Fe	Cr	Ni	C	N	O	Si	P	S	Mn	Co	T	SFE
A1	exp	68.674	15.3	15.9	0.02	—	0.03	—	0.004	0.012	0.06	—	298.15	23 $\pm$ 4.6
A2	exp	55.103	15.8	23	0.007	6	0.03	—	0.01	0.01	0.04	—	298.15	28 $\pm$ 5.6

Continued on next page

Table A.25 – continued from previous page

name	method	Fe	Cr	Ni	C	N	O	Si	P	S	Mn	Co	T	SFE
A10	exp	42.39	15.3	15	0.006	7	0.04	—	0.01	0.014	0.04	20.2	298.15	12 $\pm$2.4
A55	exp	64.228	15.9	15.8	0.017	4	0.01	0.04	0.002	0.002	0.001	—	298.15	21 $\pm$4.2
A57	exp	52.857	15.4	24.7	0.011	7	0.01	0.015	0.002	0.002	0.003	—	298.15	30.5 $\pm$6.1
A71	exp	65.272	15.5	15.8	0.004	2	0.013	1.4	0.008	0.003	—	—	298.15	11 $\pm$2.2
A203	exp	64.35	16	10.1	—	—	—	—	—	—	—	9.55	298.15	8 $\pm$1.6

Table A.26: Singh1985 [23]: Fe-Cr-Ni

name	method	Fe	Cr	Ni	C	Si	$A_s^{\alpha' \to \gamma}$	$A_s^{\epsilon \to \gamma}$
304	exp	68.63	18.8	11.5	0.07	1	673	473

Table A.27: Swann1963 [8]: Fe-Cr-Ni

name	method	Fe	Cr	Ni	C	N	T	SFE
Tab1:line1	exp	74.4	17.6	7.9	0.06	0.04	298.15	7 $(+1.6/-1.7)$
Tab1:line2	exp	69.676	17.6	12.7	0.02	0.004	298.15	15.1 $(+1.8/-1.6)$
Tab1:line3	exp	64.366	17.8	17.8	0.03	0.004	298.15	19.1 $(+1.6/-1.1)$

Continued on next page

Table A.27 – continued from previous page

name	method	Fe	Cr	Ni	C	N	T	SFE
Tab1:line9	exp	74.83	17.9	7.1	0.06	0.11	298.15	5.9 $(+1.2/-1.2)$
Tab1:line10	exp	68.96	18.1	12.8	0.02	0.12	298.15	12.6 $(+1.8/-1.5)$

Table A.28: Tavares2000 [27]: Fe-Cr-Ni

name	method	Fe	Cr	Ni	C	Si	S	$A_s^{\alpha'\to\gamma}$	$A_5 0^{\alpha'\to\gamma}$	$A_f^{\alpha'\to\gamma}$
	exp	72.946	18.34	8.53	0.066	0.1	0.018	718.15 ± 5	838.15 ± 5	997.15 ± 5
	exp	72.946	18.34	8.53	0.066	0.1	0.018	713.15 ± 5	832.15 ± 5	978.15 ± 5
	exp	72.946	18.34	8.53	0.066	0.1	0.018	706.15 ± 5	822.15 ± 5	967.15 ± 5
	exp	72.946	18.34	8.53	0.066	0.1	0.018	708.15 ± 5	828.15 ± 5	969.15 ± 5
	exp	72.946	18.34	8.53	0.066	0.1	0.018	706.15 ± 5	846.15 ± 5	983.15 ± 5

Acknowledgements

Obviously, this work could not be done without help of many others. I am most grateful to my supervisor, Prof. Claudia Draxl, who gave me a chance to enter the field, and taught me how to do research. I would like to appreciate her effort in providing a scientific — and, at the same time, friendly — environment at the *chair of atomistic modeling and design of materials* (AMDM) at the University of Leoben.

I am extremely thankful to Prof. Peter Puschnig, who often helped me by his brilliant scientific advises. I would like to appreciate his effort in reading the thesis and giving me suggestions for its improvement.

I am grateful to Dr. Andrei Reyes-Huamantinco for steady scientific support, in particular, for introducing me to the EMTO code, and also for discussing my results. His suggestions helped me to improve this thesis a lot.

I would like to thank Prof. Andrei Ruban, who kindly provided us the EMTO code. His willingness to answer our code-related questions is appreciated.

I would like to appreciate fruitful discussions with Dr. Jürgen Spitaler, Dr. Lorenz Romaner, and Dr. Vsevolod Razumovskiy. Jürgen Spitaler also helped me with translating the thesis abstract to German.

I am grateful to Maxim N. Popov, my best friend during my PhD program in Leoben, for many discussions and help in science, computer techniques, *etc.*

This work was carried out in the framework of the Competence Centers for Excellent Technologies (COMET) on Integrated Research in Materials, Processing and Product Engineering (MPPE), financed by the Austrian Federal Government and the Styrian Provincial Government. We thank our industrial partners, the voestalpine AG, Linz, Austria, and Bohler Special Steels, Kapfenberg, Austria, for substantial financial support.

Finally, I would like to thank my parents and my wife, whose love and support are simply invaluable.

List of Figures

List of Tables

References

[1] E. Photos. **The Question of Meteoritic versus Smelted Nickel-Rich Iron: Archaeological Evidence and Experimental Results**. *World Archaeology*, **20**(3, Archaeometallurgy):403–421, February 1989. Publisher: Taylor & Francis, Ltd. 1

[2] Peter R. Knowles. *Design of Structural Steelwork*. Taylor & Francis Group, 2 edition, 2005. ISBN (Adobe eReader Format): 0-203-26795-8, ISBN (Print Edition):0-903384-59-0. 1, 22

[3] Anita Wolff. *Britannica Concise Encyclopedia*. Encyclopedia Britannica, Inc., 2006. ISBN13: 978-1-59339-492-9. 1

[4] There are numerous institutes performing researches in material science and metallurgy with special focus on iron and steels: *American Iron and Steel Institute (AISI)* [152], *The Iron and Steel Institute of Japan* [153], *Stahlinstitut VDEh* [154], *etc.* There are also scientific and engineering journals reflecting the development trend of science and technology in iron and steel industry: *Iron and Steel Technology* [155], *Steel Research International* [156], *ISIJ International* [157], *Journal of Iron and Steel Research, International* [158], *etc.* 1

[5] Georg Frommeyer, Udo Brüx, and Peter Neumann. **Supra-Ductile and High-Strength Manganese-TRIP/TWIP Steels for High Energy Absorption Purposes**. *ISIJ Int.*, **43**(3):438–446, May 2003. 1, 13, 18, 71

[6] O. Grässel, L. Krüger, G. Frommeyer, and L. W. Meyer. **High strength Fe–Mn–(Al, Si) TRIP/TWIP steels development—properties—application**. *Int. J. Plast.*, **16**(10–11):1391–1409, 2000. 18

[7] S. Allain, J. P. Chateaua, O. Bouazizb, S. Migota, and N. Guelton. **Correlations between the calculated stacking fault energy and the plasticity mechanisms in Fe–Mn–C alloys**. *Mater. Sci. Eng., A*, **387-389**:158–162, Dec 2004. 1, 13, 18, 71

[8] P. R. Swann. **Dislocation Substructure vs Transgranular Stress Corrosion Susceptibility Of Single Phase Alloys**. *Corrosion*, **19**:102t–112t, March 1963. 1, 4, 150, 163

[9] J. F. Breedis. **Martensitic Transformations in Iron-Chromium-Nickel Alloys**. *Transactions of the Metallurgical Society of AIME*, **230**:1583–1596, December 1964. 111, 136, 163

[10] J. M. Silcock, R. W. Rookes, and J. Barford. **Twin frequency and stacking fault energy in austenite steels**. *J. Iron Steel Inst.*, **204**:623–627, 1966. 149, 163

[11] R. Fawley, M. A. Quader, and R. A. Dodd. **Compositional Effects on Deformation Modes Annealing Twin Frequencies and Stacking Fault Energies of Austenitic Stainless Steels**. *Trans. TMS-AIME*, **242**(5):771–776, May 1968. ISSN: 0543-5722. 51, 137, 163

[12] P. C. J. Gallagher. **The Influence of Alloying, Temperature, and Related Effects on the Stacking Fault Energy**. *Metallurgical Transactions*, **1**:2429–2461, September 1970. 138, 163

[13] F. Lecroisey and B. Thomas. **On the variation of the Intrinsic Stacking Fault Energy with Temperature in Fe-18 Cr-12 Ni Alloys**. *Phys. Stat. Sol. A*, **2**:K217–K220, 1970. 140, 163

[14] J. F. Breedis and L. Kaufman. **Formation of hcp and bcc Phases in Austenitic Iron Alloys**. *Metallurgical Transactions*, **2**(9):2359–2371, September 1971. 136, 163

[15] R. M. Latanision and A. W. Ruff. **The Temperature Dependence of Stacking Fault Energy in Fe-Cr-Ni Alloys**. *Metall. Trans.*, **2**:505–509, February 1971. 139, 163

[16] F. Lecroisey and A. Pineau. **Martensitic transformations induced by plastic deformation in the Fe-Ni-Cr-C system**. *Metall. Trans.*, **3**(2):391–400, February 1972. Print ISSN: 0360-2133, Online ISSN: 1543-1916, Publisher: Springer-Verlag. 140, 163

[17] Francois Abrassart. **Stress-Induced $\gamma \rightarrow \alpha'$ Martensitic Transformation in Two Carbon Stainless Steels. Application to Trip Steels**. *Metall. Trans.*, **4**(9):2205–2216, September 1973. Print ISSN: 0360-2133 Online ISSN: 1543-1916 Publisher: Springer-Verlag. 85, 111, 132, 163

[18] G. B. Olson and Morris Cohen. **A general mechanism of martensitic nucleation: Part I. General concepts and the fcc→hcp transformation**. *Metall. Trans. A*, **7**(12):1897–1904, December 1976. Print ISSN: 0360-2133, Online ISSN: 1543-1940, Publisher: Springer-Verlag. 143, 163

[19] C. C. Bampton, I. P. Jones, and M. H. Loretto. **Stacking fault energy measurements in some austenitic stainless steels**. *Acta Metall.*, **26**(1):39–51, January 1978. 19, 134, 163

[20] K. B. Guy, E. P. Butler, and D. R. F. West. **Reversion of bcc α' martensite in Fe–Cr–Ni austenitic stainless steels**. *Metal Science*, **17**(4):167–176, April 1983. 111, 139, 163

[21] H. M. Ledbetter. **Monocrystal-Polycrystal Elastic Constants of a Stainless Steel**. *Phys. Stat. Sol. A*, **85**(1):89–96, 1984. 93, 141, 163

[22] Yu. N. Petrov. **Effect of Alloying on the Stacking Fault Energy of Austenite in Steel**. *Phys. Met.*, **6**(4):735–741, 1985. ISSN: 0275-9144. 50, 146, 147, 163

[23] Jogender Singh. **Influence of deformation on the transformation of austenitic stainless steels**. *J. Mater. Sci.*, **20**(9):3157–3166, September 1985. Print ISSN: 0022-2461 Online ISSN: 1573-4803 Publisher: Kluwer Academic Publishers. 110, 150, 163

[24] Luis G. Martinez, Kengo Imakuma, and Angelo F. Padilha. **Influence of niobium on stacking-fault energy of all-austenite stainless steels**. *Steel Res.*, **63**(5):221–223, May 1992. ISSN: 0177-4832. 141, 163

[25] Yu. N. Petrov. **On the carbon distribution at structural imperfections in manganese austenite**. *Scr. Metall. Mater.*, **29**(11):1471–1476, Dec 1993. 51, 70, 147, 157, 163

[26] James Chen-Min Li. *Microstructure and Properties of Materials*, **2**. World Scientific Pub Co Inc, September 2000. ISBN-10: 9810241801, ISBN-13: 978-9810241803. 141, 163

[27] S. S. M. Tavares, D. Fruchart, and S. Miraglia. **A magnetic study of the reversion of martensite α' in a 304 stainless steel**. *J. Alloys Compd.*, **307**(1–2):311–317, July 2000. 111, 151, 163

[28] Hong Chul Shin, Tae Kwon Ha, and Young Won Chang. **Kinetics of deformation induced martensitic transformation in a 304 stainless steel**. *Scr. Mater.*, **45**(7):823–829, October 2001. 110, 149, 163

[29] Yu. N. Petrov. **Effect of carbon and nitrogen on the stacking fault energy of high-alloyed iron-based austenite**. *Z. Metallkd.*, **94**(9):1012–1016, September 2003. ISSN: 0044-3093. 148, 149, 163

[30] Axel Knutsson, Peter Hedström, and Magnus Odén. **Reverse martensitic transformation and resulting microstructure in a cold rolled metastable austenitic stainless steel**. *Steel Res. Int.*, **79**(6):433–439, 2008. ISSN: 1611-3683. 111, 139, 163

[31] M. Ojima, Y. Adachi, Y. Tomota, Y. Katada, Y. Kaneko, K. Kuroda, and H. Saka. **Weak Beam TEM Study on Stacking Fault Energy of High Nitrogen Steels**. *Steel Res. Int.*, **80**(7):477–481, July 2009. 142, 163

[32] P. Behjati and A. Najafizadeh. **Role of Chemical Driving Force in Martensitic Transformations of High-Purity Fe-Cr-Ni Alloys**. *Metall. Mater. Trans. A*, **42**(12):3752–3760, December 2011. 1, 4, 85, 111, 135, 163

[33] P. Hohenberg and W. Kohn. **Inhomogeneous Electron Gas**. *Phys. Rev.*, **136**(3B):B864–B871, November 1964. 2, 35, 36, 51

[34] W. Kohn and L. J. Sham. **Self-Consistent Equations Including Exchange and Correlation Effects**. *Phys. Rev.*, **140**(4A):A1133–A1138, November 1965. 35, 36, 38, 40, 51

[35] R. O. Jones and O. Gunnarsson. **The density functional formalism, its applications and prospects**. *Rev. Mod. Phys.*, **61**(3):689–746, July 1989.

[36] Walter Kohn. **Nobel Lecture: Electronic structure of matter — wave functions and density functionals**. *Rev. Mod. Phys.*, **71**(5):1253–1266, October 1999. 2, 39, 40

[37] L. Vitos, P. A. Korzhavyi, and B. Johansson. **Evidence of Large Magnetostructural Effects in Austenitic Stainless Steels**. *Phys. Rev. Lett.*, **96**(11):117210–117213, Mar 2006. 2, 52, 71, 78, 103, 108, 158

[38] Andrei Reyes-Huamantinco, Peter Puschnig, Claudia Ambrosch-Draxl, Oleg E. Peil, and Andrei V. Ruban. **Stacking-fault energy and anti-Invar effect in Fe-Mn alloy from first principles**. *Phys. Rev. B*, **86**(6):060201, Aug 2012. 2, 52, 76, 97

[39] S. Kibey, J. B. Liu, M. J. Curtis, D. D. Johnson, and H. Sehitoglu. **Effect of nitrogen on generalized stacking fault energy and stacking fault widths in high nitrogen steels**. *Acta Mater.*, **54**(11):2991–3001, Jun 2006. 2, 51, 73

[40] Afshin Abbasi, Alexey Dick, Tilmann Hickel, and Jörg Neugebauer. **First-principles investigation of the effect of carbon on the stacking fault energy of Fe–C alloys**. *Acta Mater.*, **59**(8):3041–3048, May 2011. 2, 51, 52, 64, 67, 69, 70, 157

[41] Hojjat Gholizadeh, Claudia Draxl, and Peter Puschnig. **The influence of interstitial carbon on the γ-surface in austenite**. *Acta Mater.*, **61**(1):341–349, January 2013. 2, 73

[42] P. Blaha, K. Schwarz, G. Madsen, D. Kvasnicka, and J. Luitz. **WIEN2k**. `http://www.wien2k.at`. 2, 44

[43] Paul Soven. **Coherent-Potential Model of Substitutional Disordered Alloys**. *Phys. Rev.*, **156**(3):809–813, April 1967. 2, 47

[44] D. W. Taylor. **Vibrational Properties of Imperfect Crystals with Large Defect Concentrations**. *Phys. Rev.*, **156**(3):1017–1029, April 1967.

[45] B. L. Gyorffy. **Coherent-Potential Approximation for a Nonoverlapping-Muffin-Tin-Potential Model of Random Substitutional Alloys**. *Phys. Rev. B*, **5**(6):2382–2384, March 1972. 2, 47, 48, 72

[46] B. L. Gyorffy, A. J. Pindor, J. Staunton, G. M. Stocks, and H. Winter. **A first-principles theory of ferromagnetic phase transitions in metals**. *J. Phys. F: Met. Phys.*, **15**(6):1337–1386, 1985. 2, 48, 72

[47] Levente Vitos. *Computational Quantum Mechanics for Materials Engineers: The EMTO Method and Applications*. Springer, 1 edition, August 2007. ISBN-10: 1846289505, ISBN-13: 978-1846289507. 2, 47, 79, 108

[48] C. Cheng, R. J. Needs, V. Heine, and N. Churcher. **Confirmation of an ANNNI-Like Model for Polytypism in SiC**. *Europhys. Lett.*, **3**(4):475–479, Feb 1987. 3, 51, 72, 74

[49] P. J. H. Denteneer and W. van Haeringen. **Stacking-Fault Energies in Semiconductors from First-Principles Calculations**. *J. Phys. C: Solid State Phys.*, **20**(32):L883–L887, 1987. 3, 51, 72, 74

[50] John Price Hirth and Jens Lothe. *Theory of Dislocations*. John Wiley & Sons, 2 edition, 1982. ISBN: 0-471-09125-1. 5, 9, 10, 14, 15, 64

[51] Donald E. Sands. *Introduction to Crystallography (Dover Books on Chemistry)*. W. A. Benjamin, Inc., January 1994. ISBN-10: 0486678393, ISBN-13: 978-0486678399. 6

[52] Derek Hull and D. J. Bacon. *Introduction to Dislocations*. Butterworth-Heinemann, Elsevier, fifth edition, April 2011. ISBN-10: 0080966721, ISBN-13: 978-0080966724. 9, 13, 14, 15, 18

[53] R. P. Reed and R. E. Schramm. **Relationship between stacking-fault energy and x-ray measurements of stacking-fault probability and microstrain**. *J, Appl. Phys.*, **45**(11):4705–4711, November 1974. 18, 19, 101, 162

[54] V. M. Adeev and Yu. N. Petrov. **Influence of carbon on the stacking fault energy of austenite in plain carbon steel**. *Ukrayins'kyi Fizychnyi Zhurnal*, **20**(12):2004–2007, December 1975. 19, 101

[55] Charles Kittel. *Introduction to Solid State Physics*. John Wiley & Sons, 8th edition, November 2004. ISBN-10: 047141526X, ISBN-13: 978-0471415268. 20

[56] John D. Verhoeven. *Steel Metallurgy for the Non-Metallurgist*. ASM International, 2007. 20, 23, 88

[57] T. B. Massalski, Hugh Baker, L. H. Bennett, and Joanne L. Murray. *Binary Alloy Phase Diagrams*, **2**. American Society for Metals (ASM International), 1 edition, 1986. ISBN-13: 9780871702616, ISBN-10: 0871702614. 21, 22, 29, 30, 154, 155

[58] Herman W. Pollack. *Materials Science and Metallurgy (4th Edition)*. Prentice Hall, 4 edition, January 1988. ISBN-10: 0835942872, ISBN-13: 978-0835942874. 21, 154

[59] Roger L. Brockenbrough and Frederick S. Merritt. *Structural Steel DesignerâĂŹs Handbook: AISC, AASHTO, AISI, ASTM, AREMA, and ASCE-07 Design Standards*. McGraw-Hill Professional, fourth edition, October 2005. ISBN-10: 0071432183, ISBN-13: 978-0071432184. 22

[60] Arthur C. Reardon. *Metallurgy for the Non-Metallurgist*. ASM International, second edition, Octuber 2011. ISBN-10: 1615038213, ISBN-13: 978-1615038213. 23

[61] George Krauss. *STEELS: Processing, Structure, and Performance*. ASM International, ASM International, Materials Park, Ohio 44073-0002, www.asminternational.org, third, 2005 edition, August 2005. ISBN-10: 0871708175, ISBN-13: 978-0871708175. 23, 26, 27, 31, 32, 85, 88

[62] D. H. Jack and K. H. Jack. **Invited review: Carbides and nitrides in steel**. *Mater. Sci. Eng.*, **11**(1):1–27, January 1973. 23

[63] D. E. Jiang and Emily A. Carter. **Carbon dissolution and diffusion in ferrite and austenite from first principles**. *Phys. Rev. B*, **67**(21):214103–214113, June 2003. 23, 25, 50, 52

[64] webelements. *http : //www.webelements.com/*. [link]. 23

[65] C. A. Wert. **Diffusion Coefficient of C in α-Iron**. *Phys. Rev.*, **79**(4):601–605, August 1950. 25

[66] William D. Callister. *Materials science and engineering : an introduction*. John Wiley & Sons, Inc., 7 edition, 2007. ISBN-13: 978-0-471-73696-7, ISBN-10: 0-471-73696-1. 25, 26, 27

[67] B. D. Butler and J. B. Cohen. **The location of interstitial carbon in austenite**. *J. Phys. I*, **2**(6):1059–1065, June 1992. 25, 50

[68] V. Rosato. **Comparative behavior of carbon in b.c.c. and f.c.c. iron**. *Acta Metall.*, **37**(10):2759–2763, Oct 1989. 25, 50

[69] R. P. Smith. **The Diffusivity of Carbon in Gamma Iron-Cobalt Alloys**. *Trans. TMS-AIME*, **230**(3):476–480, 1964. ISSN: 0543-5722. 25

[70] I. G. Wood, L. Vocadlo, K. S. Knight, D.P. Dobson, W. G. Marshall, G. D. Pricea, and J. Brodholta. **Thermal expansion and crystal structure of cementite, Fe3C, between 4 and 600 K determined by time-of-flight neutron powder diffraction**. *J. Appl. Cryst.*, **37**:82, 2003. 26

[71] A. K. Arzhnikov, L. V. Dobysheva, and C. Demangeat. **Structural peculiarities of cementite and their influence on magnetic characteristics**. *J. Phys.: Condens. Matter*, **19**(19):196214–196222, April 2007. 26, 69

[72] Bruce L. Bramfitt and Arlan O. Benscoter. *Metallographer's Guide: Practices and Procedures for Irons and Steels*. ASM International, December 2002. ISBN-10: 0871707489, ISBN-13: 978-0871707482. 27

[73] Pierre-Jean Cunat. *Alloying Elements in Stainless Steel and Other Chromium-Containing Alloys*. International Chromium Development Association, ICDA, 45 Rue de Lisbonne, F-75008 Paris, 2004. 27, 30

[74] Michael F. McGuire. *Stainless Steels for Design Engineers*. ASM International, December 2008. ISBN-13: 978-0-87170-717-8, ISBN-10: 0-87170-717-9, SAN: 204-7586. 27, 28, 29, 30, 31, 32

[75] J-O Andersson, Thomas Helander, Lars Höglund, Pingfang Shi, and Bo Sundman. **Thermo-Calc & DICTRA, computational tools for materials science**. *Calphad*, **26**(2):273–312, June 2002. 28, 155

[76] **Thermo-Calc**. `http://www.thermocalc.com/`. 28, 155

[77] A. H. Eichelman and F. C. Hull. **The Effect of Composition on the Temperature of Spontaneous Transformation of Austenite to Martensite in 18-8 Type Stainless Steel**. *Trans. Am. Soc. Met.*, **45**:77–104, 1953. 31, 88

[78] R. P. Reed. **The spontaneous martensitic transformations in 18% Cr, 8% Ni steels**. *Acta Metall.*, **19**(9):865–877, September 1962. 32

[79] Stanislaw M. Dubiel and Jakub Cieslak. **Sigma-phase in Fe-Cr and Fe-V alloy systems and its physical properties**. *Crit. Rev. Solid State Mater. Sci.*, **36**(4):191–208, December 2011. 32

[80] Roser Valentí. *Introduction to the Density Functional Theory*. 2009. Lecture notes presented in the "Institut for Theoretical Physics", university of Frankfurt. 33, 42, 43, 44

[81] Peter Puschnig. *Excitonic Effects in Organic Semi-Conductors - An Ab-initio Study within the LAPW Method*. PhD thesis, Karl-Frazens-Universität Graz, January 2002. 33

[82] Oleg E. Peil. *Theory of Disordered Magnets*. PhD thesis, Uppsala University, 2009. ISSN: 1651-6214, ISBN:978-91-554-7391-4. 33, 45, 46, 47

[83] Tetyana Khmelevska. *Influence of magnetic and chemical disorder on physical properties of metallic alloys*. PhD thesis, Vienna University of Technology, February 2009. 33, 45, 48

[84] Philip Peter Rushton. *Towards a Non-Local Density Functional Description of Exchange and Correlation*. PhD thesis, University of Durham, November 2002. 33

[85] Erwin Schrödinger. **DEUTSCH: Quantisierung als Eigenwertproblem (Erste Mitteilung) / ENGLISH: Quantisation as a Problem of Proper Values (Part I)**. *Ann. Physik*, **79**:361–376, 1926. 33

[86] Erwin Schrödinger. **DEUTSCH: Quantisierung als Eigenwertproblem (Zweite Mitteilung) / ENGLISH: Quantisation as a Problem of Proper Values (Part II)**. *Ann. Physik*, **79**:489–527, 1926. 33

[87] Richard M. Martin. *Electronic Structure: Basic Theory and Practical Methods*. Cambridge University Press, April 2004. ISBN-10: 0521782856, ISBN-13: 978-0521782852. 34, 35, 37, 39, 40, 42, 75, 155

[88] M. Born and J. R. Oppenheimer. **DEUTSCH: Zur Quantentheorie der Molekeln / ENGLISH: On the Quantum Theory of Molecules**. *Ann. Physik*, **84**:457, 1927. 34

[89] Robert G. Parr and Weitao Yang. *Density-Functional Theory of Atoms and Molecules*. Oxford University Press, Oxford, April 1989. ISBN: 0-19-504279-4. 37, 38, 39

[90] Murray Gell-Mann and Keith A. Brueckner. **Correlation Energy of an Electron Gas at High Density**. *Phys. Rev.*, **106**(2):364–368, April 1957. 39

[91] D. Ceperley. **Ground state of the fermion one-component plasma: A Monte Carlo study in two and three dimensions**. *Phys. Rev. B*, **18**(7):3126–3138, October 1978. 39

[92] D. M. Ceperley and B. J. Alder. **Ground State of the Electron Gas by a Stochastic Method**. *Phys. Rev. Lett.*, **45**(7):566–569, August 1980. 39

[93] John P. Perdew, Kieron Burke, and Matthias Ernzerhof. **Generalized Gradient Approximation Made Simple**. *Phys. Rev. Lett.*, **77**(18):3865–3868, October 1996. 40, 59, 94

[94] Georg K. H. Madsen, Peter Blaha, Karlheinz Schwarz, Elisabeth Sjöstedt, and Lars Nordström. **Efficient linearization of the augmented plane-wave method**. *Phys. Rev. B*, **64**(19):195134–195142, October 2001. 41, 42, 43

[95] James C. Phillips. **Energy-Band Interpolation Scheme Based on a Pseudopotential**. *Phys. Rev.*, **112**(3):685–695, November 1958. 41

[96] James C. Phillips and Leonard Kleinman. **Crystal Potential and Energy Bands of Semiconductors. IV. Exchange and Correlation**. *Phys. Rev.*, **128**(5):2098–2102, December 1962.

[97] Marvin L. Cohen and Volker Heine. **The Fitting of Pseudopotentials to Experimental Data and Their Subsequent Application**. *Solid State Physics*, **24**:37–248, 1970. 41

[98] J. C. Slater. **Wave Functions in a Periodic Potential**. *Phys. Rev.*, **51**(10):846–851, May 1937. 41

[99] Terry L. Loucks. *Augmented Plane Wave Method: a guide to performing electronic structure calculations*. W.A. Benjamin, January 1967. 41

[100] O. Krogh Andersen. **Linear methods in band theory**. *Phys. Rev. B*, **12**(8):3060–3083, October 1975. 42

[101] D. D. Koelling and G. O. Arbman. **Use of energy derivative of the radial solution in an augmented plane wave method: application to copper**. *J. Phys. F: Met. Phys.*, **5**(11):2041, 1975. 42

[102] David Singh. **Ground-state properties of lanthanum: Treatment of extended-core states**. *Phys. Rev. B*, **43**(8):6388–6392, March 1991. 43

[103] E. Sjöstedt, L. Nordström, and D. J. Singh. **An alternative way of linearizing the augmented plane-wave method**. *Solid State Commun.*, **114**(1):15–20, March 2000. 44

[104] K. Schwarz, P Blaha, and G. K. H. Madsen. **Electronic structure calculations of solids using the WIEN2k package for material sciences**. *Comput. Phys. Commun.*, **147**(1–2):71–76, August 2002. 44

[105] Andrei V. Ruban and Igor A Abrikosov. **Configurational thermodynamics of alloys from first-principles: Effective cluster interactions**. *Rep. Prog. Phys.*, **71**(4):046501–046530, April 2008. 44, 45, 46, 47, 48, 77

[106] J. Korringa. **On the calculation of the energy of a Bloch wave in a metal**. *Physica*, **13**(6–7):392–400, August 1947. 45

[107] W. Kohn and N. Rostoker. **Solution of the Schrödinger Equation in Periodic Lattices with an Application to Metallic Lithium**. *Phys. Rev.*, **94**(5):1111–1120, June 1954. 45, 46

[108] Jan Zabloudil, Robert Hammerling, László Szunyogh, and Peter Weinberger. *Electron Scattering in Solid Matter: A Theoretical and Computational Treatise (Springer Series in Solid-State Sciences)*. Springer, 2005 edition, November 2004. ISBN-10: 3540225242, ISBN-13: 978-3540225249. 45, 46

[109] E. Badralexe and A. J. Freeman. ***T* operators and their matrix elements for a general periodic potential**. *Phys. Rev. B*, **36**(3):1389–1400, July 1987.

[110] A. Gonis, X. G. Zhang, A. J. Freeman, P. Turchi, G. M. Stocks, and D. M. Nicholson. **Configurational energies and effective cluster interactions in substitutionally disordered binary alloys**. *Phys. Rev. B*, **36**(9):4630–4646, September 1987.

[111] A. R. Williams and J. van W Morgan. **Multiple scattering by non-muffin-tin potentials**. *J. Phys. C: Solid State Phys.*, **5**(22):L293–L298, 1972.

[112] A. R. Williams and J. van W Morgan. **Multiple scattering by non-muffin-tin potentials: general formulation**. *J. Phys. C: Solid State Phys.*, **7**(1):37–60, January 1974. 46

[113] S.-H. Wei, L. G. Ferreira, James E. Bernard, and Alex Zunger. **Electronic properties of random alloys: Special quasirandom structures**. *Phys. Rev. B*, **42**(15):9622–9649, November 1990. 47

[114] Alex Zunger, S.-H. Wei, L. G. Ferreira, and James E. Bernard. **Special quasirandom structures**. *Phys. Rev. Lett.*, **65**(3):353–356, July 1990. 47

[115] A. V. Ruban and H. L. Skriver. **Screened Coulomb interactions in metallic alloys. I. Universal screening in the atomic-sphere approximation**. *Phys. Rev. B*, **66**(2):024201–024215, June 2002. 48

[116] A. V. Ruban, S. I. Simak, P. A. Korzhavyi, and H. L. Skriver. **Screened Coulomb interactions in metallic alloys. II. Screening beyond the single-site and atomic-sphere approximations**. *Phys. Rev. B*, **66**(2):024202–024213, June 2002. 48

[117] R. E. Schramm and R. P. Reed. **Stacking fault energies of seven commercial austenitic stainless steels**. *Metall. Mater. Trans. A*, **6**(7):1345–1351, Jul 1975. 50, 69, 70, 101, 157

[118] P. Yu Volosevich, V. N. Gridnev, and Yu. N. Petrov. **Influence of manganese and the stacking fault energy of iron–manganese alloys**. *Fiz. metal. metalloved.*, **42**(2):372–376, 1976. 50

[119] Jinichiro Nakano and Pascal J. Jacques. **Effects of the thermodynamic parameters of the hcp phase on the stacking fault energy calculations in the Fe–Mn and Fe–Mn–C systems**. *Calphad*, **34**(2):167–175, June 2010. 50

[120] P. J. Brofman and G. S. Ansell. **On the Effect of Carbon on the Stacking Fault Energy of Austenitic Stainless Steels**. *Metall. Mater. Trans. A*, **9**(6):879–880, Jun 1978. 51, 70, 157

[121] P. Blaha, K. Schwarz, G. K. H. Madsen, D. Kvasnicka, and J. Luitz. **WIEN2k, An Augmented Plane Wave + Local Orbital Program for Calculating Crystal Properties**. Technical report, Vienna University of Technology, Vienna, 2001. 51, 59

[122] R. B. McLellan and C. Ko. **The C–C interaction energy in iron-carbon solid solutions**. *Acta Metall.*, **35**(8):2151–2156, Aug 1987. 52

[123] F. D. Murnaghan. **The Compressibility of Media under Extreme Pressures**. *Proc. Nat. Acad. Sci. U.S.A.*, **30**(9):244–247, September 1944. PMCID: PMC1078704. 53, 85

[124] P. Entel, H. C. Herper, E. Hoffmann, G. Nepecks, E. F. Wassermann, M. Acet, V. Crisan, and H. Akai. **Understanding iron and its alloys from first principles**. *Philos. Mag. B*, **80**(2):141–153, 2000. 62

[125] L. Vitos, J.-O. Nilsson, and B. Johansson. **Alloying effects on the stacking fault energy in austenitic stainless steels from first-principles theory**. *Acta Mater.*, **54**(14):3821–3826, Aug 2006. 71, 108

[126] L Vitos, P. A. Korzhavyi, J-O Nilsson, and B Johansson. **Stacking fault energy and magnetism in austenitic stainless steels**. *Phys. Scr.*, **77**(6):065703–065705, June 2008. 71

[127] A. V. Ruban and H. L. Skriver. **Calculated surface segregation in transition metal alloys**. *Comput. Mater. Sci.*, **15**(2):119–143, June 1999. 72

[128] I. A. Abrikosov, S. I. Simak, B. Johansson, A. V. Ruban, and H. L. Skriver. **Locally self-consistent Green's function approach to the electronic structure problem**. *Phys. Rev. B*, **56**(15):9319–9334, October 1997. 72

[129] N. David Mermin. **Thermal Properties of the Inhomogeneous Electron Gas**. *Phys. Rev.*, **137**(5):A1441–A1443, March 1965. 75

[130] Tôru Moriya. *Spin fluctuations in itinerant electron magnetism*. Springer-Verlag Berlin, 1985. ISBN: 3-540-15422-1, ISBN: 3-387-15422-1. 75

[131] A. V. Ruban, S. Khmelevskyi, P. Mohn, and B. Johansson. **Temperature-induced longitudinal spin fluctuations in Fe and Ni**. *Phys. Rev. B*, **75**(5):054402–054408, Feb 2007. 76, 97

[132] A. van de Walle and G Ceder. **The effect of lattice vibrations on substitutional alloy thermodynamics**. *Rev. Mod. Phys.*, **74**(1):11–45, January 2002. 77

[133] Göran Grimvall. **Spin disorder in paramagnetic fcc iron**. *Phys. Rev. B*, **39**(16):12300, June 1989. 78, 79

[134] Göran Grimvall. **Polymorphism of Metals: III. *Theory of the Temperature-Pressure Phase Diagram of Iron***. *Phys. Scr.*, **13**(1):59–64, 1976. 78

[135] D. L. Williamson, S. Bukshpan, and R. Ingalls. **Search for Magnetic Ordering in hcp Iron**. *Phys. Rev. B*, **6**(11):4194–4206, December 1972. 78

[136] Göran Grimvall. **Polymorphism in Metals: II. *Electronic and Magnetic Free Energy***. *Phys. Scr.*, **12**(3):173, 1975. 78

[137] Wolfgang Pfeiler. *Alloy Physics: A Comprehensive Reference*. WILEY-VCH Verlag GmbH & Co. KGaA, 1st edition, September 2007. Print ISBN: 978-3-527-31321-1, Online ISBN: 978-3-527-61419-6. 78

[138] Enrico Fermi. **ITALIAN: Sulla quantizzazione del gas perfetto monoatomico / ENGLISH: On the Quantization of the Monoatomic Ideal Gas**. *Rend. Lincei*, **3**:145–149, 1926. 79

[139] P. A. M. Dirac. **On the Theory of Quantum Mechanics**. *Proc. R. Soc. London, Ser. A*, **112**(762):661–677, October 1926. 79

[140] D. Liberman, J. T. Waber, and Don T. Cromer. **Self-Consistent-Field Dirac-Slater Wave Functions for Atoms and Ions. I. Comparison with Previous Calculations**. *Phys. Rev.*, **137**(1A):A27–A34, January 1965. 83, 162

[141] U. von Barth and C. D. Gelatt. **Validity of the frozen-core approximation and pseudopotential theory for cohesive energy calculations**. *Phys. Rev. B*, **21**(6):2222–2228, March 1980. 82

[142] Pat L. Mangonon and Gareth Thomas. **The martensite phases in 304 stainless steel**. *Metall. Trans.*, **1**(6):1577–1586, June 1970. 85

[143] M. Humbert, B. Petit, B. Bolle, and N. Gey. **Analysis of the $\gamma - \epsilon - \alpha'$ variant selection induced by 10% plastic deformation in 304 stainless steel at -60 °C**. *Mater. Sci. Eng., A*, **454–455**:508–517, April 2007.

[144] Cyril Cayron, Françoise Barcelo, and Yann de Carlan. **The mechanisms of the fccâĂŞbcc martensitic transformation revealed by pole figures**. *Acta Mater.*, **58**(4):1395–1402, February 2010.

[145] Cyril Cayron, Françoise Barcelo, and Yann de Carlan. **Reply to âĂIJComments on âĂŸThe mechanisms of the fcc–bcc martensitic transformation revealed by pole figuresâĂŹ âĂİ**. *Scr. Mater.*, **64**(1):103–106, January 2011. 85

[146] L. Delczeg, B. Johansson, and L. Vitos. ***Ab initio* description of monovacancies in paramagnetic austenitic Fe-Cr-Ni alloys**. *Phys. Rev. B*, **85**(17):174101–174107, May 2012. 90

[147] H. L. Zhang, N. Al-Zoubi, B. Johansson, and L. Vitos. **Alloying effects on the elastic parameters of ferromagnetic and paramagnetic Fe from first-principles theory**. *J. Appl. Phys.*, **110**(7):073707–073718, October 2011.

[148] M. Ekholm and I. A. Abrikosov. **Structural and magnetic ground-state properties of γ-FeMn alloys from *ab initio* calculations**. *Phys. Rev. B*, **84**(10):104423–104438, Sep 2011. 90

[149] John P. Perdew and Yue Wang. **Accurate and simple analytic representation of the electron-gas correlation energy**. *Phys. Rev. B*, **45**(23):13244–13249, June 1992. 94

[150] A. V. Ruban, S. Shallcross, S. I. Simak, and H. L. Skriver. **Atomic and magnetic configurational energetics by the generalized perturbation method**. *Phys. Rev. B*, **70**(12):125115–125133, September 2004. 94

[151] S. Cottenier, B. De Vries, J. Meersschaut, and Rots. M. **What density-functional theory can tell us about the spin-density wave in Cr**. *J. Phys.: Condens. Matter*, **14**(12):3275–3283, March 2002. 94

[152] **American Iron and Steel Institute (AISI)**. `http://www.steel.org`. 164

[153] **The Iron and Steel Institute of Japan**. `https://www.isij.or.jp`. 164

[154] **DEUTSCH: Stahlinstitut VDEh / ENGLISH: Steel Institute (VDEh)**. `http://www.stahl-online.de/english/obere_Navigation/The_StahlZentrum/Steel_Institute_VDEh.php`. 164

[155] *Iron & Steel Technology*. The Association for Iron & Steel Technology (AIST), 1999–present. 164

[156] *Steel Research International*. Wiley-VCH Verlag, 2003–present. Print ISSN: 1611-3683, Online ISSN: 1869-344X. 164

[157] *ISIJ International*. The Iron and Steel Institute of Japan, 1961–present. 164

[158] *Journal of Iron and Steel Research, International*. Elsevier Ltd., 1996–present. ISSN: 1006-706X, Sponsored by Central Iron and Steel Research Institute. 164